2-2-2016

Controlling the structure and dynamics of magnetoresponsive particle suspensions for enhanced transport phenomena

Kyle J. Solis

Kyle J. Solis
Candidate

Chemical and Biological Engineering
Department

This dissertation is approved, and it is acceptable in quality and form for publication:

Approved by the Dissertation Committee:

Dr. Dimiter N. Petsev , Chairperson

Dr. James E. Martin

Dr. Sang Eon Han

Dr. Frank H. van Swol

Dr. Peter Vorobieff

CONTROLLING THE STRUCTURE AND DYNAMICS OF MAGNETORESPONSIVE PARTICLE SUSPENSIONS FOR ENHANCED TRANSPORT PHENOMENA

by

KYLE J. SOLIS

B.S., Chemical Engineering, University of New Mexico, 2003
M.S., Chemical Engineering, University of New Mexico, 2010

DISSERTATION

Submitted in Partial Fulfillment of the
Requirements for the Degree of

Doctor of Philosophy
Engineering

The University of New Mexico
Albuquerque, New Mexico

May, 2015

Dedications

I dedicate this dissertation to my advisor, mentor, and friend Dr. James E. Martin. Without his undying enthusiasm, insatiable curiosity, brilliant intellect, and infinite patience the work comprising this dissertation would never have come to fruition. Jim, the last eight years have truly been a privilege, an honor, and a grand adventure! Thank you.

I also thank my loving parents, Bobbie and Joey, and my brother Tony for their unconditional support and always believing in me.

I also thank my wonderful friends Doug and Nate for always being so supportive and patient with me over the years.

Finally, I thank Therese for being a guiding light in my life.

Acknowledgements

Research Advisor

Dr. James E. Martin, PhD (Sandia National Laboratories)

Dissertation Committee Chair

Dr. Dimiter N. Petsev, PhD (University of New Mexico)

Dissertation Committee Members

Dr. Sang Eon Han, PhD (University of New Mexico)

Dr. Frank van Swol, PhD (Sandia National Laboratories, University of New Mexico)

Dr. Peter Vorobieff, PhD (University of New Mexico)

Research Institution

The entirety of this work was performed at Sandia National Laboratories.*

* Sandia National Laboratories is a multi-program laboratory managed and operated by Sandia Corporation, a wholly owned subsidiary of Lockheed Martin Corporation, for the U.S. Department of Energy's National Nuclear Security Administration under contract DE-AC04-94AL85000.

Funding

The work comprising this dissertation was supported by the Division of Materials Science, Office of Basic Energy Sciences, U.S. Department of Energy (DOE).

Finally, the author gratefully acknowledges Vladimir Raksha, Paul Coombs, Tom Markantes, Bill Kittler, and Kees-Jan Delst at JDSU Flex Products and Matt Groo at Novamet for supplying magnetic materials.

Controlling the Structure and Dynamics of Magnetoresponsive Particle Suspensions for Enhanced Transport Phenomena

by

Kyle J. Solis

B.S., Chemical Engineering, University of New Mexico, 2003
M.S., Chemical Engineering, University of New Mexico, 2010
Ph.D., Engineering, University of New Mexico, 2015

ABSTRACT

The work contained herein describes the use of various magnetic fields to control the structure and dynamics of magnetic particle suspensions, with the practical aim of enhancing momentum, heat, and mass transport. The magnetic fields are often multiaxial and can consist of up to three orthogonal components that may be either static (dc), time-dependent (ac), or some combination thereof. The magnetic particles are composed of a ferromagnetic material—such as iron, nickel, cobalt, or Permalloy—and can exist in a variety of shapes, including spheres, platelets, and rods. The *shape* of the particles is particularly important, as this can determine the type of behavior the suspension exhibits and can strongly affect the efficacy of various transport properties. The continuous phase can be almost any fluid so long as it possesses a viscosity that allows the particles to orient and aggregate in response to the applied field. Additionally, if the liquid is polymerizable (*e.g.*, an epoxy system), then composite materials with particular, field-directed particle assemblies can be created.

Given the many combinations of various particles, suspending fluids, and magnetic fields, a vast array of behavior is possible: the formation of anisotropic particle structures for directed heat transport for use as advanced thermal interface materials; the stimulation of emergent dynamics in platelet suspensions, which give

rise to field-controllable flow lattices; and the creation of *vortex fluids* that possess a uniform torque density, enabling such strange behaviors as active wetting, a negative viscosity and striking biomimetic dynamics. Because the applied fields used to produce many of these phenomena are *uniform* and modest in strength, such adaptive fluids open up the possibility of tuning the degree of mixing or heat/mass transfer for specific operating conditions in a number of processes, ranging from the microscale to the industrial scale. Moreover, the very nature of magnetism provides for the manipulation of magnetic materials in a *noncontact* manner, making the application of these effects simple and robust by eliminating the need for complex, moving parts that may require maintenance and be prone to failure.

Table of Contents

Preface

Far and away the best prize that life has to offer is the chance to work hard at work worth doing.—Theodore Roosevelt

Due to the possibility that the structure of this dissertation may appear somewhat unorthodox, I thought it suitable to provide a preface to orient the reader. The work contained herein, perhaps seemingly disparate at first glance, is unified by a common theme as exemplified by the title: *Controlling the structure and dynamics of magnetoresponsive particle suspensions for enhanced transport phenomena*. Despite this common theme, however, each research topic is sufficiently distinct as to deserve its own treatment. As such, this dissertation is comprised of four parts:

Part I: Directed heat transfer in magnetic-field–structured composites presents a class of magnetic particle-polymer composite materials for use as enhanced thermal interface materials (TIMs). Unlike conventional TIMs, which rely upon very high loadings (~70 vol.%) of highly thermally conductive particles resulting in a paste-like consistency and achieving only modest thermal conductivities; our approach makes use of magnetic fields to structure the magnetic particle phase, which is suspended in the polymer resin, prior to curing. In this way, we can optimize a composite's effective thermal conductivity (in any desired direction) at a given volume fraction without incurring the penalty of an unworkable viscosity. Additionally, the use of anisometric particles such as platelets is shown to substantially increase the effective thermal conductivity of the composite as compared to spherical particles.

Part II: Vortex magnetic field mixing introduces a technique for mixing liquids that relies on the propensity of magnetic particles in a suspension to

form numerous chains that whirl around in perpetual pursuit of the dynamic magnetic field vector of the vortex magnetic field, thereby agitating the suspending liquid. The concept of a vortex magnetic field (which underlies this technique) and the mechanism responsible for mixing are established. Also covered, are the experimentally-observed trends for the mixing torque on the relevant parameters (*i.e.*, magnetic field strength, frequency, vortex field angle, and fluid viscosity), which compare well with prior theory.

Part III: Isothermal Magnetic Advection introduces an entirely new class of fluid flows that are stimulated when platelet-shaped magnetic particles in suspension are subjected to particular biaxial magnetic fields. At once, a lattice of interdigitated columns transporting fluid in each of two principal directions emerges. The morphological characteristics of this flow lattice can be manipulated by selecting particular values for the magnetic field frequencies, strengths, or phase relationship between the two field components. This technique, which requires neither gravity nor a thermal gradient, is ideally suited to situations where conventional cooling solutions cannot work (*e.g.*, convection in microgravity environments).

Part IV: Dynamics of vortex fluids introduces the concept and realization of creating deterministic vorticity in magnetic particle suspensions by applying complex, time-dependent magnetic fields of two principal types: *Symmetry-breaking rational magnetic fields* and *Rational triad magnetic fields*. The ratios of the component frequencies form small rational numbers (*e.g.*, 1:2:3). (In fact, symmetry-breaking fields generalize the concept of the "vortex magnetic field" introduced in Part II, which is the particular case of 1:1:dc.) In general, these complex magnetic fields need not possess a net circulation to produce vorticity. A phenomenological theory is presented for these fields

that relies on the symmetries of the applied field vector, and that predicts many of the trends observed in experiments. These *vortex fluids* possess a uniform torque density making them capable of such bizarre phenomena as active wetting, negative viscosity, and stunning biomimetic dynamics.

Each of these four parts is comprised of "self-contained" chapters, wherein each chapter is based on an article that has already undergone peer review and been published in a scientific journal. (As of the date of writing of this dissertation Chapter 12 has not yet been published.) The citation for each original source journal article is included as a footnote on the bottom of the first page of each chapter. As can be expected, each chapter is in a format typical of a scientific article: (1) an Introduction to establish the context, background, and purpose of the work; (2) an Experimental section outlining the particular techniques, apparatus, and considerations involved in performing the work; (3) Results and Discussion sections; and (4) a Conclusions section to discuss the implications of the work, emphasize key results and limitations, and possible extensions or interesting directions for future related work. The references are provided at the end of each chapter. A key advantage of organizing the material in this way is that any particular chapter that a reader may find interesting can be read on its own.

Finally, an introductory Background and Significance section is provided, establishing motivation for the work and discussing some general concepts, which the reader is encouraged to read before any other parts.

Kyle J. Solis

Albuquerque, New Mexico

February 2015

Background and Significance

The subject of transport phenomena is central to the study of chemical engineering operations, and encompasses the topics of *fluid dynamics*, *heat transfer*, and *mass transfer*. The respective transfer of *momentum*, *energy*, and *mass* are important concepts in many areas of engineering and science because they occur in most physical, biological, and chemical processes, and oftentimes simultaneously [1]. Moreover, effectively managing various transport phenomena is critical for ensuring the success and economic feasibility in many technological and industrial processes.

Take the production of automobile tires as an example. All of the constituents that will comprise the finished tire: natural/synthetic elastomers; reinforcing fillers such as carbon black and silica; resin/oil plasticizers; and chemical additives such as antioxidants, antiozonants, and the "cure package" must first be thoroughly mixed—a process termed compounding [2]. While the mixing process itself is an example of momentum transfer, the mixing also generates considerable heat due to shearing and internal friction [3] as well as the heat evolved by the vulcanization reaction [4]. As is typical of chemical reactions, the vulcanization reaction rate possesses a large temperature coefficient ($\sim 2.65\times$ per 10 °C) [4], and this generated heat must be carefully controlled to prevent premature vulcanization or scorching of the batch.

The Importance of Mixing

Mixing is a commonly-encountered unit operation in many industrial and engineering processes, the aim of which is to ensure that two or more different substances or phases are spatially distributed such that the resultant mixture can be considered homogeneous—exhibiting uniform desired properties. Oftentimes this description of *ideal* mixing cannot be realized in practice, so consideration must be given to the requirements and constraints of the particular mixing problem at hand [5]. Two primary considerations accompanying any

mixing problem are the relevant scales of length and time [6], which determine the "extent" of mixing required for a system to be considered well-mixed. Thus the extent of mixing required for a batch of concrete will be different than for a gasoline blend because the relevant length scale of homogeneity for concrete is much larger than for gasoline.

Mixing problems have gained a reputation for being notoriously difficult to address both from a theoretical and practical standpoint. The difficulties concerning mixing depend on any combination of a variety of factors, such as the *states* of the substances being mixed (*i.e.*, solid, liquid, gas), the *material properties* of the components (*e.g.*, miscibility, density, viscosity, particle shape and size), the *scale* of the mixing problem (*e.g.*, industrial, laboratory, microfluidic), and the *geometry* and *design* of the mixing equipment. Another concern regarding mixing operations is the *stability* of the mixture. That is, once mixed, will the dispersed components segregate or separate over time, and under what conditions? Familiar examples of segregation/separation include the so-called 'Brazil nut effect' [7] in which the migration of larger nuts to the top of a container of variously-sized mixed nuts occurs upon mechanical agitation (*i.e.*, granular convection), and the phase separation in vinegar-and-oil salad dressings (*i.e.*, emulsions), which occurs rather quickly even after vigorous shaking. The means by which segregation is mitigated depends on the particular destabilizing mechanism. For the mixed nut example, a solution would be to process the nuts so they are all roughly the same size; whereas, to stabilize the immiscible components of the salad dressing, an emulsifier—such as mustard—is required.

Not only is mixing one of the most challenging unit operations encountered, it is arguably one of the most important [5,6]. One reason is that mixing operations are essential and pervasive to so many industries. Some examples include chemical processing, petrochemicals, pharmaceuticals, food processing, drinking and wastewater treatment, paints, polymer processing, and pulp/paper. Moreover, within each industry the efficacy of mixing operations can drastically affect product yield and quality. Another reason mixing holds such importance is its impact on manufacturing costs. There are the obvious costs

associated with the design, implementation, and operation of *successful* mixing processes. However, the lost revenues due to improper scaling up of mixing processes can be quite substantial [5,6], making the investments in addressing problems at the process development stage well worth their cost. While the scaling *up* of mixing processes has many associated complexities [8], so does their scaling *down*. In fact, some particularly challenging mixing problems are encountered with micro- and nanofluidic technologies, wherein the small length scales involved mitigate against inducing turbulence [9].

The Importance of Moving Fluids

With regard to the transport of mass and heat in fluids, the ability to generate bulk motion of the fluid (*i.e.*, convection) is far more efficient than the comparatively "passive" process of molecular collisions (*i.e.*, diffusion/conduction). This fact is illustrated by comparing the characteristic time for convection, which scales with distance, to that for diffusion, which scales as the square of distance. Thus, doubling the distance over which some quantity is transported results in a four-fold decrease in the timescale for convection as compared to diffusion. From this consideration it becomes clear why for many transport processes involving fluids, such as mixing and heat transfer operations, it is desirable to achieve turbulent rather than laminar flow in the working fluid.

In reality, momentum transport within a fluid is ultimately mediated by molecular collisions regardless of the flow regime. The kinetic energy of a turbulent flow "cascades" down a hierarchy of progressively smaller eddies until molecular diffusion dominates—at the Kolmogorov length scale—causing viscous dissipation of energy [10]. Nonetheless, it is the macroscopic motions of the fluid that accelerates this process of chaotic mixing, which makes turbulence so efficient at transport. This description of turbulence is elegantly articulated in the following verse by the English mathematician Lewis F. Richardson [11], "*Big whirls have little whirls that feed on their velocity, and little whirls have lesser whirls and so on to viscosity*."

The word *convection*, in the context of thermal transport, generally refers to the exchange of energy between a surface that is in relative motion to an adjacent fluid. However, a distinction is made between *forced* or *artificial* convection—in which bulk motion of the fluid is effected by some external means, such as a pump or fan, and *natural* or *free* convection—in which an unstable, temperature-induced, density gradient in the fluid sustains buoyancy-driven circulation.

Under the proper conditions,[†] natural convection in a fluid can form an exquisitely-ordered pattern of hexagonal flow cells. Thermal transport by such convection cells was first visualized by French physicist Henri Bénard in 1900 [13]. In 1916, Lord Rayleigh developed a theoretical understanding [14] of the experimental conditions that give rise to convection by analyzing Bénard's experiments. (In fact the dimensionless number that characterizes the onset of convection is now called the Rayleigh number.) Depending on the particular experimental conditions, convection cells can assume a variety of complex and beautiful patterns including rolls, circles, and linear and square patterns. Such rich displays of nonlinear dynamics, the implications for heat transfer, and the simple, well-defined, experimentally-accessible conditions have made convective phenomena one of the most intensively studied self-organizing, non-linear systems over the last century [15–17].

Around 1970, it was discovered that applying a magnetic field *gradient* along the thermal gradient could enhance natural convection in magnetic fluids [18,19]. However, the enhancement is dependent upon the thermal gradient and does not lead to new flow patterns. Such thermomagnetic convection [20] can be explained in terms of the

[†] Some comments are necessary to clarify the particular conditions that give rise to the various convective phenomena in fluids. Bénard's original experiments on convection, wherein a thin layer of liquid with a *free top surface* was heated from below, were actually demonstrating the thermocapillary effect. While Bénard attributed the buoyancy of the fluid near the hot surface as the mechanism by which the convection cells formed, it was later discovered [12] that the free liquid surface develops temperature-induced surface tension gradients that drive the convection. Thus, the case of convection with a free fluid surface is now called thermocapillary convection or Bénard–Marangoni convection (in honor of the 19th century Italian scientist Carlo Marangoni, who studied surface-tension-driven flows); whereas, the case of convection in a liquid confined between two horizontal plates, which is buoyancy-driven, is called Rayleigh–Bénard convection or simply Bénard convection.

temperature dependence of the Kelvin force (the force on a magnetic object in a field gradient) on an individual particle. This Kelvin force increases with decreasing temperature, due to the negative pyromagnetic coefficient of ferrofluids. So if the magnetic field gradient is applied along the thermal gradient, the body force is larger on the cooler fluid, which adds to the buoyancy that drives natural convection. Thus, the possibility of using magnetic fields to influence the behavior of magnetic fluids and thereby controlling transport properties becomes evident.

Magnetoresponsive particle-fluid dynamics

In this dissertation we review recent work on structure formation and emergent phenomena in suspensions of magnetic particles driven by time-dependent, multiaxial magnetic fields. This work is focused on magnetic systems, because almost all of the phenomena we will describe were discovered in this context, for reasons given below.

Driving particle systems with time-dependent fields can generate a variety of behavior, and we discuss two categories of field-driven assembly. The first category can be called *static assembly*. Static assembly occurs in instances where the frequencies of the field components are sufficiently high that the particles and the fluid they are coupled to cannot follow the changing field vector. Static particle assemblies then form that are directed by their time-averaged interactions. These particle assemblies can be highly organized and exhibit unique and interesting symmetries that are strongly dependent on the relative amplitudes of the field components. (In one particular case, the static assemblies that result from a time-dependent uniaxial field are identical to those created using a static dc field.)

The second category, *dynamic assembly*, can occur when the field frequencies are sufficiently low that the particles or their assemblies can couple to the dynamic field vector. In this case a variety of highly organized emergent behaviors can arise that are dependent on the nature of the driving field, the particle geometry, coupling to the fluid, and the dimensionality of the system. These behaviors tend to be robust, due to the significant

power that the dynamic field can impart to the system, which is dissipated through the vigorous fluid flows that occur. Examples of such behavior include the simple rotational flow that occurs when spherical particles assemble in "vortex fields" and the much more complicated emergence of advection and vortex lattices when magnetic platelets are driven by particular multiaxial fields.

It is clear that the range of phenomena that can be produced is broad, and includes the formation of particle composites having a variety of optimized structures, novel methods of magnetic mixing, the stimulation of advection lattices, and the creation of vortex fluids. While most of these phenomena have application to sensors, actuators, fluid mixing and heat and mass transfer, some are also quite scientifically intriguing, such as the animation of suspended magnetic fluid droplets to produce striking biomimetic dynamics.

Why magnetic systems?

Before introducing the body of the work, it is helpful to discuss why the focus of this work is on magnetic systems. A dipole is a dipole, so in principle any of the magnetic phenomena of interest here can also be created with time-dependent electric fields. This fact has the practical implication that dielectric particles can be used to create composites with possible applications as dielectric materials for capacitors, electrostrictive actuators, capacitance-based sensors and so forth. However, there are important *practical* differences between electric and magnetic systems. Foremost among these is that free magnetic monopoles don't exist, so magnetic interactions are not "charge" screened. Highly cooperative, long-range phenomena are thus easily stimulated and observed [21].

The lack of free magnetic monopoles also eliminates the concern over breakdown at the high fields required to create structure in particle suspensions. Consequently, magnetic fields are capable of generating extremely large particle interactions. These interactions are proportional to the energy density of the field, and an electric field that is 10 kV/cm has the same energy density as a magnetic field of only 35 Oe. Electric fields of the order of

40 kV/cm can easily create breakdown in particle suspensions, whereas an applied magnetic field of 140 Oe, which has comparable energy density, is quite modest and far below the saturation field of most ferrous materials in particle form. Moreover, a magnetic field of this magnitude is easily generated over a large volume with open-air Helmholtz coils. In addition to breakdown issues, electric fields can also cause charge injection, which leads to chaotic advection instead of structure formation. Free charge causes another practical difficulty: in order to create interactions mediated by the dielectric contrast between the particle and liquid phase, the field frequency must be fast compared to the RC time of the fluid. Satisfying this condition can require field frequencies in excess of 1 kHz and the finite slew rate of amplifiers can severely limit the gap over which such high frequency fields can be applied.

The ease of creating uniform multiaxial magnetic fields over large volumes is perhaps the greatest experimental benefit of magnetism. Open-air Helmholtz coils can create remarkably uniform fields over a roughly spherical volume that fills their accessible interior volume, which is also visually accessible. Orthogonal Helmholtz coils do not have mutual inductance, nor does one coil distort the field produced by another, since the permeability of copper is essentially that of free space. The induction of eddy currents can be eliminated by the appropriate wire gauge selection, so proximity effect losses can be negligible below some characteristic frequency. Coils *can* have high inductances, but running the coils in series resonance with a capacitor bank confines the high voltages to the coils and the banks, allowing an ordinary audio amplifier to be used to drive the circuit since this is attached across the low voltage points on the resonant circuit and sees a purely nonreactive impedance [22]. The triaxial magnet used to perform much of the research discussed herein is shown in **Figure 1**, and can create homogeneous, time-dependent fields over a roughly spherical volume 8 cm in diameter and can operate at frequencies up to 1 kHz and produce

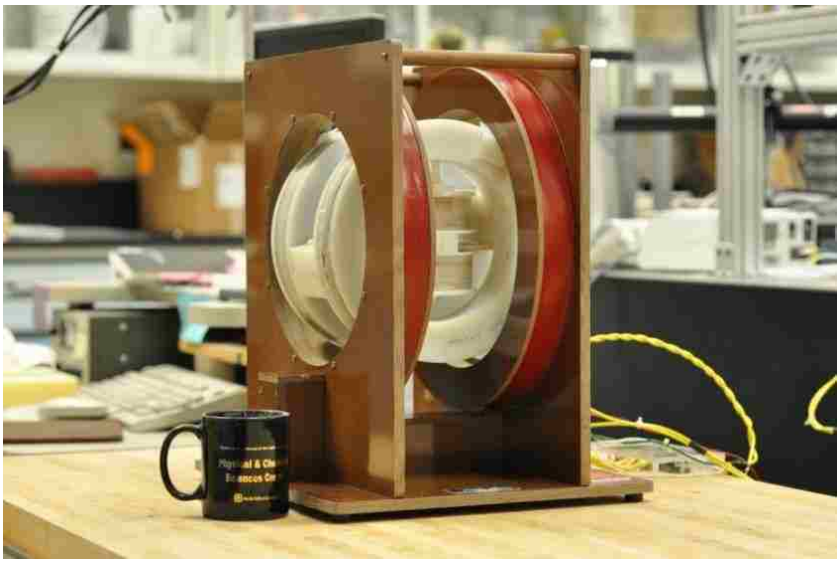

Figure 1. Triaxial Helmholtz coil magnet assembly used in the research comprising this dissertation.

fields as large as 300 Oe rms. In contrast, creating uniform multiaxial electric fields over a significant volume is difficult because the permittivity of the conducting electrode material is not that of free space, but is infinite. Each set of electrodes thus interferes with the fields produced by the other sets, creating severe fringing fields and poor field homogeneity. Creating a triaxial field is especially problematic because at least one electrode must be transparent (*e.g.*, indium tin oxide) to observe the suspension. On the other hand, it is clear that the effects of free charge are responsible for some of the complex phenomena that have yet to be observed in magnetic systems, such as the observation of transverse bands of circulating particles in confined dielectric particle suspensions subjected to uniaxial ac electric fields [23,24].

The principal difficulty with magnetic field studies is determining the macroscopic field within the sample. This is not generally a problem with electric fields since the electrodes are in contact with the sample. The macroscopic field can be substantially lower than the applied field, due to the demagnetizing fields [25] that occur in a typical experiment wherein the field is applied to a sample by magnetic coils. In electric field studies the corresponding depolarizing fields can be zero if the field is applied to the sample via

contacting electrodes, which is often the case. Accurately accounting for demagnetizing fields is especially important for samples of large relative permeabilities, and can so thoroughly dominate magnetostriction measurements on composites that the sign of the effect is altered. However, for much of the work described here the particle suspensions are sufficiently dilute that demagnetization fields are weak. When these fields are significant, the macroscopic internal field can always be accurately computed.

Hopefully the reader can appreciate the possibilities and advantages for using magnetism to control transport phenomena in a variety of systems.

References

1. R.B. Bird, W.E. Stewart, E.N. Lightfoot, *Transport Phenomena 2nd Ed.* (John Wiley & Sons, Inc., New York, 2002).
2. B. Rodgers, W.H. Waddell, S. Solis, and W. Klingensmith, *Rubber Compounding* in J.I. Kroschwitz and A. Seidel, *Kirk-Othmer Encyclopedia of Chemical Technology, 5th ed.* **vol. 21**, 758–815 (John Wiley-Interscience, New Jersey, 2004–2007).
3. Tire Manufacturing, (http://en.wikipedia.org/wiki/Tire_manufacturing).
4. W.K. Lewis, L. Squires, and R.D. Nutting, Mechanism of rubber vulcanization with sulfur, *Ind. Eng. Chem.* **29** (10), 1135–1144 (1937).
5. D.S. Dickey, *Mixing and Blending* in J.I. Kroschwitz and A. Seidel, *Kirk-Othmer Encyclopedia of Chemical Technology, 5th ed.* (John Wiley-Interscience, New Jersey, 2004–2007).
6. *Handbook of Industrial Mixing: Science and Practice*, edited by E.L. Paul, V.A. Atiemo-Obeng, and S.M. Kresta (John Wiley & Sons, Inc., New York, 2004).
7. M.E. Möbius, B.E. Lauderdale, S.R. Nagel, and H.M. Jaeger, Brazil-nut effect: Size separation of granular particles, *Nature* **414**, 270 (2001).
8. W. Himmelsbach, D.A. Houlton, W. Keller, and M. Lovallo, Mixing systems: Design and scale up (cover story), *Chem. Eng.-New York* pp. 46–53, April 2006.

9. V. Hessel, H. Löwe, and F. Schönfeld, Micromixers—a review on passive and active mixing principles, *Chem. Eng. Sci.* **60**, 2479–2501 (2005).
10. G. Falkovich and K.R. Sreenivasan, Lessons from hydrodynamic turbulence, *Phys. Today* pp. 43–49, April 2006.
11. L.F. Richardson, in *Weather Prediction by Numerical Process*, (Cambridge University Press, 1922).
12. J.R.A. Pearson, On convection cells induced by surface tension, *J. Fluid Mech.* **4** (5), 489–500 (1958).
13. H. Bénard, Les tourbillons cellulaires dans une nappe liquide transportent de la chaleur par convection en régime permanent, *Ann. Chim. Phys.* **23**, 62–144 (1901).
14. L. Rayleigh, On convection currents in a horizontal layer of fluid, when the higher temperature is on the under side, *Philos. Mag.* **32**, 529–546 (1916).
15. S. Chandrasekhar, *Hydrodynamic and Hydromagnetic Stability* (Dover, New York, 1981), pp. 9–71.
16. A.V. Getling, *Rayleigh-Bénard Convection: Structures and Dynamics* (World Scientific, Singapore, 1997).
17. *Dynamics of Spatio-Temporal Cellular Structures: Henri Bénard Centenary Review*, edited by I. Mutabazi, J.E. Wesfreid, and E. Guyon (Springer, Berlin, 2005).
18. D.P. Lalas and S. Carmi, Thermoconvective stability of ferrofluids, *Phys. Fluids* **14**, 436–437 (1971).
19. R.A. Curtis, Flows and wave propagation in ferrofluids, *Phys. Fluids* **14**, 2096–2102 (1971).
20. R.E. Rosensweig, *Ferrohydrodynamics* (Dover, New York, 1997), pp. 228–232.
21. J.E. Martin, R.A. Anderson, and R.L. Williamson, Generating strange magnetic and dielectric interactions: Classical molecules and particle foams, *J. Chem. Phys.* **118** (3) 1557–1570 (2003).

22. J.E. Martin, A resonant biaxial Helmholtz coil employing a fractal capacitor bank, *Rev. Sci. Instrum.* **84**, 094704 1–11 (2013).
23. B.R. Jennings and M. Stankiewicz, Electrooptic observations of electrohydrodynamic band formation in colloidal suspensions, *Proceedings of the Royal Society of London Series A-Mathematical Physical and Engineering Sciences*, **427** (1873), 321-330 (1990).
24. Y. Hu, J.L. Glass, A.E. Griffith, and S. Fraden, Observation and simulation of electrohydrodynamic instabilities in aqueous colloidal suspensions, *J. Chem. Phys.* **100**, 4674-4682 (1994).
25. R.M. Bozorth, *Ferromagnetism*, (Wiley-IEEE Press, 1993).

Part I

Directed heat transfer in magnetic-field–structured composites

Chapter 1

Field-structured magnetic platelets as a route to improved thermal interface materials[1]

The development of high-performance thermal interface materials (TIMs) is crucial to enabling future generations of microelectronics because the TIM is usually the limiting thermal resistance in the heat removal path. Typical TIMs achieve modest thermal conductivities by including large volume fractions of randomly-dispersed, highly-conductive, spherical particles in a polymer resin. This chapter explores field-structured magnetic platelet composites as a new approach to more effective TIMs. The motivation for this approach is rooted in shape functional theory, which shows that when the particle material has a significantly higher thermal conductivity than that of the polymer, the particle *shape* and *orientation* are the factors that limit conductivity enhancement. Oriented platelets are highly effective for heat transfer and if these are magnetic, then magnetic fields can be used to both orient and agglomerate these into structures that efficiently direct heat flow. In this paper we show that such field-structured composites have a thermal conductivity anisotropy of ~3, and at the highest particle loading of 16 vol.% we have achieved a 23-fold conductivity enhancement, which is 3-times larger than that achieved in unstructured platelet composites and 8-times greater than unstructured spherical particle composites.

1.1 Introduction

The increasing power densities of microsystems have created a need for significantly improved thermal interface materials (TIMs). TIMs are used to bond a die to a heat sink and must efficiently conduct heat for the operating device to remain within an acceptable temperature range. A TIM should have a large thermal conductivity, small coefficient of

[1] Originally published as: K.J. Solis and J.E. Martin, Field-structured magnetic platelets as a route to improved thermal interface materials, *Journal of Applied Physics* **111**, 073507 1–10 (2012).

thermal expansion, good adhesive/cohesive strength, and workable rheology. In some cases a large electrical resistivity and significant dielectric standoff are required. Interest in TIMs is currently quite high, as they are often the largest thermal resistance encountered in the heat removal path from many microsystems and are a key impediment to the implementation of many high-power-density devices.

One standard approach to TIMs is to produce a polymer resin that contains particles of a material that has substantially greater thermal conductivity than that of the polymer phase, the so-called *high contrast* case. Unfortunately, most such particles are nearly spherical, and when a spherical particle is placed in a continuous phase having an initially uniform thermal gradient, the isotherms tend to mostly steer around the particle, leaving only a small thermal gradient within the particle [1.1,1.2]. The thermal conduction inside such a particle is consequently only a few times larger than that of the unfilled polymer. Using spherical particles of exceptionally high contrast is of little benefit, since as the thermal contrast increases, the internal thermal gradient decreases, with the result that at reasonable loadings a spherical particle never exhibits an *apparent* thermal conductivity greater than four times that of the polymer. (The apparent thermal conductivity is that value that gives the correct effective composite thermal conductivity at low particle loadings using a parallel rule of mixing. It is sometimes referred to as the virial coefficient [1.3]. For example, adding 10 vol.% spherical particles of infinite thermal conductivity to a polymer of thermal conductivity 0.20 W/m·K would give a composite with a thermal conductivity of $\sim(4\times0.10+0.90)\times0.20$ W/m·K $=0.26$ W/m·K , which is only marginally greater than that of the polymer. To obtain high thermal conductivities one can increase the particle loading, but at best this increases the resin viscosity commensurately [1.3] and can even result in Bingham plastic rheology. A second approach is to increase the loading such that the particles percolate and then sinter the composite. This approach requires processing temperatures that are above the reflow temperature of the bonding materials used in many microsystems and results in a highly electrically conductive material that is not suitable for

all applications. In this chapter we report a new approach that is based on resins containing a modest loading of magnetic platelets that are magnetically aligned and agglomerated to create a TIM with efficient, directed heat flow.

Much greater enhancements are possible with anisometric particles [1.3–1.8], especially if they are preferentially aligned with their long axes along the thermal gradient and agglomerated into appropriate structures. Rods are a highly effective shape, but even very modest loadings create severe congestion and poor flow rheology, so we have chosen to use magnetic platelets. As we will show, aligned Ni platelets have good thermal transport, yet have a manageable rheology even at relatively high loadings.

For any given choice of particles, polymer, and loading, the thermal conductivity of a composite will depend on the only remaining variable, the orientation of the particles and their relative positions, which we will collectively call the composite *structure*. In principle, one could develop a simulation to find the optimal structure for thermal transport, but even if this were known it would be technically very challenging to actually create this structure in the lab. Fortunately, in the case of magnetic particles, simply applying a magnetic field both determines and creates the optimal composite structure, at least in the presence of thermal fluctuations. So using magnetic fields to optimize composite conductivity is not simply hopeful, but is founded on the known isomorphism between the magnetic permeability and the thermal conductivity of particle composites [1.9]. (This isomorphism is only exact in the absence of the Kapitza resistance, which may somewhat reduce the measured thermal conductivity enhancement from that which obtains for the magnetic permeability.)

In the case where the particle material has both a much greater magnetic permeability and thermal conductivity than the polymer, and where the *apparent* particle magnetic permeability and thermal conductivity are *limited* by particle shape, then both the permeability and thermal conductivity enhancements of a particle composite will be identical. For example, Ni has a relative magnetic permeability of ~600, which is,

therefore, ~600× that of a diamagnetic or paramagnetic material and has a thermal conductivity (at 300 K) of 91 W/m·K, which is ~400× that of an epoxy. These contrast ratios are sufficiently large that the *apparent* particle properties will be shape-limited for the platelets of interest here, as described in detail below. When a suspension of such Ni platelets is subjected to a structuring magnetic field (*i.e.*, a field well below that which causes magnetic saturation), the platelets will orient and agglomerate to minimize their magnetostatic contribution to the free energy. Because the energy of an induced particle dipole in an applied field is negative, this minimization maximizes the composite permeability and therefore the composite thermal conductivity. This principle of magnetically maximizing the thermal conductivity has already been demonstrated for spherical particle composites [1.10], where both the permeability and thermal conductivity enhancements have been shown to be both substantial and equal. In the following we describe the results of applying this principle to magnetic platelets to produce composites with extremely large specific thermal conductivities.

1.2 Theory

Platelets offer a substantial advantage over spherical particles for property enhancement because their shape results in much greater field (*i.e.*, thermal gradient) penetration for the component of the field that lies in the platelet plane and this consequently results in a much larger in-plane apparent particle thermal conductivity. In the following we will describe some of the theory of composites containing these particles.

The apparent particle thermal conductivity K_{app} is defined through the parallel mixing rule for the effective composite thermal conductivity, $K_{eff} = K_{poly}(1-\phi) + K_{app}\phi$, where K_{poly} is the polymer thermal conductivity and ϕ is the particle volume fraction. For most systems of interest, K_{app} has little dependence on the thermal conductivity of the material of which the particle is comprised, but is strongly dependent on the particle shape, orientation, and spatial correlations between particles. At low particle loadings, the effective thermal

conductivity K_{eff} of a random composite of particles can be expressed as the so-called virial expansion

$$K_{eff} = K_{poly}(1+\alpha\phi+...), \tag{1-1}$$

where α is the first virial coefficient [1.3], which in the limit of low particle loading is given by $\alpha = K_{app}/K_{poly} - 1$. In the present context it is more descriptive to refer to α as the *transport* virial coefficient. As mentioned above, for high-contrast spherical particles the transport virial coefficient approaches $4-1=3$, so the thermal conductivity enhancement is very modest. However, in the high-contrast limit the transport virial coefficient is a strong function of particle shape, particle orientation, and particle agglomeration. Platelets offer the opportunity to exploit all of these effects to obtain unusually large specific conductivity enhancements (the relative increase in the effective thermal conductivity of the composite per volume fraction of particles).

The computation of the transport virial coefficient is the subject of shape functional theory [1.3] and has been worked out exactly for generalized ellipsoids [1.11] and some other elementary shapes, such as tori [1.3]. For an ellipsoid placed in an initially uniform thermal gradient, the steady-state *internal* thermal gradient is constant, regardless of particle orientation. This condition makes the determination of the virial coefficient a tractable problem with a simple solution. The principal components of the so-called "polarizability" tensor (a term that derives from the consideration of the isomorphic dielectric properties) can generally be expressed in terms of the relative thermal conductivity $K_r = K_p/K_{poly}$ of the particle phase to the continuous (polymer) phase by

$$\alpha_w = \frac{K_r - 1}{1 + n_w(K_r - 1)}, w = x, y, z. \tag{1-2}$$

In general, the "demagnetization" or "depolarization" factors n_w are positive numbers that are strong functions of particle *shape* and weak functions of the contrast factor. For general

ellipsoids these demagnetization factors are functions of particle shape *alone* and are subject to the sum rule $n_x + n_y + n_z = 1$. In the remainder of this discussion we will focus on prolate and oblate spheroids and to be definite we will take the *z* axis to be along their polar axis and the *x* and *y* axes along their diameter, so $n_x = n_y$. For any given aspect ratio (which is greater than 1 for prolate spheroids and less than 1 for oblate spheroids), there will be certain demagnetization factor values for the principal moments, and it is only important at this point to know that along a long axis these values become very small. In other words, for prolate spheroids, $n_z < n_{x,y}$ and for oblate spheroids, $n_z > n_{x,y}$. For prolate spheroids, it is useful to write the depolarization factors along the diameter as $n_{x,y} = \frac{1}{2} - n_z$. The parameter n_z approaches zero quadratically with inverse aspect ratio for large aspect ratios, so for acicular particles $n_{x,y} \approx 1/2$. For oblate spheroids the depolarization factor along the polar axis can be written as $n_z = 1 - 2n_{x,y}$, where $n_{x,y}$ vanishes as the aspect ratio for small aspect ratios. For highly oblate spheroids $n_z \approx 1$.

In the limit of large contrast, defined as $n_{\min}^{-1} << K_r$, where n_{min} is the minimal principal component of the polarizability tensor, the transport virial coefficient is a function of particle shape alone. This is the usual experimental situation. For the simple case of randomly oriented particles, the virial coefficient is 1/3 the trace of the polarizability tensor [1.3], $\alpha = (\alpha_x + \alpha_y + \alpha_z)/3$, so in the large contrast limit $\alpha = (n_x^{-1} + n_y^{-1} + n_z^{-1})/3$. For highly prolate spheroids the virial is $\alpha_{pro} \approx (4 + n_z^{-1})/3 \approx \frac{1}{3} n_z^{-1}$ and for highly oblate spheroids it is $\alpha_{obl} \approx (1 + 2n_{x,y}^{-1})/3 \approx \frac{2}{3} n_{x,y}^{-1}$. For randomly dispersed particles with their long axes oriented along the thermal gradient, these virials are $\alpha_{pro} = n_z^{-1}$ and $\alpha_{obl} = n_{x,y}^{-1}$, so field orientation alone can increase the virial by a factor of 3 and 3/2, respectively, for such strongly anisometric particles. An applied field also causes particle agglomeration, with the result that the experimental enhancements can be much larger than that due to particle orientation alone, as we shall see. The effect of field agglomeration is amenable to theoretical analysis

for spherical particles forming a wide variety of agglomerations [1.4,1.10,1.12], but is a very complex issue that has not yet been treated for other shapes.

In the work of Douglas *et al.* [1.3] there are presented extensive tables of the principal moments of the polarizability tensor for ellipsoids in the limit of infinite contrast. Citing some experimentally relevant examples gives an appreciation for the importance of particle shape. For the sphere the sum rule gives $n_w = 1/3$, so $\alpha = 3$. For a prolate spheroid of aspect ratio 40, the principal components are 2.004, 2.004, and 473. Randomly-aligned rods would give $\alpha = 159$, and magnetically-oriented rods would give $\alpha = 473$. For an oblate spheroid of aspect ratio 40, the principal components are 1.04, 52.6, and 52.6. Such randomly-aligned particles would give a virial of ~35.4 and oriented particles would give 52.6. So particle shape is an appreciable effect for physically attainable aspect ratios, especially when field alignment is employed.

Field alignment can also be useful in directing thermal transport, since in the directions orthogonal to the alignment field the thermal conductivity is relatively low. For highly prolate spheroids aligned along the *z*' axis, the transverse virial will be $\alpha_{x',y'} = n_{x,y}^{-1} \approx 2$ (primed coordinates denote the direction of the applied thermal gradient in the composite material). For highly oblate spheroids magnetically aligned along the *z*' axis the transverse virial will be $\alpha_{x',y'} = (n_{x,y}^{-1} + n_z^{-1})/2 \approx \frac{1}{2} n_{x,y}^{-1}$, showing that in this instance the thermal conductivity anisotropy will be only a factor of 2 (although we shall see that particle agglomeration will cause it to be more substantial). The anisotropy for highly oblate spheroid composites can be much larger if a biaxial field is used to align the platelets in the *x*'-*y*' plane. In the plane of the platelets the transport virial will be $n_{x,y}^{-1}$ and in the *z*' direction it will be only $n_z^{-1} = 1/(1 - 2n_{x,y}) \approx 1$. For such biaxially-oriented platelets the conductivity anisotropy can be extremely large, being limited only by the contrast factor K_r. Such materials could be highly effective heat spreaders.

In the following we discuss in further detail the demagnetization factor and the isomorphism between the magnetic permeability and thermal conductivity, which ultimately derives from the fact that the magnetostatic potential and the temperature field during steady-state heat conduction both obey Laplace's equation. This discussion will clarify the role of the demagnetization factor in predicting the thermal conductivity of particle composites.

1.2.1. The demagnetization factor

When a magnetic particle is inserted into an initially uniform magnetic field the particle magnetizes, producing capping magnetic "monopole" layers that create a field within the particle that opposes the applied field $\mathbf{H}_0$. This effect can be quantified by the so-called demagnetization factor *n* [1.11], defined by

$$\mathbf{H}_{\text{int}} = \mathbf{H}_0 - n\mathbf{M}, \tag{1-3}$$

where $\mathbf{H}_{\text{int}}$ is the internal macroscopic field, and $\mathbf{M}$ is the particle magnetization. This equation implies that the internal field is uniform, which is the case for particles in the shape of ellipsoids and tori [1.13]. We recall from above that for ellipsoidal particles the demagnetization factors along the principal axes *x*, *y*, *z* are positive, subject to the sum rule $n_x + n_y + n_z = 1$, and independent of the susceptibility of the material of which the particle is comprised. In the following we treat the case where the particle is aligned with the field along one of its principal axes.

In the linear response regime the magnetization of a particle is related to the internal macroscopic field by its susceptibility, $\mathbf{M} = \chi\mathbf{H}_{\text{int}}$. Here χ is $\mu_r - 1$, where μ_r is the permeability of the material of which the particle is comprised relative to that of the continuous phase. Substituting this relation into Equation 1-3 gives $\mathbf{H}_{\text{int}} = \mathbf{H}_0/(1+n\chi)$ for the internal field. The *apparent* particle susceptibility is defined by $\mathbf{M} = \chi_{app}\mathbf{H}_0$ and thus is

$$\chi_{app} = \frac{\chi}{1+n\chi} = \frac{\mu_r - 1}{1+n(\mu_r - 1)} . \qquad (1\text{-}4)$$

The effective permeability of a composite can be computed by considering the magnetization per unit field, with the result $\mu_{eff} = \mu_{poly}(1+\chi_{app}\phi+...)$, which is analogous to the virial expansion presented for the thermal conductivity. The first virial coefficient is thus simply the *apparent* particle susceptibility from this magnetics perspective. The apparent particle permeability and apparent susceptibility are related through $\mu_{app} = (1+\chi_{app})\mu_{poly}$ [1.14]. This calculation shows that at least for ellipsoidal objects, the dependence of the virial coefficient on the permeability contrast factor μ_r is simple, since n is independent of this contrast factor. Numerical work on the virial coefficient can thus be restricted to n as a function of particle shape. (For general shapes, where the internal field is not uniform, the demagnetization factor is a function of the contrast factor, a point to which we will return in the simulation section §1.5 of this chapter.) As a matter of interest, for large positive contrast ($\mu_r = \infty$) the virial coefficient approaches $1/n$, and for large negative contrast ($\mu_r = 0$) this virial is $-1/(1-n)$. For a sphere these limits are 3 and $-3/2$. Finally, the magnetic induction inside the particle can be computed from $\mathbf{B}_{\text{int}} = \mu_0(\mathbf{H}_{\text{int}} + \mathbf{M})$, which gives $\mathbf{B}_{\text{int}} = \frac{1+\chi}{1+n\chi}\mathbf{B}_0$. The case of finite contrast factor has been considered by Garboczi and Douglas from a somewhat different perspective [1.15].

The heat conduction problem can be mapped onto the permeability problem because in steady state both the magnetic induction **B** and the heat flux density **J** obey Laplace's equation. By definition the heat flux within the particle is $\mathbf{J}_{\text{int}} = -K_p \nabla T_{\text{int}}$. The thermal gradient is isomorphic to the magnetic field, so the thermal gradient *within* the particle is related to the applied thermal gradient by $\nabla T_{\text{int}} = \nabla T_0 / (1+n\chi)$, where the *relative thermal susceptibility* χ is defined by $\chi = K_r - 1$ in terms of the relative thermal conductivity $K_r = K_p / K_{poly}$ of the particle and polymer phases. Combining these expressions gives

$\mathbf{J}_{\text{int}} = \frac{1+\chi}{1+n\chi}\mathbf{J}_0$, showing that the thermal flux density is analogous to the magnetic flux density. From this relation the demagnetization factor can be written as $n = \frac{K_r - J_r}{(K_r - 1)J_r}$ in terms of the relative thermal flux density $J_r = J_{\text{int}}/J_0$ (note that $\mathbf{J}_{\text{int}}$ and $\mathbf{J}_0$ are parallel vectors when a principal axis is aligned with the applied field). The incremental thermal flux density within the particle is $\Delta\mathbf{J}_{\text{int}} = -(K_p - K_{poly})\nabla T_{\text{int}} = \chi_{app}\mathbf{J}_0$, where we recall that the *apparent* thermal susceptibility $\chi_{app} = \chi/(1+n\chi)$ is the transport virial coefficient. The incremental flux density is thus analogous to the magnetization. For the sake of completeness we mention that in the numerical studies described below we obtain the virial coefficient from $\chi_{app} = \frac{K_r - 1}{K_r}J_r$.

1.3 Experimental

The formation of functional composites with high effective conductivities requires both a high transport virial coefficient and a high particle loading. To achieve both we structured our platelet composites with a magnetic field having a strong gradient parallel to the field. This gradient field orients the particles and then draws them into the high field region. This is done in a 1 cm square cuvette that is initially filled to a level of 3 cm with the dilute epoxy-particle suspension. The field gradient concentrates the particles into the bottom of the cuvette, to a height that is typically ~5 mm. After the epoxy cures, a 1.5 mm thick, 1 cm square composite is machined for laser flash diffusivity measurements. With this procedure the platelets consistently achieve a loading of ~10%. Loadings as high as 16 vol.% were produced by vibrating the sample in the structuring field. The image in **Figure 1-1** was taken parallel to the structuring field and shows unexpected texture.

Figure 1-1. Photograph illustrating the textured ordering of Ni platelets observed in a composite in which the magnetic field was applied normal to the plane of the picture.

We used four grades of Novamet platelets, marketed as: Conductive Ni platelets, Fine Water Grade Ni, Fine Leafing Grade Ni, and Standard Leafing Grade Ni. These platelets differ in their typical thicknesses and are quite irregular in shape, with a typical width of ~20 μm. These thicknesses are 0.7, 0.5, 0.5, and 0.6 μm, respectively, so the typical aspect ratios range from ~30 to 40. (In both the experimental and simulation sections that follow we will define the aspect ratio as the particle diameter divided by its thickness. This is the inverse of the definition used in the discussion above, where we sought to avoid confusion with prolate ellipsoids, but is much more intuitive in all that follows.)

As a matter of interest, composites were also made of some magnetic Novamet particles having exceedingly complex shapes, including Ni-coated graphite and filamentary Ni powder. These field-structured composites are included for comparison to the platelets and were made in the hope that they might actually give greater enhancements.

Finally, spherical particle composites were produced in a uniform field and were made at loadings from ~5–30%, using 10 μm Novamet Conductive Nickel Spheres (CNS). These composites were made to demonstrate the ability of field structuring to direct heat flow and to quantitatively demonstrate the advantage of using platelets.

1.4 Experimental Results

Before presenting our experimental results, it is necessary to point out that we cannot make measurements at extremely low particle concentrations, due to the errors associated with these measurements for samples with low thermal conductivities. Because of this fact, and the manner in which our samples are synthesized, our samples have loadings that are typically around 10 vol.%. Much of our experimental data is therefore presented as a *specific* conductivity enhancement, defined through

$$\hat{\alpha} = \frac{K_{eff} - K_{poly}}{\phi K_{poly}}. \tag{1-5}$$

In the limit of zero particle volume fraction this parameter is equal to the virial coefficient. The advantage of reporting our measurements in this form, rather than as a thermal conductivity, is that $\hat{\alpha}$ is independent of the polymer thermal conductivity and is more weakly dependent on the particle volume fraction. For unstructured spherical particle composites the Maxwell theory gives $\hat{\alpha} = \alpha/(1-\phi)$, so at 10 vol.% the specific conductivity enhancement is just 11% larger than the virial coefficient. In any case, we will specify the loadings of our samples.

In the following we first give results for field-structured Ni spherical particle composites as a basis for comparison to platelet composites. We then give results for Ni and stainless steel platelets, and finally describe field-structured composites containing particles having complex geometries.

1.4.1. Spherical particle composites

Spherical particle composites can be fabricated over a wide range of loadings, so many samples were made at specified loadings and in a uniform structuring field. The thermal conductivities of these materials, presented in **Figure 1-2**, show a significant conductivity anisotropy, about 3:2 at the highest loading, with the thermal conductivity highest along the

chains. The field enhancement is purely due to particle agglomeration, since multi-domain spherical particles cannot orient. However, the thermal conductivities are not that high, not exceeding even 1 W/m·K at 30 vol.%. Samples structured in a field gradient achieved an average loading of 37.9% and a thermal conductivity of 1.44 W/m·K, for a specific enhancement of 16.4. Higher loadings resulted in a composite precursor that was too viscous to degas reliably and otherwise process, so something like a conductivity of 1.5 W/m·K is about the performance limit for this spherical material. Random composites give conductivities comparable to the transverse results shown here. Noteworthy also is the essentially linear dependence of the thermal conductivity on particle loading, an effect we have discussed at length elsewhere, and which can be understood through self-consistent local field calculations of simulated field-structured composites [1.10].

(Another spherical Ni Novamet powder marketed as 4SP Ni gave a somewhat higher loading of 43.3 vol.% under field gradient structuring, resulting in a thermal conductivity of 2.14 W/m·K. The reason for this improved performance is not clear.)

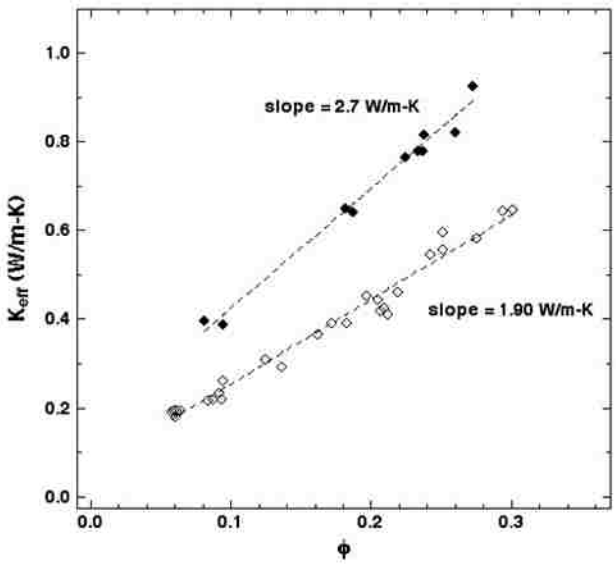

Figure 1-2. Thermal conductivity as a function of particle volume fraction for composites containing spherical Ni particles. Measurements were made parallel (♦) and transverse (◊) to the structuring field. The conductivity anisotropy is purely due to particle chain formation.

1.4.2. Platelet composites

Platelet composites were fabricated using four types of Novamet particles, marketed as: Conductive Ni platelets, Fine Water Grade Ni, Fine Leafing Grade Ni, and Standard Leafing Grade Ni. These platelets differ in their typical aspect ratio and size. All of these materials gave composites with loadings of about 10.6–11.4 vol.%, save the Conductive Ni platelets, which attained 16.6 vol.%. The measured specific conductivity enhancements were 38.8, 81.0, 86.5, and 97.6, respectively and the corresponding conductivities were 1.56, 1.93, 2.16, and 2.41 W/m·K. These values are much higher than the spherical particle composites even though the loadings are much lower. Both particle orientation and agglomeration are at play in these results.

Because the standard leafing grade platelets produced the best result, we used this material to develop composites with higher loadings and to investigate the conductivity anisotropy. When mechanical vibrations were applied to the sample during field structuring, we found we could increase the particle loading to as much as 16.1 vol.%, ultimately achieving a thermal conductivity of 4.4 W/m·K (**Figure 1-3**), which is a specific enhancement of 121, significantly better than the value of 3.6 expected for an unstructured spherical particle composite at this loading. This value is ~3× higher than that obtained for field-structured spherical particle composites, even though the loading was 2.4× lower. Figure 1-3 also shows that transverse to the structuring field the specific enhancement is 3.5× lower, demonstrating that these materials can effectively direct heat flow. This anisotropy is much greater than that observed for the spherical particle composites, because of the dominant effect of particle orientation in such high aspect ratio particles. The unstructured platelet composite has a thermal conductivity comparable to the transverse conductivity, so field structuring increases the specific conductivity enhancement by a factor of ~3.5.

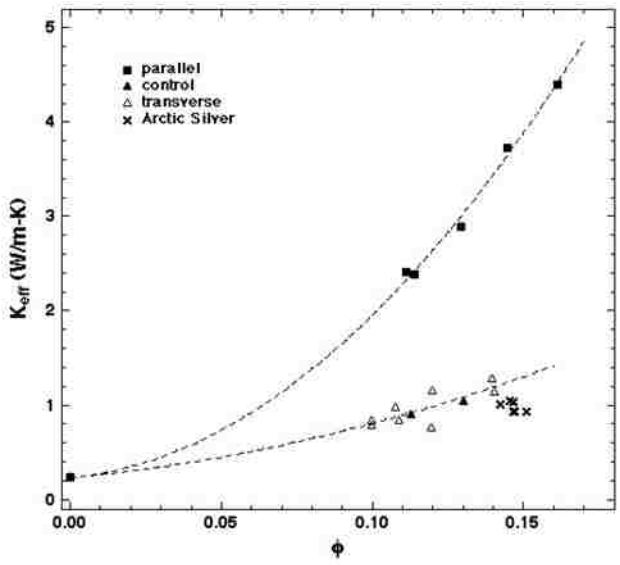

Figure 1-3. Summary of results for the composites made of Novamet standard leafing grade Ni platelets. The thermal conductivity parallel to the structuring field is much higher than transverse, and the unstructured platelet sample is comparable to the transverse result. Arctic Silver is a commercial material that was cured under the same conditions and is included to show how it compares to the field-structured platelets.

It is of some interest to compare our results to a commercially available high performance thermal interface material marketed as "Arctic Silver" that is also made at a low cure temperature and is therefore not sintered. Under the same conditions of cure this material gave a specific enhancement of 25.5 and a thermal conductivity of 0.98 W/m·K. We conclude that field-structured magnetic platelet composites show significant potential as thermal interface materials.

We also obtained 316L stainless steel platelets from Novamet marketed as Standard Water Grade and Fine Water Grade. The Standard Water Grade materials gave samples in the range of 11.9–14.1 vol.% and specific enhancements from 24.3 to 27.0. The Fine Water Grade platelets gave samples in the range of 6.4–11.6 vol.% and specific enhancements from 21.4 to 30.0. Neither of these materials produced conductivities even close to the Ni, and this is not entirely unexpected, as the thermal conductivity of 316L is only 16.2 W/m·K, almost 6× lower than that of Ni. This issue of contrast is discussed in more detail in the simulation section below (§ 1.5).

1.4.3. Composites of magnetic particles having complex geometries

Novamet produces a variety of other magnetic particles, some of which have extremely complex morphologies, and we made field-structured composites out of several of these just to satisfy our curiosity. In all cases the particles were concentrated and aligned with a field gradient, so the loadings vary in accordance with the dictates of the particle geometry. The first type is marketed as 525 Conductive Ni powder, and it has an exciting filamentary structure that looked as though it might really work. It did not: The loading achieved was only 12.8 vol.% and the conductivity was only 0.75 W/m·K, for a specific enhancement of 21.5. Vale Inco markets a filamentary powder as T255 Ni Powder, and it is similar in structure to the Novamet 525 product. It gave a loading of 10.1 vol.%, a conductivity of 0.58 W/m·K and a specific enhancement of 19.0.

Novamet Ni-Coated Graphite particles of an irregular but compact shape with significant anisometry gave a loading of 42.5 vol.% and a conductivity of 2.8 W/m·K, for a specific enhancement of 30.6. This material is quite good but the particles can easily approach 100 μm in size, too large to achieve the very thin bond lines needed for most thermal interface applications. None of the more complex particles exceed the platelet results so these seem to present the best opportunity for developing high performance moldable composites.

1.5 Simulations

To obtain a detailed understanding of thermal transport in these composite materials would require a simulation of structure formation in magnetic fields, in order to quantify the contributions from both particle orientation and agglomeration. This is a fairly easy task for spherical particle composites, since a simple point dipole approximation to the magnetic interactions is sufficient to give physically compelling structures from Brownian dynamics simulations. (In fact, numerous papers have been published on structure formation in such systems, many in connection with electro- and magnetorheology.) These structures can then

be used to compute the thermal conductivity by treating the local field self-consistently, again in the point dipole approximation. This is the approach we have taken in computing the thermal conductivity, magnetic permeability, and electrostriction of magnetic field-structured spherical particle composites, including those structured by multi-axial ac fields. Unfortunately, simulating the field-structuring of platelet suspensions is a *much* more challenging task because the self-consistent point dipole approximation is completely unrealistic, and could even lead to such unphysical phenomena as spontaneous magnetization. In this study we will take a first step in understanding our results by considering the virial coefficient of field-aligned platelets as a function of aspect ratio and thermal conductivity contrast.

There are two basic approaches to the numerical computation of the virial coefficient: discrete element and Brownian walk algorithms [1.16]. We have taken the discrete element approach. The virial coefficient can be computed in a straightforward manner by simply meshing the desired object in a simulation volume, then relaxing Laplace's equation to find the effective thermal conductivity, which we accelerate by using over-correction. The transport virial coefficient can then be estimated by inverting the first order virial expansion to obtain

$$\alpha_\kappa(\Delta,\phi)=\frac{K_{eff}-K_{poly}}{\phi K_{poly}}. \qquad (1\text{-}6)$$

This estimated virial coefficient is a function of the relative thermal conductivity $K_r = K_p / K_{poly}$, where K_p is the thermal conductivity of the material of which the particle is comprised, as well as both the discrete mesh size Δ and the volume fraction of the particle in the simulation volume, ϕ. To compute the first virial coefficient accurately requires that both the mesh size dependence and particle volume fraction dependence be removed by extrapolations to zero. The volume fraction extrapolation is analytic in form, being related

to the image fields created by the boundary conditions of the simulation volume, which to first order are dipolar in form.

In practice we do not actually compute our transport virial coefficients from the increase in thermal conduction, but from the "demagnetizing fields" within the particle (these could be called "dethermalizing fields" in this context), an approach we find is more accurate. Our simulations are 2-D, so we consider heat conduction along the principal axes *normal* to the long axis of infinite rods with a generally rectangular cross section. The field inside a particle is not uniform, so the demagnetization factor is defined for average properties and becomes a weak function of the relative thermal conductivity. Because of the symmetry of these particles, the flux density averaged over the particle volume is parallel to the applied thermal gradient, so $\overline{\mathbf{G}}_{\text{int}}$ and $\mathbf{G}_0$ are parallel. The average internal flux density can be computed from the average internal thermal gradient, which is just the average of the temperature difference on the two surfaces normal to the applied gradient divided by the gap between these surfaces. Computing the demagnetization factor from this average flux density gives exactly the same result as Equation 1-6, but we find the extrapolation to zero mesh size is more accurate, due to the weaker dependence of the results of this approach on mesh size. A second advantage of this approach is the weak dependence of the demagnetization factor on the relative conductivity, compared to the strong dependence of the transport virial coefficient on this factor. We find we can fit the demagnetization factor from our simulations to

$$n_K = n_\infty + \frac{a}{1+K_r}, \tag{1-7}$$

where $a/(1+K_r)$ is generally quite small compared to n_∞. The transport virial coefficient is computed from Equation 1-7 using $\alpha = (K_r - 1)/[1 + n_K(K_r - 1)]$.

To test the accuracy of our numerical approach, we consider the square, because for the limiting case of infinite thermal contrast (where $\alpha = 1/n_\infty$) this problem has been solved

exactly by Douglas *et al.* using a conformal mapping calculation. **Figure 1-4(a)** shows the extrapolation to zero mesh size for a relative thermal conductivity of 16. **Figure 1-4(b)** shows the extrapolation to zero volume fraction, which eliminates the effect of image fields. Analysis of the image fields in 2- or 3-D shows their effect is linear in the volume fraction, as this plot demonstrates. These extrapolations were repeated for each value of the contrast ratio and the dependence of the demagnetization factor on this variable is shown in **Figure 1-5(a)**. A best fit gives $n_\infty = 0.45{,}744$ and $a = 0.96{,}392 \times 10^{-1}$, so for infinite conductivity contrast this gives $\alpha = n_\infty^{-1} \approx 2.1861$. The exact result is $\alpha = \frac{1}{4}\Gamma^2(1/4)/\pi^{3/2} \approx 2.1884$ [1.3]. Our result is about 0.11% lower than this exact value, which is certainly adequate for comparison to experiment. This double extrapolation was repeated for aspect ratios up to 8, and the results are shown in **Figure 1-5(b)**. The rectangular objects were modeled by simply increasing the conductivities of *all* the bonds transverse to its major axis by the aspect ratio squared, relative to those parallel to its major axis. In other words, the discrete elements were mathematically similar rectangles.

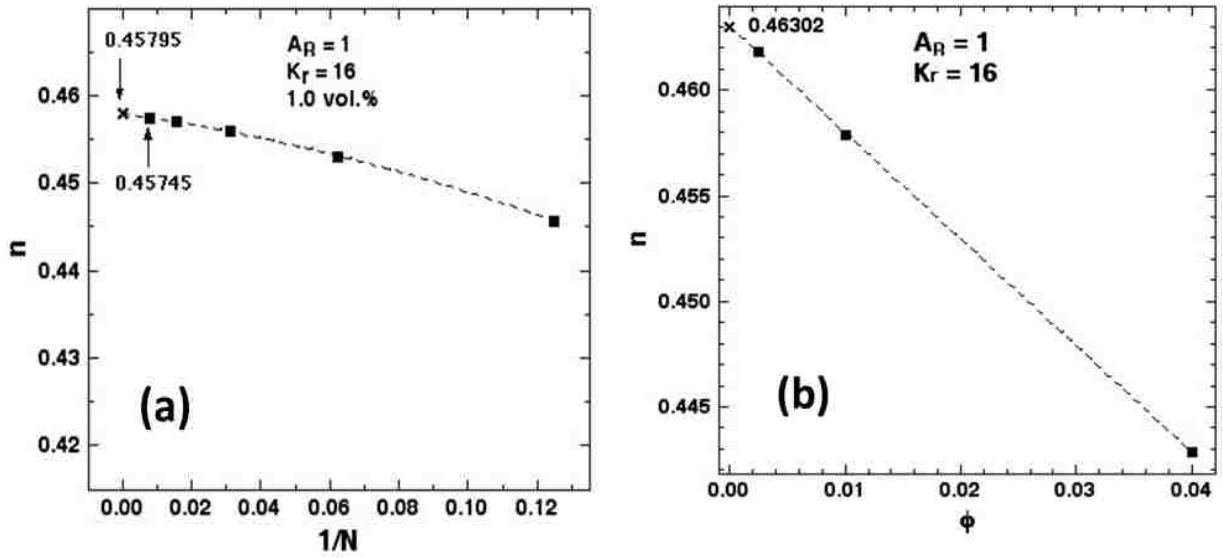

Figure 1-4. (a) The extrapolation to zero mesh size for the square, which is comprised of N^2 discrete elements. **(b)** The extrapolation to zero volume fraction for the square eliminates the effect of image fields.

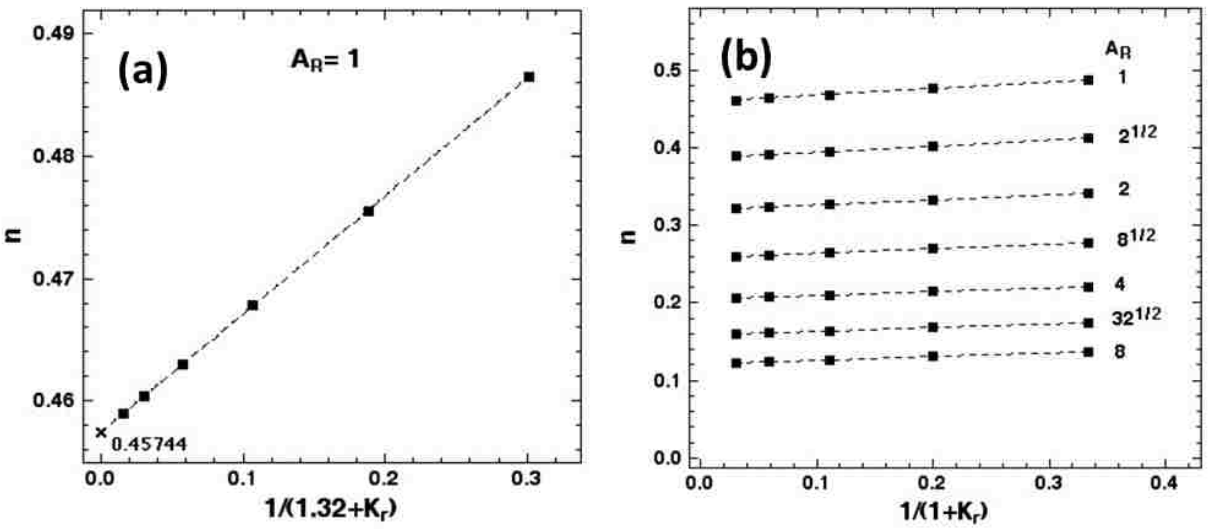

Figure 1-5. (a) Extrapolation to infinite thermal contrast for the square. The value 1.32 is used here to give greater accuracy in the extrapolation. **(b)** Summary of the demagnetization factor as a function of contrast ratio for rectangles of a range of aspect ratios, each aspect ratio differing from the next by a factor of √2.

An adequate description of the functional dependence of the transport virial coefficient on both aspect ratio and contrast ratio can be obtained by reference to the plots in **Figures 1-6(a)** and **(b)**, which show that to good accuracy $n_\infty^{-1} = 1.343 + 0.8829 A_R$ and $a/n_\infty = 0.1824 + 8.337 \times 10^{-3} A_R^{3/2}$. The demagnetization factor is consequently described by

$$n_K = \frac{1}{1.343 + 0.8829 A_R}\left[1 + \frac{0.1824 + 8.337 \times 10^{-3} A_R^{3/2}}{1 + K_r}\right], \qquad (1\text{-}8)$$

which is valid for thermal contrast ratios and aspect ratios greater than 1. Substituting this expression into Equation 1-2 gives the desired expression for the virial coefficient, which is plotted for various aspect ratios as a function of contrast ratio in **Figure 1-7(a)**.

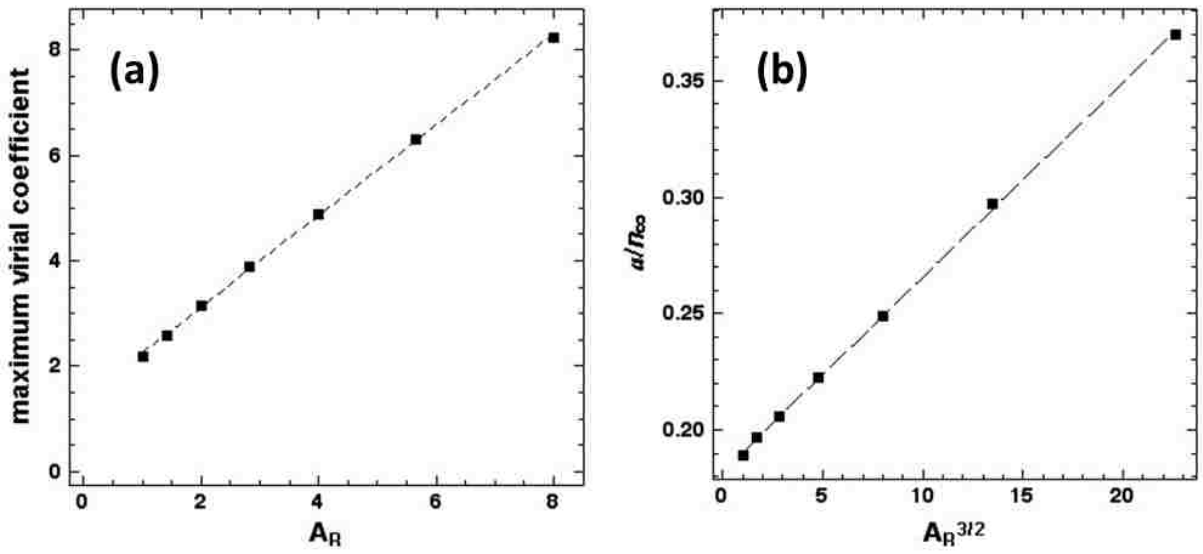

Figure 1-6. (a) The maximum virial coefficient, obtained for the case of infinite thermal contrast K_r, is a linear function of particle aspect ratio for aspect ratios >>1. **(b)** The ratio a/n_∞ is essentially a linear function of the three halves power of the aspect ratio.

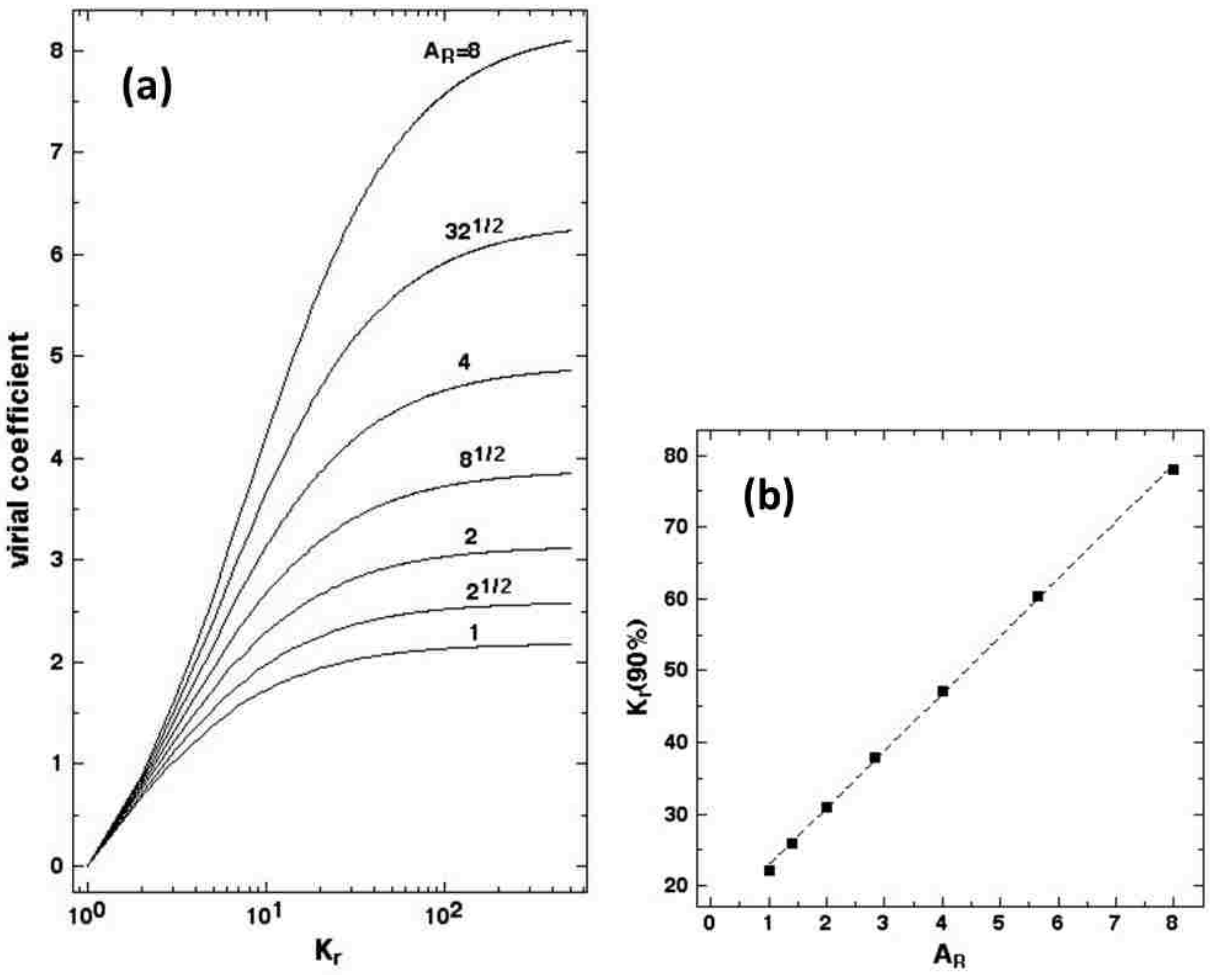

Figure 1-7. (a) The virial coefficient saturates at ever-higher contrast ratios as the aspect ratio increases. **(b)** The contrast ratio required to achieve 90% of the maximum virial coefficient is shown as a function of aspect ratio.

The transport virial coefficient saturates at high contrast ratios, so it is interesting to determine the contrast ratio required to achieve nearly the maximum possible virial coefficient for any particular aspect ratio. **Figure 1-7(b)** shows that to achieve 90% of the maximum virial coefficient requires a contrast ratio that is roughly 10× the aspect ratio. For the Ni platelets used in our composites, the contrast ratio is $(91\,\mathrm{W/m\cdot K})/(0.23\,\mathrm{W/m\cdot K}) \approx 400$, which is sufficient to take full advantage of an aspect ratio of 40, which is characteristic of the thinnest platelets we studied. The stainless steel platelets have a contrast ratio of ~70, so a high aspect ratio of the platelets is not appropriate

for this material. In this case an aspect ratio of ~7 would be much better, as this would enable much higher packing densities.

1.6 Discussion

There have been a number of studies of the use of platelets to enhance the thermal conductivity of polymers. Though none of these used field alignment, it is interesting to compare their results to those obtained herein. A very nice paper by Tekce *et al.* [1.5] compares the conductivity enhancement of 45 μm Cu platelets, 600 μm short Cu fibers, and 50 μm Cu spheres. The micrographs show that the aspect ratio of the fibers and platelets is quite large, and Cu has a thermal conductivity in the range of 350–384 W/m·K, which is much larger than that of the polyamide matrix, 0.32 W/m·K. At loadings of 16.0 vol.% we can compute from the data in their Figure 4 the thermal conductivity enhancements they achieved (K_{eff}/K_{poly}). For the Cu platelets the enhancement was 4.6, which is in excellent agreement with our own results for both control samples and the thermal conductivity of field-structured Ni platelets transverse to the structuring field. Parallel to the structuring field our Ni platelet composites gave a conductivity enhancement of 20. For the Cu fiber samples Tekce *et al.* [1.5] achieved an enhancement of ~10.8 and for the Cu spheres the enhancement is ~1.7, though it is difficult to extract this latter value from their plot. In any case, our Ni spheres gave an enhancement of 1.6 transverse to the structuring field and 2.8 parallel to the field at 16.0 vol.%. We conclude that the higher thermal conductivity of Cu in comparison to Ni is not an important factor for these composites. However, the field orientation and agglomeration is a significant benefit.

The thermal conductivity of epoxy composites containing graphite nano-platelets made from exfoliating graphite particles were studied by Yu *et al.*, [1.8] who achieved a thermal conductivity of 4.0 W/m·K at 16.0 vol.% particles. This is a good result for a random composite and is close to the value of 4.5 W/m·K we obtained at the same loading.

Presumably the large aspect ratio of their nanoparticles, which they estimate as 28, is responsible for this high value.

Hill *et al.* [1.6] studied the thermal conductivity of a variety of platelet-filled epoxy composites, using Al_2O_3, TiB_2, SiC, and BN. The aspect ratios of these platelets were 10.4, 3.8, 4.0, and 9.8, respectively. The thermal conductivities of these materials were all much larger than that of the epoxy molding compound they used, which was given as 0.21 W/m·K. In this study it was found that composites of Al_2O_3, TiB_2, and SiC prepared at filler loadings higher than 45 vol.% did not have enough mechanical strength to remain intact. Even at 45 vol.% the thermal conductivity of these materials did not exceed 3.9 W/m·K, and at 16 vol.% the thermal conductivity was only ~0.5 W/m·K. The BN was similar in performance up to loadings of about 30 vol.%, but then showed a significant increase in performance. At 45 vol.% the conductivity was ~4.6 W/m·K. Again, one would expect a material prepared at this loading to have a paste-like rheology that might not be suitable for some applications.

Shahil *et al.* [1.17] studied graphene sheets as a filler material for epoxy resin and achieved a factor of 5 conductivity enhancement at a loading of 5 vol.%, which would give a conductivity of ~1.0 W/m·K. For some specific samples made at the same loading they report an enhancement twice this large, but no details were given about the cause of such variations or their reproducibility.

Some of these studies on platelet composites give good thermal conductivities, even if the loading is fairly high. What then is the benefit of using field structuring? Why worry about the loading? The main benefit of field structuring derives from the observation [1.3] that the suspension viscosity enhancement is very nearly the same as the thermal conductivity enhancement provided the filler particles are essentially rigid and have a large thermal contrast to the resin, as is typically the case. This observation, which seems to be valid to ~1%, [1.3] is based on the finding [1.3] that the rotationally-averaged Green's

function for the Stokes equation (the so-called Stokeslet or Oseen tensor) is the Green's function for the Laplacian. Thus no matter what filler particles are used to achieve a particular thermal conductivity enhancement, a commensurate viscosity enhancement will occur. Field-structuring reduces this viscosity penalty by a factor of a little more than three, since the field can be applied after the filled resin has flowed into place.

Future work will focus on the use of multilayered magnetic platelets, comprised of a magnetic core coated with a dielectric, to enhance the polymer thermal conductivity. These platelets will not electrically conduct, yet should be as effective as the pure Ni platelets investigated here in raising the effective thermal conductivity of composites.

1.7 Conclusions

In this study we have explored field structuring of magnetic particle suspensions as a method for substantially increasing the thermal conductivity of polymer composites, for applications such as thermal interface materials. This approach is based on the isomorphism between the effective thermal conductivity and effective magnetic permeability of particle composites comprised of particles whose relative thermal conductivity and relative magnetic permeability are either large enough that particle shape is the limiting factor in determining their intrinsic properties—the typical experimental case—or are closely matched. (This isomorphism is limited: the Kapitza resistance will reduce the effective thermal conductivity enhancement relative to the magnetic permeability enhancement.) When a magnetic field is applied to a particle suspension the particles orient and agglomerate so as to minimize their magnetostatic contribution to the free energy, which maximizes the effective permeability of the composite and thus the effective thermal conductivity. In more physical terms, the particles structure in such a way as to maximize their local magnetic field, which in light of the isomorphism maximizes their local thermal gradient when the applied thermal gradient is aligned with the structuring field.

We have demonstrated the efficacy of field structuring for a variety of particle morphologies, with emphasis on Ni spheres and platelets. In both cases field structuring increases the thermal conductivity substantially along the applied field without a significant reduction transverse to the field. Results for the Ni platelets are especially encouraging: an epoxy composite with a 16 vol.% particle loading gave a conductivity of 4.5 W/m·K which is ~23 times that of the unloaded epoxy. Field structuring increases the thermal conductivity by a factor of three over that of the same composite formulation cured in the absence of a field, so a given thermal conductivity can be achieved without the usual commensurate increase in the filled resin viscosity. Field structuring also introduces a three-fold anisotropy in the thermal conductivity and so can be used to direct heat flow.

Finally, we have presented an analysis of thermal conduction in platelets in terms of the demagnetization factor. Discrete element calculations for 2-D platelets show how the demagnetization factor depends strongly on particle shape and weakly on the relative thermal conductivity. The apparent single particle conductivity was then expressed as a function of its shape and relative thermal conductivity and for any given particle aspect ratio one can then determine the necessary relative thermal conductivity required to substantially benefit from the particle shape. These calculations explain why the measured conductivity enhancements for the stainless steel platelet composites are much less than those observed for the Ni platelets.

Acknowledgements

Sandia National Laboratories is a multiprogram laboratory operated by Sandia Corporation, a Lockheed Martin Company, for the United States Department of Energy under Contract No. DE-AC04–94AL85000. This work was supported by the Division of Materials Science, Office of Basic Energy Sciences, U.S. Department of Energy (DOE). The authors wish to thank Matt Groo at Novamet for supplying materials.

References

1.1 J.C. Maxwell, *A Treatise on Electricity and Magnetism* (Dover, New York, 1954).

1.2 A. Eucken, Allgemeine gesetzmabigkeiten fur das warmeleitvermogen verschiedener stoffarten and aggregatzustande, *Forschung Gabiete Ingenieur* **11**, 6–20 (1940).

1.3 J.F. Douglas and E.J. Garboczi, Intrinsic viscosity and the polarizability of particles having a wide range of shapes, *Adv. Chem. Phys.* **91**, 85–153 (1995).

1.4 J.E. Martin, E. Venturini, J. Odinek, and R.A. Anderson, Anisotropic magnetism in field-structured composites, *Phys. Rev. E.* **61**, 2818–2830 (2000).

1.5 H.S. Tekce, D. Kumlutas, and I.H. Tavman, Effect of particle shape on thermal conductivity of copper reinforced polymer composites, *J. Reinf. Plast. Compos.* **26**, 113–121 (2007).

1.6 R.F. Hill and P.H. Supancic, Thermal conductivity of platelet-filled polymer composites *J. Am. Ceram. Soc.* **85**, 851–857 (2002).

1.7 R.H. Khiabani, Y. Joshi, and C.K. Aidun, Thermal characteristics of TIMs with elliptical particles, 26th IEEE SEMI-THERM Symposium (2010).

1.8 A. Yu, P. Ramesh, M.E. Itkis, E. Bekyarova, and R.C. Haddon, Graphite nanoplatelet-epoxy composite thermal interface materials, *J. Phys. Chem. Lett.* **111**, 7565–7569 (2007).

1.9 G.K. Batchelor, Transport properties of two-phase materials with random structure, *Annu. Rev. Fluid Mech.* **6**, 227–255 (1974).

1.10 J.E. Martin and G. Gulley, Field-structured composites for efficient, directed heat transfer, *J. Appl. Phys.* **106**, 084301 1–7 (2009) [reprinted in *Virt. J. Nanoscale Sci. & Tech.* 20 19 (2009)].

1.11 J.A. Osborn, Demagnetizing factors of the general ellipsoid, *Phys. Rev.* **67**, 351–357 (1945).

1.12 J.E. Martin, E. Venturini, G. Gulley, and J. Williamson, Using triaxial magnetic fields to create high susceptibility particle composites, *Phys. Rev. E* **69**, 021508 1–15 (2004).

1.13 V. Belevitch and J. Boersma, Some electrical problems for a torus, *Philips J. Res.* **38**, 79–137 (1983).

1.14 Douglas *et al.* (Ref. 1.3) have generalized the intrinsic viscosity terminology from polymer science, and systematically refer to the virial coefficient for property "X" as the "intrinsic X" (*e.g.*, intrinsic conductivity, intrinsic thermal conductivity, …). This terminology is as descriptive as "thermal susceptibility." Which of the three terms ("thermal susceptibility," "intrinsic conductivity", or "transport virial coefficient") to use is problematic, since each stresses the analogy to other properties of particle suspensions, specifically the magnetic permeability, viscosity, or equation of state. We'll use the term transport virial coefficient here for computed properties because of its connection to some of the other literature we cite, even though in a previous paper we preferred the term "thermal susceptibility." This term does not specify the property under discussion, which seems reasonable given that many properties are isomorphic.

1.15 E.J. Garboczi and J.F. Douglas, Intrinsic conductivity of objects having arbitrary shape and conductivity, *Phys. Rev. E* **53**, 6169–6180 (1996).

1.16 M.L. Mansfield, J.F. Douglas, and E.J. Garboczi, Intrinsic viscosity and the electrical polarizability of arbitrarily shaped objects, *Phys. Rev. E.* **64**, 061401 1–16 (2001).

1.17 K.M.F. Shahil, V. Goyal, and A.A. Balandin, Thermal properties of graphene: Applications in thermal interface materials, *ECS Trans.* **35**(3), 193–195 (2011).

Chapter 2

Field-structured, multilayered platelets enable high performance, dielectric thermal composites[2]

Moldable, thermally conductive polymer composites have broad applications as thermal interface materials and encapsulants. These thermal composites are generally comprised of single-phase particles that are randomly oriented and dispersed. Magnetic platelets have been shown to give exceptionally high thermal conductivities when magnetically aligned along the intended direction of heat flow, but produce composites that are electrically conductive. We have designed precision multilayered platelets that enable the development of high performance thermal composites that are electrically insulating. These platelets consist of a thin Ni core that permits field alignment, Al or Cu coatings that facilitate heat transport, and dielectric layers of MgF_2 or SiO_2 that ensure that the final composite is electrically insulating. These platelets can be made flat or corrugated, square or irregular, and the thickness of the various layers can be varied over a wide range. Thermal conductivity data for a variety of platelet compositions, layer thicknesses, and geometries demonstrate that these platelets are highly effective at producing composites with thermal conductivities much greater than that of the resin. Simulation data are presented that show that multilayer platelets have surprising dependencies of their efficiency for heat transfer on the relative thermal conductivities of the various layers. In fact, analysis shows that if the thermal conductivity of the particle phase is much greater than that of the resin, then the thermal conductivity of the composite, at fixed number density of particles, is insensitive to the platelet thickness. These electrically insulating composites would be especially useful as thermally conductive encapsulants for electronic devices.

[2] Originally published as: J.E. Martin, K.J. Solis, D. Rademacher, and V. Raksha, Field-structured, multilayered platelets enable high performance, dielectric thermal composites, *Journal of Applied Physics* **112**, 054306 1–10 (2012).

2.1 Introduction

Composites based on moldable polymeric resins are used as thermal interface layers for a variety of microsystems, and thus there is considerable interest in their development [2.1-2.6]. To increase the thermal conductivity of the composite, the polymer is often filled with randomly dispersed, thermally conductive particles. If the particles are spherical, the effective thermally conductivity of the composite is surprisingly insensitive to the thermal conductivity of the particle phase, and significant conductivity enhancements require high particle loadings. Anisometric particles such as platelets give significantly better results, but high performance materials require that the platelets be oriented and agglomerated along the direction of heat flow. Magnetic platelets, such as Ni, enable manipulation with magnetic fields, but particle agglomeration leads to appreciable electrical conductivity, which is unsuitable for many applications. To produce high performance thermal composites that are electrically insulating, we have designed and fabricated a series of precision multilayered platelets that are comprised of a thin magnetic core (Ni), coated with thermally conducting layers (Al or Cu), and over-coated with dielectric materials (MgF_2 or SiO_2). In this chapter, we demonstrate that these multilayered platelets enable the development of field-structured thermal composites that are electrically insulating, yet have high thermal conductivity enhancements at low particle loadings.

The principal advantage of field-structuring is that it enables the production of composites with thermal conductivity enhancements that are large compared to the (undesirable) viscosity enhancement of the filled resin. In traditional composites, substantial particle loadings are required to achieve a significant increase in the thermal conductivity, and even in the absence of Kapitza resistance the particles incur a commensurate increase in the resin viscosity, regardless of particle shape or loading [2.7]. The underlying reason for this proportionality is that the rotationally averaged Green's function for the Stokes equation is the Green's function for Laplace's equation [2.8], so these properties are essentially

isomorphic, at least within ~1%. (When the Kapitza resistance is significant, the viscosity enhancement will be even larger than the conductivity enhancement, and the same is true when the thermal conductivity of the particle phase is not substantially greater than that of the resin.) Field-structuring the particles during resin cure breaks this coupling, because field structuring can be used to substantially raise the thermal conductivity of the loaded resin after it has flowed into position, in which case the viscosity increase is of no concern.

Results for spherical particle composites show the benefit of field structuring, as well as the limitations the spherical particle shape imposes. Using a uniaxial field to organize roughly spherical magnetic particles into chains increases the *specific* thermal conductivity (the relative thermal conductivity increase per unit volume fraction of particles, Equation 2-4 below) of the particle phase by a factor of ~2, relative to that of randomly dispersed particles [2.9]. Somewhat greater thermal conductivity enhancements can be achieved by structuring with heterodyned ac triaxial magnetic fields, which produce complex particle networks. But the spherical particle shape limits the achievable increase in thermal conductivity, even after optimizing the particle structure. Our best spherical particle epoxy-based field-structured composite (FSC) had a thermal conductivity of 1.5 W/m·K at a particle loading of 41 vol. % (epoxy itself is 0.21 W/m·K). So, although field-structuring can optimize the thermal conductivity at a given particle loading, highly conductive composites cannot be made with spherical particles at reasonable loadings.

As was demonstrated in Chapter 1, field-structuring single-phase magnetic Ni platelets dispersed in polymeric resins gives significantly better enhancements, because of the combined effects of the anisometric particle shape, orientation, and agglomeration [2.10]. The applied field orients the platelets such that their director (a unit vector parallel to their minor axis) is normal to the applied field, to produce structures such as those shown in **Figure 2-1**. This figure also shows that the platelet director is randomly oriented in the

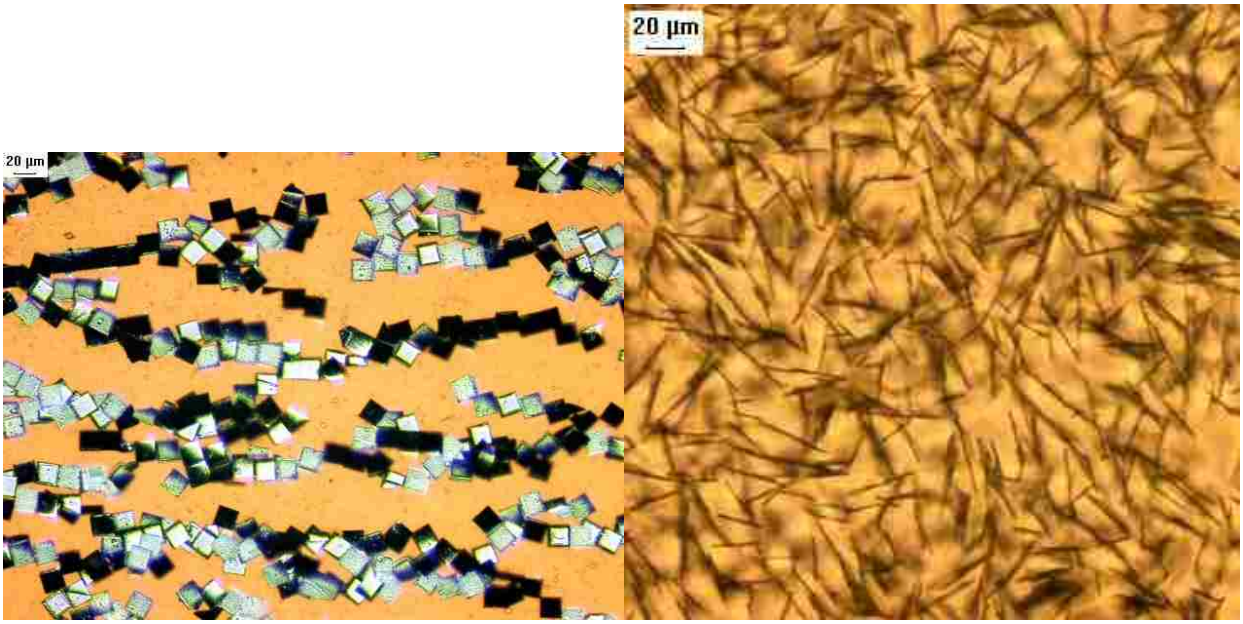

Figure 2-1. Optical images of field-structured composites containing square multilayered platelets made by JDSU Flex Products Group. In the **(left)** image the field is applied horizontally, and the platelets are oriented such that their director is normal to the field. Platelet chaining is also evident. The **(right)** image is viewed parallel to the field, and shows that the director is randomly oriented in the plane orthogonal to the field.

plane orthogonal to the field. Such platelet composites have significantly enhanced thermal conductivity along the direction of the structuring field. In fact, we have shown in Chapter 1 that field-structuring increases the specific thermal conductivity of the platelets by a factor of 3, relative to that of unstructured controls, enabling us to achieve a thermal conductivity of 4.5 W/m·K for an epoxy containing 16.1 vol.% Ni platelets. However, these composites are electrically conducting, and so they are not suitable for all applications, especially device encapsulation.

The magnetic platelets that are the subject of this study were made by JDSU Flex Products using a precise deposition process. These five-layered platelets consist of a magnetic core that is typically 60 nm thick (Ni or stainless steel) coated on both sides with a thermally conductive layer (Al or Cu) whose uniform thickness is a design variable, ranging from 80 to 200 nm in this study. The thickness of the dielectric over-coatings (MgF_2 or SiO_2) is another design parameter and ranges from 80 to 470 nm. The platelets are typically ~20 µm across, less than 1 µm thick, and can also differ in form and texture. The form is

either irregular or square, and the texture is flat, corrugated, or cross-corrugated. In all cases, composites of these materials are electrically insulating, yet the thermal conductivity enhancements are comparable to those achieved with uncoated Ni platelets. In this chapter, we explore the dependence of the specific thermal conductivity enhancement on various platelet parameters to determine the platelet geometry and composition that optimizes thermal transport in field-structured composites. Simulations of thermal transport through multilayered platelets are presented that help explain some of the unexpected results we find.

2.1.1 Background

Magnetic fields are highly effective at increasing the specific thermal conductivity of the particle phase because they organize the particles into optimally conductive structures. To understand this effect, one must appreciate that a wide variety of the physical properties of particle systems are isomorphic under suitable conditions of contrast, a subject discussed at length by Batchelor [2.11]. Examples include the hydrodynamic effective virtual mass, dielectric permittivity, magnetic permeability, thermal conductivity, electrical conductivity, suspension viscosity, and so forth. These isomorphisms are based on the fact that these properties can be computed from a field that is subject to Laplace's equation in regions interior and exterior to the particle surfaces, and that there are boundary conditions for the field that can be expressed in the same form. For example, when comparing the thermal conductivity to the magnetic permeability, the magnetic field **H** plays the same role as the thermal gradient, and the induction field **B**, which quantifies the material polarization response, plays the same role as the thermal flux density. The permeability corresponds to the thermal conductivity. When a magnetic field is applied to a particle suspension, the particles will orient and agglomerate so as to minimize their magnetostatic contribution to the free energy. This contribution is minimized when the permeability, and therefore the thermal conductivity, is maximized. Of course, the ratio of the particle and polymer

permeabilities might not be equal to the ratio of their conductivities, but in many cases of interest both these ratios are large. Kapitza resistance complicates the relationship between these properties, reducing the thermal conductivity enhancement relative to the permeability enhancement by creating temperature discontinuities at material interfaces. This effect can be difficult to quantify in complex composite materials. At this point, the use of magnetic fields to create optimized composite properties has had impact on chemical sensors, strain sensors, magnetostrictive actuators, and composite magnets. The development of electrically insulating thermal composites presents a new challenge for this class of materials.

2.2 Experimental

The magnetic platelets were made in experimental quantities for these thermal conductivity studies by JDSU Flex Products Group using a vacuum deposition process. Multilayered stacks were coated in vacuum on a microstructured substrate having an organic release layer. The deposited material was subsequently removed from the substrate and in the case of the irregular platelets ground to the desired size of 20 μm. **Table 2-1** summarizes the properties of the platelets employed in this study. The formation of functional composites with high effective conductivities requires both a high virial coefficient and a high particle loading. To achieve both, we have structured our platelet composites with a magnetic field having a strong gradient parallel to the field. This gradient field orients the particles and then draws them into the high field region. Field structuring was performed in a 1 cm square cuvette that was initially filled to a level of 3 cm with the dilute epoxy-particle suspension. The field gradient concentrates the particles into the bottom of the cuvette, to a height that is typically ~5 mm or more. After the epoxy cured, a number (from 1 to 4) of 1.5 mm-thick, 1 cm square composite wafers were precision machined for laser flash diffusivity measurements. The volume fraction of platelets is computed from the composite density, which was determined for each wafer. With this procedure, any particular platelet type

sample	form	core	coating 1	coating 2	vol. %	K (W/m-K)	specific conductivity
M1315-3490	irr. corr.	60 nm Ni	80 nm Al	200 nm MgF_2	12.1	1.72	59.4±0.9
M1315-3491	irr. corr.	60 nm Ni	120 nm Al	200 nm MgF_2	10.5	1.58	62.1±1.2
M1315-3492	irr. corr.	60 nm Ni	160 nm Al	200 nm MgF_2	8.9	1.28	57.3±12.4
M1315-3493	irr. corr.	60 nm Ni	200 nm Al	200 nm MgF_2	8.4	1.02	46.0±3.4
M1315-3494	sq. flat	60 nm Ni	80 nm Al	200 nm MgF_2	15.4	1.82	49.6±0.5
M1315-3495	sq. flat	60 nm Ni	120 nm Al	200 nm MgF_2	15.1	1.78	50.2±5.8
M1315-3496	sq. flat	60 nm Ni	160 nm Al	200 nm MgF_2	14.7	1.99	57.4±0.4
M1315-3497	sq. flat	60 nm Ni	200 nm Al	200 nm MgF_2	13.7	1.82	56.0±0.3
M1315-3498	irr. flat	60 nm Ni	80 nm Al	200 nm MgF_2	11.0	1.13	39.9±0.5
M1315-3499	irr. flat	60 nm Ni	120 nm Al	200 nm MgF_2	11.6	1.34	46.5±0.3
M1315-3500	irr. flat	60 nm Ni	160 nm Al	200 nm MgF_2	11.2	1.36	48.8±0.4
M1315-3501	irr. flat	60 nm Ni	200 nm Al	200 nm MgF_2	11.3	1.38	49.3±0.8
M1315-3503	irr. flat	60 nm Ni	160 nm Cu	200 nm MgF_2	7.3	0.98	50.2±0.3
M1315-3504	sq. flat	60 nm Ni	160 nm Cu	200 nm MgF_2	7.1	1.01	53.9±0.5
M1315-3505	irr. corr.	60 nm Ni	160 nm Cu	200 nm MgF_2	5.3	0.72	46.1±0.8
CDL-7442	irr. flat	60 nm Ni	160 nm Al	200 nm MgF_2	12.6	1.50	49.0±0.5
CDL-7942	irr. corr.	60 nm Ni	160 nm Al	200 nm MgF_2	12.2	2.00	70.0±0.3
1315-3455	sq. corr.	50 nm Ni	80 nm Cu	80 nm Si	7.5	1.43	76.9±5.7
1315-3456	irr. xcorr.	50 nm Ni	80 nm Cu	102 nm Si	5.0	0.72	48.5±1.3
1315-2676	irr. flat	60 nm Ni	80 nm Al	470 nm MgF_2	21.7	1.59	30.2
1315-2678	irr. flat	60 nm Ni	80 nm Al	240 nm MgF_2	13.9	1.31	37.8
1315-2683	irr. flat	60 nm Ni	160 nm Al	240 nm MgF_2	13.8	1.33	38.5
1315-2686	irr. flat	30 nm Ni	160 nm Al	470 nm MgF_2	14.3	1.28	35.6
1315-2688	sq. flat	60 nm Ni	80 nm Al	470 nm MgF_2	21.7	1.53	28.6
1315-2693	sq. flat	60 nm Ni	80 nm Al	240 nm MgF_2	16.5	1.57	41.1
1315-2695	sq. flat	60 nm Ni	160 nm Al	240 nm MgF_2	18.8	2.23	51.9
1315-2697	sq. flat	30 nm Ni	160 nm Al	470 nm MgF_2	18.4	1.97	45.5

Table 2-I. Platelet description and results for their composites. irr., irregular; sq, square; corr., corrugated; and xcorr., cross-corrugated.

generally achieves a consistent loading, but the loadings achieved are dependent on the platelet morphology. Finally, when more than one wafer could be machined from the sample, the standard deviation of the mean was computed for the specific thermal conductivity.

Thermal conductivities were computed from the measured thermal diffusivities by multiplying by the volumetric heat capacity of the composite. The volumetric heat capacity

of the composite was computed as a volume-fraction–weighted average of the known heat capacities of each phase (*e.g.*, polymer, Ni, Al, MgF_2).

2.3 Results

Most of our measurements were made at low particle concentrations, so it is helpful to have some appreciation of the dependence of the effective properties on particle shape in this regime. The effective thermal conductivity K_{eff} of a random composite of particles can be expressed as a Taylor expansion

$$\frac{K_{eff}}{K_{poly}} = 1 + \alpha\phi + \ldots, \tag{2-1}$$

where K_{poly} is the thermal conductivity of the polymer phase. Because this expression is similar in form to the virial expansion of a gas, the coefficient α has sometimes been referred to as the first virial coefficient [2.7]. This *transport* virial coefficient is a strong function of particle shape when the contrast ratio $K_r \equiv K_p / K_{poly}$ is large. Under these conditions, the transport virial coefficient can be independent of the thermal conductivity, K_p, of the material of which the particle is comprised. When the contrast ratio is infinite, the virial coefficient has simple values for elementary shapes [2.7]. Normal to the surface of a thin platelet the virial coefficient is 1, normal to the cylindrical axis of a long rod the virial is 2, and for a sphere [2.12] the virial is 3. Parallel to the major axis of a long prolate ellipsoid (roughly a rod), the virial increases asymptotically as the square of the aspect ratio, and so can be very large, and in the plane of an oblate spheroid (roughly a platelet) the virial increases asymptotically as the inverse aspect ratio. If the particles are organized into structures, this can significantly affect the virial. For example, simulations of sphere chaining in a uniaxial field give a computed virial of ~7.25 parallel to the chains and ~2.3 perpendicular to the chains [2.13].

In Chapter 1 [also Ref. 2.10] we computed the transport virial coefficient for solid 2-d platelets as a function of aspect ratio A_R and contrast factor K_r and found that *parallel to the platelet plane* the virial is given by

$$\alpha = \frac{K_r - 1}{1 + n_K(K_r - 1)}, \tag{2-2}$$

where

$$n_K = \frac{1}{1.343 + 0.8829A_R}\left[1 + \frac{0.1824 + 8.337 \times 10^{-3} A_R^{3/2}}{1 + K_r}\right]. \tag{2-3}$$

Equation 2-2 is a general relation that expresses the virial coefficient in terms of the demagnetization factor n_K [2.14]. The demagnetization factor is strongly dependent on geometry and weakly dependent on the contrast ratio. Equation 2-3 is an empirical relation that gives this demagnetization factor as a function of the contrast factor and the aspect ratio. This expression, developed for platelet aspect ratios between 1 and 8, shows that as the aspect ratio increases, the virial approaches $K_r - 1$. Even for solid Ni platelets in epoxy, this computed virial can approach ~450, but measurements we have reported on solid Ni platelets show virial coefficients not higher than 85 [2.10], suggesting that the measured virial is limited by sample geometry and/or Kapitza resistance.

Before presenting our experimental results, it is necessary to point out that we cannot make accurate measurements at extremely low particle concentrations. Because of this limitation, and the manner in which our samples are synthesized, our samples have significant loadings. Much of our experimental data are therefore presented as a *specific* conductivity enhancement, defined through

$$\hat{\alpha} = \frac{K_{eff} - K_{poly}}{\phi K_{poly}}. \tag{2-4}$$

At vanishingly small particle concentrations, this specific conductivity enhancement can be termed the intrinsic thermal conductivity of the particles, in analogy to the intrinsic viscosity

concept used in polymer science [2.7]. This intrinsic property terminology is more descriptive than "virial coefficient" and is also used in the literature.

2.3.1. Effect of platelet morphology and thickness

We first present the results of a study of the specific thermal conductivity of platelet composites made at loadings averaging ~12 vol.%. These platelets vary in shape, texture, and thickness. There are three platelet morphologies: irregular flat, **Figure 2-2**, irregular corrugated, **Figure 2-3**, and square flat, **Figure 2-4**. The corrugated platelets have a spacing of 1500 lines/mm. All of these platelets are comprised of five layers: a 60 nm Ni core, Al layers varying in thickness from 80 to 200 nm, and 200 nm outer coatings of MgF_2. The platelet thickness thus ranges from 620 nm to 860 nm. The ambient thermal conductivities of the three platelet materials are 91, 237, and 10.0 W/m·K, respectively, all of which are significantly larger than that of the epoxy, which we recall is ~0.21 W/m·K. The volume-averaged thermal conductivity of these platelets ranges from 76 to 121 W/m·K, so the virial is limited to ~361–575, values that could only be achieved for extremely high aspect ratio platelets that do not exhibit Kapitza resistance in epoxy.

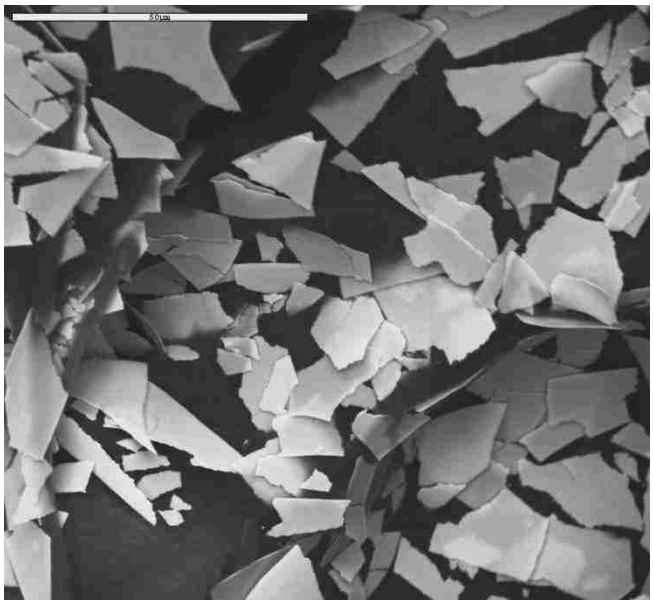

Figure 2-2. An SEM image of irregular flat platelets illustrates their complex shape. These platelets are typically 20 μm in size.

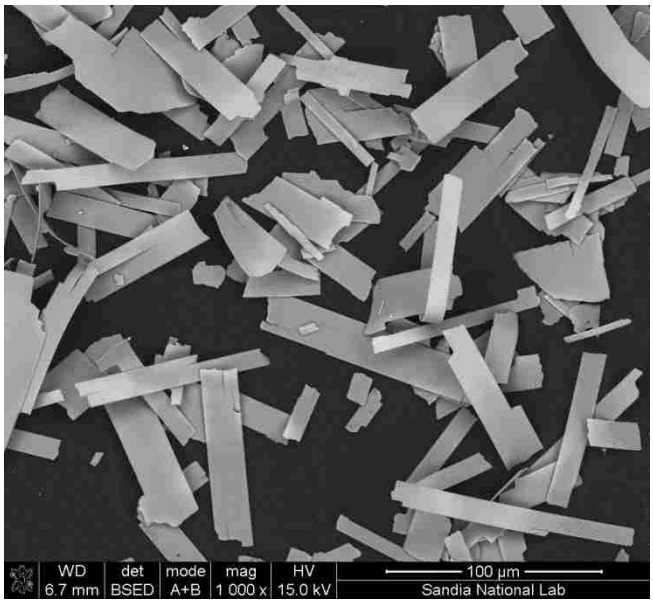

Figure 2-3. An SEM image of irregular corrugated platelets shows their highly elongated fracture pattern, with the corrugation lines parallel to the long axis of the platelets. The wavelength of the corrugations is 670 nm.

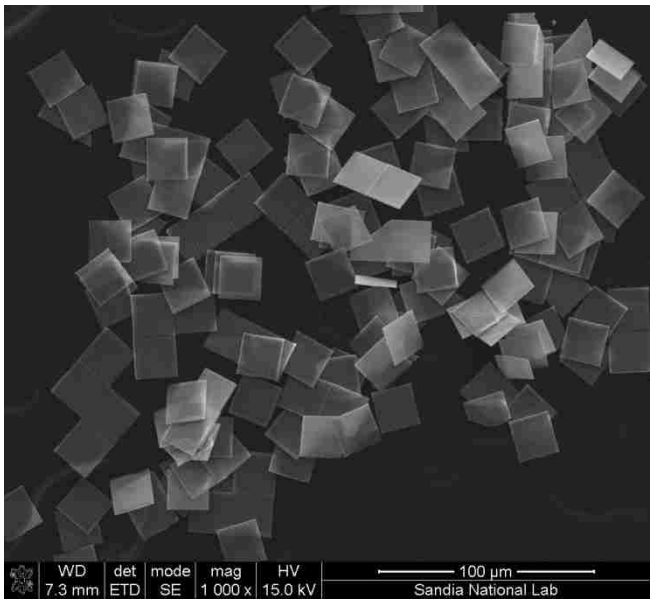

Figure 2-4. An SEM image of square flat platelets shows the uniform size of the platelets, though some twins are evident.

Figure 2-5 shows that the specific thermal conductivities for both flat platelets are weakly dependent on the thickness of the Al layers, but are significantly greater for the square platelets, achieving a maximum of 57.4 ± 0.4, than for the irregular platelets, for

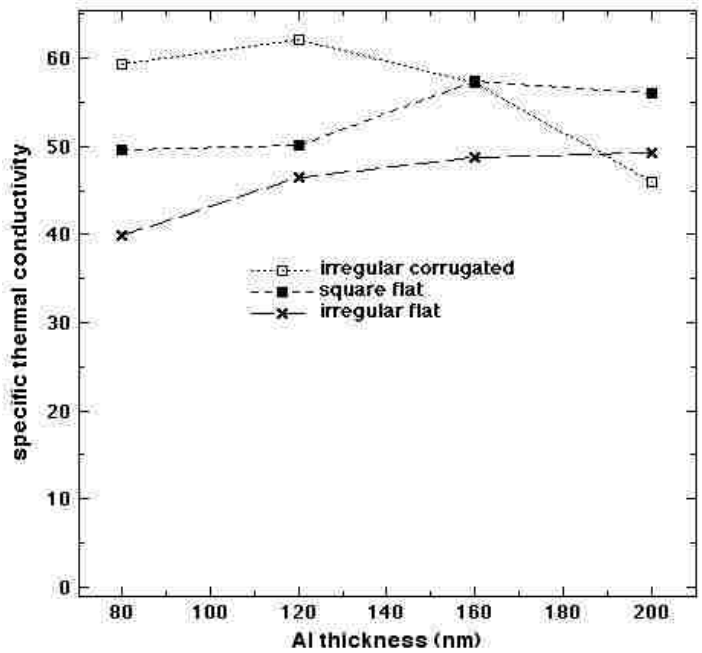

Figure 2-5. The dependence of the specific thermal conductivity on the thickness of the Al layers of three different platelet morphologies is shown. In all cases, the Ni core is 60 nm thick and the outer MgF_2 layers are 200 nm thick. The irregular corrugated platelets offer the best performance, peaking at an Al layer thickness of 120 nm.

which the values do not exceed 49.3 ± 0.8. Increasing the thickness of the Al layers reduces the aspect ratio of the platelets (which we hereafter define as the ratio of the platelet width to thickness), which one would expect to reduce the virial coefficient, but decreases the relative proportion of the low conductivity MgF_2 layers. The irregular corrugated platelets achieve an even greater specific conductivity than the flat platelets, attaining a value of 62.1 ± 1.2 at an Al coating thickness of 120 nm. Curiously, the specific conductivity falls off significantly as the Al layer thickness increases. All of these composites exhibit negligible electrical conductivity over the frequency range of our LCR bridge, $20–10^6$ Hz, and these specific thermal conductivities are much greater than the virial coefficient of 3, which applies to a random composite of spherical particles having asymptotically large thermal contrast.

Because the corrugated shape proved so effective, a second set of both irregular corrugated and irregular flat platelets were made in the same vacuum deposition chamber at

the same time in order to ensure that they would have precisely the same layer thicknesses, thus isolating only the shape difference. These platelets have a 60 nm Ni core, 160 nm Al layers, and 200 nm MgF_2 layers. Four composites were made of each platelet type and the measured specific conductivities were 49.0 ± 0.5 and 70.0 ± 0.3 for the flat and corrugated platelets, respectively, thus affirming that platelet corrugation can significantly increase the thermal conductivity. At only 12.7 vol.%, the corrugated platelet composite gave a thermal conductivity of 2.1 W/m·K. Figure 2-3 shows that the corrugated platelets tend to fragment into rectangular shapes with the corrugations parallel to their long axis. Both the direction of the corrugations and the rectangular shape cause these platelets to field align in the direction of their long axis, which would tend to increase the virial coefficient.

2.3.2. Copper versus aluminum

Five-layered platelets having the same three morphologies—irregular flat, square, and irregular corrugated—were prepared with Cu instead of Al, to determine if the greater thermal conductivity of Cu (401 W/m·K) increases the specific thermal conductivity of the platelets. In these platelets, the Ni core remains at 60 nm, the Cu layers are 160 nm, and the MgF_2 coatings are 200 nm, enabling a direct comparison to one of the Al-based platelets described previously. The specific thermal conductivity of the irregular flat platelets was found to be 50.2 ± 0.3, which is comparable to the 48.8 ± 0.4 obtained for the corresponding Al-based platelet. The square flat Cu-based platelets gave 53.9 ± 0.5, which is slightly lower than the Al analogue, which gave 57.4 ± 0.4. The Cu-based corrugated platelets gave a specific conductivity of 46.1 ± 0.8, which is significantly lower than the value 57.3 ± 6 obtained for the Al-based platelets. The high thermal conductivity of Cu provides no real advantage for the aspect ratio of platelets we are using, and actually reduces thermal transport probably because its Kapitza resistance is larger. In fact, for platelets having the aspect ratio we are using, even if the Cu had infinite thermal conductivity the

specific thermal conductivity of the platelets would not be appreciably greater. This point is discussed in greater detail in Section 2.4.

2.3.3. Square corrugated platelets

The aforementioned results indicate that corrugated square platelets might give very high specific conductivities. To investigate this possibility, some special platelets were fabricated, **Figure 2-6**, in the form of 25 μm corrugated squares with 1500 lines/mm. These platelets are very thin, 390 nm, consisting of a 50 nm Ni core surrounded by 80 nm Cu layers coated with 80 nm of SiO_2 on one side and 100 nm of SiO_2 on the other (the unequal SiO_2 layers were not intentional). The specific thermal conductivity was found to be 76.9 ± 5.7, which is significantly higher than that of the other samples. This high value might be a consequence of the extremely large aspect ratio (64) of these platelets, but it is interesting to note that this high specific conductivity occurs despite the very low thermal conductivity (1.3 W/m·K) of amorphous silica. We will address this point in greater detail in the discussion below.

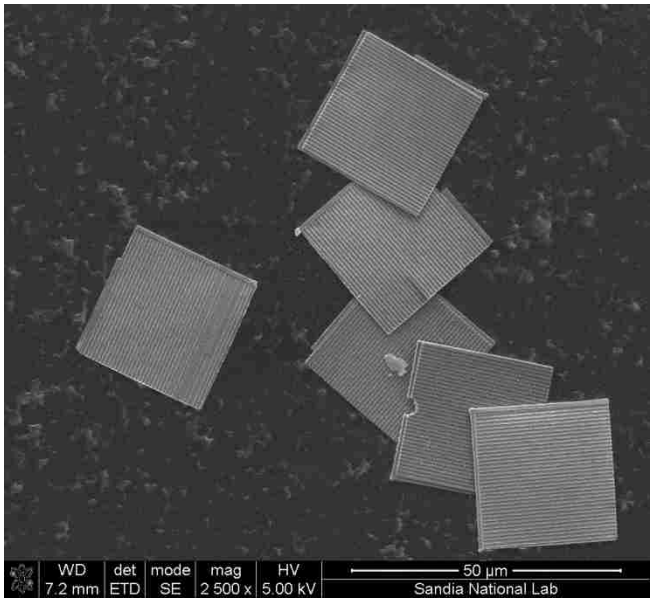

Figure 2-6. An SEM of 25 μm corrugated square platelets shows a high degree of platelet uniformity. These platelets gave a specific conductivity of 76.9, which corresponds to a ten-fold thermal conductivity increase of the composite over the base polymer at a loading of only 11.7 vol.%. The wavelength of the corrugations is 670 nm.

2.3.4. Irregular cross-corrugated platelets

Cross-corrugated platelets were fabricated by JDSU Flex Products Group with 3500 lines/mm. The extremely fine structure of these platelets can be observed in the scanning electron micrographs in **Figure 2-7**. The layers were 102 nm SiO_2/80 nm Cu/50 nm Ni/80 nm Cu/107 nm SiO_2. There is no compelling reason to suspect that these platelets might have a really high specific thermal conductivity, and in fact our measurements gave only 48.5 ± 1.3.

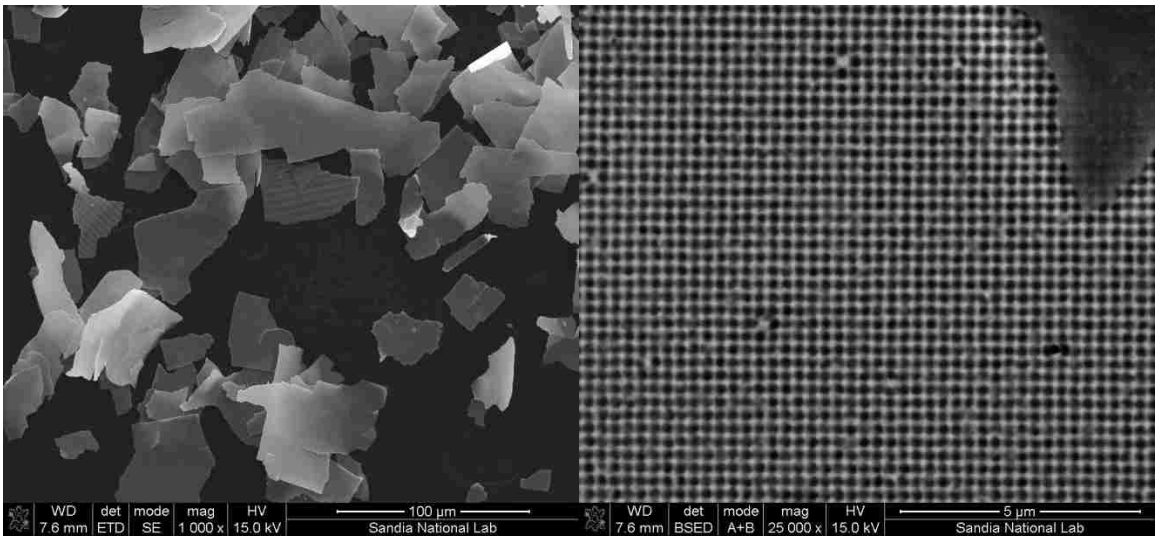

Figure 2-7. An SEM image of irregular cross-corrugated platelets with a corrugation wavelength of 286 nm. Although these are fascinating structures, they did not give unusually large specific thermal conductivities, unlike those platelets that are corrugated in a single direction. This is probably because the cross-corrugations do not lead to elongated fragments.

2.3.5. MgF_2 thickness

Flat platelets were made with very thick MgF_2 coatings to determine the effect of the dielectric coating thickness on thermal transport. Because MgF_2 has such a low thermal conductivity, it might be expected that platelets with thick MgF_2 coatings have very low specific thermal conductivities. In addition, these platelets were made in both irregular and square shapes, to further investigate the shape effect. The thickest platelets had 470 nm layers of MgF_2 surrounding 80 nm thick Al layers and a 60 nm Ni core. The MgF_2 component thus comprised 81% of the platelet volume. Measurements gave a specific

thermal conductivity of 28.6 for the square platelets and 30.2 for the irregular platelets, **Figure 2-8**. These values are understandably low and the difference is not significant. When the MgF_2 layers were reduced to 240 nm (68.6 vol. %), the specific conductivities increased to 37.8 and 41.1 for the square and irregular platelets. Increasing the Al layers to 160 nm reduced the MgF_2 component to 55.8 vol.% and increased the specific conductivities to 51.9 and 38.5, a significant increase for the square platelets. Finally, it was thought that by reducing the thickness of the magnetic cores, the magnetic interactions between platelets would be reduced relative to the Kelvin force drawing the platelets into the high field region. This occurs because the platelet-platelet interaction scales as the square of the core thickness, whereas the Kelvin force is proportional to the thickness. These platelets had a 30 nm Ni core, 160 nm Al layers, and 470 nm MgF_2 layers. Despite the high MgF_2 content (72.9 vol.%), a surprisingly high specific conductivity of 45.5 was obtained for the square platelets, whereas the irregular platelets measured only 35.6.

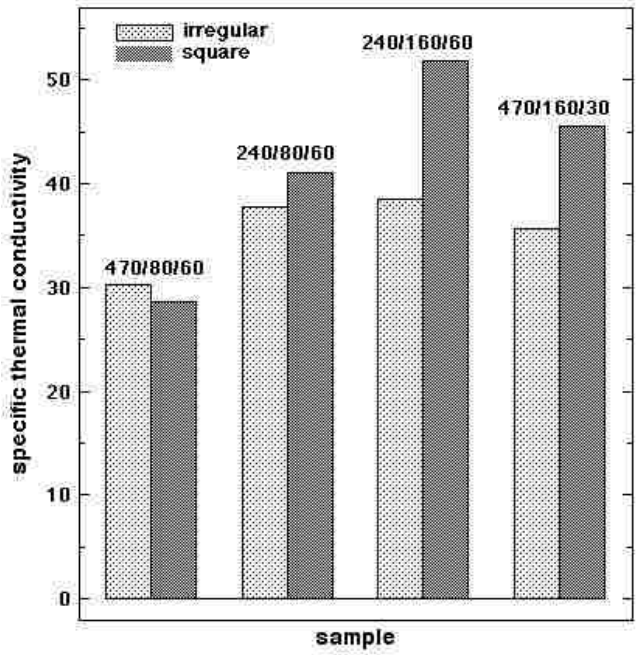

Figure 2-8. Specific thermal conductivity results for irregular and square MgF_2/Al/Ni platelets with thick MgF_2 layers. The numbers above the bars refer to the layer thicknesses in nm. The square platelets give significantly better performance.

2.4 Discussion

Understanding the data we have presented would require an accurate model of the composite structure in order to compute the specific thermal conductivity. Such a model is not forthcoming, as it would require the simulation of field structuring of particles that have complex magnetic interactions. We have written field-structuring simulations for spherical particles, where the magnetic interactions can be reasonably described by a simple self-consistent point dipole approximation. But, such an approach can lead to mathematical singularities for proximal interacting platelets. Modeling the interactions between platelets would seem to require a discrete element computation, which would then have to be coupled with a suitable dynamics code. Such a code would require significant computing resources and is beyond the scope of this experimental study. Nonetheless, relatively simple isolated platelet computations lead to some interesting and surprising insights about heat conduction in multilayered platelets.

The issue of platelet orientation is straightforward. In the absence of a structuring field, the platelets would be randomly oriented and thus the virial coefficient for the thermal conductivity would be $\frac{1}{3}\mathrm{tr}\,\mathbf{P}$, where $\mathbf{P}$ is the polarizability tensor (in the case where Kapitza resistance can be ignored the permittivity and thermal conductivity are isomorphic). For very thin platelets, the polarizability normal to the plane of the platelets is negligible, so the virial is $\frac{2}{3}p_{\parallel}$, where $p_{\parallel}$ is the in-plane polarizability. For field-oriented platelets, the virial is just the in-plane polarizability, so platelet orientation alone should increase the virial by 50%. Two issues remain: the determination of the in-plane virial of an isolated multilayered platelet and the effect of field agglomeration on the virial.

The field-agglomeration effect has been extensively studied for spherical particles, and the results of analysis, simulation, and experimental work [2.15] show that it is less than an 8/3 enhancement over non-structured controls at low particle loadings. For solid Ni platelets, we have shown in Chapter 1 [also Ref. 2.10] that field-structuring increases the

specific thermal conductivity by a factor of 3, relative to that of the non-structured control. Therefore, given that the platelet orientation effect is a factor of 1.5, the agglomeration effect must be a factor of ~2.

The computation of the in-plane transport virial coefficient for solid 2-d platelets is given in Equations 2-2 and 2-3 above. For multilayered platelets, there are additional parameters to consider, since each layer has its own aspect ratio and contrast. Still, illustrative results can be obtained by considering the simple case of a core coated on both sides, such that all three layers have identical thicknesses. We consider two cases. In the first case, the core (of thickness L_1) has a high fixed thermal contrast to the embedding matrix, and the dependence of the virial coefficient on the coating thermal contrast is determined. In the second case, the coating (each layer of thickness L_2) has fixed high contrast and the thermal contrast of the core is varied. The virial expansion can now be expressed as

$$\frac{K_{eff}}{K_{poly}} = 1 + \left(\alpha_1 \frac{L_1}{L} + \alpha_2 \frac{2L_2}{L} \right) \phi + \ldots , \tag{2-5}$$

where α_1 and α_2 are the core and coating virials and the platelet thickness is $L = L_1 + 2L_2$. The total virial coefficient α is the term in the parentheses.

A 2-d discrete mesh algorithm was used to relax Laplace's equation with the appropriate boundary conditions (continuity of heat flow). The details of our approach have been described elsewhere. To compute the virial for each phase, we use the expression [2.10]

$$\alpha_i = \left(K_{r,i} - 1 \right) \frac{\nabla T_{\text{int}}}{\nabla T_0} , \tag{2-6}$$

where ∇T_{int} is the average internal thermal gradient within either the core or coating, and ∇T_0 is the applied thermal gradient, which is uniform. We set the aspect ratio of the platelet to $\sqrt{32}$ (which is a good compromise between high aspect ratio and facile numerics) and set

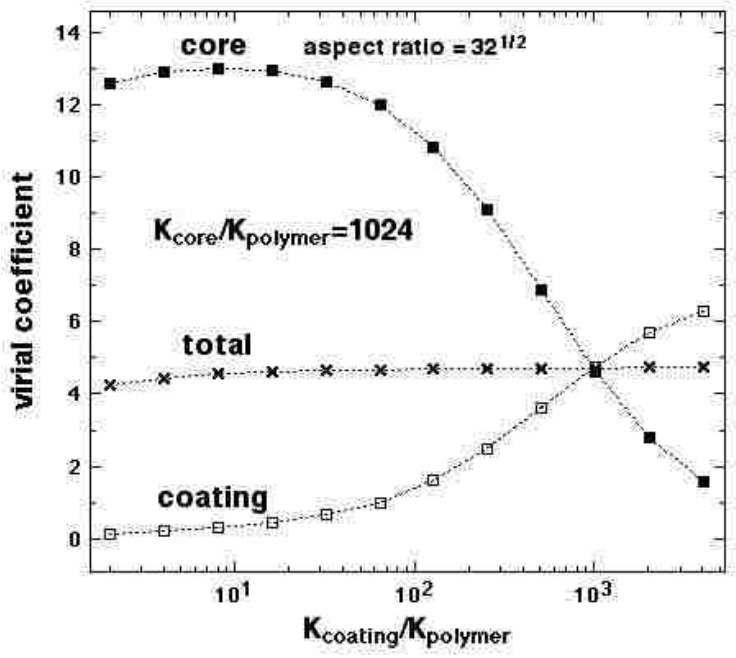

Figure 2-9. Dependence of the computed virial coefficient on the coating thermal conductivity contrast of platelets that have a high (1024) thermal contrast of the core relative to the polymer. Note that although the core and coating virials vary significantly, the total virial is almost unaffected.

the core/polymer conductivity ratio to 1024, which is close to the ratio for Al and epoxy (217/0.21 ~ 1033) and about twice that for Ni and epoxy. We varied the thermal conductivity ratio for the coating to the epoxy from 2 to 4096, and obtained the results shown in **Figure 2-9**.

We were surprised to discover that increasing the conductivity of the coating has an insignificant effect on the total thermal transport through the platelet, which at least superficially seems absurd. However, as the coating conductivity increases, heat conduction through the coating increases and heat conduction through the core decreases commensurately. This decrease occurs because a high coating thermal conductivity reduces the thermal gradient in the coatings, which in turn reduces the thermal gradient in the core. As the coating thermal conductivity approaches infinity, the thermal gradient in the core approaches zero. Considering two tractable limits is helpful: when the coating contrast ratio is unity the coating virial is zero. The core virial is then given by Equations 2-2 and 2-3 for a

platelet with an aspect ratio of $3\sqrt{32}$, and is ~ 16.3 in the limit of infinite core thermal contrast. The total virial is $\alpha = \frac{1}{3}\times 16.3 + \frac{2}{3}\times 0 \approx 5.4$. When the coating thermal contrast is equal to that of the core, the total virial can be computed by substituting the aspect ratio $\sqrt{32}$ into Equations 2-2 and 2-3. If we again take the infinite thermal contrast limit, this total virial is 6.34. As a result, increasing the coating conductivity, which is 2/3 the volume of the platelet, from that of the polymer to infinity does not really help much at this aspect ratio. For other aspect ratios, the result is somewhat different, Figure 2-9, but the conclusion is the same: *When the thermal contrast of the core is sufficiently large that the core virial is dominated by geometry alone, then the total virial depends weakly on the thermal contrast of the coating*. In fact, the coating contrast becomes even less important as the aspect ratio increases. By sufficiently large we specifically mean that $n_K(K_r - 1) >> 1$, (the typical experimental condition) such that Equation 2-2 becomes $\alpha_K \approx n_K^{-1}$. In terms of the core volume fraction ϕ_1, the total platelet virial ratio is

$$\frac{\alpha(K_{coat} = K_{poly})}{\alpha(K_{coat} = K_{core})} = \frac{L_1}{L} \times \frac{1.343 + 0.8829 \times \frac{L}{L_1} A_R}{1.343 + 0.8829 A_R} \qquad (2\text{-}7)$$

in terms of the platelet aspect ratio A_R. **Figure 2-10** is simply a plot of this equation for various relative core thicknesses. Provided that the condition $n_K(K_r - 1) >> 1$ is satisfied, even a core whose thickness is *much* smaller than that of the coatings will give essentially the same benefit as a thick core. These conclusions might still seem counterintuitive, but consider that we are working in the high thermal contrast limit.

In the opposite limit, where $n_K(K_r - 1) << 1$, the platelet virial is limited not by geometry, but by the thermal conductivity of its constituents. In this case, the virial ratio in Equation 2-7 is just L/L_1, so the coating thermal conductivity can become extremely important, especially if the core is relatively thin. This circumstance is not the typical experimental case, as it would require extremely large aspect ratio particles to attain this

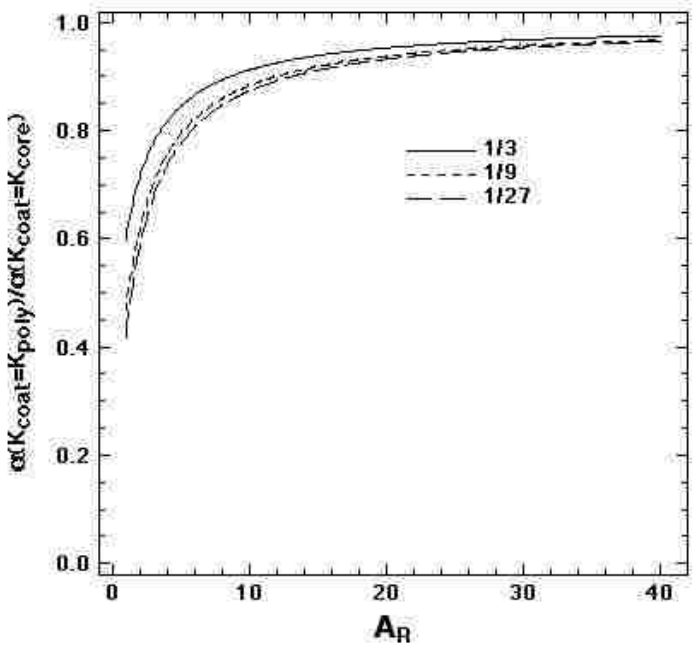

Figure 2-10. The ratio of virial coefficients as a function of platelet aspect ratio A_R. The numerator is the virial for the case where the coating thermal conductivity is that of the polymer, the denominator is for the case when the coating thermal conductivity is that of the core. In both cases, the core thermal conductivity is assumed to be infinite. The three curves are for when the core thickness is 1/3, 1/9, and 1/27 of the total platelet thickness. For aspect ratios greater than ~10, the coating thermal conductivity has little effect on thermal transport.

limit for the kinds of high thermal conductivity materials of which the added particles are normally comprised. For example, substituting $n_K = 1/(K_r - 1)$ into Equation 2-3 shows that the required aspect ratio is $A_R \approx 1.1K_r$ for large K_r. For a pure Ni platelet, this is an aspect ratio of nearly 500, which is far beyond what is practically attainable or useable, since at this aspect ratio the particles would incur a severe viscosity increase in the loaded resin at even very small volume fractions.

Similar computations on a platelet with the same aspect ratio of $\sqrt{32}$ were performed wherein the coating was assigned a high thermal contrast ratio and the core thermal conductivity was varied. The results in **Figure 2-11** show that varying the core thermal conductivity has little effect on the total platelet virial. The principal effect of increasing the core thermal conductivity is to increase the thermal flux in the core and

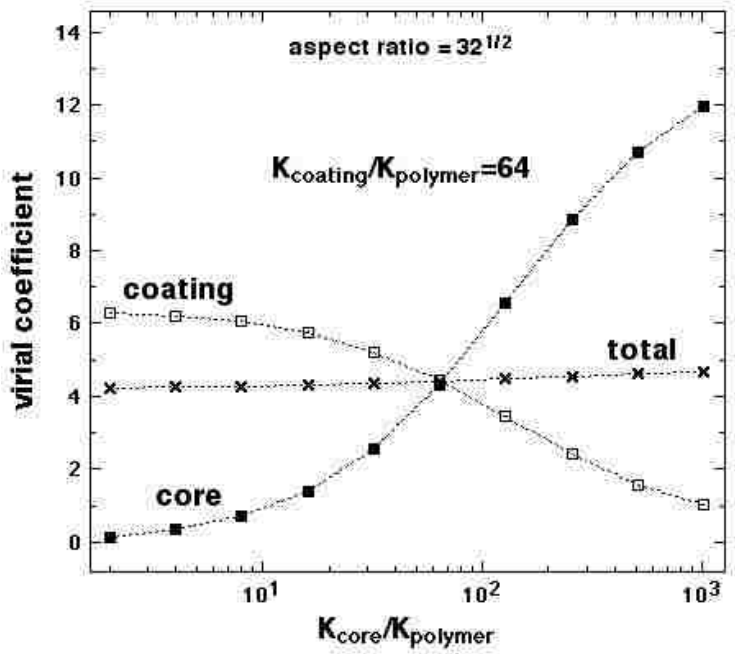

Figure 2-11. Dependence of the computed virial coefficient on the core thermal conductivity contrast of platelets that have a high (64) thermal contrast of the coating relative to the polymer. As in Figure 2-9, the core and coating virials vary significantly, but the total virial is almost unaffected.

decrease the flux in the coatings. This occurs because increasing the core thermal conductivity to a value much greater than that of the coating causes the thermal gradient in the coating to decrease drastically. This situation is opposite, but similar to, the case presented in Figure 2-9.

These calculations demonstrate that there is a great deal of latitude in designing multilayered platelets to enhance thermal transport. If either the coatings or the core have a high thermal contrast to the polymer, then the controlling parameter for an isolated platelet will be its aspect ratio. For the platelets studied in this paper, the Ni core always has a high thermal contrast ratio (~433), so all of our attempts to add thermally conductive Al or Cu coatings to this core did not produce any significant trends. Moreover, even rather thick MgF_2 coatings gave reasonable virials, and the highest virial was indeed obtained for highest aspect ratio particles. However, a clear dependence of the virial on aspect ratio was not

obtained, possibly because of the unknown effect of particle agglomeration and Kapitza resistance.

The insights provided by these 2-d numerical results have led us to make an interesting analytical observation about the use of platelets to increase the thermal conductivity of a polymer or any other continuous phase. The in-plane demagnetization factor of an oblate spheroid is given by [2.14]

$$n = \frac{1}{2\left(A_R^2 - 1\right)}\left[\frac{A_R^2}{\sqrt{A_R^2 - 1}}\arcsin\left(\frac{\sqrt{A_R^2 - 1}}{A_R}\right) - 1\right] \approx \frac{\pi}{4A_R} - \frac{1}{A_R^2} \text{ for } A_R >> 1. \tag{2-8}$$

In the large contrast case, where $n\left(K_r - 1\right) >> 1$, the in-plane platelet virial coefficient is simply the inverse of this demagnetization factor, so for high aspect ratio platelets

$$\frac{K_{eff}}{K_{poly}} \approx 1 + \frac{4A_R}{\pi}\phi\,. \tag{2-9}$$

The volume fraction of particles is simply the product of the particle number density N times the particle volume, which in terms of the platelet width W and thickness L is $\frac{\pi}{6}W^2 L = \frac{\pi W^3}{6A_R}$. The effective thermal conductivity is thus

$$\frac{K_{eff}}{K_{poly}} = 1 + \frac{2}{3}W^3 N = 1 + \frac{2}{3}N'. \tag{2-10}$$

The effective thermal conductivity of the composite is thus given simply by N', which is the average number of platelets within a box of volume W^3, and is *completely independent of the platelet thickness*. For spheres of diameter W, the corresponding expression is

$$\frac{K_{eff}}{K_{poly}} = 1 + \frac{\pi}{6}W^3 N \approx 1 + \frac{\pi}{6}N', \tag{2-11}$$

thus an isolated and field-aligned platelet of width W increases the thermal conductivity of a continuous phase somewhat less than does a sphere of diameter W. The platelet thickness can therefore be minimized if cost is an issue, but other factors, such as platelet stiffness and surface scattering, might be limiting factors if the platelets are made too thin.

Although the focus of this study is platelets, a similar computation can be made for high contrast rods. The demagnetization factor of a prolate spheroid parallel to its long axis, of length W, is

$$n = \frac{1}{A_R^2 - 1}\left[\frac{A_R}{2\sqrt{A_R^2 - 1}} \ln\left(\frac{A_R + \sqrt{A_R^2 - 1}}{A_R - \sqrt{A_R^2 - 1}}\right) - 1\right] \approx \frac{1}{A_R^2} \ln(2A_R - 1) \text{ for } A_R >> 1. \quad (2\text{-}12)$$

The effective thermal conductivity of a composite of aligned prolate spheroids is thus

$$\frac{K_{eff}}{K_{poly}} \approx 1 + \frac{A_R^2}{\ln(2A_R - 1)}\phi = 1 + \frac{\pi}{6}\frac{W^3}{\ln(2A_R - 1)}N = 1 + \frac{\pi}{6}\frac{1}{\ln(2A_R - 1)}N'. \quad (2\text{-}13)$$

Because the width of the prolate spheroid only appears in the logarithmic term, a rod of length W increases the thermal conductivity of a continuous phase on the same order of magnitude of a sphere whose diameter is the rod length.

In the classical computations presented here, it would seem that increasing the aspect ratio of the particles is desirable if the goal is to increase the thermal conductivity of the polymer at low filler volume fraction (and thus cost). However, because the platelet size is already comparable to the bond layer thickness of typical thermal interfaces, the only way to increase the aspect ratio is to decrease the platelet thickness. This would, however, increase surface scattering of phonons and electrons, which is known to decrease thermal transport [2.16]. To clarify this issue, future work will focus on measuring transport in thin layers of the materials of which these platelets are comprised.

2.5 Conclusions

We have shown that field-structured multilayer magnetic platelets can be used to create efficient thermally conductive polymers that are electrically insulating. These platelets are 10–25 times more effective than spherical particles in raising the thermal conductivity, and computations and experiments show that they remain effective even when very thick electrically insulating layers are used as coatings. In fact, both experiments and computations show that their efficiency at increasing thermal transport is very insensitive to their composition, provided that at least one of the layers has a thermal conductivity greatly exceeding that of the polymeric phase. For the best platelets tested, the specific thermal conductivity was ~77, so raising the polymer thermal conductivity by a factor of 10 would require only 11.7 vol.% particles. These materials would be suitable as thermal interface materials and as encapsulants for electronic devices.

Acknowledgements

Sandia National Laboratories is a multi-program laboratory operated by Sandia Corporation, a wholly owned subsidiary of Lockheed Martin Company, for the U.S. Department of Energy's National Nuclear Security Administration under Contract DE-AC04-94AL85000. This work was supported by the Division of Materials Science, Office of Basic Energy Sciences, U.S. Department of Energy (DOE). We thank Paul Coombs, Bill Kittler, and Kees-Jans Delst at JDSU/FlexProducts for their support in providing the magnetic platelets for this research.

References

2.1 R.H. Khiabani, Y. Joshi, and C.K. Aidun, Thermal characteristics of TIMs with elliptical particles, 26th IEEE SEMI-THERM Symposium (2010).

2.2 A. Yu, P. Ramesh, M.E. Itkis, E. Bekyarova, and R.C. Haddon, Graphite nanoplatelet-epoxy composite thermal interface materials, *J. Phys. Chem. Lett.* **111**, 7565–7569 (2007).

2.3 H.S. Tekce, D. Kumlutas, and I.H. Tavman, Effect of particle shape on thermal conductivity of copper reinforced polymer composites, *J. Reinf. Plast. Compos.* **26**, 113–121 (2007).

2.4 V. Belevitch and J. Boersma, Some electrical problems for a torus, *Philips J. Res.* **38**, 79–137 (1983).

2.5 K.M.F. Shahil, V. Goyal, and A.A. Balandin, Thermal properties of graphene: Applications in thermal interface materials, *ECS Trans.* **35**(3), 193–195 (2011).

2.6 R.F. Hill and P.H. Supancic, Thermal conductivity of platelet-filled polymer composites *J. Am. Ceram. Soc.* **85**, 851–857 (2002).

2.7 J.F. Douglas and E.J. Garboczi, Intrinsic viscosity and the polarizability of particles having a wide range of shapes, *Adv. Chem. Phys.* **91**, 85–153 (1995).

2.8 J.B. Hubbard and J.F. Douglas, Hydrodynamic friction of arbitrarily shaped Brownian particles, *Phys. Rev. E* **47**, R2983–2986 (1993).

2.9 J.E. Martin and G. Gulley, Field-structured composites for efficient, directed heat transfer, *J. Appl. Phys.* **106**, 084301 1–7 (2009) [reprinted in *Virt. J. Nanoscale Sci. & Tech.* 20 19 (2009)].

2.10 K.J. Solis and J.E. Martin, Field-structured magnetic platelets as a route to improved thermal interface materials, *J. Appl. Phys.* **111**, 073507 1-10 (2012).

2.11 G.K. Batchelor, Transport properties of two-phase materials with random structure, *Annu. Rev. Fluid Mech.* **6**, 227–255 (1974).

2.12 J.C. Maxwell, *A Treatise on Electricity and Magnetism* (Clarendon, Oxford, 1873).

2.13 J.E. Martin, R.A. Anderson, and C.P. Tigges, Simulation of the athermal coarsening of composites structured by a uniaxial field, *J. Chem. Phys.* **108**, 3765–3778 (1998).

2.14 J.A. Osborn, Demagnetizing factors of the general ellipsoid, *Phys. Rev.* **67**, 351–357 (1945).

2.15 J.E. Martin, E. Venturini, J. Odinek, and R.A. Anderson, Anisotropic magnetism in field-structured composites, *Phys. Rev. E.* **61**, 2818–2830 (2000).

2.16 *Microscale Energy Transport*, edited by C.L. Tien, A. Majumdar, and F.M. Gerner (Taylor & Francis, Washington D.C., 1998).

Part II

Vortex magnetic field mixing

Chapter 3

Strong intrinsic mixing in vortex magnetic fields[3]

We report a method of magnetic mixing wherein a "vortex" magnetic field applied to a suspension of magnetic particles creates strong homogeneous mixing throughout the fluid volume. Experiments designed to elucidate the microscopic mechanism of mixing show that the torque is quadratic in the field, decreases with field frequency, and is optimized at a vortex field angle of ~55°. Theory and simulations indicate that the field-induced formation of volatile particle chains is responsible for these phenomena. This technique has applications in microfluidic devices and is ideally suited to applications such as accelerating the binding of target biomolecules to biofunctionalized magnetic microbeads.

3.1 Introduction

There are many cases where improved methods of fluid mixing are needed, especially in small confined geometries, such as microfluidic channels, where the low Reynolds numbers make it difficult to induce turbulence. There have been numerous attempts to address this problem with magnetic fields, and these fall into two classes: *field gradient* and *uniform field* techniques. Field gradients are used to generate forces on magnetic particles, and uniform fields are used to generate torques on acicular magnetic structures, or Lorentz forces on charges. The resulting fluid flow vastly accelerates mixing when compared to fluid diffusion times at the relevant length scales.

Methods relying on field gradients include shuttling particles through the fluid with a moving permanent magnet [3.1], spinning the fluid across permanent magnetic arrays [3.2], and flowing the fluid across wires that create a field gradient by current flow [3.3]. A strong roughly uniform dc magnetic field has been used to create a Lorentz force on ions

[3] Originally published as: J.E. Martin, L. Shea-Rohwer, and K.J. Solis, Strong intrinsic mixing in vortex magnetic fields, *Physical Review E* **80**, 016312 1–6 (2009).

transported between two electrodes [3.4], and a strong ac magnetic field has been used to rotate glass particles containing magnetite inclusions, apparently due to their small remanence [3.5].

Stir-bar strategies have been extended to the microscale by exposing either permanent or volatile acicular magnetic structures to a spatially uniform rotating magnetic field. Permanent structures include fabricated magnetic rods [3.6,3.7] and magnetite-loaded microbeads chemically bonded into chains [3.8]. These *extrinsic* methods produce a mixing torque that is limited by the low volume fraction of acicular structures that can be loaded into a fluid without serious congestion. A modest level of mixing can be achieved by exposing a fluid containing magnetite-loaded microbeads to a rotating field. At low volume fractions and field frequencies these beads will self-assemble into volatile chains, providing a modest level of mixing within the fluid [3.9,3.10]. When these beads are used to bind target biomolecules this mixing may be called *intrinsic*, since no foreign objects need be introduced to effect mixing. However, at higher field frequencies and particle loadings the time-average dipolar interaction between fixed spherical particles becomes negative, so particles form sheets, not chains, and mixing does not occur [3.11,3.12].

We have developed a different method of intrinsic magnetic mixing that generates large torques with modest fields. Our approach is to apply a *vortex* magnetic field to a suspension of spherical magnetic particles. A vortex field is a rotating field created from two ac fields of identical frequency in quadrature phase, to which a third dc field component normal to the rotating field plane is added. The resulting field vector has the precession-like motion illustrated in **Figure 3-1**, and when the root-mean-square (rms) values of the three field components are equal we call the vortex field *balanced*.

To the first order, the time-average dipolar interaction between stationary particles vanishes in balanced triaxial fields [3.13], of which a balanced vortex field is a special case, so particles can only interact strongly when they form chains that follow the vortex field vector

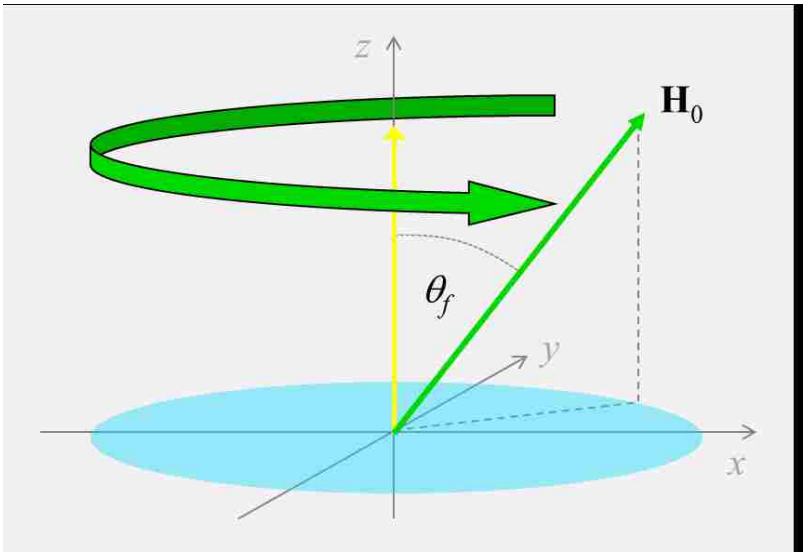

Figure 3-1. The combination of a rotating field (blue) with an orthogonal dc field component (yellow) produces a *vortex magnetic field* (green) of magnitude H_0 that makes a constant angle θ_f to the z-axis, and sweeps out a conical surface.

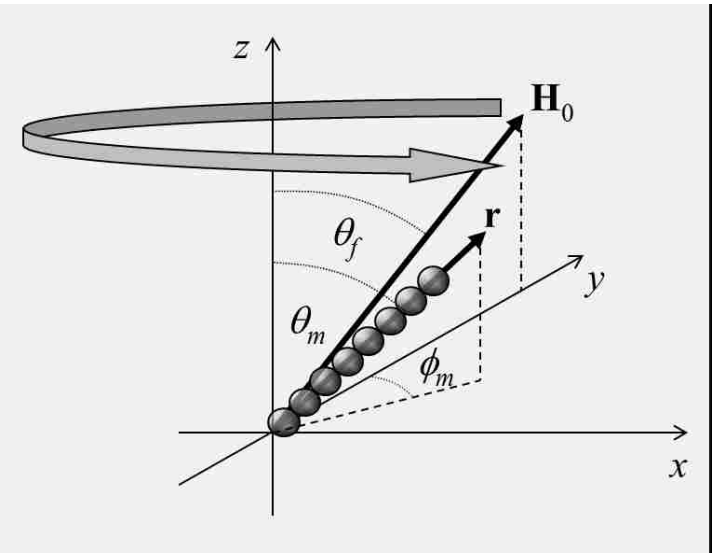

Figure 3-2. The vortex field makes a constant angle θ_f to the z axis, which is parallel to the dc field. The rotating field component is created by applying ac fields in quadrature phase along the x and y axes. A spherical particle chain makes an angle θ_m with the z axis and exhibits an azimuthal phase lag ϕ_m.

(**Figure 3-2**). The mixing torque is independent of particle size, so nanoscale volumes can be mixed with nanoparticles, and only the very modest fields that can be produced with Helmholtz coils are required. This method is effective with particles that do not have magnetic remanence, so it would be an ideal method of accelerating the binding of target biomolecules to functionalized "paramagnetic" microbeads, which would simultaneously provide the mixing torque.

The mixing effects created by a vortex field are striking. When 4–7 μm iron particles are added to a low viscosity liquid they quickly settle. Subjecting this sediment to a 200 Hz rotating magnetic induction field produces no discernible effect until a dc magnetic field of comparable amplitude is applied normal to the rotating field plane. The sediment then disperses to form a suspension that whirls around in the sample cell. Increasing or decreasing the dc field greatly reduces this mixing. Vortex fields with amplitudes as modest as 0.02 T (200 G) rotate the fluid fast enough that the centrifugal force moves the opaque suspension up onto the walls of the cell, so that the cell bottom is free of fluid.

In this chapter we report experiments designed to elucidate the microscopic mechanism of mixing, and these show some surprising effects. First, the mixing torque does not increase with field frequency. By contrast, a stir bar gives a mixing torque proportional to frequency until stagnation occurs. Second, the mixing torque is quadratic in the field, whereas with a stir bar the torque is field independent above the stagnation field. Third, with a soft magnetic material such as iron, the torque is nearly zero in a rotating field and maximizes when the dc component is comparable to the rotating field magnitude. Stir bars function optimally in a simple rotating field.

3.1.1 Mechanisms of torque production

There are several factors that could give rise to a torque on a particle suspension in a vortex field. Each of these factors has a unique dependence on the strength of the vortex field, on

the relative strength of the dc component of the vortex field, on the field frequency, and on the fluid viscosity.

a) PARTICLE SHAPE ANISOTROPY will cause a soft magnetic particle to preferentially align with its long axis parallel to the instantaneous magnetic field. In a vortex field an acicular particle will have a precession-like motion that will impart torque to the fluid. Above the stagnation field this mixing torque will be independent of the field, since the particle will rotate at the field frequency. The torque will be optimal in a simple rotating field, because this maximizes the moment of the particle around the mixing axis, and will increase in proportion to field frequency until stagnation occurs. Finally, the torque will increase with fluid viscosity until stagnation occurs and, thus, will vanish for particles in a solid matrix. An analysis of a nanorod in a vortex field explores these issues [3.14], and a more recent paper on isolated ellipsoidal particles explores some of these issues as well, including the residual asynchronous motion that occurs in the stagnation regime [3.15].

b) A FREQUENCY-DEPENDENT SUSCEPTIBILITY will cause the dipole moment of a particle to lag behind the field, creating torque. This torque will increase with frequency, reach a maximum, and then decrease. This torque will be insensitive to fluid viscosity and will persist even for particles in a solid matrix. The torque will be strong in a rotating field.

c) PARTICLE AGGLOMERATES can lead to a fluid torque if the agglomerates have a susceptibility anisotropy. For example, a low-frequency rotating field applied to a very dilute suspension will assemble particles into chains. Magnetic measurements on particle chains show that the susceptibility parallel to a chain is nearly three times larger than perpendicular. Because

of this, a chain will rotate with the applied field. However, a chain is not a simple stir bar; it is a volatile structure that can grow through aggregation or shrink through fragmentation induced by hydrodynamic forces. A full consideration of particle chaining in a vortex magnetic field is involved [3.14], but the results are easily summarized. The torque will increase with the field energy density, will be roughly independent of the field frequency, and will vanish for a solid composite. Finally, the application of a dc field is essential to torque production. If the dc field is too small the agglomerates will have a sheet-like structure with a negligible susceptibility anisotropy; if the dc field is too large, the chains will tend to grow without bound and collapse along the vertical (mixing) axis, producing negligible torque.

3.2 Experiment

Torque measurements were made on 4–7 μm carbonyl Fe powders obtained from Lord Corporation, chosen for their low remanence. These particles were either dispersed in liquids of differing viscosities η [ethanol, with $\eta = 1$ cP at 25 °C, benzyl alcohol (8 cP) or ethylene glycol (16 cP)] or immobilized by a polymerizable resin to create a solid composite. Typically, 150 mg of Fe particles were dispersed in 2 mL of liquid to create a 1.0 vol.% suspension.

Torques were measured by suspending the samples into the triaxial magnet with a 0.75-mm-diameter nylon torsion fiber and measuring the angular displacement of the vial in the field. The vortex field has three parameters: frequency f, magnitude H_0, and polar field angle θ_f. These parameters are defined through

$$\mathbf{H}_0 = H_0 \left\{ \sin\theta_f \left[\sin(2\pi f t)\hat{\mathbf{x}} + \cos(2\pi f t)\hat{\mathbf{y}} \right] + \cos\theta_f \hat{\mathbf{z}} \right\}, \tag{3-1}$$

so the dc field (mixing axis) is in the z direction. For a balanced vortex field the three rms field components are equal, so $\sin\theta_f = \sqrt{2/3}$, $\cos\theta_f = \sqrt{1/3}$, and $\theta_f \approx 54.7°$.

3.3 Results

We first examine the dependence of the mixing torque on the magnitude of a *balanced* vortex field, comprised of a rotating field and a vertical field whose magnitude is equal to the rms value of either of the rotating field components. The vortex angle of such a field is $\text{atan}(\sqrt{2}) \approx 54.7°$, the so-called magic angle in NMR. Measurements on an ethanol suspension show a nearly field-squared dependence, **Figure 3-3(a)**, over the frequency range of 100–500 Hz, but the more viscous ethylene glycol suspensions show a complex field dependence, **Figure 3-3(b)**, especially at 500 Hz, where the torque is low at low fields. These measurements indicate that particle agglomerates, probably chains, produce mixing. The vortex field produces little torque on the solidified suspension, so the frequency-dependent susceptibility of Fe plays a negligible role.

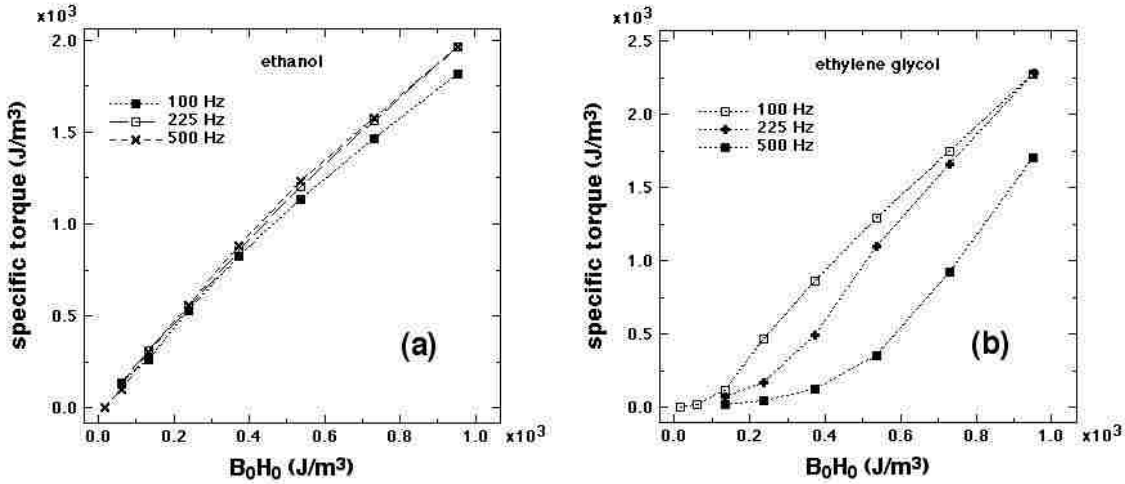

Figure 3-3. The specific torque density (torque per unit volume of particles) of Fe particles in balanced vortex fields ($\theta_f \approx 54.7°$) is shown as a function of field strength. **(a)** The specific torque density in ethanol is essentially independent of field frequency and roughly quadratic in the field, although at higher fields the effect of magnetic saturation is apparent. **(b)** In ethylene glycol, which has a viscosity 16 times that of ethanol, the field dependence is much more complex, especially at 500 Hz, where mixing is very weak at low fields.

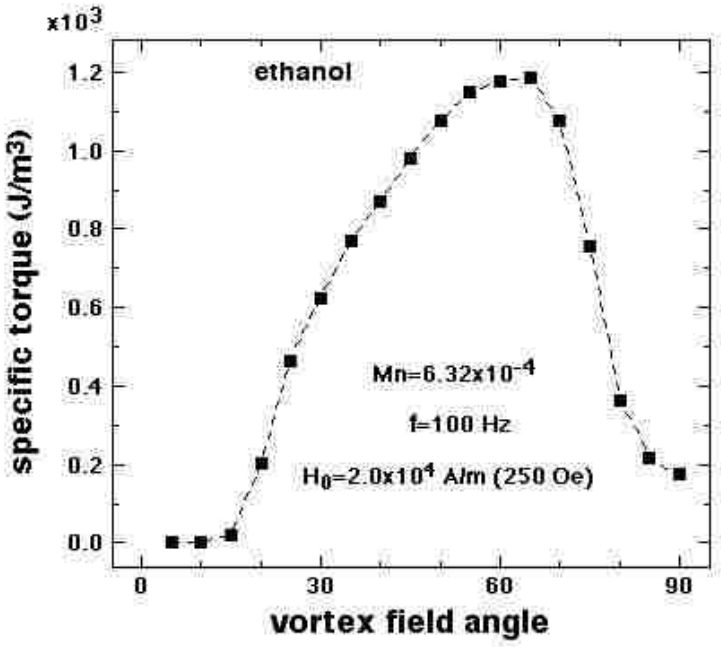

Figure 3-4. The specific torque density of Fe particles in ethanol is strongly dependent on the vortex field angle, with a maximum near a balanced vortex field.

The second issue is the dependence of the torque on the vortex field angle θ_f. The results in **Figure 3-4** show a maximum torque at a vortex field angle near 60°—essentially a balanced vortex field. The torque falls off rapidly at higher angles because the particles form sheet-like structures [3.12] that have negligible susceptibility anisotropy in the plane. The falloff at lower angles is discussed below.

The ethylene glycol data in **Figure 3-5(a)** show that the mixing torque is essentially independent of frequency at the highest field strength and falls off rapidly with frequency at the lowest. Furthermore, **Figure 3-5(b)** shows that at 500 Hz the torque decreases with increasing viscosity. These trends are opposite to that expected for fluid mixing by particle rotation, which should be quite similar to mixing with a magnetic stir bar, and we shall see that this is a complex aspect of torque production by volatile agglomerates.

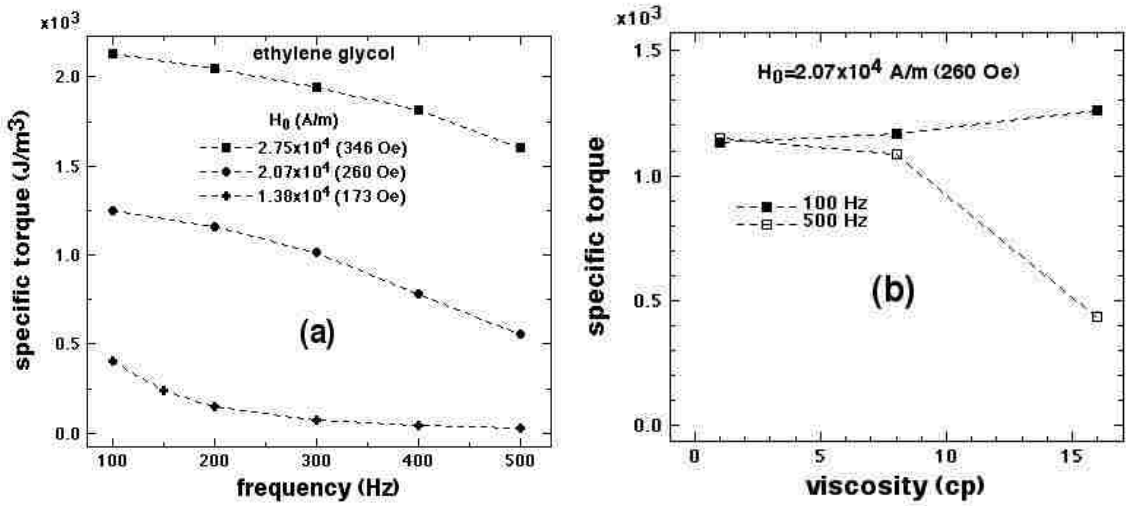

Figure 3-5. The specific torque density of Fe particles in balanced vortex fields ($\theta_f \approx 54.7°$) is shown as a function of frequency and viscosity. **(a)** At the highest field the torque is essentially independent of frequency, but at the lowest field it decreases rapidly with frequency. **(b)** The torque density is independent of liquid viscosity at 100 Hz but decreases with viscosity at 500 Hz.

3.4 Discussion

The experimental results we have shown can be explained by the field-induced formation of particle chains, the shape of which is shown in the dynamical simulation in **Figure 3-6**. As shown in Figure 3-2, these chains follow the vortex field, but with a phase lag ϕ_m in the azimuthal angle swept out by the field. This phase lag decreases with field strength and increases with chain length, field frequency, and fluid viscosity. As the phase lag increases, the polar angle of the chain to the dc field θ_m decreases. This reduces the moment of the chain and thus the mixing torque.

Particle chains are volatile structures that are held together by the magnetic interactions between particles, which must be strong enough to balance the viscous forces on the spinning chains. Larger fields promote the formation of longer chains, and higher frequencies reduce the average chain length. In general, spinning chains will aggregate to form longer chains until the viscous forces dominate the magnetic forces, at which point a chain will fragment near its center. The physical picture is similar to the chain model of electro-rheology and magneto-rheology [3.16], but the geometry is more complex.

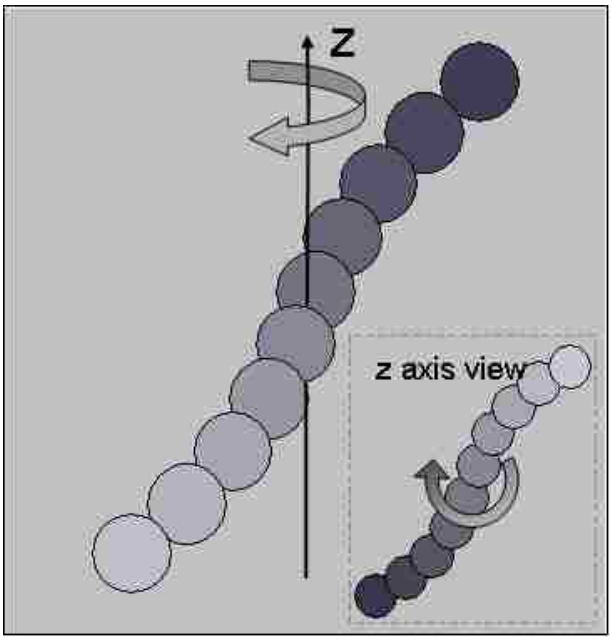

Figure 3-6. Brownian dynamics simulation of a chain in a balanced vortex field shows the curvature of a chain near its maximum possible length. Inset is the view along the mixing axis.

An analysis of chains in a vortex field [3.14] leads to results that are consistent with our experimental observations. First, the torque density in the fluid is given by

$$\mathrm{T} = \frac{1}{12}\phi_p \mu_0 M^2 \sqrt{\sin^2\theta_f - \cos^2\theta_f} \text{ for } \theta_f \geq 45°, \tag{3-2}$$

where ϕ_p is the particle volume fraction, M is the particle magnetization, and μ_0 is the vacuum permeability. This expression predicts that the mixing torque is proportional to the field squared at low fields and is *independent* of field frequency, fluid viscosity, and most notably, particle size. Our data show these effects, as well as more complex behavior that arises when the experimental conditions do not strongly support mixing (*i.e.*, low field, high frequency, high viscosity).

The transition from mixing to quiescent regimes is governed by the so-called Mason number Mn, a ratio of the viscous forces that tend to fragment particle agglomerates to the magnetic forces that cause agglomeration. In terms of the liquid viscosity η and the field frequency ω,

$$\mathrm{Mn} = \frac{9}{2}\frac{\eta\omega}{\mu_0 M^2}. \tag{3-3}$$

Our expression for the mixing torque is only valid for very small Mn, where the dominant magnetic interactions promote particle chaining. A calculation shows that the maximum stable chain size is related to the Mason number through

$$N_{\max}^2 = \frac{1}{16Mn\sqrt{\sin^2\theta_f - \cos^2\theta_f}} \text{ for } \theta_f \geq 45°, \tag{3-4}$$

where the number of particles in a chain is $2N$. The maximum chain size increases with the field, decreases with increasing viscosity and field frequency, and is independent of the particle size. Remarkably, the change in the chain size with these parameters is exactly what is needed to keep the mixing torque constant. This strange behavior is a manifestation of the well-known shear-thinning viscosity of magnetorheological fluids in an applied field.

The transition from the mixing to quiescent regimes is due to the failure of chain formation. Above a *critical Mason number* Mn* the viscous forces so dominate the magnetic forces that even particle dimers do not form. By substituting $N_{\max} = 1$ into Equation 3-4 this *critical* Mason number is shown to be

$$\mathrm{Mn}^* = \frac{1}{16\sqrt{\sin^2\theta_f - \cos^2\theta_f}} \text{ for } \theta_f \geq 45°. \tag{3-5}$$

In a balanced vortex field particles chain only when the Mason number is smaller than roughly 0.1.

Although we cannot predict how the mixing torque will fall off when the Mason number exceeds Mn*, we can still use the Mason number to create a master curve that demonstrates that particle agglomeration is responsible for mixing. To compute the Mason number at low fields we use $M = \chi_p H_0$ for the particle magnetization and the theoretical

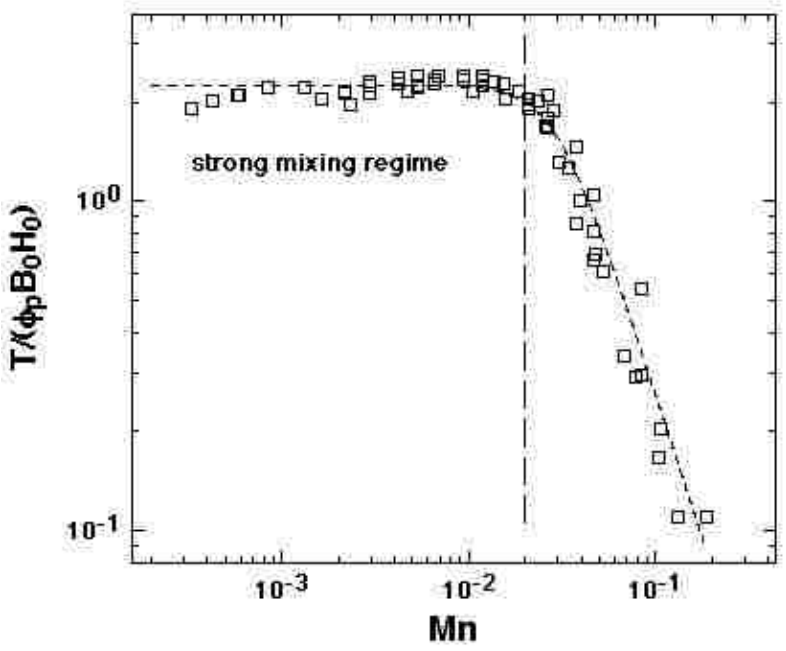

Figure 3-7. Plotting all of the balanced vortex field data in Figures 3-3, and 3-5 on dimensionless axes suggested by the chain model results in a master curve that affirms the conclusion that particle agglomeration is responsible for mixing. Strong mixing, described by Eq. 3-2 and indicative of robust chaining, is observed for Mn<0.02. Mixing is essentially nonexistent (90% lower) above the critical Mason number of 0.1.

value $\chi_p = 3$ for the *apparent* susceptibility of a sphere of high susceptibility magnetic material such as iron [3.17]. The torque density should then be of the form $\mathrm{T} = \frac{\sqrt{3}}{4}\phi_p B_0 H_0 g(\mathrm{Mn})$, where g(Mn)=1 for Mn$\ll$Mn* and is monotonically decreasing for Mn$\gg$Mn*. Data plotted on the dimensionless axes $T/(\phi_p B_0 H_0)$ versus Mn should thus yield a master curve. Plotting the data in Figures 3-3 and 3-5 on these axes indeed yields the master curve in **Figure 3-7**. The chain model thus predicts the mixing behavior in the strong mixing regime, where $\mathrm{Mn} < 0.02$. Above the predicted critical Mason number of 0.1 the torque should technically be zero, and it is indeed 90% smaller than in the strong mixing regime. The maximum amplitude of ~ 2 of the dimensionless torque $T/(\phi_p B_0 H_0)$ is more than four times our predicted value of $\sqrt{3}/4 \approx 0.43$. In fact, accounting for local dipolar fields increases the predicted dimensionless torque amplitude to 1.0 (see Eq. 34 of Ref. [3.14]), and the remaining factor-of-2 discrepancy can be partly attributed to the fact that

the particles are somewhat aspherical, which increases their magnetization in a given applied field [3.17]. But an additional source of this discrepancy is that the chain model we have proposed only accounts for dipolar interactions, which is only correct in saturating magnetic fields. For multidomain particles in low fields multipolar interactions significantly increase the interaction force [3.16].

The dependence of the measured torque on vortex field angle is not easily explained. Equation 3-2 predicts that the torque should vanish for vortex field angles smaller than 45°, a trend seen in the experimental data. This falloff occurs because for low vortex angles it is possible for particle chains to grow without limit and align with the dc field, becoming stationary. For vortex field angles larger than 45° this alignment cannot occur because the chains become unstable and fragment as their phase lag increases and their polar angle decreases. For large vortex angles Equation 3-2 does not apply because the particles form stationary sheets, not chains, under such circumstances [3.13]. In fact, vortex mixing works better than predicted at smaller vortex angles, and we attribute this to the fact that the shear field in the fluid itself causes the chains to fragment at lower field angles. The *single* chain model we have proposed assumes that this fluid is stationary, in other words, we have ignored the collective hydrodynamic interactions of a many-chain system.

The second reason a balanced vortex field is so effective for mixing is that it does not strongly favor the formation of competing stationary structures. This is because in a balanced field the negative dipolar interaction produced by the rotating field on a pair of *stationary* particles cancels, to the first order, the positive dipolar interaction produced by the dc field [3.13]. In fact, the formation of stationary structures is possible, but only for Mason numbers exceeding Mn^*.

3.5 Conclusions

We have shown that magnetic particle suspensions can be efficiently mixed in a balanced vortex field. This mixing is much more effective than that produced by a simple rotating

field and is due to the formation of volatile particle chains that follow the field with a precession-like motion. In the low Mason number, chain-forming regime, the mixing torque increases quadratically with the field and is independent of the field frequency, fluid viscosity, and particle size. This mixing technique is a viable technology for mixing problems on any scale, including mixing in microchannels and accelerating the binding of biomolecules to surface-functionalized magnetite-loaded microbeads.

Acknowledgements

Sandia is a multiprogram laboratory operated by Sandia Corporation, a Lockheed Martin Company, for the United States Department of Energy under Contract No. DE-AC04-94AL85000. This work was supported by the Division of Materials Science, Office of Basic Energy Sciences, U.S. Department of Energy (DOE).

References

3.1 M. Herrmann, T. Veres, and M. Tabrizian, Enzymatically-generated fluorescent detection in micro-channels with internal magnetic mixing for the development of parallel microfluidic ELISA, *Lab Chip* **6**, 555–560 (2006).

3.2 M. Grumann, A. Geipel, L. Riegger, R. Zengerle, and J. Ducrée, Batch-mode mixing on centrifugal microfluidic platforms, *Lab Chip* **5**, 560–565 (2005).

3.3 H. Suzuki, N. Kasagi, and C.-M. Ho, Chaotic mixing of magnetic beads in micro cell separator, *Proceedings of the 3rd International Symposium on Turbulence and Shear Flow Phenomena*, Sendai Japan, 2003 , pp. 817–822 (unpublished).

3.4 H.H. Bau, J. Zhong, and M. Yi, A minute magneto hydro dynamic (MHD) mixer, *Sens. Actuators B* **79**, 207–215 (2001).

3.5 A. Rida and M.A.M. Gijs, Manipulation of self-assembled structures of magnetic beads for microfluidic mixing and assaying, *Anal. Chem.* **76**, 6239–6246 (2004).

3.6 L.-H. Lu, K.S. Ryu, and C. Liu, A magnetic microstirrer and array for microfluidic mixing, *J. Microelectromech. Syst.* **11**, 462–469 (2002).

3.7 P.K. Yuen, G. Li, Y. Bao, and U.R. Müller, Microfluidic devices for fluidic circulation and mixing improve hybridization signal intensity on DNA arrays, *Lab Chip* **3**, 46–50 (2003).

3.8 S.L. Biswal and A.P. Gast, Micromixing with linked chains of paramagnetic particles, *Anal. Chem.* **76**, 6448–6455 (2004).

3.9 S. Melle, G.G. Fuller, and M.A. Rubio, Structure and dynamics of magnetorheological fluids in rotating magnetic fields, *Phys. Rev. E* **61**, 4111–4117 (2000).

3.10 S. Melle and J.E. Martin, Chain model of a magnetorheological suspension in a rotating field, *J. Chem. Phys.* **118**, 9875–9881 (2003).

3.11 T.C. Halsey, R.A. Anderson, and J.E. Martin, The rotary electrorheological effect, *Int. J. Mod. Phys. B* **10**, 3019–3025 (1996).

3.12 J.E. Martin, R.A. Anderson, and C.P. Tigges, Simulation of the athermal coarsening of composites structured by a biaxial field, *J. Chem. Phys.* **108**, 7887–7900 (1998).

3.13 J.E. Martin, R.A. Anderson, and R.L. Williamson, Generating strange magnetic and dielectric interactions: Classical molecules and particle foams, *J. Chem. Phys.* **118**, 1557–1570 (2003).

3.14 J.E. Martin, Theory of strong intrinsic mixing of particle suspensions in vortex magnetic fields, *Phys. Rev. E* **79**, 011503 1–12 (2009).

3.15 P. Tierno, J. Claret, F. Sagués, and A. Cēbers, Overdamped dynamics of paramagnetic ellipsoids in a precessing magnetic field, *Phys. Rev. E* **79**, 021501 1–6 (2009).

3.16 J.E. Martin and R.A. Anderson, Chain model of electrorheology, *J. Chem. Phys.* **104**, 4814–4827 (1996).

3.17 J.A. Osborn, Demagnetizing factors of the general ellipsoid, *Phys. Rev.* **67**, 351–357 (1945).

Chapter 4

Vortex magnetic field mixing with anisometric particles[4]

In Chapter 3, we introduced a vigorous, scale-adaptive mixing technique suitable for microfluidic applications, wherein a suspension of spherical magnetic particles is subjected to a vortex magnetic field, which induces the formation of dynamic particle chains that efficiently stir the solution. Here we explore the dependence of the mixing torque on particle shape, and show that increasing degrees of shape anisometry (*i.e.*, spheres, platelets, rods) give increased mixing torque at the same particle volume fraction. Moreover, all particles, regardless of shape, exhibit similar dependencies of the mixing torque on the vortex field parameters: the torque is maximized in a balanced vortex magnetic field, is proportional to the square of the field strength, and is independent of the field frequency. However, the torque advantage of anisometric particles is somewhat offset by their increased packing volume, which can make the removal of trapped fluid difficult.

4.1 Introduction

Strong, efficient mixing in microfluidic devices is challenging due to the extremely small Reynolds numbers encountered in such flows. However, we have recently developed a mixing technique based on subjecting suspended magnetic particles to *vortex* magnetic fields. Such a field is defined as a rotating field, to which a dc component is added normal to the field plane, to give the field vector a precession-like motion. Vortex fields cause spherical, magnetically-soft, suspended particles to assemble into whirling chains that vigorously stir the fluid. Despite the superficial resemblance to stir-bar mixing, a theoretical analysis [4.1] for spherical particles shows that vortex mixing has sharply distinguishing attributes, due to the volatile nature of the particle chains. For example, in stir-bar mixing the torque

[4] Originally published as: K.J. Solis, R.C. Bell, and J.E. Martin, Vortex magnetic field mixing with anisometric particles, *Journal of Applied Physics* **107**, 114911 1–4 (2010).

increases with frequency and fluid viscosity, is independent of the field strength (above the stagnation field), and is strongest in a simple rotating field. Conversely, in vortex mixing the torque is expected to be independent of frequency and viscosity, proportional to the square of the applied field, and a rotating field should produce little torque. These predictions have indeed been confirmed by experiment in Chapter 3 [also Ref. 4.2].

Suspensions of anisometric particles, such as platelets and rods, should exhibit greater mixing torque than those of spherical particles, because the magnetic field will cause anisometric particles to orient so as to give significantly larger induced particle magnetization. This effect is due to the much greater particle magnetization when the applied field is in the plane of the platelet, or parallel to the rod. The purpose of this chapter is to explore the effects of particle shape anisometry on the mixing behavior of particle suspensions subjected to vortex magnetic fields.

4.2 Experiment

Four separate magnetic particle suspensions were created by dispersing 12.5 wt % (~1.25 vol %) of ferromagnetic particles in ethyl alcohol ($\eta \approx 1$ cP at 25 °C). The particles, shown in **Figure 4-1**, exhibited progressive degrees of shape anisometry: spheres [three dimensional (3D)], platelets [two dimensional (2D)], and rods [one-dimensional (1D)]. The "3D" material was 3–7 μm carbonyl nickel powder (Goodfellow) whose particle morphology is popcorn-like spherical agglomerate. The "2D" structures consisted of either 300 nm-thick, 20 μm nickel platelets coated with magnesium fluoride (JDSU), or 1 μm-thick, 20 μm conductive Ni platelets (Novamet HCA-1). The "1D" particles were cobalt nanorods (d=310±56 nm, l=3.2±0.6 μm) , synthesized as in Ref. 4.3.

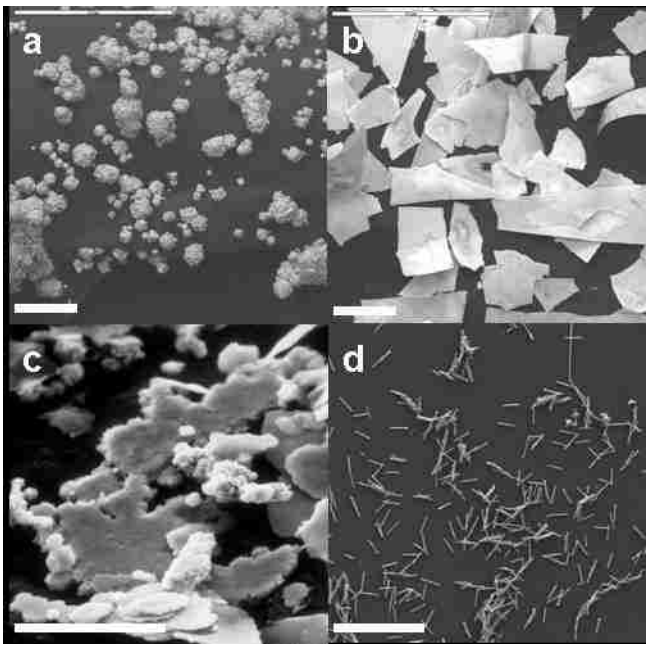

Figure 4-1. Scanning electron micrographs of the experimental materials. **(a)** 3–7 μm spherical Ni particles, **(b)** JDSU 20 μm MgF_2-coated Ni platelets, **(c)** Novamet 20 μm Ni platelets, and **(d)** 3.2 μm Co nanorods. The white scale bars at the bottom of each image represent 20 μm.

The magnetic fields were created by three orthogonal Helmholtz coils in series resonance with tunable, computer-controlled capacitor banks. With this magnet arrangement, we can create numerous time-dependent magnetic fields, but in this study we focus on vortex magnetic fields, which are comprised of two orthogonal, ac components of equal amplitude and frequency in quadrature phase, to which a third dc component is added perpendicular to the biaxial-field plane (*x*-*y* plane). The result is a magnetic field vector that sweeps out the surface of a cone about the *z*-axis (see **Figure 4-2**). The experimental field parameters are the vortex field angle (θ_f) , field frequency (f) , and the field strength (H_0) , defined through the relation,

$$\mathbf{H}_0 = H_0\left\{\sin\theta_f\left[\sin(2\pi ft)\hat{\mathbf{x}} + \cos(2\pi ft)\hat{\mathbf{y}}\right] + \cos\theta_f\hat{\mathbf{z}}\right\}, \qquad (4\text{-}1)$$

where the vortex field angle θ_f is the angle the field vector makes to the *z*-axis. So a simple rotating field has a vortex field angle of 90°, and a *balanced* vortex field—one in which all three rms field components are equal—has a vortex angle of 54.7°.

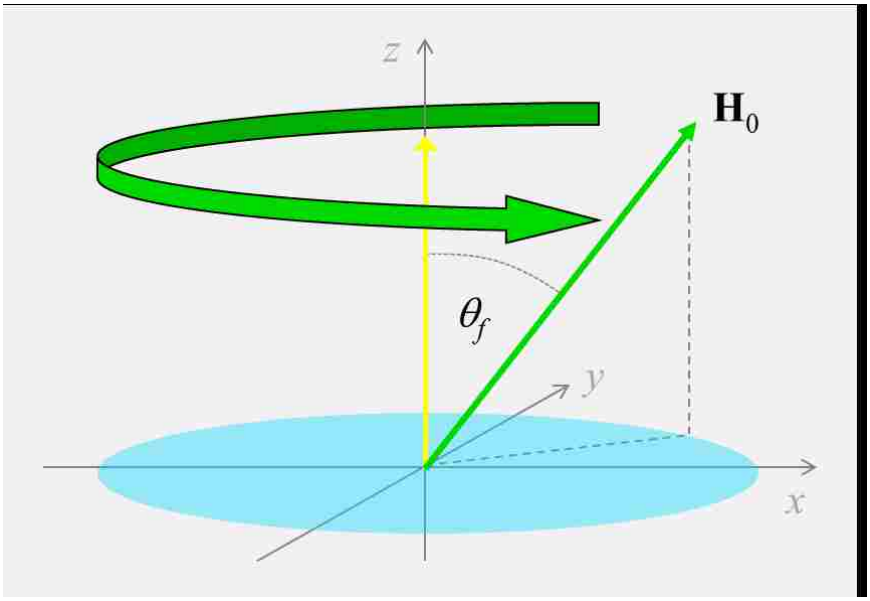

Figure 4-2. Schematic representation of a vortex magnetic field of magnitude H_0 and field angle θ_f.

Mixing torques were measured using a simple torsion balance. A vial containing the sample suspension was suspended into the triaxial magnet cavity by a nylon torsion fiber with a torsion constant of 10 μN·m/rad. The desired vortex magnetic field was then applied, and from the measured angular displacement the mixing torque was computed. Angular displacements were measured with the biaxial field rotating both clockwise and counterclockwise to increase the accuracy of the results.

4.3 Results

4.3.1. Vortex field angle dependence

In our first experiment, we investigated the dependence of the mixing torque on the vortex field angle θ_f. **Figure 4-3** shows that for all of the particle suspensions the mixing torque maximizes at a field angle of approximately 60°, which is essentially a balanced vortex field. As the field angle decreases from this maximum, we observe a strong fall-off of the mixing torque, as predicted by the theory for spherical particles [4.1]. This fall-off at small vortex field angles is due to the tendency for chains to aggregate into ever-longer chains that eventually just align with the z-axis. At large vortex field angles, the particles form

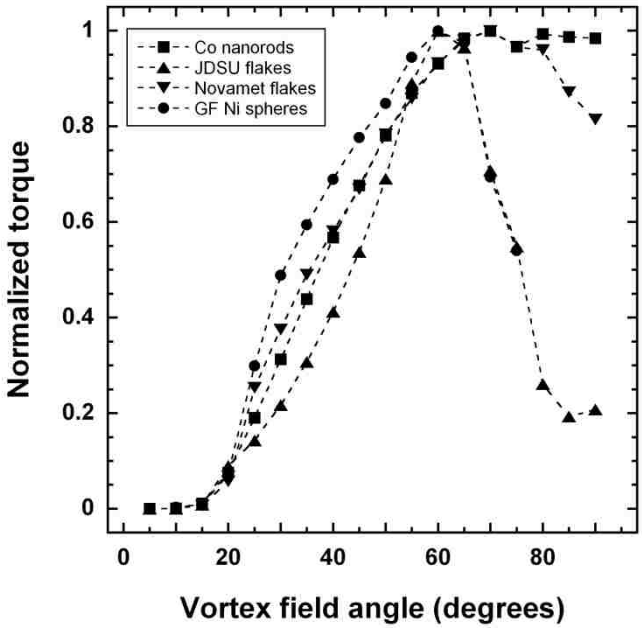

Figure 4-3. Normalized torques of magnetic particles as a function of applied vortex field angle. For small field angles, chains grow unbounded and co-align with the mixing axis (z-axis) producing no torque. The mixing torques maximize for a balanced vortex field near 60°. Finally, at large field angles, spherical particles and JDSU platelets produce little torque due to structure formation, while nanorods and Novamet platelets exhibit strong mixing and torque production.

stationary sheets because the time-average magnetic interactions are a negative dipolar interaction [4.4]. These sheets are static structures so there is no mixing; however, a finite torque still exists because the frequency-dependent susceptibility of nickel causes the magnetization of the material to lag behind the field. In a balanced vortex field, various instabilities prevent unlimited chain aggregation, yet the time-average dipolar interactions do not favor sheet formation. This same behavior is observed for platelets, and we have indeed observed sheet formation with platelets in high viscosity solvents.

In a simple rotating field, each type of particle suspension displays differentiating behavior: the spherical particles form static sheets, the JDSU platelets develop columnar structures that whirl around the vial, the Novamet platelets mix while exhibiting a fine sheet-like structure, and the nanorods mix strongly, as shown in **Figure 4-4**. The strong mixing torque of the nanorod dispersion in a simple rotating field is expected because a rod

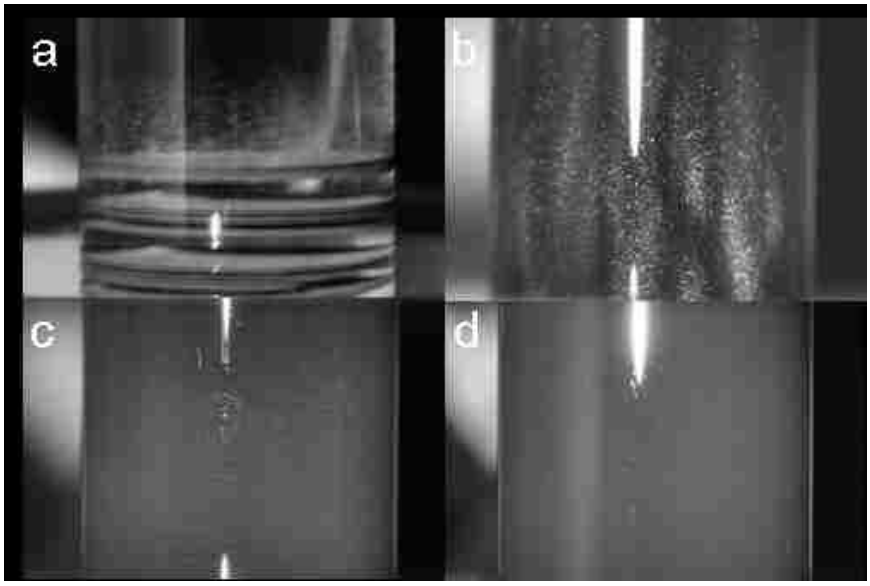

Figure 4-4. Photographs of particle suspensions in simple rotating fields (θ_f=90°). Each particle shape displays distinct structures or dynamics: **(a)** spherical particles form horizontal, static sheets parallel to the rotating field plane, **(b)** JDSU platelets form columnar structures (faint vertical striations) that whirl around the vial, **(c)** Novamet platelets form fine sheet-like structures with mixing, and **(d)** Co nanorods display strong mixing.

will tend to follow a rotating field, just like a stir bar. The ability to mix with only two field components is a clear advantage of nanorods over spherical particles. The Novamet platelets also stir well in a rotating field, retaining over 80% of their peak mixing torque, probably because of their somewhat ellipsoidal shape.

An interesting issue is whether the nanorods form agglomerates. Studies of the field and frequency dependence will determine this: if nanorod agglomeration occurs, the torque should be independent of frequency and should increase with the field. If the nanorods do not agglomerate, they should act like stir bars and the torque will increase with frequency and be independent of field.

4.3.2. Field strength dependence

To investigate the field strength dependence of the mixing torque, we subjected the suspensions to a balanced vortex magnetic field. This field scheme yields a vortex angle of 54.7°, which is close to the optimal mixing angle of ~60°. The results of these experiments are in **Figure 4-5**. Just above the stagnation field the torque increases as the field-squared

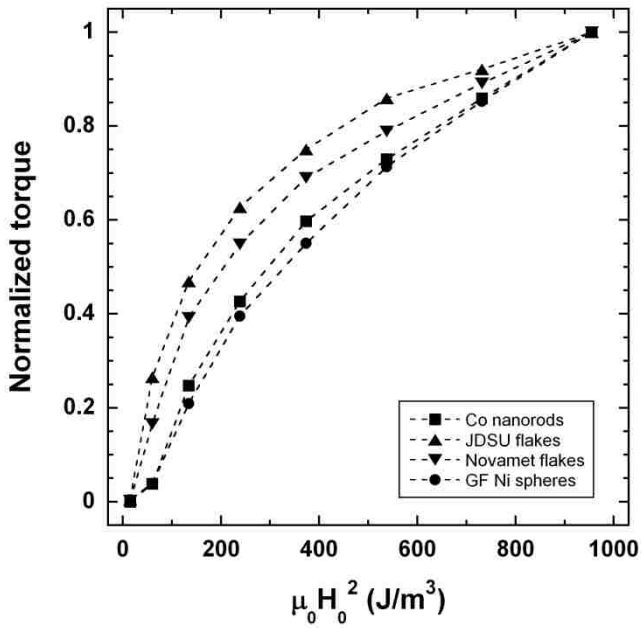

Figure 4-5. Normalized torques of magnetic particles as a function of applied field strength for a balanced vortex field (θ_f=54.7°). Stagnation occurs for low fields and magnetic saturation develops at high field strengths.

for all four particle shapes, then levels off at higher fields due to magnetic saturation. This field-squared dependence agrees with the theory for spherical particles, and is just a consequence of field-induced particle agglomeration. In essence, under any particular field conditions the agglomerates will increase in size until they become unstable. At higher fields the agglomerates are larger, so the mixing is stronger.

4.3.3. Frequency dependence

In our final experiments, we examined the frequency dependence of the mixing torque by subjecting the particle suspensions to balanced vortex fields at different frequencies. **Figure 4-6** shows that the mixing torques for all particles are essentially frequency independent, which again agrees with the spherical particle theory [4.1]. This behavior is also due to particle agglomeration, demonstrating that the magnetic mixing is not due to single particles. Certainly for single nanorods, the torque would simply be proportional to field frequency, provided stagnation does not occur. The greatest specific torque is generated by the

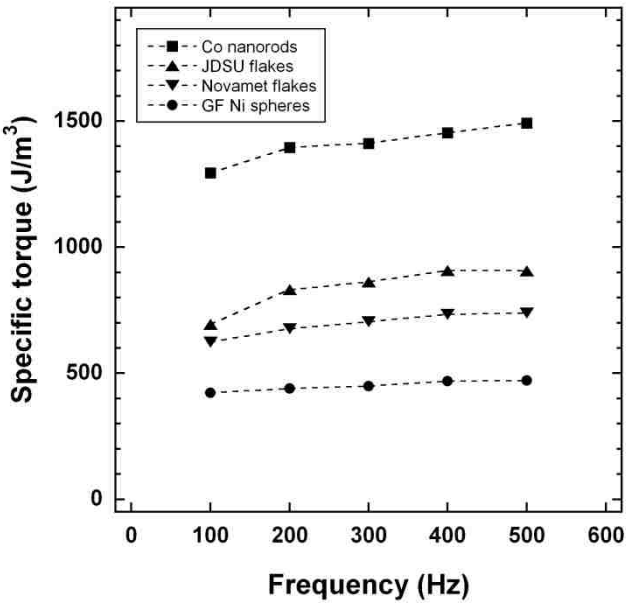

Figure 4-6. Specific torques of magnetic particles as a function of applied field frequency. The mixing torque is essentially frequency-independent for all particles, and increases with shape anisometry. All data acquired in balanced vortex fields (θ_f=54.7°).

nanorods, followed by the platelets (JDSU, then Novamet), and finally the spherical particles.

4.4 Discussion

So what particles are best for mixing? Are anisometric particles advantageous? For every field parameter tested (*i.e.*, field angle, strength, and frequency), we have found that the torque is greatest for the nanorods, followed by the platelets, and then the spherical particles. Thus, a primary conclusion from the results of these experiments is *increasing degrees of shape anisometry produce greater mixing torque*.

If the only consideration is achieving maximum mixing torque for a given volume of material, then the choice of particle shape is clear—rods. However, one needs to also consider the relative packing density of the particles, since a low packing density could impede flow in a microchannel and cause undesirable retention of the working fluid. Retention could be problematic for sequential batch-mode analysis unless a purge fluid was used. In **Figure 4-7**, the settling heights are shown for the different particle shapes at equal

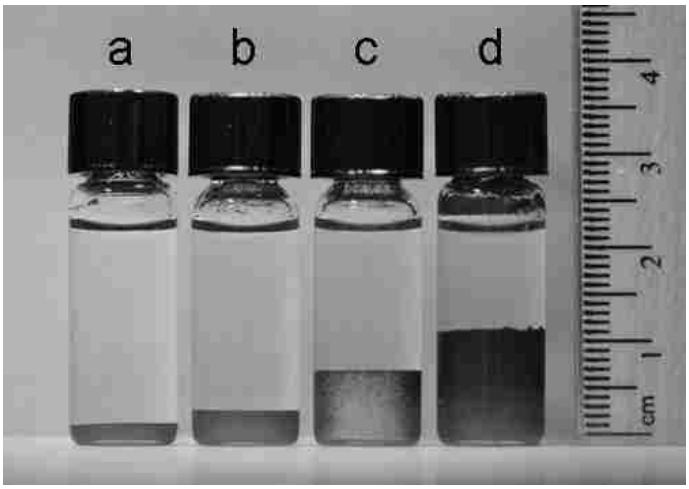

Figure 4-7. Photograph of the settling heights of the various particles illustrating steric effects, which increase with shape anisometry. **(a)** 3–7 μm spherical Ni powder, **(b)** 20 μm Novamet Ni platelets, **(c)** 20 μm JDSU MgF_2-coated Ni platelets, and **(d)** 3.2 μm Co nanorods. All suspensions are at 1.25 vol% of particles.

volume fractions (1.25 vol%) . We observe a trend for packing efficiencies reversed from that of torque production. The sedimentation volume for the Novamet Ni platelets is 1.6× that of the spherical particles, the JDSU Ni platelets are 3.5×, and the Co nanorods 5.4×. So *increasing degrees of shape anisometry correspond to greater steric interactions*.

In a practical microfluidic mixing device, the particles would likely be retained in the mixing volume by a field gradient when not in use. We find that the disparity in sedimentation heights is greatly attenuated when a magnetic field gradient (supplied by NdFeB permanent magnet) is applied. The dramatic change in settling heights is due to the way the different particles interact in the presence of a magnetic field gradient. The spherical particles form spikes that extend further than their gravity-induced sediment, whereas the nanorods pack much more tightly in a field gradient as compared to gravity. **Figure 4-8** compares the sedimentation heights under gravity and a magnetic field gradient, as well as the maximum mixing torques at a fixed balanced vortex field magnitude of 260 G for each particle suspension, relative to the values for spherical particles. (Because the JDSU platelets are a composite material, its specific torque was computed based on the volume of nickel content, as opposed to the total particle volume.)

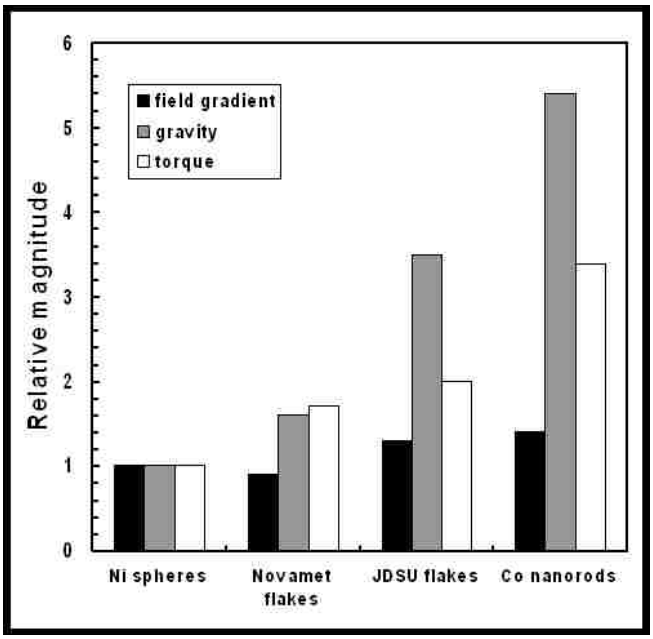

Figure 4-8. Comparison of the relative magnitudes of the mixing torque, and sedimentation heights under gravity and a magnetic field gradient. For each condition, the values are normalized to those for spherical particles.

Another consideration is the price and availability of the materials. The spherical Ni particles and Novamet Ni platelets are off-the-shelf materials available in large quantities for reasonable prices. The JDSU Ni platelets and Co nanorods are more costly, exotic materials that require advanced manufacturing. However, for mixing in microfluidic applications, the required material volumes are quite small and price may not be a prohibitive factor.

4.5 Conclusions

We have investigated the mixing effects of suspensions of anisometric ferromagnetic particles with respect to the parameters of a vortex magnetic field: the vortex field angle, field strength, and frequency. Consistent with theory, the measured mixing torque is observed to maximize near a balanced vortex magnetic field (~55–60°); display a field-squared dependence; and be independent of the field frequency for all particles, regardless of shape. In contrast to spherical particles and JDSU platelets, which exhibit diminished torque production in rotating fields due to structure formation, Novamet platelets and nanorods display strong mixing, consistent with stir-bar behavior. For all field parameters,

we observe that increasing degrees of shape anisometry of the particles result in greater torque production. Nanorods produce the most torque, followed by platelets, and then spherical particles. However, the sedimentation volume increases with shape anisometry as well. Each material has its own merits, and is probably well-suited for particular applications.

Acknowledgements

This work is supported by the Division of Materials Sciences and Engineering, Office of Basic Energy Sciences, U.S. Department of Energy. Sandia National Laboratories is a multiprogram laboratory operated by Sandia Corporation, a Lockheed Martin Co., for the Department of Energy's National Nuclear Security Administration under Contract No. DE-AC04-94AL85000. The authors wish to thank Vladimir Raksha, Paul Coombs, Tom Markantes, and Bill Kittler at JDSU, as well as Matt Groo at Novamet for supplying materials.

References

4.1 J.E. Martin, Theory of strong intrinsic mixing of particle suspensions in vortex magnetic fields, *Phys. Rev. E* **79**, 011503 1–12 (2009).

4.2 J.E. Martin, L. Shea-Rohwer, and K.J. Solis, Strong intrinsic mixing in vortex magnetic fields, *Phys. Rev. E* **80**, 016312 1–6 (2009).

4.3 R.C. Bell, E.D. Miller, J.O. Karli, A.N. Vavreck, and D.T. Zimmerman, Influence of particle shape on the properties of magnetorheological fluids, *Int. J. Mod. Phys. B* **21**, 5018–5025 (2007).

4.4 J.E. Martin, R.A. Anderson, and C.P. Tigges, Simulation of the athermal coarsening of composites structured by a biaxial field, *J. Chem. Phys.* **108**, 7887–7900 (1998).

Part III

Isothermal Magnetic Advection

Chapter 5

Isothermal Magnetic Advection: Creating functional fluid flows for heat and mass transfer[5]

Natural convection has been of interest for over a century due to its rich nonlinear dynamics and applications to heat transfer. However, convection occurs only when both gravity and a destabilizing thermal gradient exist. We have discovered a unique class of vigorous, emergent fluid flows that have the full functionality of natural convection but can be stimulated regardless of gravity or thermal gradients, simply by subjecting a platelet suspension to certain time-dependent biaxial magnetic fields of modest strength. This enigmatic phenomenon may facilitate cooling in microgravity environments and in other circumstances where convection fails.

5.1 Introduction

Thermal transport by convection cells was first visualized in 1900 by Henri Bénard [5.1], in an experiment wherein a thin layer of liquid with a free top surface was heated from below. This experiment produced a hexagonal pattern of flow cells that Bénard attributed to the buoyancy of the fluid near the hot surface. In 1916, Rayleigh [5.2] obtained a theoretical understanding of the experimental conditions that give rise to "Rayleigh–Bénard" convection—at least for the case where the liquid surfaces are bounded by contacting plates—and predicted convective rolls, circles, and linear and square patterns. Experimental and theoretical work in the ensuing century elucidated many such complex and beautiful convection patterns [5.3–5.5].

Around 1970, it was discovered that applying a magnetic field *gradient* along the thermal gradient could enhance natural convection in magnetic fluids [5.6,5.7]. The

[5] Originally published as: K.J. Solis and J.E. Martin, Isothermal Magnetic Advection: Creating functional fluid flows for heat and mass transfer, *Applied Physics Letters* **97**, 034101 1–3 (2010).

enhancement is dependent upon the thermal gradient and does not lead to unique flow patterns.

We have now discovered a method of stimulating heat and mass transport in fluids that requires neither a thermal or magnetic field gradient, nor gravity. This method gives rise to a unique class of vigorous, magnetic-field-stimulated flow patterns we call *advection lattices*, which can be used to transport heat or mass along any desired direction, using only the modest magnetic fields produced by Helmholtz coils. The scale of these flow lattices is fully controllable by the applied field, enabling either the efficient transfer of heat *and* mass, or the transport of mass *without* the extraction of heat. Especially surprising are the variety of effects that can occur, including the production of helical flows, the spontaneous formation of freestanding fluid structures, and the creation of chaotic advection. A theoretical understanding of these effects does not appear to be immediately forthcoming, but in the following we describe our experiments and observations.

5.2 Experimental

The formation of advection lattices occurs when a suspension of magnetic platelets is subjected to particular time-dependent, *biaxial* magnetic fields [5.8]. These biaxial fields consist of two orthogonal components whose relative frequencies can be expressed as a ratio of small integers. For such *just intervals*—in music terminology: octaves, perfect fourths and fifths, major thirds, *etc*.—a variety of flow patterns can be produced whose structure is largely determined by the phase between field components. These patterns generally consist of a checkerboard of antiparallel flow columns that are normal to the biaxial field plane, as illustrated in **Figure 5-1**. With the 20 μm platelets we employ, vigorous flow patterns can be produced with field frequencies in the low audio range (10–1000 Hz) and component amplitudes in excess of ~0.01 T.

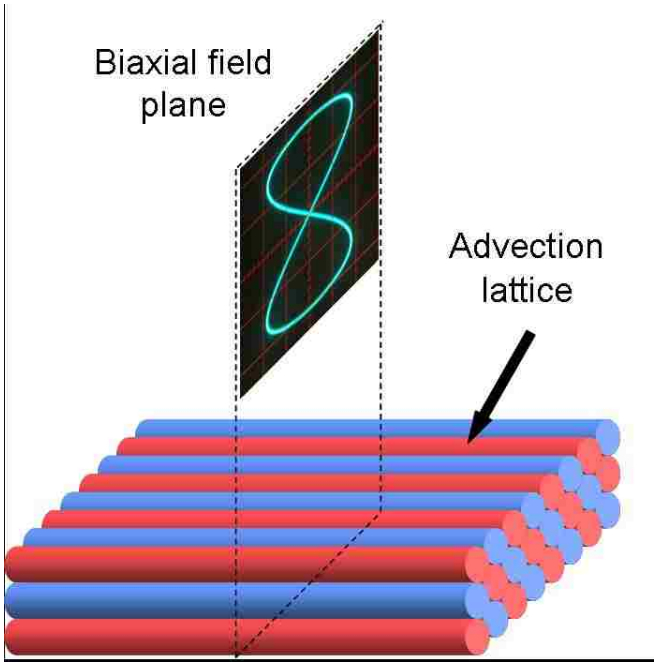

Figure 5-1. Schematic illustrating the geometry of the advection lattice and biaxial magnetic field, showing the columns form normal to the magnetic field plane. Red columns are flowing oppositely to the blue ones.

5.3 Results and discussion

The simplest flow pattern we have observed occurs with an octave biaxial field having a phase angle of 45°. (This phase angle is added to the high-frequency field component with both components expressed as sinusoids.) A Lissajous plot of the field vector makes the bowed figure eight in **Figure 5-2(a)**. Applying this field to the platelet suspension immediately stimulates the striking flow pattern in **Figure 5-2(b)**, which consists of 1.3 mm-diameter flow columns that span the 3 cm cell. Each column has a sharp tail and a diffuse tip, with the flow running from tail-to-tip. Tracer particle studies show that the flow rate is about 3 $cm \cdot s^{-1}$, and that adjacent columns flow in opposite directions. A tracer particle in the dark regions between columns rapidly spins either clockwise or counterclockwise, due to the high shear rate in these regions. **Figure 5-2(c)** shows that these columns pack "antiferromagnetically" into a rectangular lattice, so the advection lattice can be described as a checkerboard of columns, as in **Figure 5-3**. This symmetric flow

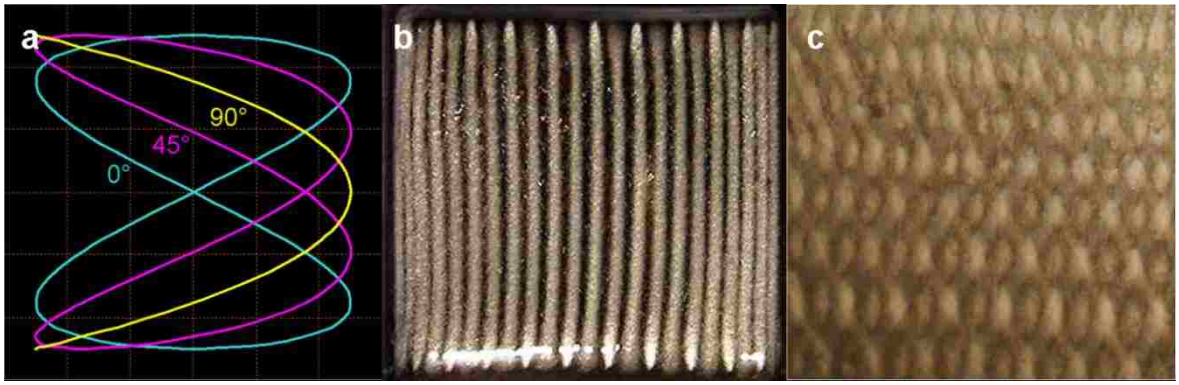

Figure 5-2. **(a)** Lissajous plots of the magnetic field vector for an octave field at selected values of the phase angle. **(b)** View in the plane of the magnetic field of the advection lattice for an octave field (75 and 150 Hz components with rms amplitudes of 150 G) at a 45° phase angle. The pattern is insensitive to the boundaries, and the flow runs from the sharp column tails to the diffuse tips. (see Supplementary Movie 5-1) **(c)** View of the advection lattice normal to the field plane shows the columns form a rectangular lattice.

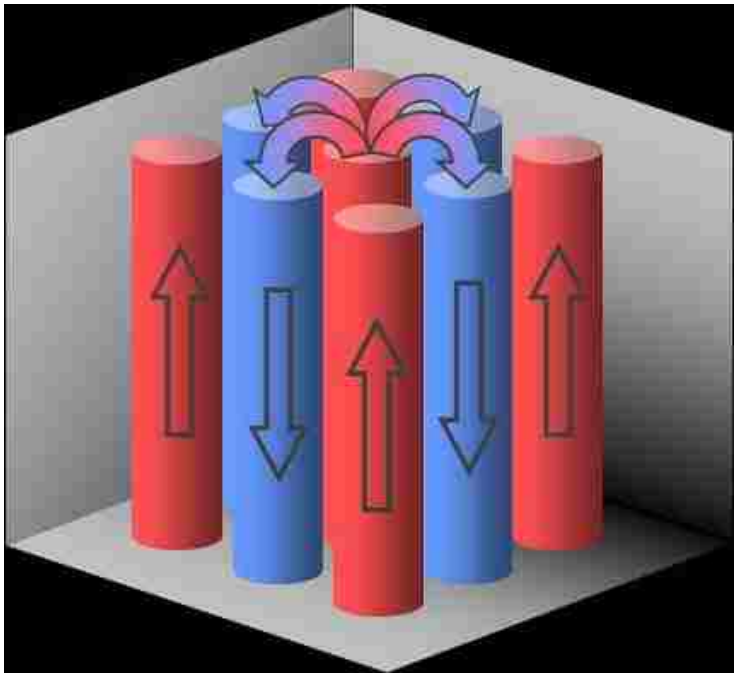

Figure 5-3. Schematic illustrating the flow at each column tip feeding the four adjacent columns.

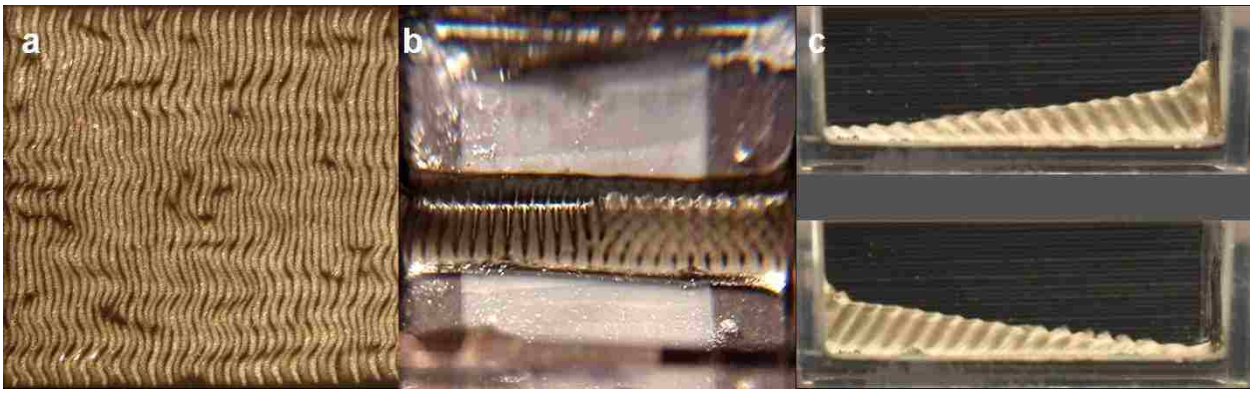

Figure 5-4. (a) At a phase angle of 0° the advection lattice produced by an octave field becomes wavy and animated, due to chiral symmetry breaking that produces alternating helical flow within the columns. [see Supplementary Movie 5-2] **(b)** Large particle concentrations result in surface instabilities, such as this nearly vertical view of a 1 cm-high ridge produced by an octave field with a 0° phase angle. This ridge consists of both striped and checkered phases. [see Supplementary Movie 5-3] **(c)** A 300:100 Hz field with a 0° phase angle produces helical flow of the same vorticity in all columns, resulting in a body torque on the fluid ridge that causes it to flow up the right side of the cell. This view is normal to the field plane. A phase angle of 180° reverses the torque so the fluid flows up the left side of the cell.

pattern is unique to this effect and does not occur in Rayleigh–Bénard convection, presumably because in that case gravity breaks up-down symmetry.

To explore the dependence of the flow pattern on the phase between field components, we phase modulated the octave interval by increasing the high-frequency component by 0.1 Hz. This phase modulation produces a striking sequence of complex flow patterns that repeat every 10 seconds. At a phase angle of 0° the columns are wavy and writhing and exhibit defects such as bifurcation at the free surface of the liquid, as in **Figure 5-4(a)**. High resolution video suggests that this pattern is a result of spontaneous chiral symmetry breaking, with adjacent columns having opposing helical flow. Near a phase angle of 45°, these writhing columns become straight and stationary. At a phase angle of ~90°, the columns become faint and fine, roughly half the diameter of the 45° columns. The transitions between phases are mesmerizing, as some patterns transform in most unexpected ways, whereas others suddenly appear, then vanish abruptly.

Experiments with a biaxial field having a 3:1 frequency ratio (a twelfth interval) produce helical flow within the columns, but in this case the vorticity is in the same sense for all columns, producing a body torque. These helical flows reach a maximum intensity at

phase angles of 0° and 180°, and are equal and opposite in sign, as determined by measuring the body torque with a torsion balance. The flow vorticity also produces a rapid migration of the columns normal to their flow direction, which causes the fluid to pile up on one or the other side of the cell, depending on the phase angle. (This effect does not constitute chiral symmetry breaking, as the sign of the torque is deterministic.) The appearance of a body torque is surprising: the torque on a platelet that has an induced magnetic moment is due to the rotation of the magnetic field, $\mathbf{H}\times\dot{\mathbf{H}}$, but this quantity varies periodically and averages to zero for biaxial fields comprised of sinusoidal components of differing frequencies.

At higher particle concentrations, one can observe surface instabilities in the form of stationary ripples that run parallel to the intersection of the field plane with the fluid surface. If one starts with a dry powder of platelets, the dropwise addition of solvent causes the progressive emergence of a freestanding fluid ridge supported only by the vigorous flow contained within, **Figure 5-4(b)**. In a phase-modulated twelfth field, the alternating helical flow causes this ridge to slosh from side-to-side, **Figure 5-4(c)**.

Finally, if a strong dc field component is applied normal to the biaxial field, the advection becomes chaotic, producing extremely strong mixing. This chaotic advection could be useful for mixing in microfluidic devices.

The effects we have described cannot be understood in terms of a magnetic force on a single particle suspended in a liquid, but are an emergent behavior of an ensemble. This distinguishes *isothermal* magnetic advection in a fundamental way from thermomagnetic convection [5.9], which can be explained in terms of the temperature dependence of the Kelvin force (the force on a magnetic object in a field gradient) on an individual particle. This Kelvin force increases with decreasing temperature, due to the negative pyromagnetic coefficient of ferrofluids. So if the magnetic field gradient is applied along the thermal gradient, the body force is larger on the cooler fluid, which adds to the buoyancy that drives natural convection.

Although the origin of isothermal magnetic advection is enigmatic, we can identify the key ingredients of this effect. A uniform magnetic field in an isothermal fluid cannot exert a force on a particle, but it can exert a torque on anisometric particles, such as platelets or rods. Experiments show that advection lattices do not form in suspensions of spherical particles subjected to biaxial fields [5.8], but neither do they form in nanorod suspensions. Something more than a field-induced torque is at issue, and it is apparent that the emergent dynamics is a consequence of hydrodynamically coupled platelet fluttering in the time-dependent fields. In a static field, a magnetically soft platelet will orient such that the local field vector (the sum of the applied and particle fields) lies in the platelet plane—a so-called demagnetizing field effect that minimizes its magnetostatic energy [5.10]. The orientation of the platelets will be strongly coupled by their magnetic interactions, yet each platelet will still be free to rotate around this local field vector, so a soft orientational degree of freedom remains, as in a weather vane. In a time-dependent field, the platelets will continuously reorient in an attempt to minimize their magnetostatic energy. These field-driven motions couple hydrodynamically to produce the emergent behavior we have observed.

It will likely prove a significant theoretical and computational challenge to understand isothermal magnetic advection. A typical column produced in our experiments contains approximately 10^{5-7} platelets, so a large-scale continuum simulation will be required. However, experiments over one decade in field frequency show an inverse dependence of column diameter on frequency (**Figure 5-5**), so it is possible that the scale of the computation can be significantly reduced. This ability to control the scale of the advection lattice also has the practical implication of optimizing heat transport at different scales, and enables the possibility of transporting mass in a fluid without transporting heat. This effect will occur when the column diameter is small compared to the column length, causing the fluid to act like a counter-current heat exchanger, and could be useful for fueling chemical and biological processes without heat extraction.

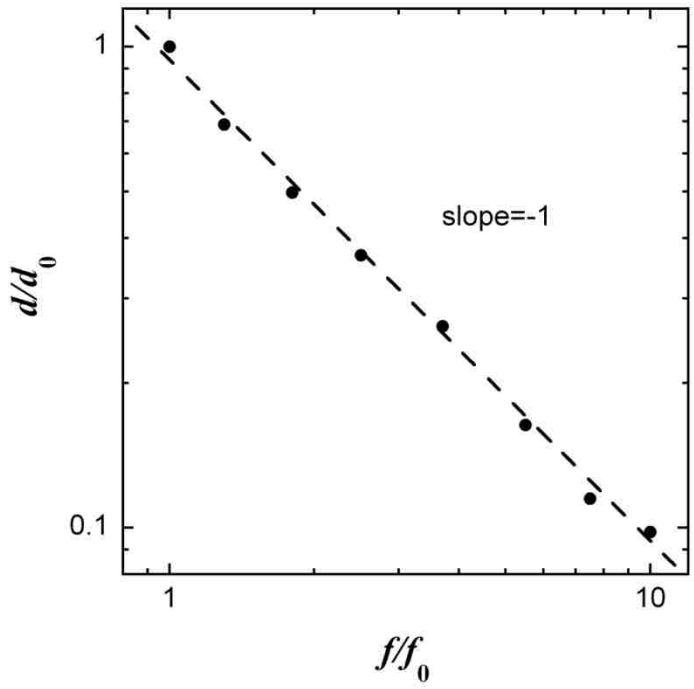

Figure 5-5. The advection lattice column diameter is inversely proportional to the magnitude of the field frequency. These data are for an octave biaxial magnetic field. Here f_0=100 Hz and d_0=1.5 mm is the measured column diameter for a biaxial field having components of 100 and 50 Hz.

5.4 Conclusions

Isothermal magnetic advection is a useful technology that enables the transfer of heat and mass without pumps, seals or contact with the fluid—even in microgravity environments—and without the need for a thermal gradient of *any* magnitude. Understanding the unique symmetries of the flow patterns is an exciting scientific challenge, and we have only begun to explore the experimental possibilities. How do these advection lattices interact with natural convection? Will unique flow patterns emerge? Does the use of larger particles lead to commensurately broader columns? Are unique flow patterns possible in ac triaxial fields or in biaxial fields whose components are periodic but non-sinusoidal? We hope that the investigation of these and other issues will lead to a greater understanding of this phenomenon and its technical implications.

Acknowledgements

Sandia National Laboratories is a multiprogram laboratory operated by Sandia Corporation, a wholly owned subsidiary of Lockheed Martin Co., for the U.S. Department of Energy's National Nuclear Security Administration under Contract No. DE-AC04-94AL85000. This work was supported by the Division of Materials Science, Office of Basic Energy Sciences, U.S. Department of Energy (DOE). The authors wish to thank Vladimir Raksha, Paul Coombs, Tom Markantes, Bill Kittler, and Kees-Jan Delst at JDSU for supplying the magnetic platelets.

References

5.1 H. Bénard, Les tourbillons cellulaires dans une nappe liquide transportent de la chaleur par convection en régime permanent, *Ann. Chim. Phys.* **23**, 62–144 (1901).

5.2 L. Rayleigh, On convection currents in a horizontal layer of fluid, when the higher temperature is on the under side, *Philos. Mag.* **32**, 529–546 (1916).

5.3 S. Chandrasekhar, *Hydrodynamic and Hydromagnetic Stability* (Dover, New York, 1981), pp. 9–71.

5.4 A.V. Getling, *Rayleigh-Bénard Convection: Structures and Dynamics* (World Scientific, Singapore, 1997).

5.5 *Dynamics of Spatio-Temporal Cellular Structures: Henri Bénard Centenary Review*, edited by I. Mutabazi, J.E. Wesfreid, and E. Guyon (Springer, Berlin, 2005).

5.6 D.P. Lalas and S. Carmi, Thermoconvective stability of ferrofluids, *Phys. Fluids* **14**, 436–437 (1971).

5.7 R.A. Curtis, Flows and wave propagation in ferrofluids, *Phys. Fluids* **14**, 2096–2102 (1971).

5.8 J.E. Martin, E. Venturini, J. Odinek, and R.A. Anderson, Anisotropic magnetism in field-structured composites, *Phys. Rev. E.* **61**, 2818–2830 (2000).

5.9 R.E. Rosensweig, *Ferrohydrodynamics* (Dover, New York, 1997), pp. 228–232.

5.10 J.A. Osborn, Demagnetizing factors of the general ellipsoid, *Phys. Rev.* **67**, 351–357 (1945).

Chapter 6

Controlling the column spacing in isothermal magnetic advection to enable tunable heat and mass transfer[6]

Isothermal magnetic advection (IMA) is a recently discovered method of inducing highly organized, non-contact flow lattices in suspensions of magnetic particles, using only uniform ac magnetic fields of modest strength. The initiation of these vigorous flows requires neither a thermal gradient nor a gravitational field, and so can be used to transfer heat and mass in circumstances where natural convection does not occur. These advection lattices are comprised of a square lattice of antiparallel flow columns. If the column spacing is sufficiently large compared to the column length and the flow rate within the columns is sufficiently large, then one would expect efficient transfer of both heat and mass. Otherwise, the flow lattice could act as a countercurrent heat exchanger and only mass will be efficiently transferred. Although this latter case might be useful for feeding a reaction front without extracting heat, it is likely that most interest will be focused on using IMA for heat transfer. In this chapter, we explore the various experimental parameters of IMA to determine which of these can be used to control the column spacing. These parameters include the field frequency, strength, and phase relation between the two field components, the liquid viscosity, and particle volume fraction. We find that the column spacing can easily be tuned over a wide range to enable the careful control of heat and mass transfer.

6.1 Introduction

Isothermal magnetic advection (IMA), introduced in Chapter 5 [also Ref. 6.1], is a recently discovered, non-contact technique for stimulating flow in dilute suspensions of magnetic

[6] Originally published as: K.J. Solis and J.E. Martin, Controlling the column spacing in isothermal magnetic advection to enable tunable heat and mass transfer, *Journal of Applied Physics* **112**, 094912 1–7 (2012).

platelets. IMA occurs when these suspensions are subjected to particular uniform biaxial magnetic fields, generally comprised of two orthogonal ac induction fields of modest strength (~0.015 T rms) having a carefully selected frequency ratio and phase relation. Although a variety of flow patterns can be stimulated, of particular interest is a highly regular advection lattice that consists of antiparallel flow columns arranged in a square lattice, such that any column transporting fluid in one direction is surrounded by four countercurrent columns. In other words, the flow columns form a square lattice with "antiferromagnetic" ordering. This flow symmetry is not observed in natural convection, but seems well configured for efficient heat and mass transfer, provided the column spacing can be appropriately adjusted to the scale of the volume over which the thermal gradient is applied. The goal of the study reported herein is to isolate those experimental factors that control the column spacing.

IMA possesses some unique characteristics that distinguish it from forced and natural convection. Unlike natural convection which requires an *unstable* thermally induced density gradient within the fluid, IMA requires neither a thermal gradient nor gravity. Moreover, the direction of the advection lattice is always normal to the biaxial field plane, so by simply changing the orientation of the applied field, the flow direction of the advection lattice can be controlled. These characteristics make IMA an attractive technique for situations where convection does not occur, such as cooling under hot objects, in microgravity environments, and when the thermal gradient is simply insufficiently large to exceed the critical Rayleigh number for convection. In contrast to forced convection, IMA is a non-contact method that does not rely on pumps, valves, or any other moving parts to function, and so is a particularly simple and robust technique. Thermomagnetic convection is another non-contact method of initiating fluid flow and occurs in non-uniformly heated ferrofluids subjected to strong magnetic field gradients [6.2,6.3], and is due to temperature dependent magnetization of such fluids. However, a substantial thermal gradient is required to initiate

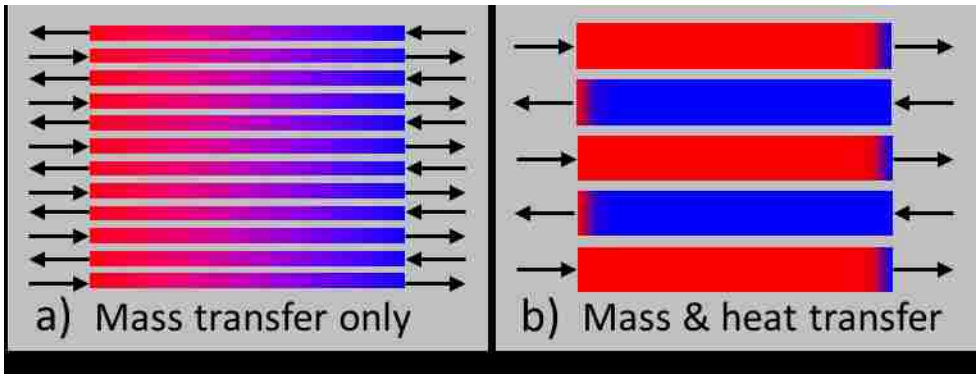

Figure 6-1. Schematic illustrating the two transfer modes possible with IMA, depending on the sizes of the advection lattice columns. **(a)** For small column diameters, the lattice serves as a countercurrent heat exchanger, allowing mass transport without heat transport. **(b)** For large column diameters, both mass and heat are effectively transported.

flow and the resultant flow patterns have the symmetries of natural convection. The requirement of having a significant field gradient makes scaling thermomagnetic convection to large volumes challenging. A uniform magnetic field has also been predicted to induce thermomagnetic convection [6.4], but only within very thin fluid layers (~1 mm).

The ability to control the advection lattice column spacing has the practical implication of determining the type of transport that will occur within a given fluid gap across which a thermal gradient is imposed. Small column diameters, slow fluid flow, and high fluid thermal diffusivity will favor heat transfer between columns, causing the advection lattice to act as a countercurrent heat exchanger, albeit one without actual pipes [**Figure 6-1(a)**]. This regime could be useful for feeding a reaction front without extracting heat. Large column diameters, rapid laminar flow, and low fluid thermal diffusivity will favor heat transfer across the gap [**Figure 6-1(b)**]. The timescale for the transverse thermal equilibration of an "antiferromagnetic" lattice of flow columns is $\tau_T \propto R^2 / D_t$, where D_t is the thermal diffusivity and R is the column spacing. The timescale for fluid transit across the gap is $\tau_{advec} \propto G/\mathrm{v}$, where G is the gap width and v is the magnitude of the fluid velocity within a column. Efficient heat transport will occur when the advection time is short compared to the transverse thermal equilibration time, so $\frac{R^2 \mathrm{v}}{G D_t} >> 1$. The column spacing

dependence is quadratic, so efficient heat transfer will be strongly dependent on this parameter. Understanding of how the experimental parameters affect the column spacing and dynamics of advection lattices not only has the practical implication of enabling different modes of heat and mass transfer, but also may aid in eventually developing a mechanistic understanding of the processes that govern this intriguing emergent phenomenon.

6.2 Experimental

The platelet suspensions were created by dispersing a fixed amount (~0.87 g) of magnetic platelets (supplied by JDSU Flex Products Group) into varying amounts of liquid to achieve a desired volume fraction, which ranged from ~2–9 vol.%. The multilayer magnetic platelets possessed an irregular shape, and were ~20 μm across by ~234 nm thick, consisting of a 50 nm nickel core sandwiched between 92 nm-thick layers of magnesium fluoride. A variety of liquids were used for the viscosity study, including acetone ($\eta_{25\,^{\circ}C} = 0.306$ cP), ethanol ($\eta_{25\,^{\circ}C} = 1.074$ cP), isopropanol ($\eta_{25\,^{\circ}C} = 2.038$ cP), and benzyl alcohol ($\eta_{25\,^{\circ}C} = 5.474$ cP). All of the suspensions were contained in a square glass cell of interior width 3 cm and 6 cm high.

The suspensions were placed in the central cavity of two orthogonally nested Helmholtz coils that were operated in series resonance using computer-controlled capacitor banks. The time-dependent biaxial fields had components that ranged over the frequency range of ~72–1000 Hz and rms induction field amplitudes from 0.005 to 0.020 T. The biaxial fields can be classified according to the frequency relationship between their two components. For instance, a simple rotating field, one in which both components have the same frequency but are in quadrature phase, is referred to as a 1:1 biaxial field. Biaxial fields with *just intervals* are those comprised of components whose frequencies are related by a ratio of small integers *n*:*m* (*e.g.*, 2:1, 3:2, 3:1, *etc.*). *Harmonic* biaxial fields, which we most often use to stimulate IMA, have a frequency relationship of *n*:1, where *n* is a small integer. In all cases, the phase relation between the field components is critical to the symmetry of

the flow pattern produced. We define this phase angle to be that which is applied to the high-frequency field component.

The column spacing data were acquired from overhead photographs taken of the suspension with one field component along the vertical axis and the other horizontal. Regardless of which parameter was being investigated (*e.g.*, field strength, viscosity, *etc.*), all data were acquired for 2:1 fields, or *octave* fields, with a 45° phase angle. This phase was chosen because it produces advection lattices of fairly calm, straight, and ordered columns, which are much more easily characterized than the writhing columns produced at 0° phase angle.

6.3 Results and Discussion

We now consider how the structure, dynamics, and column spacing of advection lattices are affected by the magnetic field parameters, which we discuss first, and the suspension properties.

6.3.1 Magnetic field parameters

As we have mentioned before, IMA occurs when a suspension of magnetic platelets is subjected to particular magnetic fields. Although only one component of the biaxial field needs to be time-dependent for IMA to occur [6.5], the variety of achievable advection lattices and their dynamics is limited as compared to those achievable with fully ac biaxial fields, which are used exclusively in this study. Fully ac biaxial fields have two addition parameters, the frequency ratio and phase angle, and these can be used to stimulate a much richer variety of flow patterns. In general, the applied field can be expressed as

$$\mathbf{H}(t) = H_x \sin(\omega t)\hat{\mathbf{x}} + H_y \sin(n\omega t/m + \phi)\hat{\mathbf{y}}\,, \tag{6-1}$$

where $n/m \geq 1$ is the just interval and ϕ is the phase angle. The complexity of these biaxial fields, and their dependence on the phase angle ϕ, can be appreciated by examining their associated Lissajous curves (plots of H_x versus H_y). Although the detailed mechanism of IMA

is not understood, each platelet is at a magnetostatic energy minimum when the local field is orthogonal to the platelet director (surface normal). Therefore, the detailed shape of the Lissajous plot determines the platelet dynamics. For completeness, we mention that we recently demonstrated that IMA also occurs in ac-ac-dc *triaxial* magnetic fields, and results in novel advection lattice patterns and the stimulation of vigorous rotational flows [6.5], which is the topic of Chapter 7.

Frequency

The frequency dependence of the column spacing was studied using a 2:1 harmonic field with a phase angle of 45°, which gives very regular and straight flow columns. Over the range of particle volume fractions studied (2.3%–9.3%), the column spacing is proportional to the inverse of the field frequency (**Figure 6-2**), so the wavenumber is proportional to the

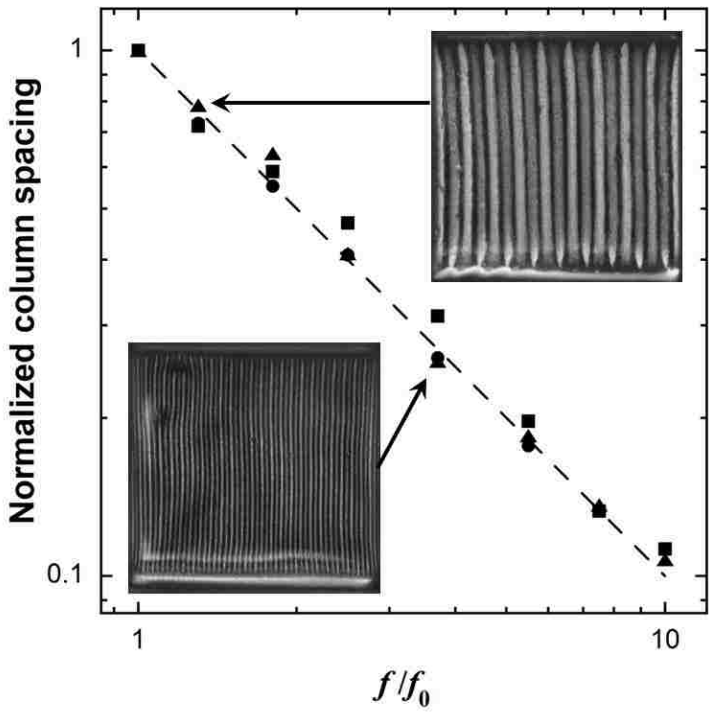

Figure 6-2. The column spacing is inversely proportional to the magnitude of the field frequency. These data are for octave biaxial fields (2:1) with a 45° phase angle, and an rms component magnetic induction of 0.015 T. The column spacing at each frequency is normalized to the value at f_0 = 100 Hz, for a 100:50 Hz field. Data for three different volume fractions are shown (● 2.3%, ■ 5.8%, and ▲ 9.3%), as well as a plot of $y(x)=x^{-1}$, where $x = (f/f_0)$.

frequency. The field frequency is thus a simple and effective way to select the column spacing. Insets in Figure 6-2 are images of flow lattices for a 130:65 Hz field and a 370:185 Hz field.

Phase angle

The phase relation between the field components is another variable that can be used to control the flow pattern and column spacing. The results in **Figure 6-3** show that the effect is not large, roughly 50%, with the column spacing for the 45° phase angle being larger than that at 0°. In Section 6-2, we mentioned that virtually all of the column spacing data were acquired for octave biaxial fields that have a 45° phase angle. The reason for this definite preference is that the *dynamics* of advection lattices depend strongly on the phase relationship

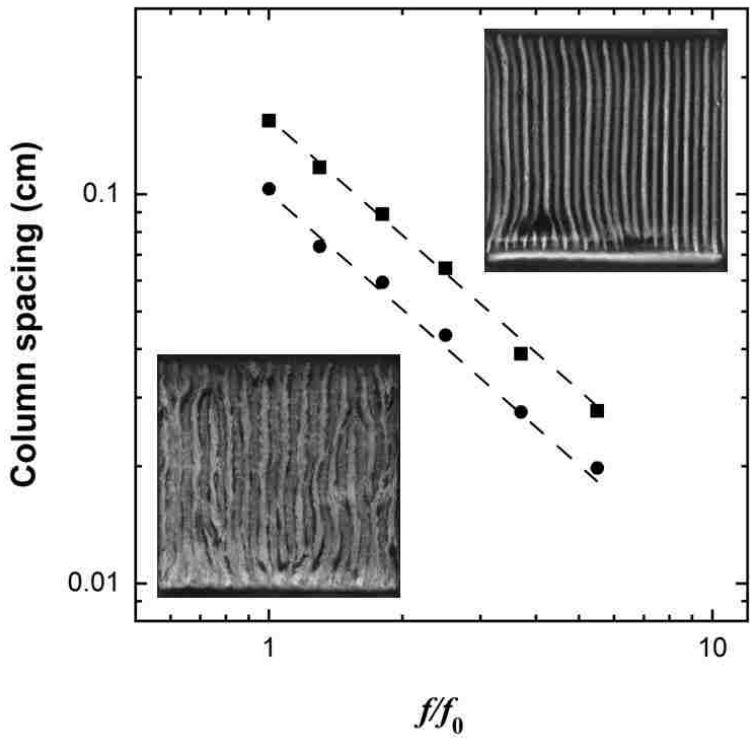

Figure 6-3. The column spacing varies inversely with the magnitude of the field frequency for an octave biaxial field (2:1) with phase angles of 0° (●) and 45° (■), with the column spacing at 45° being on average ~1.5× that at 0°. These data are for a 2.3 vol.% isopropanol-platelet suspension subjected to octave biaxial fields with rms component induction amplitudes of 0.015 T. The insets illustrate the effect of the phase angle on the advection lattice morphology, and are for a 180:90 Hz field.

between the two field components. At a phase of 0°, the advection lattice has significant dynamic disorder that is characterized by writhing motions of the columns, the continual creation, and annihilation of bifurcations, Figure 6-3(inset), which makes a determination of the column spacing less accurate. The 45° phase angle renders the columns rather straight, uniform, and stationary, Figure 6-3(inset), which facilitates accurate measurement. And the flow within these straight columns is still vigorous enough to be of interest for heat transfer. (At a phase of 90°, the advection lattice becomes faint, and the flow within the columns is significantly reduced, making this phase angle a poor choice for heat and mass transfer.)

Finally, we mention that the phase dependence of the advection lattices that are produced by any just frequency interval can be conveniently and continuously explored by phase modulating the field, which is accomplished by a slight alteration of the frequency of one of the field components. Phase modulation yields visually stunning transitions between the different flow patterns.

Field strength

To investigate the field dependence of the column spacing we dispersed 2.3 vol.% platelets into isopropanol and subjected them to a harmonic field of 100:50 Hz at a phase angle of 45°. **Figure 6-4** shows that the column spacing increases as the power law, $const \times (B - B_c)^{0.30}$, at least over the range of the data we are able to collect. Here $B_c \sim 0.005$ T is a critical field whose meaning is discussed below. This dependence implies that efficient heat transfer requires a reasonably uniform magnetic field, especially parallel to the thermal gradient. Otherwise, the column spacing would change along the thermal gradient, which would cause flow columns to terminate.

In addition to changing the column spacing, the field strength alters the characteristic flow pattern. At high fields (0.0125 T rms), the advection lattices are animated [**Figure 6-5(a)**] with significant column writhing, probably due to the increasing importance of fluid inertia as the flow rates within the columns increase. Conversely, as the field is reduced to

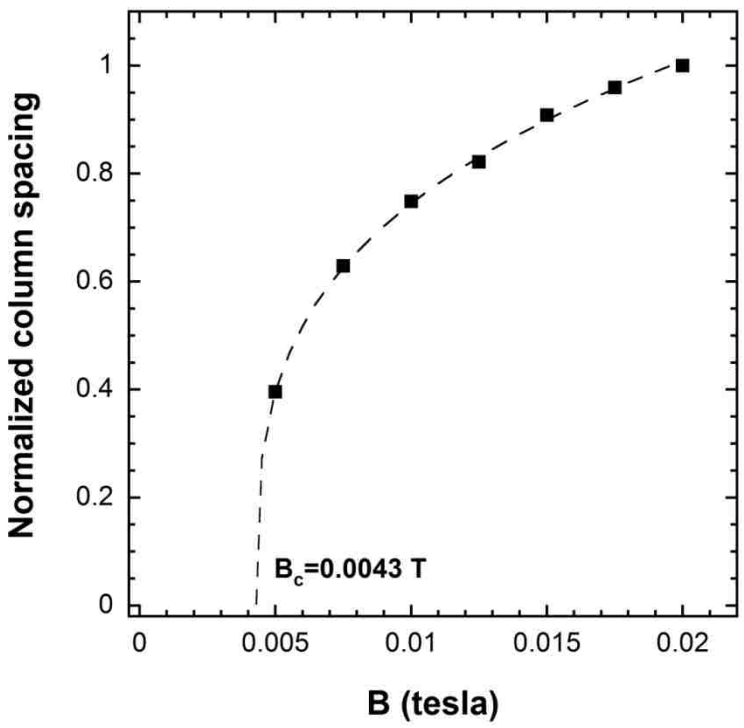

Figure 6-4. The advection lattice column spacing increases as a power law with the magnetic induction amplitude. The abscissa is the rms value of the magnetic induction for each field *component*. These data are for a 2.3 vol.% isopropanol-platelet suspension subjected to a 100:50 Hz biaxial field with a 45° phase angle.

0.005 T rms the pronounced writhing motions of advection lattices produced with a 0° phase angle diminish [**Figure 6-5(b)**], eventually becoming nearly as calm, straight, and ordered as those produced with the 45° phase angle. Upon decreasing the applied field further, the columns become progressively smaller, until they vanish and static layered sheets emerge parallel to the biaxial field plane, and thus normal to the flow of the advection lattice. The nascent fine layers can be seen in the upper and lower portions of **Figure 6-5(c)**, but they are more clearly observed after being given time to more fully develop, **Figure 6-5(d)**. This transition occurs at a critical field B_c of ~0.005 T.

If the field is then progressively increased, these layered sheets persist at fields well above the layering transition threshold under decreasing field conditions. The transition back to an advection lattice occurs as a wave-like instability in the pronounced sheets that form when the field is increased to ~0.010 T, **Figure 6-5(e)**. From these instabilities, columns

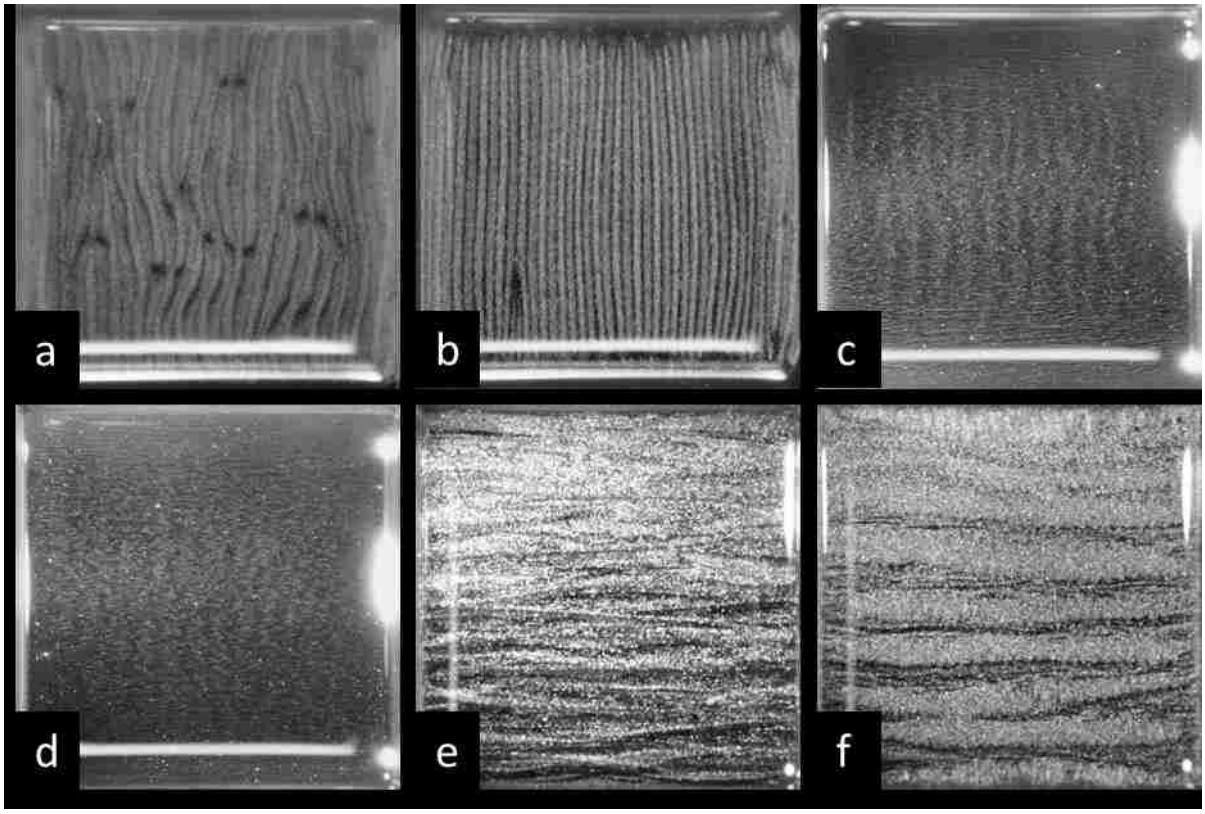

Figure 6-5. Photographs illustrating the effect of the magnetic induction amplitude on the morphology of an advection lattice formed in a 2.3 vol.% isopropanol-platelet suspension subjected to a 100:50 Hz field with a 0° phase angle. **(a)** B_{rms} = 0.0125 T produces an animated advection lattice with wavy columns and defects actively propagating throughout the lattice. **(b)** Reducing the component magnetic induction to B_{rms} = 0.005 T produces an advection lattice with subdued dynamics and straight, ordered columns. **(c)** At a component magnetic induction of B_{rms} = 0.0025 T faint, static, column-like structures form that are composed of parallel sheet segments, **(d)** which eventually coarsen into sheet structures that are aligned with the biaxial field plane. **(e)** Upon increasing the magnetic induction to B_{rms} = 0.01 T, the sheet structures become disrupted and undergo wavy instabilities. **(f)** Domains of fine advection lattice column segments emerge, appearing as horizontal bands, which will eventually coalesce into a fully formed advection lattice.

eventually emerge in bands that eventually coarsen into a coherent advection lattice. This incipient transition can be seen in **Figure 6-5(f)**.

The layered sheet structures are similar to those previously observed for spherical particles [6.6,6.7], but spherical particles do not exhibit a transition to advection lattices (at least over the conditions of field which we are able to apply). Although the layered phase is not of interest to the transfer of heat and mass, understanding the nature of this transition

would be worthwhile, so that the regime of effective heat and mass transfer can be identified.

6.3.2 Suspension parameters

Liquid viscosity

The viscosity of the liquid phase is important to both the formation of the advection lattice and to the magnitude of the flow within the columns. We have investigated a variety of fluids spanning a range in viscosity of nearly 3 decades, including air ($\eta = 0.017$ cP), acetone ($\eta_{25\,^\circ C} = 0.306$ cP), and ethylene glycol ($\eta_{25\,^\circ C} = 16.1$ cP), and some manner of advection lattice forms in all of them, although at high liquid viscosities the flow is extremely slow. The formation of an advection lattice in air was simply to demonstrate that IMA *can* occur with fluids of such low viscosity. However, in air the lattice is not particularly robust, so air is not an ideal medium for the study of IMA. Alternatively, if the fluid viscosity is very large, as is the case for ethylene glycol, the flow patterns are extremely faint and sluggish. Liquids having viscosities on the order of 1 cP (*e.g.*, isopropanol, ethanol, water) yield the most diverse range of behavior, so isopropanol ($\eta_{25\,^\circ C} = 2.038$ cP) was chosen as the solvent for all of the other parameter studies.

A plot of the dependence of the column spacing on solvent viscosity is shown in **Figure 6-6**, where it is observed that no significant viscosity effect exists. This is an important result, as it demonstrates that an advection lattice *possessing a single column spacing* can span a thermal gradient and therefore very effectively transport heat and mass. A significant viscosity dependence would require a continual adjustment of the column spacing parallel to the thermal gradient, and the continual termination of flow columns would result in relatively poor transport.

The viscosity dependence was probed using frequency as a tuning parameter for the column spacing and using a biaxial field comprised of 0.015 T rms components. A 1-decade

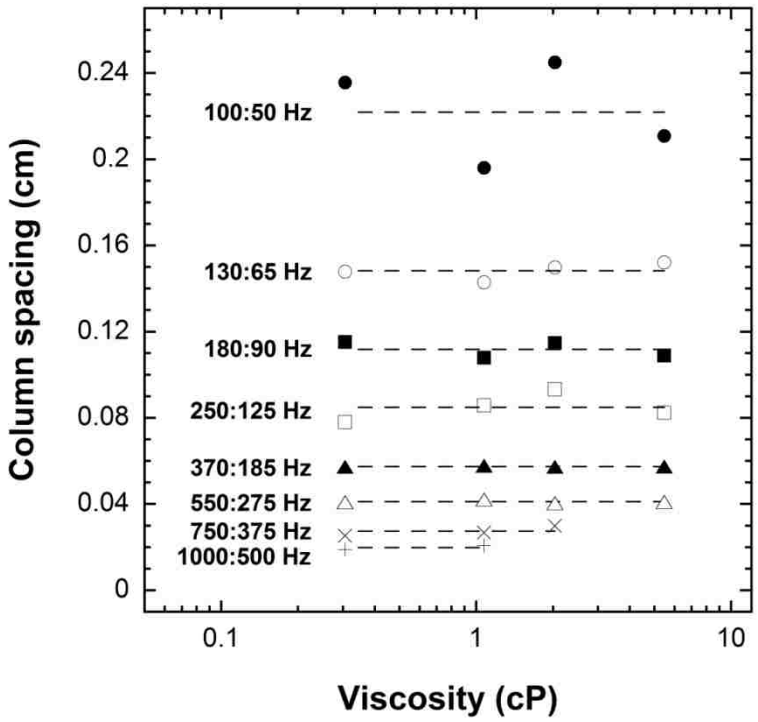

Figure 6-6. The column spacing is essentially independent of the viscosity of the liquid phase for a given frequency. All suspensions were prepared at 5.8 vol.% and subjected to octave biaxial fields with a 45° phase angle and rms component magnetic induction of 0.015 T.

frequency range was investigated for each viscosity; however, we were not able collect data for all solvents at all frequencies. For example, in a benzyl alcohol suspension ($\eta_{25\,^{\circ}C}$ = 5.474 cP) with 2.3 vol.% platelets, an advection lattice does not form at frequencies above 250:125 Hz, at the chosen component amplitudes of 0.015 T. Instead, the suspension appears dark and quiescent, due to the static sheet formation described above. This effect is not entirely surprising, since advection lattice formation and its dynamics are likely governed by the ratio of the hydrodynamic torque that results from the rotation of a platelet in a viscous liquid, to the field-induced magnetic torque on a platelet. This dimensionless ratio is conceptually similar to the Mason number, which is the dimensionless ratio of particle viscous forces to polarization forces [6.8,6.9]. (We have successfully used the Mason number to describe the dynamics of other magnetic suspensions, such as the apparent viscosity of electro- and magneto-rheological suspensions [6.10], and the mixing torques generated by vortex magnetic fields [6.11].) However, the Mason number pertains to

collections of interacting spherical particles, since uniform fields do not create a magnetic force on an isolated particle. However, a uniform field does exert a magnetic torque on an isolated platelet. If this torque dominates the hydrodynamic torque, then isolated particle motion will be significant. Indeed, when the component induction fields are increased to 0.020 T, advection lattices are observed up to frequencies of 550:275 Hz for the 2.3 vol.% benzyl alcohol-platelet suspension. For an induced dipole the magnetic torque is proportional to the field squared, whereas the viscous torque is proportional to the frequency. Thus, the magnetic torque is increased by a factor of $(20/15)^2 \sim 1.7$, whereas the viscous torque is increased by a factor of $275/125 \sim 2.2$, which is only a rough agreement. A detailed study of the transition field will be the subject of future work.

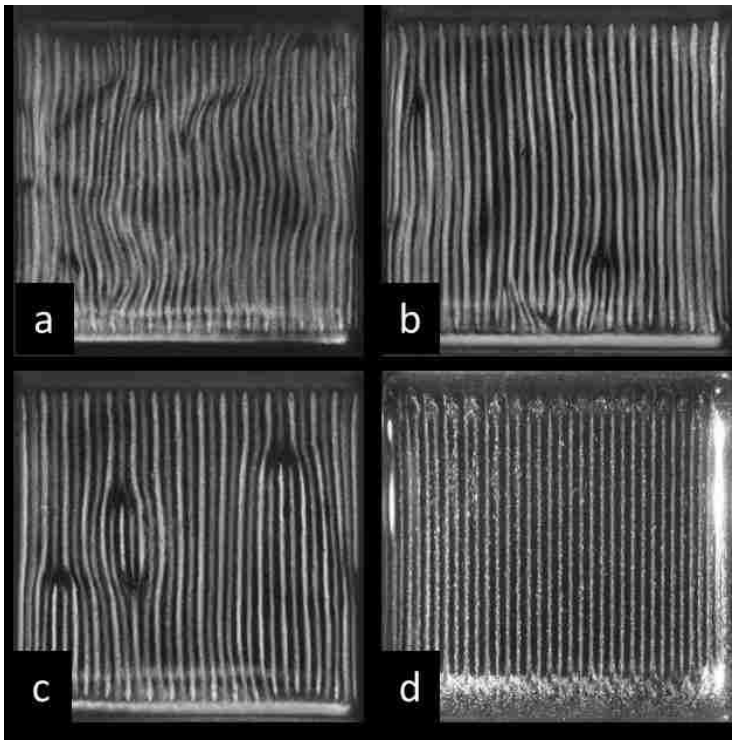

Figure 6-7. Photographs of advection lattices formed in a 250:125 Hz field with a 45° phase angle and rms component magnetic induction of 0.015 T in **(a)** acetone, **(b)** ethanol, **(c)** isopropanol, and **(d)** benzyl alcohol. While the column spacing for these advection lattices is similar regardless of the liquid viscosity (see Figure 6-6), their appearances and dynamics vary considerably.

Although the solvent viscosity does not significantly impact the column spacing, it has a pronounced effect on the flow rate within the columns and thus on the dynamics of the advection lattice. Low viscosity liquids, such as acetone, produce lattices of writhing columns that vigorously transport the suspension [**Figure 6-7(a)**]. More viscous liquids, such as ethanol and isopropanol, produce straighter, more uniform columns, and less vigorous flow, as seen in **Figures 6-7(b) and (c)**. Benzyl alcohol, which has a viscosity ~18× that of acetone, yields the highly ordered advection lattice in **Figure 6-7(d)**, but the flow rate is quite low. Finally, when ethylene glycol is used as a suspending fluid, an advection lattice forms, but the flow is barely discernible, on the order of 0.1 $cm \cdot s^{-1}$ for a 100:50 Hz field at a 0° phase angle with 0.015 T rms components.

The writhing columns produced in acetone are evidently due to the importance of fluid inertia at the high flow rates that low viscosity fluids can generate. Optimal heat transfer is promoted by such high flow rates, but the instabilities that characterize the ragged columns are undesirable. It is very easy to produce advection lattices in acetone, so liquid nitrogen with a viscosity smaller by a factor of ~2, could be used as a suspending medium for cryogenic heat transfer with IMA.

Particle volume fraction

The volume fraction of platelets is the most important suspension property governing IMA, since vastly different suspension dynamics are possible, depending on this value. For example, particle loadings greater than ~10 vol.% produce a suspension with a thick, slurry-like consistency. When 0.015 T rms biaxial fields are applied to such suspensions, they develop various surface instabilities, such as freestanding fluid ridges with vigorous internal flow, which are shown in Chapter 5 [also Ref. 6.1]. Here, we will limit our discussion to volume fractions large enough for advection lattices to readily form, but small enough that surface instabilities do not emerge. This gives a range of ~2–9 vol.%.

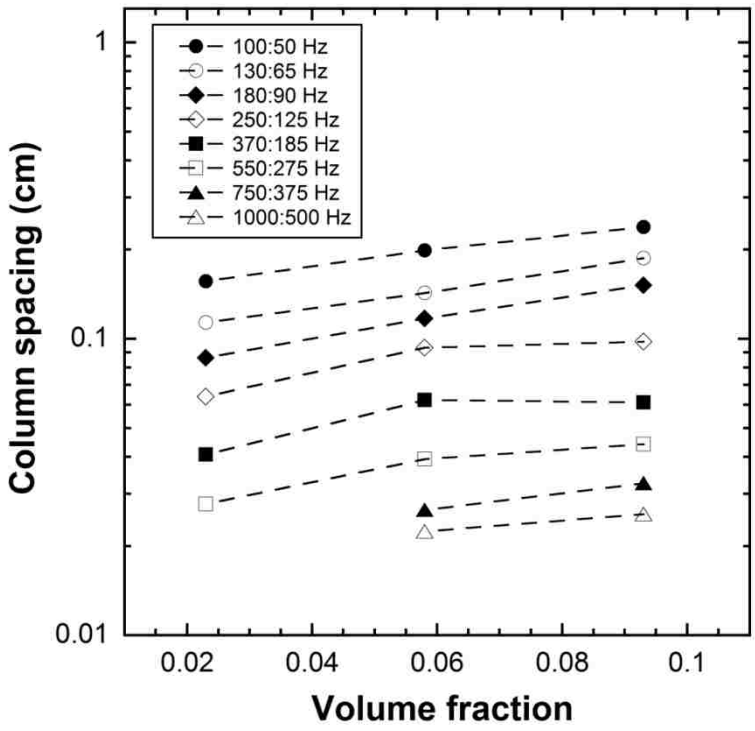

Figure 6-8. The advection lattice column spacing increases weakly with increasing volume fraction. For each volume fraction, frequency-dependent data are shown for an octave biaxial field with a 45° phase angle and rms component magnetic induction of 0.015 T.

Figure 6-8 shows that the column spacing increases only weakly with increasing particle volume fraction. However, the flow rate of the advection lattices *increases* significantly as the volume fraction of platelets *decreases*, which we find surprising. For instance, although an advection lattice that forms in an 8 vol.% suspension displays a similar overall flow pattern as that produced in a 4% suspension, the flow within the columns is slow. As the 8% suspension is progressively diluted, the flow rate increases dramatically. However, this increase in advection lattice dynamics with decreasing volume fraction has limits. Even though advection lattices will continue to form in suspensions with volume fractions below ~1 vol.%, the columns become extremely thin and faint, and the flow rate becomes very low. So there is an optimal volume fraction in which the dynamics of advection lattices are maximized, and for the platelets we use this is ~4 vol.%.

6.4 Conclusions

Isothermal magnetic advection has characteristics that make it an attractive method for heat and mass transfer. The columns can be tuned over a wide range by adjusting the field frequencies, to effect either heat and mass transfer or mass transfer alone for any given thermal gap. The column spacing is unaffected by the viscosity of the suspending fluid, so the advection lattice will remain coherent even across a significant thermal gradient, where the fluid viscosity can vary considerably. High flow rates can be obtained by the use of low viscosity liquids, such as alkanes, lower alcohols, acetones, etc., making possible the use of the Fluorinert ™ family of dielectric liquids and cryogenic fluids such as liquid nitrogen. The flow rates were also strongly dependent on the particle loading, with loadings on the order of 4 vol.% producing the most vigorous flow. The magnetic field is also an important control parameter. At low fields, a static layered phase forms, with the particle layers parallel to the biaxial field plane. The advection lattice only forms above a critical field and the column spacing increases as a power law with a small exponent above this field. Higher fields thus promote heat transfer by increasing the column size *and* the flow rate. However, reasonable field homogeneity across a thermal gap would be required to ensure that the flow columns do not terminate in order to adjust the lattice spacing *and* to prevent the magnetic particles from accumulating in a high field region. Future work will focus on quantitative measurements of flow rate within the columns and on measuring heat transfer rates.

Acknowledgements

Sandia National Laboratories is a multi-program laboratory managed and operated by Sandia Corporation, a wholly owned subsidiary of Lockheed Martin Corporation, for the U.S. Department of Energy's National Nuclear Security Administration under Contract No. DE-AC04-94AL85000. This work was supported by the Division of Materials Science, Office of Basic Energy Sciences, U.S. Department of Energy (DOE). We thank Vladimir Raksha, Paul

Coombs, Tom Markantes, Bill Kittler, and Kees-Jan Delst at JDSU for supplying the magnetic platelets.

References

6.1 K.J. Solis and J.E. Martin, Isothermal Magnetic Advection: Creating functional fluid flows for heat and mass transfer, *Appl. Phys. Lett.* **97**, 034101 1–3 (2010).

6.2 D.P. Lalas and S. Carmi, Thermoconvective stability of ferrofluids, *Phys. Fluids* **14**, 436–437 (1971).

6.3 R.A. Curtis, Flows and wave propagation in ferrofluids, *Phys. Fluids* **14**, 2096–2102 (1971).

6.4 B.A. Finlayson, Convective instability of ferromagnetic fluids, *J. Fluid Mech.* **40**, 753–767 (1970).

6.5 K.J. Solis and J.E. Martin, Stimulation of vigorous rotational flows and novel flow patterns using triaxial magnetic fields, *Soft Matter* **8** 11989 –11994 (2012).

6.6 J.E. Martin, R.A. Anderson, and C.P. Tigges, Simulation of the athermal coarsening of composites structured by a biaxial field, *J. Chem. Phys.* **108**, 7887–7900 (1998).

6.7 J.E. Martin, E. Venturini, J. Odinek, and R.A. Anderson, Anisotropic magnetism in field-structured composites, *Phys. Rev. E.* **61**, 2818–2830 (2000).

6.8 L. Marshall, C.F. Zukoski, and J.W. Goodwin, Effects of electric-fields on the rheology of non-aqueous concentrated suspensions, *J. Chem. Soc.-Faraday Trans. 1* **85**, 2785–2795 (1989).

6.9 D.J. Klingenberg, J.C. Ulicny, and M.A. Golden, Mason numbers for magnetorheology, *J. Rheol.* **51**, 883–893 (2007).

6.10 J.E. Martin and R.A. Anderson, Chain model of electrorheology, *J. Chem. Phys.* **104**, 4814–4827 (1996).

6.11 J.E. Martin, L. Shea-Rohwer, and K.J. Solis, Strong intrinsic mixing in vortex magnetic fields, *Phys. Rev. E* **80**, 016312 1–6 (2009).

Chapter 7

Stimulation of vigorous rotational flows and novel flow patterns using triaxial magnetic fields[7]

We have discovered that new flow patterns can be created by applying a dc field to the ac biaxial fields that are used to induce isothermal magnetic advection (IMA). IMA is a recently discovered fluid flow phenomenon that occurs in suspensions of magnetic *platelets* subjected to particular time-dependent, uniform, biaxial magnetic fields. IMA is characterized by the formation of emergent flow patterns called *advection lattices*. We find that a dc field can disrupt the antiparallel flow symmetry of the advection lattice and give rise to qualitatively new flow patterns, including vigorous rotational flows and a highly regular diamond lattice. The rotational flows are very robust and may have applications to heat transfer. The diamond lattice is an intriguing and challenging example of emergent dynamics. Both of these effects occur when the dc field is applied orthogonal to the plane of the biaxial field.

7.1 Introduction

In Chapter 5 we reported the discovery of magnetic-field-stimulated, noncontact fluid flows, which we termed *isothermal magnetic advection* (IMA) [7.1]. IMA occurs when a suspension of magnetic *platelets* (IMA does not occur with spherical or acicular particles) is subjected to particular time-dependent, spatially uniform, biaxial magnetic fields of modest strength ($\sim 10^{-2}$ T). The result is the emergence of striking flow patterns we call *advection lattices*. These advection lattices are generally comprised of an "antiferromagnetic" square lattice of flow columns, such that each column flows antiparallel to its four nearest neighbors. This lattice extends throughout the suspension volume and the flows are orthogonal to the plane of the biaxial field. Uniform fields cannot create a Kelvin force on an

[7] Originally published as: K.J. Solis and J.E. Martin, Stimulation of vigorous rotational flows and novel flow patterns using triaxial magnetic fields, *Soft Matter* **8**, 11989–11994 (2012).

isolated particle, so these flows are an emergent behavior of the system. The flow symmetry breaking is not characterized by a net body force; however, a uniform field *can* create a torque on an isolated particle, and we do observe a net body torque on the suspension under certain circumstances. In this chapter we demonstrate that new flow patterns and vigorous rotational flows can be stimulated by applying a dc field perpendicular to the plane of the ac biaxial field to create a triaxial field, which we define as a field created by three orthogonal components.

The ability to create bulk movement of fluids—broadly referred to as convection—is of significant importance because of the vastly increased rates of heat and mass transfer that can be achieved in comparison to conduction. *Forced* convection typically requires some combination of pumps, seals, valves, and in many cases, substantial pressures. IMA requires no moving parts, simply the application of modest, uniform magnetic fields to a platelet suspension, and, unlike *natural* convection, can create flow in any direction without requiring a thermal gradient or gravity. These attributes establish IMA as a simple, robust, noncontact method of creating functional fluid flows that offers new possibilities for applications in heat and mass transfer, especially in those circumstances where natural convection does not occur.

Although stimulating IMA with triaxial fields is a new development, triaxial fields have already been demonstrated to create interesting and useful effects in spherical particle suspensions. Examples include the field-induced formation of particle foams and classical molecular clusters [7.2], strong intrinsic vortex magnetic field mixing [7.3,7.4], field-structured composites as efficient thermal interface materials [7.5], and the dynamic self-assembly of viscoelastic paramagnetic colloidal clusters [7.6]. Even less complex field configurations can stimulate interesting phenomena, ranging from the simple chain formation that occurs in magnetorheology [7.7], to the formation of folding clusters [7.8] and even highly organized colloidal structures such as snake-like swimmers [7.9–7.11] and asters, which occur when magnetic colloids confined to an interface are driven with a

uniaxial ac field [7.12]. In the following we describe the various effects an ac-ac-dc triaxial field can have on IMA when the ac biaxial field components are harmonically related, with frequency ratios of 1:1, 2:1, and 3:1.

7.2 Experimental

The magnetic platelet suspensions were prepared by dispersing a fixed amount of platelets (~0.875 g) in varying amounts of isopropyl alcohol to achieve the desired volume fractions ϕ_p. The platelets were supplied by JDSU Flex Products Group, and are seen in the SEM of **Figure 7-1** to possess a highly irregularly shaped morphology with an average size of ~20 μm across by ~234 nm thick. The multilayer platelets are comprised of a 50 nm Ni core sandwiched between 92 nm MgF_2 coatings. The suspensions are contained in a 3 cm square glass cell that is about 6 cm tall.

For these studies we employed a variety of ac-ac biaxial and ac-ac-dc triaxial magnetic fields. The ac components of the biaxial fields were supplied by a pair of

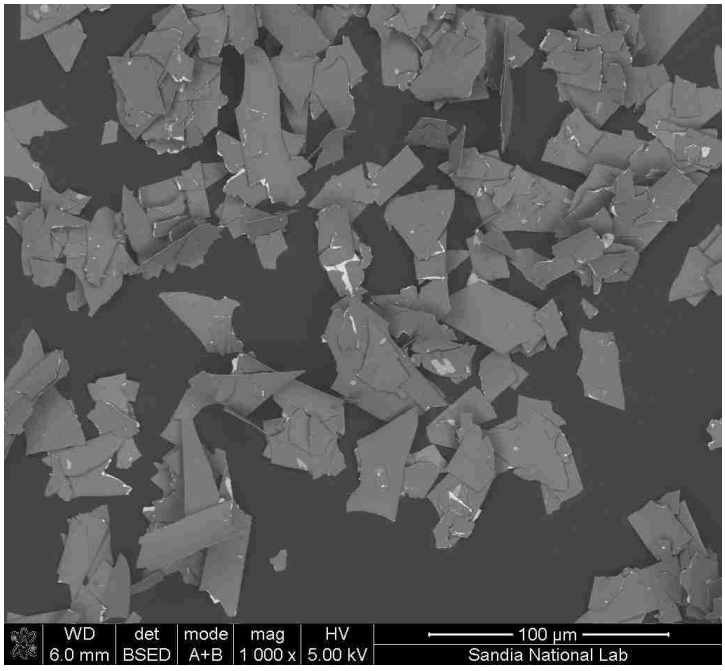

Figure 7-1. SEM image showing that the magnetic platelets possess an irregular morphology, high aspect ratio, and a fairly polydisperse size distribution.

orthogonally nested Helmholtz coils operated in series resonance with computer-controlled, fractal capacitor banks. These coils were used to create time-dependent biaxial fields in the low audio frequency range (~72 to 1000 Hz) with amplitudes up to ~200 G (rms amplitude of each *component*). The relative frequencies of the two components are *just intervals*, expressible as a ratio of small integers (*m*:*n*). *Harmonic* biaxial fields are those wherein one component is an integer multiple of the other (*i.e.*, 2:1, 3:1, *etc.*). As this ratio increases, the Lissajous plot of the two ac field components increases in complexity.

The flow patterns we observe are strongly dependent on the phase relation between the field components. To explore this dependence we phase modulate the biaxial field by adding a small frequency (0.1–1 Hz) to the *higher* frequency field component. This addition periodically modulates the phase at exactly the added frequency, enabling a rapid investigation of the phase effect. If any interesting effects or structures are noted during phase modulation, one can simply input the appropriate phase angle to the base frequencies in order to lock-in that particular feature for further study.

The ac-ac-dc triaxial fields were created from some type of *n*:1 ac biaxial field, to

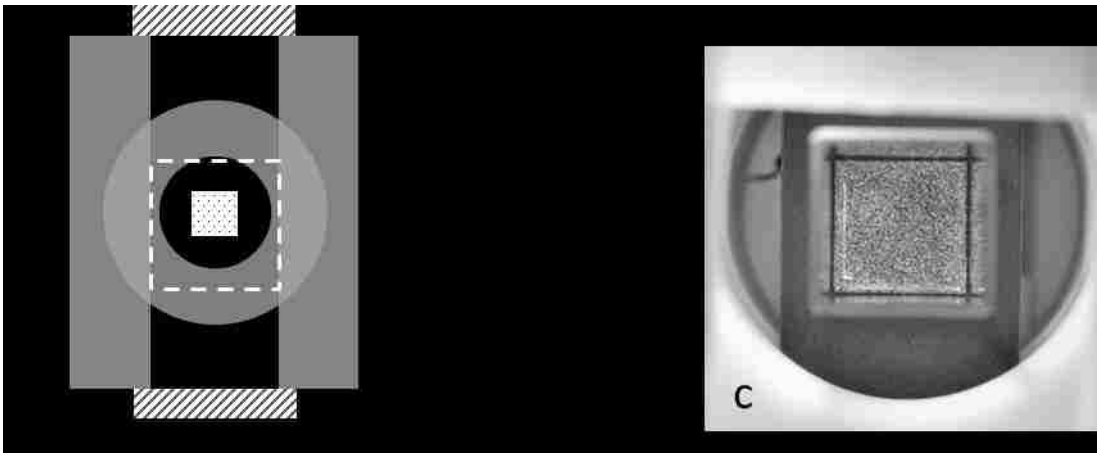

Figure 7-2. **(a)** Schematic representation of the magnetic field sources: orthogonal Helmholtz coil pairs (light and dark gray), ceramic plate magnets (striped); and the sample cell (dotted) at the center. **(b)** Compass rose indicating the convention used to refer to the various directions in describing the flow patterns and magnetic fields. **(c)** Photograph showing a quiescent suspension housed in a square glass cell within the central cavity of the Helmholtz coil pairs, one of which is partially seen as the circular enclosure. This photograph corresponds to the dashed region in (a).

which a uniform, dc field component was applied orthogonally. This dc component was supplied by two $1\times4\times6$ in^3 ceramic plate magnets, whose separation was varied to achieve the desired field strength. For example, a separation of ~9½ inches—which is imposed by the outermost Helmholtz coil pair—produces a magnetic field of about 125 G.

The geometry of the experimental apparatus, including the relationship of the magnetic fields to the suspension, is shown in **Figure 7-2(a)**. The cell containing the magnetic suspension is supported within the central cavity of the two Helmholtz coils. Taking the sample cell as the origin of a right-handed Cartesian coordinate system, one Helmholtz coil (light gray) produces a field component along the *x*-axis, while the other (dark gray) produces a field along the *z*-axis, so that all ac biaxial fields lie within the *x*–*z* plane. (The force of gravity is pointing into the page along the $-z$ direction.) The dc component (striped) is applied along the *y*-axis. However, instead of constantly referring to the *x*, *y*, and *z* axes throughout the chapter, we use the cardinal directions [**Figure 7-2(b)**], such that *north* and *south* are along the positive and negative *y* axes, and *east* and *west* are along the positive and negative *x* axes, respectively. The directions along the positive and negative *z* axes are referred to as *up* and *down*. **Figure 7-2(c)** shows a photograph of the sample cell and part of a Helmholtz coil to familiarize the reader with the layout, as most of the results will be pictures taken from this same perspective, albeit excluding the surrounding magnet. Finally, we must specify the direction of the rotating field. A rotating field created by a 90° phase shift to the coil that produces the U–D field rotates counterclockwise in the E–W, U–D plane when viewed from the south. This rotating field can be reversed by shifting the phase to 270°. (This point is only of importance for one who wishes to exactly reproduce the results described below.)

7.3 Results and Discussion

When a uniform dc magnetic field is applied orthogonal to the biaxial field plane, the advection lattice becomes altered. The manner and degree to which the dc field affects the

advection lattice depends on a number of factors, including the just interval of the biaxial field, the phase relationship of the components, the strength and polarity of the dc field, and the volume fraction of platelets in the suspension. To make the presentation of the results as clear as possible, we first summarize some general observations about the suspension dynamics in ac-ac-dc triaxial magnetic fields, and then describe the particular details for the various harmonic biaxial fields.

7.3.1 General observations

For a given biaxial or triaxial field, the particle volume fraction is a principal determinant of the suspension dynamics. For the isopropanol-platelet suspensions we study, a volume fraction of ~4.7% marks a transition in the dynamics. The pattern-forming regime is above 4.7%, and we will start by describing this regime. It is important to note that unless otherwise specified, the low frequency field component is E–W and the high frequency component is vertical. Each ac magnetic induction field has an rms amplitude of 0.015 T (150 G) unless otherwise noted.

The effects of a dc field on the suspension dynamics were explored by applying an increasing dc field to a phase-modulated biaxial field. The diagram shown in **Figure 7-3** illustrates the general effects of an increasing dc field on the various advection lattices, and corresponds to the description that follows. This diagram also points to the figures that contain images of the various lattices, and referencing this diagram frequently can clarify the following discussion. For weak dc fields (~10 to 75 G), the advection lattice becomes distorted in ways that depend on the type of biaxial field, as discussed in detail in the following sections. As the dc field is increased to ~100 G, the advection lattice produced by the biaxial field becomes barely distinguishable (Transition zone). Finally, as the dc field is increased to full strength (~125 G) the original advection lattice vanishes and the suspension sloshes back-and-forth in the sample cell at the phase modulation frequency. The two phases

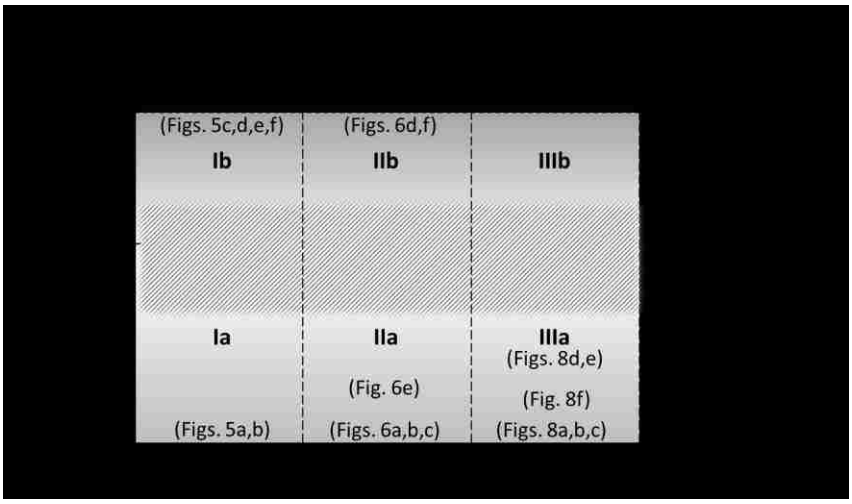

Figure 7-3. Diagram illustrating the general effects that an increasing dc field has on advection lattices formed in three different harmonic biaxial fields (*n*:1). The referenced figures are positioned according to their approximate values of relative dc field strength.

at which the fluid surface achieves maximum, but opposite, inclinations depends on the type of biaxial field, yet are always separated by 180°. These inclined fluid surfaces can be maintained indefinitely by simply locking-in the appropriate phase angle. Moreover, these inclined fluids are sustained by rotational flow, a fact that can be clearly visualized by dispensing solvent drop-wise onto the inclined surface. When a drop contacts the surface, it is quickly transported uphill in tiny rivulets. These rotational flows should be highly effective at heat and mass transfer.

Investigating a variety of *harmonic* (*n*:1) biaxial fields reveals a peculiar trend regarding the directions of the sloshing displacements: *the fluid displacements for even and odd harmonic fields are orthogonal to each other*. In other words, for odd values of *n*, E–W fluid flows occur, whereas for even values of *n*, N–S fluid flows occur. However, regardless of the value of *n*, the sign of fluid vorticity, and thus the direction of surface flow, can be reversed by changing the phase by 180°. The vorticity of fluid flow can also be reversed by changing the polarity of the dc field, but curiously only for *even* harmonic fields.

The even and odd harmonic fields differ in another important respect. For odd harmonic fields, the axis of fluid vorticity is along the north–south axis, which is parallel to the dc field. If the biaxial field components are switched, such that the low frequency field

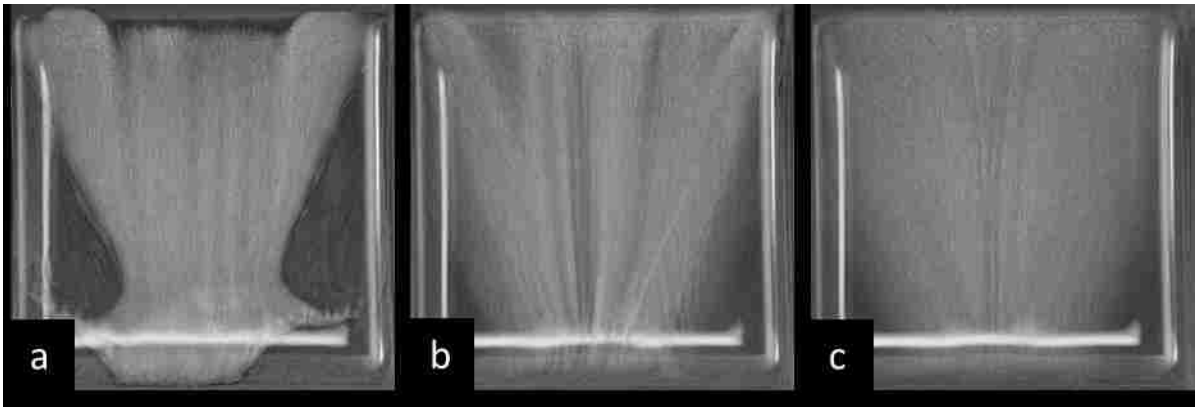

Figure 7-4. Time series development of strong rotational flow for a 3.5 vol% suspension subjected to a 150 G_{rms}, 250:125 Hz, 0° phase/125 G_{dc} ac–ac–dc triaxial field. **(a)** When the ac biaxial field is initially turned on, the platelet sediment erupts into plumes that quickly disperse throughout the supernatant. **(b)** Within a few seconds, the suspension is vigorously flowing from north to south at the surface. **(c)** After ~5 seconds the flow is nearly fully developed.

component is in the vertical direction, the axis of vorticity does not change. However, for the even harmonic fields the axis of vorticity is along the low frequency field component, which creates north–south flow when the low frequency field is applied in the east–west direction. If these biaxial field components are switched, such that the low frequency field component is in the vertical direction, the axis of vorticity *does* change, and the fluid rotates around a vertical axis.

In addition to the sloshing behavior, the surface can develop new flow patterns for certain phase angles, which again vary with the type of biaxial field employed, as described in detail below.

For platelet volume fractions less than ϕ^* ~4.7 vol%, the advection lattices are weak or nonexistent in ac-ac-dc triaxial fields. However, the rotational flows are much more vigorous (**Figure 7-4**), while the surface of the suspension is less inclined and becomes progressively more horizontal with decreasing platelet loading. This regime is undoubtedly the best for heat transfer.

Having introduced the general behavior of platelet suspensions subject to triaxial magnetic fields, we will now discuss the detailed behavior of suspensions subjected to triaxial fields having unison, first, and second harmonic biaxial field components. We will

focus on the suspension dynamics for volume fractions greater than ϕ^*, as this regime is dominated by flow patterns that display a rich variety of behavior. All of the flow patterns in the following figures are for 7 vol% suspensions.

7.3.2 1:1 Biaxial fields

When a platelet suspension is subjected to a unison biaxial field—which is simply a rotating field when the components are in quadrature phase—flow columns form that extend perpendicular to the field plane. These columns are extremely dynamic and appear to roll over each other, piling up on one or the other side of the cell depending on whether the phase is 90° or 270°. If the field components are phase modulated, the columns will migrate side-to-side commensurately with the ever-changing circulation of the field, which is generally elliptical. When the phase is either 90° or 270°, the columns accumulate to one side of the cell [**Figure 7-5(a)**], and the fluid surface becomes inclined toward that wall. A solvent droplet will flow uphill, indicating a strong rotational flow component. These behaviors suggest that the flow columns formed in rotating fields possess vorticity of the same sign. A phase of 45° or 225° attenuates the dynamics of the columns enough that they become much more ordered, as shown in **Figure 7-5(b)**, and changes the direction of their motion relative to that obtained at 90° and 270°, respectively. However, this 45° reduction in phase angle does not change the flow direction of a solvent droplet. Phases of 0° or 180° result in a completely stagnant suspension, because the biaxial field reduces to a simple uniaxial ac field in this case.

New flow patterns emerge as a dc field is applied, but this field component does not alter the overall flow vorticity. A weak dc field (~10 to 50 G, Region Ia in Figure 7-3) causes coarsening of the fluid columns. Further increasing the dc field (~50 to 100 G) distorts the columnar flow pattern, resulting in a disordered flow field (Transition zone, Figure 7-3). Finally, at a dc field of ~100 to 125 G, distinctly new flow patterns arise (Region Ib, Figure 7-3). As Figure 7-5(c) shows, for phases of 0° and 180°, a columnar

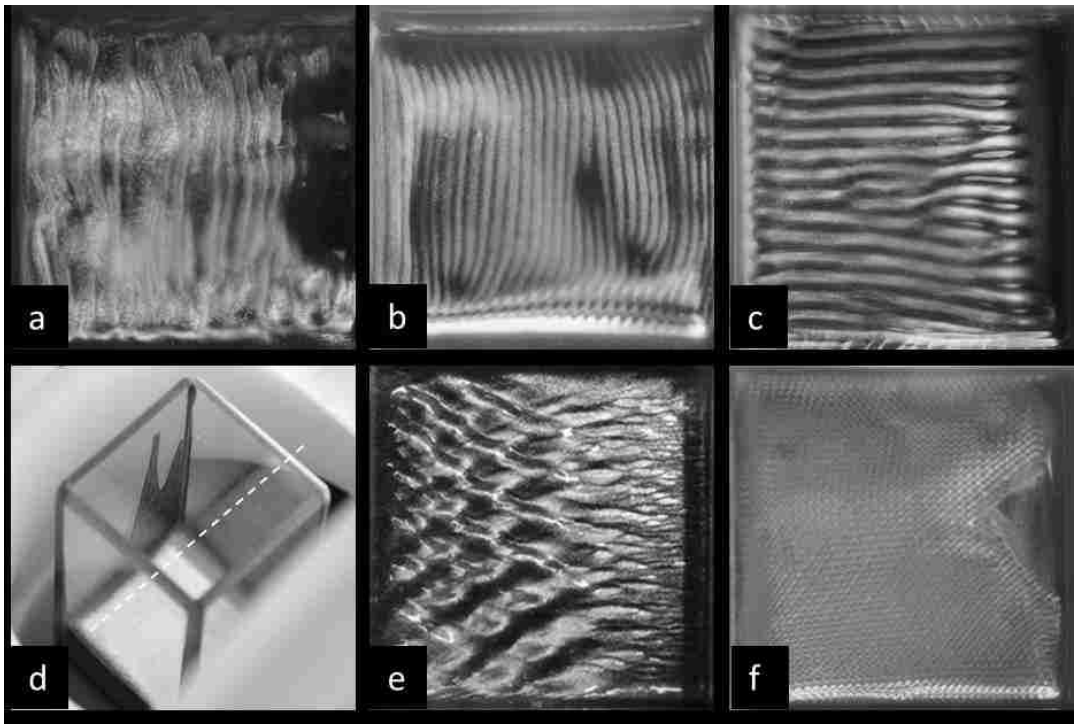

Figure 7-5. Flow patterns for 1:1 fields in a 7 vol% suspension. The biaxial field for parts (a)–(e) is a 100 Hz rotating field at 150 G_{rms}. **(a)** Dynamic columns piling up toward the left side of the cell in a rotating field (phase = 90°), leaving a region devoid of suspension, appearing as the black region at the right. The surface of the suspension is inclined toward the left. **(b)** A phase of 45° results in calmer columns that drift toward the right, while solvent dripped on the surface is transported left. **(c)** A phase of 0° with a 125 G dc field causes this columnar pattern to emerge. The surface is inclining to the left and the fluid is slowly flowing uphill within the columns. **(d)** A phase of 90° and a 125 G dc field results in a vortex magnetic field, creating strong rotational flow of the suspension, as seen by the fluid being driven up the container wall. This image is an oblique-downward view into the magnet cavity. The north–south direction is indicated by the dashed white line. **(e)** A phase of 45° and a 125 G dc field results in this diamond-like pattern. The surface is inclined to the left, and the suspension is flowing uphill. **(f)** Increasing the field frequency to 500 Hz at a phase of 0° replaces the columnar pattern in (c) with a very fine diamond mesh pattern that is flowing toward the left, exposing a region of the sample cell floor at the center-right.

pattern emerges that is perpendicular to the columnar lattice pattern that formed in the biaxial field. The surface columns are all transporting fluid along their lengths in the same direction, which can be reversed by changing the phase by 180°. These columns extend parallel to each other and are quite ordered, but occasionally contain bifurcations. Upon close inspection, these large columns are seen to be separated by extremely fine column segments. (The formation of these columnar patterns at phases of 0° and 180° in an ac-ac-dc triaxial field is in stark contrast to what the suspension does at these same phases for the

purely biaxial field—nothing.) Setting the phase to either 90° or 270° results in strong, featureless flow that drives the fluid all the way up the walls of the container if the field is applied sufficiently long [**Figure 7-5(d)**]. Such strong flow isn't entirely surprising considering that at phases of 90° and 270° the biaxial field is a rotating field, to which the addition of an orthogonal dc field constitutes what we called a *vortex* magnetic field in Chapters 3 and 4 [also Refs. 7.3,7.4], and induces very strong mixing of magnetic particle suspensions. Finally, phases of 45° and 225° produce the diamond-like pattern in **Figure 7-5(e)**.

The pattern displayed in the triaxial field also depends on the magnitude of the frequency. For biaxial field frequencies less than 140 Hz, the patterns described above are observed. However, once the frequency exceeds ~140 Hz, the columnar pattern observed at phases of 0° and 180° transitions to a diamond-like, mesh pattern whose feature size varies inversely with frequency magnitude. Other than this difference in the type of pattern formed, the general behavior discussed above in regards to the phases still applies: phases of 90° and 270° create rotational flows that climb the container walls; whereas, phases of 0° and 180° give rise to a calm diamond-structured surface [**Figure 7-5(f)**] that inclines in the same respective directions as for phases of 90° and 270°, and also demonstrates uphill flow.

7.3.3 2:1 Biaxial fields

Biaxial fields with a 2:1 frequency ratio can create three principal types of advection lattices. These types are selected by controlling the phase between the field components. (Regardless of the phase, this *first harmonic* biaxial field itself does not create body torques on the suspension, as evidenced by the lack of sloshing in the fluid upon phase modulation.) At phases of 0° and 180°, the advection lattice columns have a ragged, almost turbulent appearance [**Figure 7-6(a)**]. These ragged columns exhibit rapid writhing motions and column bifurcations that quickly propagate through the lattice. Phases of 45° and 225° result

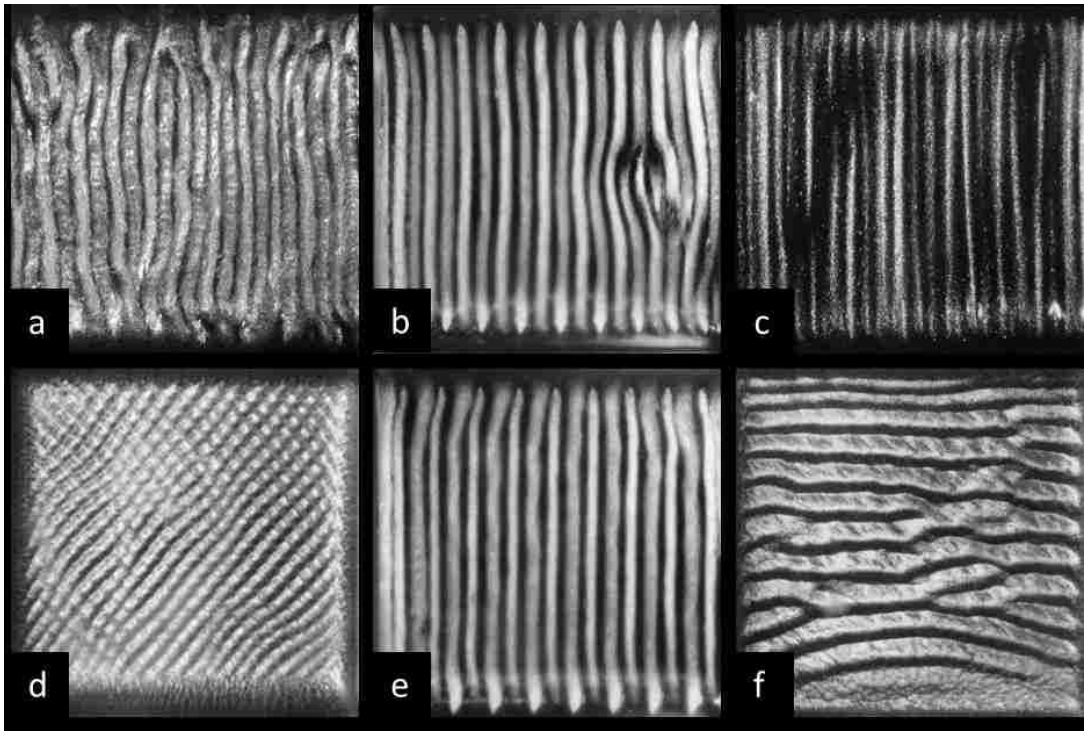

Figure 7-6. Flow patterns for 2:1 fields in a 7 vol% suspension. Parts (a)–(c) are purely biaxial fields of 150:75 Hz and 150 G_{rms} at various phases: **(a)** irregular columns at a 0° phase; **(b)** straight, uniform columns at a 45° phase, with a defect present at the right-center of the image; and **(c)** faint, fine columns at a 90° phase. Parts (d)–(f) are for various ac–ac–dc triaxial fields: **(d)** dynamic diamond pattern for a 500:250 Hz, 150 G_{rms} biaxial field at 0° phase and 125 G dc field; **(e)** column size biasing for a 150:75 Hz, 150 G_{rms} biaxial field at a 45° phase and ~20 G dc field; and **(f)** parallel herringbone pattern for a 150:75 Hz, 150 G_{rms} biaxial field at a 90° phase and 125 G dc field (the sloped surface is inclining toward the top of the image [north]).

in straight columns that are uniformly spaced, as shown in **Figure 7-6(b)**. Despite the vigorous antiparallel flow, this lattice is remarkably stable, the only interesting dynamics being an E–W drift, the direction of which fluctuates. (However, the drift direction *can* be selected by tilting the container appropriately.) Column bifurcations also occasionally form and these defects are very dynamic. At phases of 90° and 270° the columns are much finer and more indistinct, as shown in **Figure 7-6(c)**.

Applying a dc field produces a variety of effects, depending on its relative strength. When a weak dc field (~10 to 20 G, Region IIa in Figure 7-3) is applied parallel to the straight columns, a pronounced asymmetry in the column diameters occurs, as shown in **Figure 7-6(e)**. Although the average lattice spacing does not change, columns flowing south become thinner while those flowing north become thicker when the dc field direction

is south. Changing the phase of the biaxial field by 180° (or reversing the dc field) reverses this asymmetry. As the dc field is increased to ~50 G, the columns begin to display a diffuse appearance (Transition zone, Figure 7-3). At ~90 G, transverse (E–W) bands appear, and at ~125 G (Region IIb, Figure 7-3) these become more numerous and acquire a herringbone-like appearance, similar to that shown in **Figure 7-6(f)**. The suspension also inclines toward one of two walls (north or south) depending on the phase, indicating rotational flow about an E–W axis. The direction of incline and of uphill flow is in the *same direction* as the flow of the columns that become *thicker* when biased at weaker fields.

We recall that at phases of 90° and 270°, the N–S columns are thin and indistinct. However, the application of a 125 G dc field (Region IIb, Figure 7-3) creates the striking herringbone pattern shown in Figure 7-6(f). This pattern consists of parallel E–W bands that move uphill (either north or south, depending on the biaxial field phase or dc field polarity). Each band has a texture produced by alignment of platelet agglomerates that is in one of two canted orientations. These orientations alternate from one band to the next, and the pattern exhibits highly mobile band bifurcation defects, similar to those observed for columns. In addition to the herringbone pattern, the suspension is maximally inclined to either the north or south walls at these phases, and displays quite vigorous uphill flow, as evidenced by the transport of solvent dripped on the surface.

The writhing, ragged columns produced by the biaxial field at phases of 0° or 180° [Figure 7-6(a)] are transformed into the dynamic, shimmering diamond lattice in **Figure 7-6(d)** by the application of a dc field. At low field frequencies this pattern is faint, but as the frequency increases to 250:125 Hz the pattern becomes quite distinct. The characteristic scale of this diamond mesh varies inversely with frequency magnitude, so at high frequencies (>500:250 Hz) the pattern resembles a finely woven fabric. Viewing the sample container from the side reveals that this diamond mesh pattern is produced by a lattice of countercurrent columns in the vertical direction. In principle, these columns can be viewed from the top surface by interchanging the field frequencies of the two Helmholtz coils, so

that the 2:1 field becomes a 1:2 field. Remarkably, when this is done the fluid displays only a slow, churning motion, **Figure 7-7(a)**, with no visible chains. However, if the field of the high-frequency component is now reduced by half, the surface develops a mottled appearance [**Figure 7-7(b)**], and further reductions produce highly irregular columns that extend E–W, as shown in **Figure 7-7(c)**.

Returning to the original 2:1 field (250:125 Hz) and reducing the magnetic induction of the high-frequency (vertical) component from 150 G_{rms} causes the dynamic, somewhat disordered diamond pattern in **Figure 7-7(d)** to become much sharper and less active [**Figure 7-7(e)**]. Similarly, as the vertical component of the 1:2 field is reduced, a highly

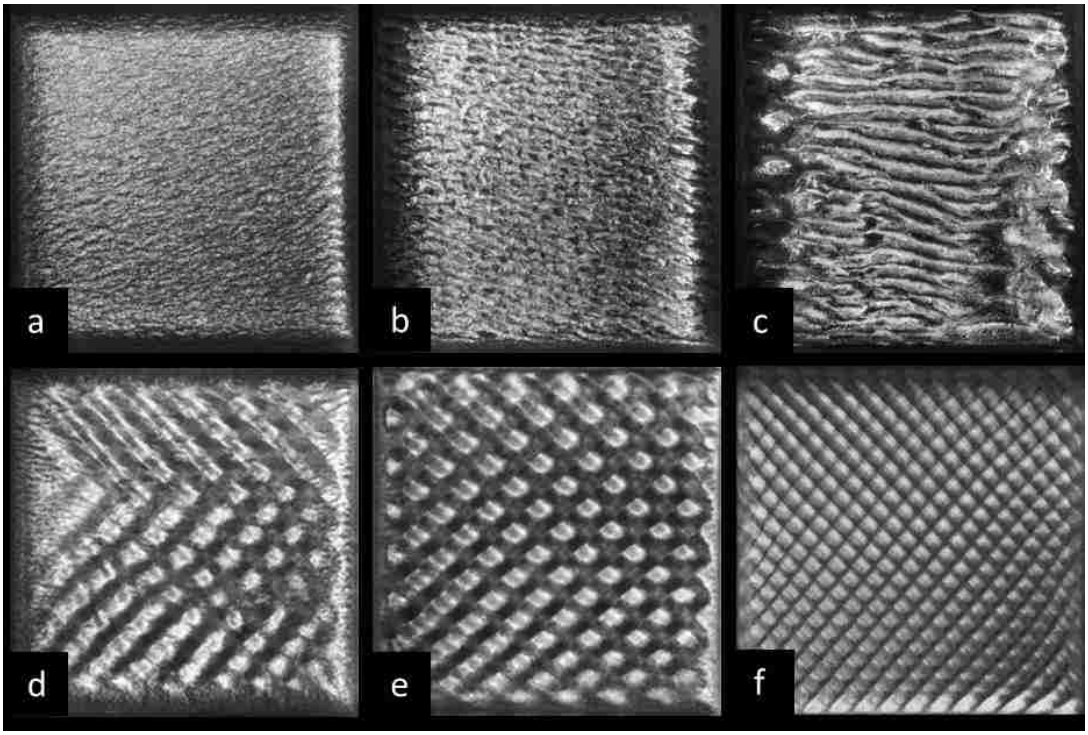

Figure 7-7. Parts (a)–(c) show the progressive emergence of an irregular advection lattice as the high-frequency component amplitude is reduced for a 125:250 Hz ac–ac–dc triaxial field. **(a)** B_{250Hz} = 150 G_{rms} results in a mostly featureless, slowly churning suspension. **(b)** Reducing the field by half (B_{250Hz} = 75 G_{rms}) causes the surface to develop a mottled structure. **(c)** When the field is reduced to a quarter of its original strength (B_{250Hz} = 37.5 G_{rms}), an E–W advection lattice with very irregular columns emerges. **(d)** A 250:125 Hz ac–ac–dc triaxial field produces a dynamic, disordered diamond lattice pattern that becomes much calmer and very ordered **(e)** when the high-frequency (vertical) component amplitude is reduced by half (B_{250Hz} = 75 G_{rms}). **(f)** A highly ordered diamond pattern also emerges when the vertical component amplitude of the 1:2 field is reduced (B_{125Hz} = 37.5 G_{rms}).

ordered diamond pattern emerges [**Figure 7-7(f)**] that is finer than for the corresponding 2:1 case because the dominant ac component frequency is now higher. In both of the above cases (*i.e.*, 2:1 and 1:2 fields), distinct flow patterns persist as the magnitude of either ac component is reduced to zero, demonstrating that only *one* component of a biaxial field needs to be time dependent to stimulate isothermal magnetic advection.

7.3.4 3:1 Biaxial fields

A second harmonic biaxial field produces flow patterns that are similar to those produced by the first harmonic field, but have some significant differences. In general, the application of a dc field distorts and eventually obliterates these patterns, producing vigorous rotational flow about the dc axis, but no new flow structures in this case.

At phases of 0° and 180° [**Figure 7-8(a)**] the advection lattice consists of ragged,

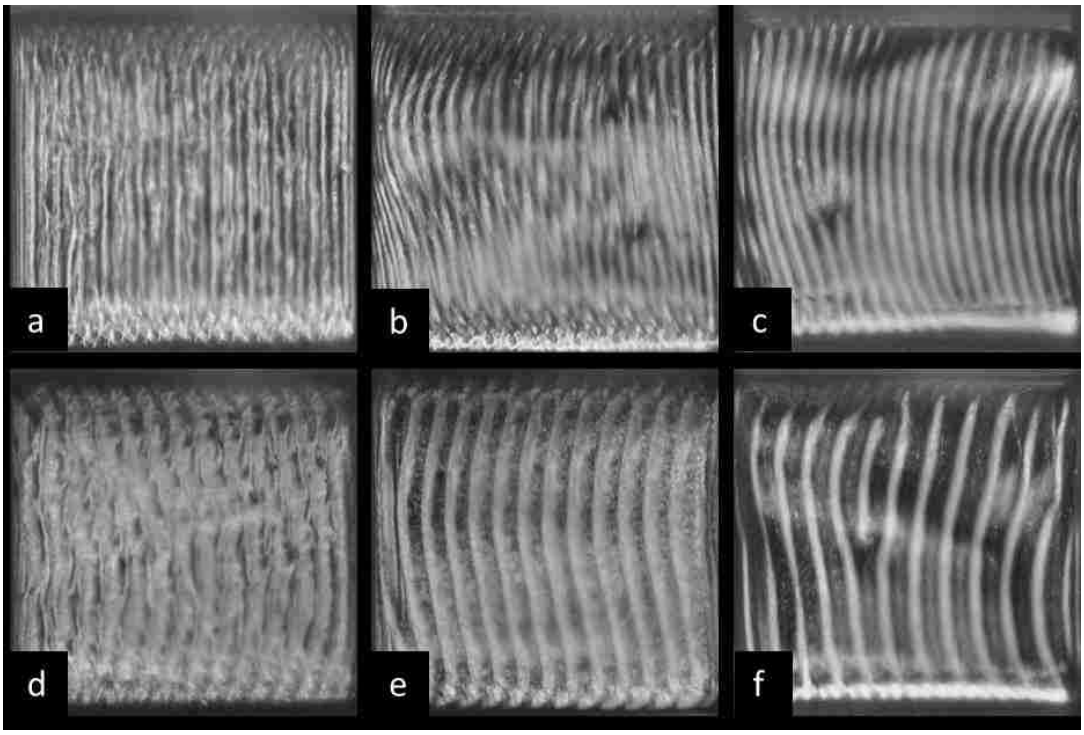

Figure 7-8. Flow patterns for 3:1 fields in a 7 vol% suspension. The biaxial field for all images is 300:100 Hz and 150 G_{rms}. Parts (a)–(c) are purely biaxial fields at various phases: **(a)** phase = 0°; **(b)** phase = 45°; and **(c)** phase = 90° (the bowed columns are drifting to the left). Parts (d)–(f) are ac–ac–dc triaxial fields: **(d)** phase = 0° and ~30 G dc field; **(e)** phase = 45° and ~30 G dc field (diffuse columns are drifting left); and **(f)** phase = 90° and ~15 G dc field (column size biasing and drifting left).

writhing columns that are similar to those produced by the 2:1 biaxial field. At phases of 90° and 270° well-defined, bowed columns emerge that drift rapidly either east or west, depending on the field phase [**Figure 7-8(c)**]. The bowing is likely due to the stick boundary conditions at the N–S walls creating parabolic flow at the fluid surface. When the phase is set to either 45° or 225°, the advection lattice is complex and difficult to describe. It consists of the moving bowed columns observed at 90°/270°, obscured by faint columns that cross these at an oblique angle and move in the opposite direction [**Figure 7-8(b)**]. Deformation of the surface was observed as well, with the fluid at one corner of the cell significantly depressed in height.

When a dc field is progressively applied to any of these flow lattices (Region IIIa, Figure 7-3), the columns progressively become more asymmetrical in diameter [**Figure 7-8(c) and (f)**], just as for the 2:1 field. For the 0° or 180° phase, the columns noticeably change their appearance as the field is increased, as in **Figure 7-8(d)**. When the dc field reaches ~125 G (Region IIIb, Figure 7-3) the columns have completely disintegrated, giving way to a textured surface and vigorous rotational flow about the dc field axis when the field phase is 0° or 180°, which is curious, since without the dc field the fluid does not exhibit vorticity. This vigorous flow should be very useful for heat and mass transfer.

7.4 Conclusions

The effects we have described demonstrate the ability to control the fluid flow direction by appropriately adjusting the magnetic field. Although the rotational flows are not visually stunning like the flow patterns that emerge at higher volume fractions, they are likely to prove useful for heat and mass transfer. Future work will focus on quantifying the heat transport in liquids using isothermal magnetic advection and evaluating the effectiveness of the various flows we have observed, as well as exploring the effects of applying a *time-dependent* third field component.

Acknowledgements

Sandia National Laboratories is a multi-program laboratory managed and operated by Sandia Corporation, a wholly owned subsidiary of Lockheed Martin Corporation, for the U.S. Department of Energy's National Nuclear Security Administration under contract DE-AC04-94AL85000. This work was supported by the Division of Materials Science, Office of Basic Energy Sciences, U.S. Department of Energy (DOE). We thank Vladimir Raksha, Paul Coombs, Tom Markantes, Bill Kittler, and Kees-Jan Delst at JDSU for supplying the magnetic platelets.

References

7.1 K.J. Solis and J.E. Martin, Isothermal Magnetic Advection: Creating functional fluid flows for heat and mass transfer, *Appl. Phys. Lett.* **97**, 034101 1–3 (2010).

7.2 J.E. Martin, R.A. Anderson, and R.L. Williamson, Generating strange magnetic and dielectric interactions: Classical molecules and particle foams, *J. Chem. Phys.* **118**, 1557–1570 (2003).

7.3 J.E. Martin, L. Shea-Rohwer, and K.J. Solis, Strong intrinsic mixing in vortex magnetic fields, *Phys. Rev. E* **80**, 016312 1–6 (2009).

7.4 K.J. Solis, R.C. Bell and J.E. Martin, Vortex magnetic field mixing with anisometric particles, *J. Appl. Phys.* **107**, 114911 1–4 (2010).

7.5 J.E. Martin and G. Gulley, Field-structured composites for efficient, directed heat transfer, *J. Appl. Phys.* **106**, 084301 1–7 (2009) [reprinted in *Virt. J. Nanoscale Sci. & Tech.* 20 19 (2009)].

7.6 P. Tierno, R. Muruganathan, and T.M. Fischer, Viscoelasticity of dynamically self-assembled paramagnetic colloidal clusters, *Phys. Rev. Lett.* **98**, 028301 1–4 (2007).

7.7 J. de Vicente, D.J. Klingenberg, and R. Hidalgo-Alvarez, Magnetorheological fluids: a review, *Soft Matter* **7**, 3701–3710 (2011).

7.8 N. Casic, S. Schreiber, P. Tierno, W. Zimmermann, and T.M. Fischer, Friction-controlled bending solitons as folding pathway toward colloidal clusters, *Europhys. Lett.* **90**, 58001 1–5 (2010).

7.9 A. Snezhko, I.S. Aranson, and W.-K. Kwok, Surface wave assisted self-assembly of multidomain magnetic structures, *Phys. Rev. Lett.* **96**, 078701 1–4 (2006).

7.10 A. Snezhko, I.S. Aranson, and W.-K. Kwok, Dynamic self-assembly of magnetic particles on the fluid interface: Surface-wave-mediated effective magnetic exchange, *Phys. Rev. E: Stat., Nonlinear, Soft Matter Phys.* **73**, 041306 1–8 (2006).

7.11 A. Snezhko, M. Belkin, I.S. Aranson, and W.-K. Kwok, Self-assembled magnetic surface swimmers, *Phys. Rev. Lett.* **102**, 118103 1–4 (2009).

7.12 A. Snezhko, Non-equilibrium magnetic colloidal dispersions at liquid-air interfaces: dynamic patterns, magnetic order and self-assembled swimmers, *J. Phys.-Condens. Mat.* **23**, 153101 1–21 (2011).

Chapter 8

Multiaxial fields drive the thermal conductivity switching of a magneto-responsive platelet suspension[8]

We demonstrate the ability to change the thermal conductivity of a magnetic platelet suspension from insulating to conducting by using either uniaxial or multiaxial ac magnetic fields to control the suspension structure and dynamics. The equivalent thermal conductivity of the suspension can be modified either by creating static particle structures that facilitate or block heat transfer, or by using multiaxial ac fields to drive emergent particle dynamics that create vigorous, organized, non-contact flow. The equivalent thermal conductivity of a single suspension can be varied over a 100-fold range, and an equivalent thermal conductivity as high as 18.3 $W \cdot m^{-1} \cdot K^{-1}$ has been achieved in an aqueous suspension containing only 2.0 vol% platelets. This value is more than twice the conductivity of liquid mercury.

8.1 Introduction

High power density microsystems are driving the need for more efficient thermal management and liquid cooling is the solution of choice for the current generation of high performance supercomputers. Better thermal management solutions could be devised if the thermal conductivity of the fluid could be actively controlled, especially if the dynamic range is significant. In recent years we have found that multiaxial magnetic fields can be used to direct the assembly of complex particle composites with highly tailorable, anisotropic properties [8.1–8.10], and can also drive highly organized flow lattices in magnetic particle suspensions, as discussed in Chapters 5, 6, and 7 [also Refs. 8.11–8.13]. In this chapter we

[8] Originally published as: K.J. Solis and J.E. Martin, Multiaxial fields drive the thermal conductivity switching of a magneto-responsive platelet suspension, *Soft Matter* **9**, 9182–9188 (2013).

combine both of these findings to create extremely large changes in thermal transport through a platelet suspension.

Because the thermal conductivity of most liquids is notoriously low, there has been a rapid increase in research intended to control, or at least increase, the thermal conductivity of simple liquids. Quite a bit of this work has focused on suspensions of nanoparticles, as it had been thought that these might provide a benefit exceeding the classical prediction of Maxwell for the thermal conductivity of spherical particle suspensions. Unfortunately, it is now reasonably well established that particle size is not a significant factor, nor is the thermal conductivity of the material of which the particles are comprised, provided it is significantly larger than that of the suspending liquid [8.14]. These findings are problematic, because the Maxwell theory predicts that adding spherical particles of infinite thermal conductivity to a liquid scarcely increases its thermal conductivity. The reason is simple: the spherical shape efficiently excludes the thermal gradient. In fact, the *apparent* thermal conductivity of such a particle is just four times the thermal conductivity of the liquid phase, so adding 10 vol% particles to a liquid increases its effective thermal conductivity by only 30%. If the particles are formed into chains along the thermal gradient the total effective thermal conductivity increase is 80% [8.17], so applying a magnetic field to magnetic spheres would give only a ~38% control range.

In this study we demonstrate that a suspension of magnetic platelets can be manipulated by a variety of static and dynamic fields to give a *substantially* larger range of effective thermal conductivity control, as much as nearly 10[redacted]000%. This increased range is due to the particle geometry, which contributes in two distinct ways. First, when a platelet is oriented such that its polar axis is normal to the thermal gradient, transport within the particle is greatly enhanced because of the much higher thermal gradient within the particle, compared to that within a spherical particle of the same volume. Because the thermal conductivity and magnetic permeability are isomorphic properties [8.18] (in the absence of Kapitza resistance), this increased transport can be quantified in terms of the

demagnetization factor of the particle, which is a known function of particle geometry *alone* for generalized ellipsoids [8.19]. This demagnetizing field effect also causes the particles to align and agglomerate in such a way as to maximize thermal transport. In Chapters 1 and 2 [also Refs. 8.20,8.21] we have shown that composites containing these field-driven, static particle assemblies can be effective in either enhancing or suppressing thermal transport, depending on their orientation.

Platelet geometry can also enable enhanced thermal transport by creating emergent flows when the suspension is driven by ac biaxial [8.11] or triaxial magnetic fields [8.12], as was demonstrated in Chapters 5 and 7. In this case the platelet geometry enables the dynamic field to persistently inject energy into the fluid by applying a torque to the particles. This coupling leads to spontaneous flow symmetry breaking and the formation of either flow lattices (see Chapters 5–7) [8.11] or fluid vorticity (see Chapters 3, 4 and 7) [8.12,8.22–8.24], depending on the nature of the multiaxial field. In this chapter, fluid vorticity is created by applying a dc field orthogonal to the plane of an ac biaxial field comprised of two orthogonal components having a 2:1 frequency ratio. The dc field creates parity in the field trajectory, which enables the development of deterministic fluid vorticity. This fluid vorticity causes highly effective thermal transport at uniform induction field amplitudes as low as 0.0075 T, and requires neither a thermal gradient nor gravity. In all cases the volume fraction of particles is less than 4%, so the heat capacity of the fluid remains essentially unaffected.

Finally, the manipulation of particles with fields mitigates the need for stable particle suspensions, since the magnetic fields can quickly disperse sedimented particles throughout the fluid volume. It also enables rapid thermal switching for feedback control of the device temperature. Generating these fields is quite simple because they are spatially uniform and sufficiently weak to be produced by open-air Helmholtz coils. Series resonant coils can be driven by low voltage power supplies, dissipate very little power, are easily scalable to any fluid volume, and contain no moving parts.

In the following we describe the method of calibrating our heat transfer cell and then present thermal transport data from resistance thermometry measurements for a variety of field strategies.

8.2 Experimental

8.2.1 Materials

Fluorinert™ FC-40 was used as the suspending liquid for most of the heat transfer measurements because it is extremely chemically inert and is a non-solvent for the polyimide laminates surrounding the resistance heater. As a result, no measurable resistance drift occurred when using this liquid. Magnetic platelets were added to this liquid at volumetric loadings in the range of 2–4%. Two types of platelets were studied: (1) a multilayered composition supplied by JDSU Flex Products Group comprising a 50 nm Ni core sandwiched between 92 nm-thick MgF_2 layers; and (2) a pure Ni Fine Leafing Grade (500 nm thick) supplied by Novamet, both of which are ~20 μm across and are shown in **Figure 8-1**.

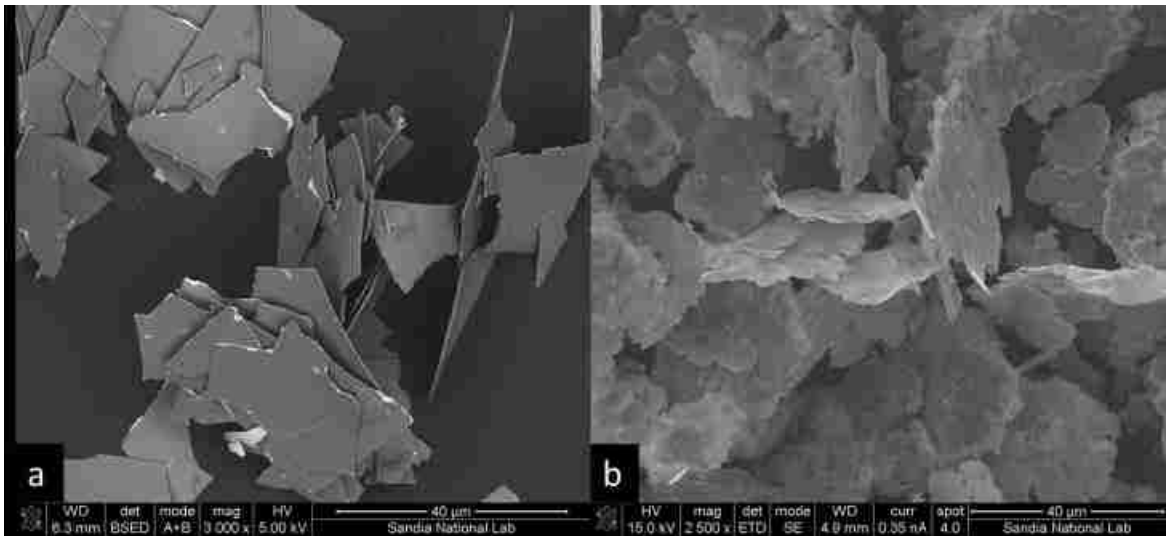

Figure 8-1. SEM images of the Ni platelets. **(a)** The multilayer flakes from JDSU, and **(b)** the Novamet Fine Leafing Grade pure Ni flakes.

8.2.2 Thermal transport cell

A steady-state thermal transport cell was constructed to fit inside the central cavity of our Helmholtz coils [**Figure 8-2(a)**]. To prevent heating the cell from eddy currents induced by the ac magnetic fields, the cell is constructed of dielectric materials such as nylon, Teflon™, and Lexan™. The schematic in **Figure 8-2(b)** identifies the main components of the cell. The cell is a symmetrical design consisting of a central, 2.54 cm^2 thin-film polyimide heater (Thermofoil™ from Minco) that bisects the fluid cavity, ensuring that heat flux is largely directed through the fluid. At either end of the cell are cooling blocks through which water is circulated. These cooling blocks are separated from the heat transport fluid by 0.67 mm thick silicon wafers. Silicon has a relatively high thermal conductivity ($k_{Si} = 149\ W \cdot m^{-1} \cdot K^{-1}$), so the thin wafers have negligible thermal resistance. The vertical orientation of the heater and parallel silicon cooling plates establishes a thermal gradient *perpendicular* to the direction of gravity, to minimize the likelihood of buoyancy-driven convection. Finally, a Lexan™ lid was fitted to the top of the cell to reduce evaporation and drafts.

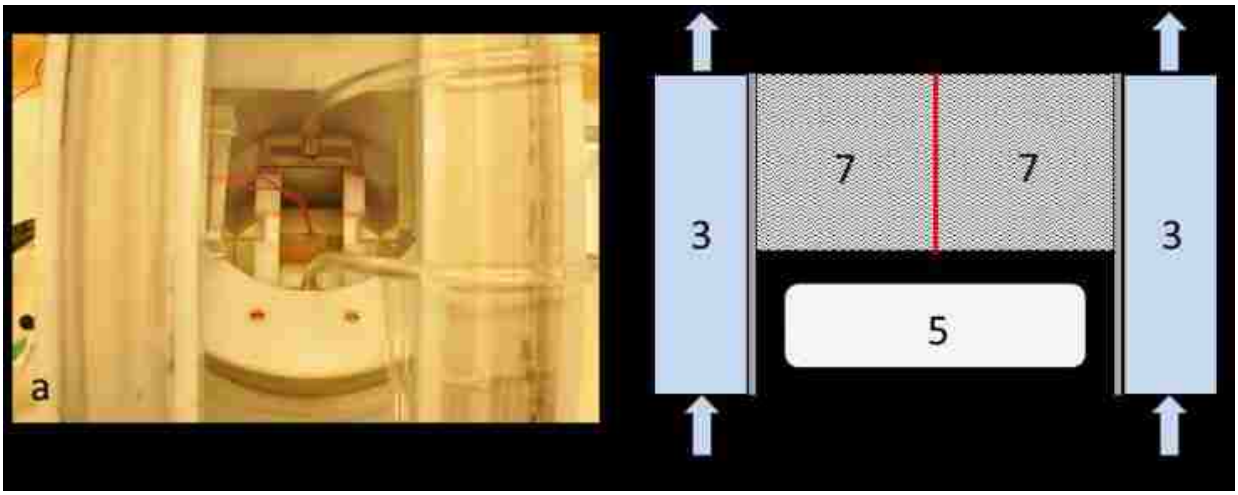

Figure 8-2. **(a)** An oblique downward view of the cell within the central cavity of two nested, orthogonal Helmholtz coils. The red wire leads can be seen extending from the heater, which bisects the fluid cavity (empty in the picture). Transparent cooling water lines are seen extending up from the cooling water blocks. **(b)** Side view, cross-section schematic of the flow cell. (1) Cooling water inlet, (2) cooling water exit, (3) cooling blocks, (4) silicon partition, (5) foam-filled cavity within the nylon body, (6) thin-film polyimide heater, (7) heat transfer fluid reservoir.

8.2.3 Resistance thermometry measurements

The equivalent thermal conductivity $k_{equiv.}$ of the magnetic platelet suspensions was determined using resistance thermometry to measure changes in the steady-state temperature of the heater under various field conditions, and thus fluid conditions. The heater thus served as both the heat source and temperature sensor. The heater thermoresistance was calibrated using a highly accurate Agilent 4284A Precision LCR bridge and the temperature coefficient of resistance was found to be $\alpha \approx 1.26 \times 10^{-4}\,\mathrm{K}^{-1}$, where

$$\alpha = \frac{1}{R_{e0}} \frac{dR_e}{dT}. \tag{8-1}$$

The reference resistance at 0 °C is $R_{e0} = 160.597\ \Omega$ and $\mathrm{d}R_e/\mathrm{d}T = 20\ \mathrm{m\Omega \cdot °C^{-1}}$. This thermoresistance is sufficient to give a measurement resolution of 0.05 °C using the Agilent bridge. Although the heater foil element is ferromagnetic (the heater is attracted to a strong NdFeB permanent magnet), measurements indicate that the heater resistance is not measurably affected by the relatively weak, uniform magnetic fields used to control the fluid. The LCR bridge was run at 182.6 Hz, a frequency chosen to be incommensurate with the magnetic field frequencies, in order to avoid interference. Because this bridge has a maximum voltage output it is used both to drive the heater and measure its resistance. The bridge is used in constant applied voltage mode, but because of the low temperature coefficient of resistance the change in the dissipated power is negligible: even a 40 °C temperature rise increases the heater resistance (and thus decreases the dissipated power) by only 0.5%.

To obtain reliable fluid thermal conductivities for our platelet suspensions requires that the heat transfer cell be calibrated with a liquid of known thermal conductivity in order to determine its stray thermal resistance, $R_{th,cell}$. The presence of such a parallel thermal path results in *measured* temperature differences smaller than if all of the heat was transferred through the fluid. Accordingly, the following expression was developed to correct the measured temperature changes by accounting for this stray thermal resistance,

$$\Delta T_{corr} = \Delta T_{meas}\left[1 - \frac{\Delta T_{meas}}{P_d R_{th,cell}}\right]^{-1}, \qquad (8\text{-}2)$$

where ΔT_{corr} is the corrected temperature difference, ΔT_{meas} is the measured temperature difference, and P_d is the power dissipated by the heater. The corrected temperature rises are those that would occur if the polymers comprising the cell were perfectly insulating. This issue of computing the cell thermal resistance cannot be neglected, especially in light of the fact that the thermal conductivity of FC-40 is only 0.065 $W \cdot m^{-1} \cdot K^{-1}$ and a typical value for the polymers of which the cell is comprised is ~0.25 $W \cdot m^{-1} \cdot K^{-1}$.

In principle, to determine $R_{th,cell}$ one would simply measure the temperature rise using pure FC-40 at a given heater power output, and compute the cell thermal resistance from Equation 8-2 knowing what the *expected* temperature rise (ΔT_{corr}) would be for pure conduction through FC-40. Unfortunately, this approach is complicated by the occurrence of convection in the pure FC-40 liquid. Although we designed the cell to minimize the likelihood of convection due to buoyancy effects, a free top fluid surface remains allowing for thermocapillary convection (aka Bénard–Marangoni convection) to occur. To prevent this surface-tension-driven convection we loaded the FC-40 with 4 vol% of the JDSU multilayer platelets and applied a 300 Hz uniaxial field to structure the platelets into vertical chains orthogonal to the thermal gradient. Although these chains prevent fluid motion, extensive experiments on particle composites show that transverse particle chains do not significantly affect the effective thermal conductivity of the continuous phase. Using the thermal conductivity of quiescent FC-40 gives a stray cell thermal resistance of 160 °C·W^{-1}.

To confirm this value of the stray thermal resistance we next loaded the cell with pure glycerin, chosen because its high viscosity (934 cP at 25 °C) reduces the possibility of convection. Steady-state temperature rise measurements were made at heater powers that were 25%, 50%, 75% and 100% of the maximum heater power of 623.6 mW. For each of these powers the thermal conductivity of glycerin was computed from Equation 8-2 using

our measured stray cell resistance, and a slight increasing dependence of the measured conductivity with heater power was noted, probably due to some slight convection. Extrapolating these conductivities to zero heater power gave a quiescent fluid conductivity of 0.292 $W \cdot m^{-1} \cdot K^{-1}$, which is the known thermal conductivity of glycerin [8.25]. Because of this excellent agreement one could take the point of view that the stray thermal resistance of our cell was determined by running glycerin.

Our measured temperature rises were corrected using $R_{th,cell} = 160\,°C \cdot W^{-1}$ in Equation 8-2. This correction is only really correct for steady-state rises, but we corrected all of our data in this way, just to have continuous temperature rises to plot, as in **Figure 8-3**. It is important to note that only the steady-state data were used to compute conductivities.

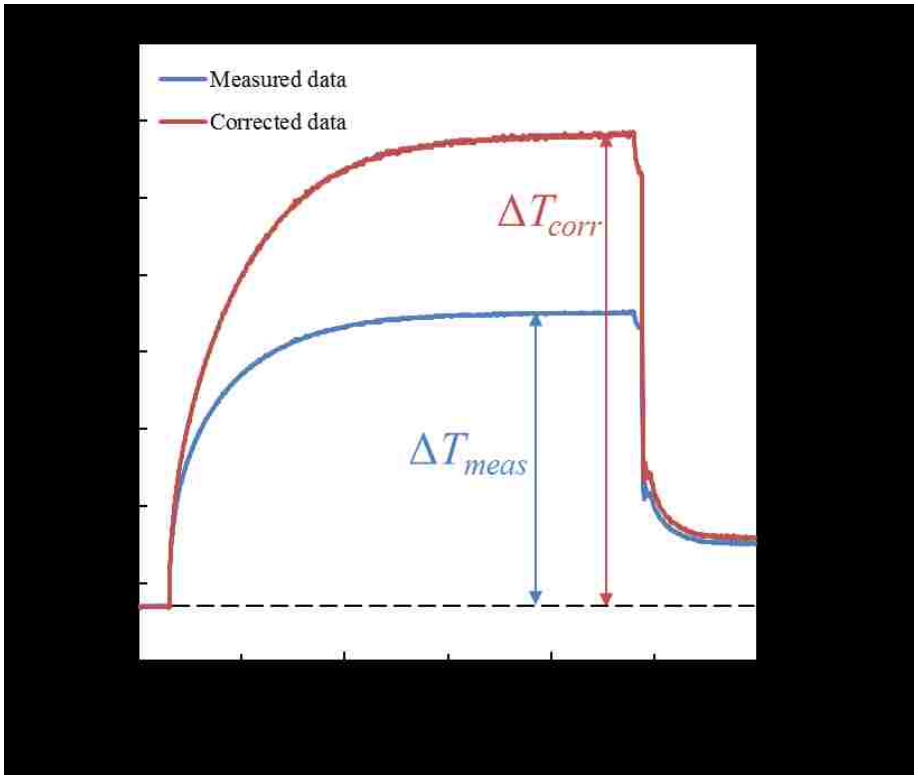

Figure 8-3. Plot showing the result of correcting for the stray cell thermal resistance. The blue curve is the measured data and the red curve is the corrected data. (The correction formula was developed for the temperature differences at steady state, but the temperature rise data are not used to determine conductivities.) The corrected heater temperature rise ΔT_1 is for a quiescent suspension, whereas ΔT_2 is for the same fluid driven by a triaxial magnetic field.

Temperature rise experiments were performed for a variety of magnetic field strategies to investigate the dependence of heat transfer on the structure and dynamics of the platelet suspensions. For each experiment an initial baseline was established by applying only 100 mV across the heater to acquire a stable signal while minimizing heating. (The dissipated power at this level is only 0.06 mW.) The applied heater voltage was then increased to 10 V to increase the dissipation by four orders of magnitude ($P_d = 623.6$ mW) to obtain a measureable temperature rise for the fluid. After steady state was achieved any of a number of magnetic fields was applied to alter thermal transport to a new steady-state value by creating either static platelet structures or dynamic flows. The data were then corrected for the stray cell thermal resistance and the equivalent suspension thermal conductivities were computed from the corrected data using Fourier's law of heat conduction. When the magnetic field is used to create advection the equivalent thermal conductivities are geometry dependent because the transport is ballistic, not diffusive. These values thus apply to our particular cell, with its 1 cm path lengths, but they nonetheless illustrate the relative differences in heat transfer for various driving fields. Increasing the path lengths would yield even higher equivalent thermal conductivities for the driven fluids.

8.3 Results and Discussion

8.3.1 Static structures

The first series of heat transfer experiments focused on creating static structures within the fluid to modify the thermal transport. By using appropriate uniaxial or biaxial magnetic fields, we created either chain-like or sheet-like particle assemblies, respectively [8.3]. In either case these structures can be aligned parallel or perpendicular to the thermal gradient. Experiments on composite materials have shown strong thermal conductivity anisotropy in field-structured nickel platelet composites (see Chapters 1 and 2) [8.20, 8.21], so the orientation of the structuring field relative to the thermal gradient is expected to be an important factor in these suspensions as well.

When 4 vol% platelets are formed into chains perpendicular to the thermal gradient it is expected that the thermal conductivity enhancement is very low and measurements bear this out. The solid Ni platelets have a thermal conductivity of $k_{eff,Nova} = 0.082\ \mathrm{W \cdot m^{-1} \cdot K^{-1}}$, which is 26% greater than that of the multilayered platelets, which we have shown above has essentially the conductivity of pure FC-40 ($0.065\ \mathrm{W \cdot m^{-1} \cdot K^{-1}}$).

In contrast, when the static chains are oriented parallel to the thermal gradient the effective thermal conductivity is greatly enhanced for both types of platelets. The multilayered platelets give $k_{eff,JDSU} = 0.23\ \mathrm{W \cdot m^{-1} \cdot K^{-1}}$, which is a 250% increase over the base fluid, and the pure Ni platelets give $k_{eff,Nova} = 0.68\ \mathrm{W \cdot m^{-1} \cdot K^{-1}}$, which is a 950% increase. The respective thermal conductivity anisotropies are ~3.5 and ~8.3, so these structures effectively direct heat transfer.

The platelets can be organized into layered structures (a bit like mica) by applying an appropriate ac biaxial field. A layered structure should suppress heat transfer if the sheets are created normal to the thermal gradient and should enhance heat transfer if the thermal gradient is in the plane of the sheets. This layered structure was created by applying a biaxial field comprised of 600 Hz and 300 Hz orthogonal components having rms component amplitudes of 0.015 T to a suspension of 4 vol% platelets. Such high frequencies are needed to prevent the formation of an advection lattice or other fluid motion. Layered structures can also be produced by applying high-frequency rotating fields, but an octave field does not produce a net body torque.

A layered structure of the pure Ni Novamet platelets strongly suppressed thermal transport when the layers were created normal to the thermal gradient. In fact, the conductivity dropped to $0.016\ \mathrm{W \cdot m^{-1} \cdot K^{-1}}$, which is 4× smaller than that of the FC-40 base fluid. Because even a series model of heat conduction (which should be very good for this composite geometry) would predict that the platelets should increase the effective conductivity, we surmise that such a highly-insulating state is due to impedance mismatch at

the platelet–liquid interfaces (*i.e.*, Kapitza resistance). This issue will be an area of future investigation.

Alternatively, if the sheets are created so they extend parallel to the thermal gradient, heat conduction through the fluid is enhanced ($k_{eff,Nova} = 0.23$ W·m^{-1}·K^{-1}), albeit not nearly as much as with the pure Ni parallel chains. Still, these measurements indicate a 14.4× anisotropy in heat conduction in these layered structures, so they could act as effective heat spreaders. In previous work on field-structured composites of spherical particles we have also noted lower in-plane enhancements for layered structures as opposed to chains [8.3, 8.17]. Sheet structures formed of the JDSU multilayer flakes were not studied. Before moving to field-induced flow, we point out that these static structures have thermal conductivities ranging from 0.016 to 0.68 W·m^{-1}·K^{-1}, which is a 42.5× control range.

8.3.2 Field-stimulated flows

In our next series of experiments we investigated heat transfer using magnetically-stimulated flows. Because the heat transfer is ballistic in this case, a comparison with heat conduction due to diffusion is problematic because the comparison will be dependent on the fluid gap in the cell. For diffusive transport the heater temperature rise will increase linearly with the gap, whereas for *perfect* ballistic transport the temperature rise will be independent of the gap. Because our flow cell has a fixed gap we cannot explore this issue and will simply quantify the heater temperature rise as an *equivalent* thermal conductivity $k_{\text{equiv.}}$ for our 1 cm gap cell. These equivalent thermal conductivities are not an intensive property of the driven suspension and would be expected to nearly double for a 2 cm gap cell, and so forth.

Before describing the results of these heat transfer experiments it is helpful to describe our method of generating these flows. These flows were created by subjecting 4 vol% platelet suspensions to ac-ac-dc triaxial fields of the form

$$\mathbf{H}(t) = H_{rms}\sqrt{2}[\sin(\omega t)\hat{\mathbf{x}} + \sin(n\omega t + \varphi)\hat{\mathbf{y}}] + H_z\hat{\mathbf{z}}. \qquad (8\text{-}3)$$

Here n is a small integer that is set to 2 in these experiments and ϕ is a phase angle. The use of this field strategy requires some explanation. If the ac biaxial field alone is applied (*i.e.*, $H_z = 0$) an advection lattice is formed. However, if a dc component is applied at an amplitude comparable to that of the rms biaxial field components, the advection lattice is obliterated and rotational flows of surprising vigor emerge (see Chapter 7). An interesting aspect of these rotational flows is that the orientation of the vorticity axis is dependent on the whether the field frequency ratio is even or odd. For a 2:1 field with a 0° phase angle the vorticity axis is parallel to the low frequency field component. In this case the fluid vorticity can be reversed by either changing the biaxial field phase angle by 180° *or* by reversing the direction of the dc field.

This fluid rotation is due to the dc field causing chiral symmetry breaking of the trajectory of the field vector and its opposite, a point that requires a little explanation. For a 2:1 field with a 0° phase angle the Lissajous plot of the field vector is a figure eight, with the zero field point at the center. The trajectory of the field vector is chiral and will circulate in the opposite sense if the phase is shifted by 180°. However, the magnetic interactions are due to *induced* magnetic moments and thus scale as the square of the applied field, so inverting the sign of the total applied field will have no effect. It is therefore the combined trajectory of the applied field and its opposite that is the critical issue: in other words, the trajectory of a line. A little thought will convince one that the trajectory of this "field line" is not chiral for the biaxial field in question, so there is no reason to expect *deterministic* rotational flow. However, if one also applies an orthogonal dc field the zero point of the field shifts outside the plane of the figure eight, as shown in **Figure 8-4**. The field line now bridges two separated figure eight curves and because it can now circulate in opposite senses it is chiral. Changing either the sign of the dc field or shifting the phase of the biaxial field causes a change in the parity of the trajectory and thus reverses the fluid vorticity. These basic parity considerations are a necessary condition for the development of deterministic rotational flow in such a field.

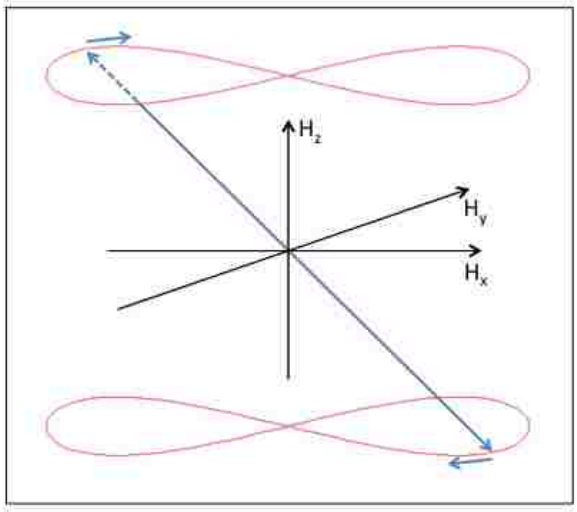

Figure 8-4. When a dc field is applied orthogonal to the plane of a 2:1 biaxial field the zero point of the field vector is shifted. Because induced dipole effects depend on the square of the field there are two equivalent field trajectories: one circulates on the upper figure eight and one on the lower. When two equivalent Lissajous plots are separated by a gap created by the dc field along the z axis it is apparent that the combined field vectors can circulate in two opposing directions, opening up the possibility of rotational flow. The parity of the trajectory can be changed by either changing the phase of the biaxial field by 180° or by changing the sign of the dc field. In fact, either of these reverse the fluid vorticity.

If the field frequency is 3:1, and the phase is 90°, strong rotational flow also occurs when a dc field is applied, but the axis of vorticity is the dc field. In this case changing the phase of the biaxial field by 180° also reverses the flow, but altering the direction of the dc field does not. These observations are also consistent with parity considerations for the simultaneous trajectory of the field line. The 3:1 field line trajectory is chiral even for the biaxial field itself, which is why a small deterministic body torque can be observed in this case. An orthogonal dc field component of either sign does not alter the parity of this trajectory, but changing the phase of the biaxial field by 180° does.

To maximize heat transfer the rotational flows were induced so fluid flow occurs along the thermal gradient. The vorticity axis was arbitrarily chosen to be horizontal as well. This 'artificial convection' should provide significantly better heat transfer than the static structures described above, whose heat transfer mode was limited to conduction.

Initial experiments were performed with a biaxial field comprised of 100 Hz and 50 Hz components having 0.015 T rms induction field amplitudes and a 0° phase angle. The dc induction field amplitude was also 0.015 T. This field resulted in values of $k_{equiv.}$ for the JDSU multilayer platelet suspensions of 1.26 $W \cdot m^{-1} \cdot K^{-1}$, and for the pure Ni Novamet platelets 1.61 $W \cdot m^{-1} \cdot K^{-1}$, which are respectively about 19× and 25× greater than that of the FC-40 base fluid. It should be emphasized that because the flow is ballistic, these conductivity values should scale as the fluid gap, providing diffusive transport makes a negligible contribution. Increasing the frequency of the biaxial field by a factor of 3 (to 300:150 Hz) produced a modest decrease in heat transfer for the multilayer flakes ($k_{equiv.,JDSU} = 0.94$ $W \cdot m^{-1} \cdot K^{-1}$), indicating that the heat transfer efficacy is not highly sensitive to field frequency, provided the frequency remains below that at which static structures form.

Biaxial fields with a 3:1 frequency ratio can also be used in ac-ac-dc triaxial fields to stimulate rotational flows (see Chapter 7) [8.12]. For these flows the axis of fluid vorticity is rotated 90° with respect to those produced using 2:1 fields, so the flow cell was rotated by 90° to maintain the flow direction parallel to the thermal gradient. As **Figure 8-5** shows, a value of $k_{equiv.} = 0.71$ $W \cdot m^{-1} \cdot K^{-1}$ was obtained using the Novamet Ni flakes subjected to such a field (150:50 Hz, 90° phase, 0.015 T rms ac components; and a 0.015 T dc component), which is over a factor of 2 lower than for the octave biaxial field case (1.61 $W \cdot m^{-1} \cdot K^{-1}$). This difference is due to the relatively slow fluid flow with this field configuration.

Field strength is obviously an important factor as it controls the flow rate and thus the efficiency of heat transfer. We progressively reduced the 100:50 Hz and dc field components from 0.015 T to 0.005 T and found that the heater temperature did not appreciably rise until the fields were reduced to 0.005 T (**Figure 8-6**). These results demonstrate that efficient heat transfer can be achieved using very modest fields

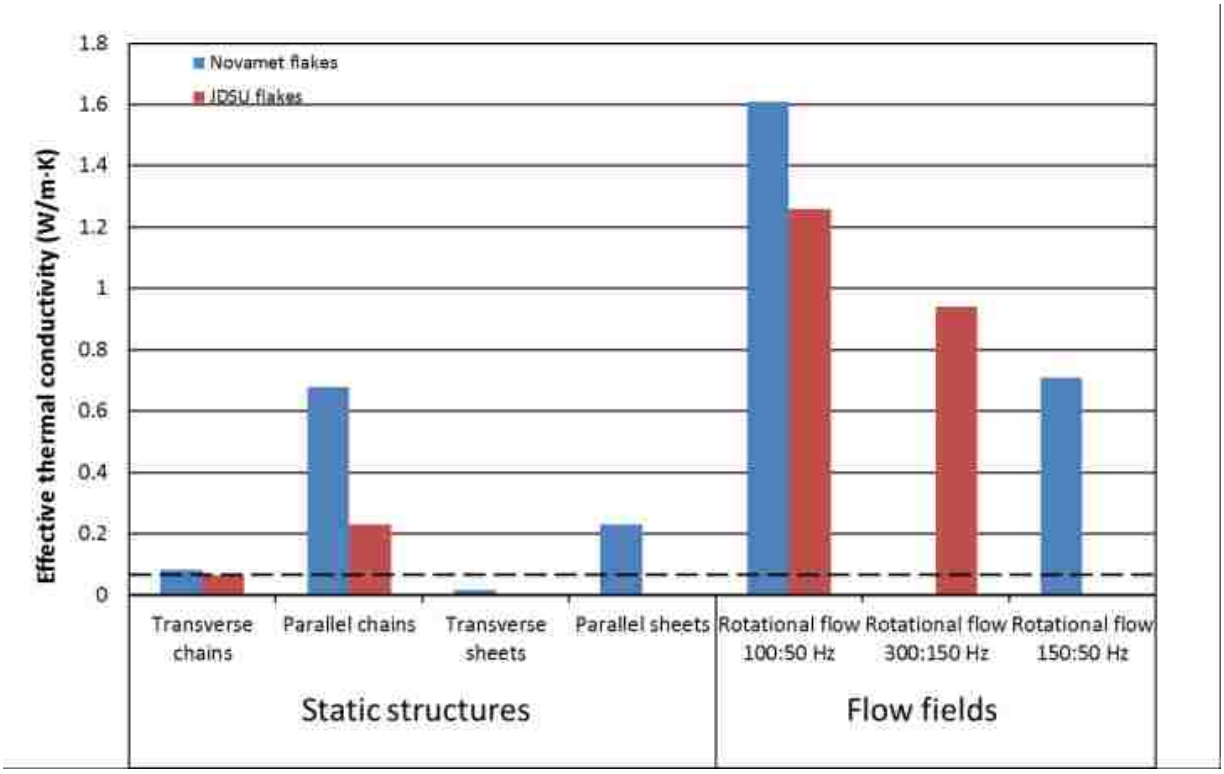

Figure 8-5. Effective and equivalent thermal conductivities for static structures and dynamic flows in FC-40. The dashed line indicates $k_{FC\text{-}40}$ = 0.065 W m^{-1} K^{-1}.

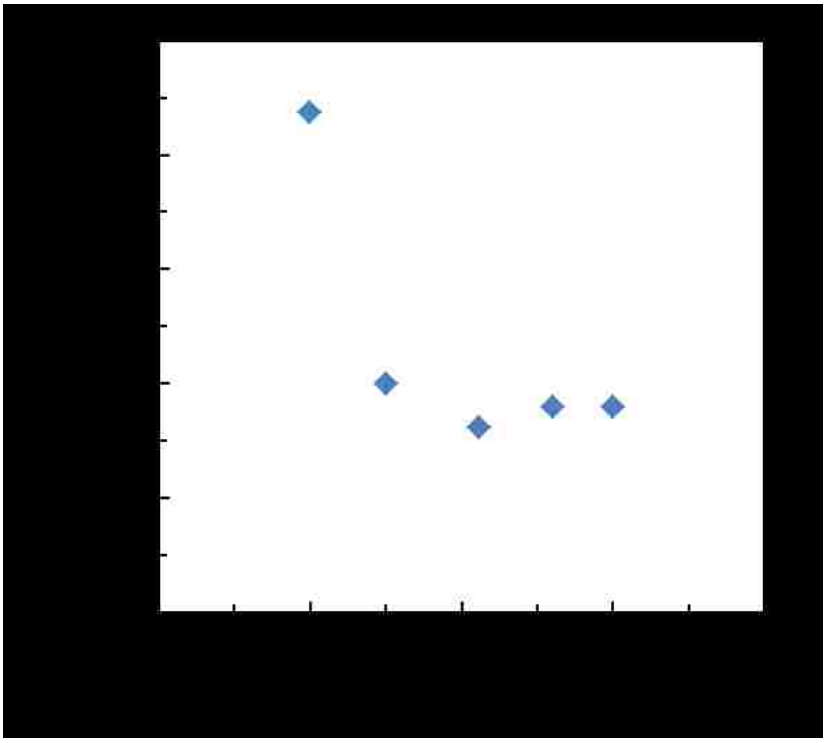

Figure 8-6. Plot of the corrected temperature differences vs. the component induction field amplitude demonstrating that efficient heat transfer occurs for fields as low as 0.0075 T.

(~0.0075 T) to stimulate the flows. This field is one quarter the energy density of the 0.015 T field and requires one quarter of the dissipated power to generate.

Using FC-40 as a base fluid we have at this point demonstrated effective and equivalent thermal conductivities for our 1 cm cell that are as low as 0.016 $W \cdot m^{-1} \cdot K^{-1}$ and as high as 1.61 $W \cdot m^{-1} \cdot K^{-1}$, which is a control range of 100. However, these thermal conductivities can be significantly increased by using water as the suspending liquid since water itself has a thermal conductivity of ~0.60 $W \cdot m^{-1} \cdot K^{-1}$, which is about 1 decade larger than that of FC-40. Water swells the polymer used to encapsulate the resistance heater, which leads to drift in the resistance measurements, but this linear drift can be accounted for very accurately for short experiments.

Water-based suspensions were created using *Fine Water Grade* Novamet Ni flakes, which have the same dimensions and morphology as the *Fine Leafing Grade* used earlier but are more easily dispersed in water, especially with the aid of the surfactant Triton X-100™. Using a 4 vol% suspension, and the same field strategy initially used for FC-40, a value of $k_{equiv.} = 9.21$ $W \cdot m^{-1} \cdot K^{-1}$ was obtained, which is 5.7× larger than the highest value obtained with the FC-40-based suspension. During the experiments, we observed that the initial startup of the rotational flows appeared more vigorous than once they became fully-developed, and so it became clear that a lower volume fraction might result in faster flow rates, and thus better heat transfer. Accordingly, we prepared and tested a 2 vol% suspension and the measured heat transfer increased by a factor of 2 for a value of $k_{equiv} = 18.33$ $W \cdot m^{-1} \cdot K^{-1}$, which is a 30× enhancement over quiescent water and 11.4× larger than the best result using FC-40. This equivalent thermal conductivity is very similar to the thermal conductivity of the metal antimony at this fluid gap. To put this in perspective, the uncorrected heater temperature rise was only 0.3 °C in this case (with the heater power at 623.6 mW), whereas it reached 58 °C for perpendicular sheets in FC-40.

Future work will focus on characterizing the heat transfer capabilities of the many possible isothermal magnetic advection flow patterns, investigating the contribution of the

interfacial thermal resistance regarding heat transfer in these adaptive fluids, and possibly studying the relationship between the mixing torque generated by the rotational flows and their heat transfer efficacy. It may also prove interesting to study the suspension dynamics using smaller platelets so this technique could be developed for use in microfluidic applications.

8.4 Conclusions

Using resistance thermometry in a symmetrical flow cell we have demonstrated the ability to use uniaxial and multiaxial magnetic fields to change the equivalent thermal conductivity of a magnetic platelet suspension over an appreciable range. These fields can be used to create a variety of static particle structures or can be used to create rotational flow. Creating static sheets of platelets perpendicular to the thermal gradient decreased heat conduction by a factor of 4, relative to the base fluid FC-40; whereas, creating chains of platelets parallel to the gradient increased heat conduction by a factor of 10.5. Using an ac-ac-dc triaxial field to drive emergent particle dynamics that creates vigorous rotational flow increased heat conduction by a factor of 25. Heat conduction of a single suspension in a 1 cm cell can thus be varied over a 100-fold range. With an aqueous suspension of only 2.0 vol% platelets an equivalent thermal conductivity as high as 18.3 $W \cdot m^{-1} \cdot K^{-1}$ has been achieved, which is more than twice the conductivity of liquid mercury and is comparable to the metal antimony.

Acknowledgements

Sandia National Laboratories is a multi-program laboratory managed and operated by Sandia Corporation, a wholly owned subsidiary of Lockheed Martin Corporation, for the U.S. Department of Energy's National Nuclear Security Administration under contract DE-AC04-94AL85000. This work was supported by the Division of Materials Science, Office of Basic Energy Sciences, U.S. Department of Energy (DOE). We thank Vladimir Raksha, Paul

Coombs, Tom Markantes, Bill Kittler, and Kees-Jan Delst at JDSU and Matt Groo at Novamet for supplying the magnetic platelets.

References

8.1 J.E. Martin, R.C. Hughes and R.A. Anderson, Sensor devices comprising field structured composites, US Pat. #6,194,769 B1, February 27, 2001.

8.2 J.E. Martin, R.C. Hughes and R.A. Anderson, Field-structured material media and methods for synthesis thereof, US Pat. #6,290,868, September 18, 2001.

8.3 J.E. Martin, E. Venturini, J. Odinek and R.A. Anderson, Anisotropic magnetism in field-structured composites, *Phys. Rev. E: Stat. Phys., Plasmas, Fluids, Relat. Interdiscip. Top.* **61**, 2818–2830 (2000).

8.4 J.E. Martin, R.A. Anderson, and R.L. Williamson, Method of using triaxial magnetic fields for making particle structures, US Pat. #6.844, 378, January 18, 2005.

8.5 J.E. Martin, R.A. Anderson and R.L. Williamson, Generating strange interactions in particle suspensions: Classical molecules and particle foams, *J. Chem. Phys.* **118**, 1557–1570 (2003).

8.6 J.E. Martin, E. Venturini, G.L. Gulley and J. Williamson, Using triaxial magnetic fields to create high susceptibility particle composites, *Phys. Rev. E: Stat., Nonlinear, Soft Matter Phys.* **69**, 021508 1–15 (2004).

8.7 J.E. Martin and R.A. Anderson, Electrostriction in Field-Structured Composites: Basis for an artificial muscle?, *J. Chem. Phys.* **111**, 4273–4280 (1999).

8.8 J.E. Martin, R.A. Anderson, D. Read, and G.L. Gulley, Magnetostriction of field-structured magnetoelastomers, *Phys. Rev. E: Stat., Nonlinear, Soft Matter Phys.* **74**, 051507 1–17 (2006).

8.9 J.E. Martin, R.A. Anderson, J. Odinek, D. Adolf and J. Williamson, Controlling percolation in field-structured particle composites: Observations of giant thermoresistance, piezoresistance and chemiresistance, *Phys. Rev. B: Condens. Matter Mater. Phys.* **67**, 94207 1–11 (2003).

8.10 D.H. Read and J.E. Martin, Field-Structured Chemiresistors, *Adv. Funct. Mater.* **20**(10), 1577–1584 (2010).

8.11 K.J. Solis and J.E. Martin, Isothermal Magnetic Advection: Creating functional fluid flows for heat and mass transfer, *Appl. Phys. Lett.* **97**, 034101 1–3 (2010).

8.12 K.J. Solis and J.E. Martin, Stimulation of vigorous rotational flows and novel flow patterns using triaxial magnetic fields, *Soft Matter* **8**, 11989–11994 (2012).

8.13 K.J. Solis and J.E. Martin, Controlling the lattice spacing in isothermal magnetic advection to enable tunable heat and mass transfer, *J. Appl. Phys.* **112**, 094912 1–7 (2012).

8.14 Results from the recent International Nanofluid Property Benchmark Exercise [8.15], which involved 34 research groups from around the world who measured the thermal conductivities of a variety of identical, standardized nanofluid samples, led to the conclusions that "classic effective medium theory for well-dispersed particles accurately reproduced the INPBE experimental data; thus, suggesting that no anomalous enhancement of thermal conductivity was observed in the limited set of nanofluids tested in this exercise" and that "the thermal conductivity enhancement afforded by the tested nanofluids increased with increasing particle loading, particle aspect ratio and decreasing basefluid thermal conductivity." Although some of the characteristics regarding nanofluids remain controversial, the subject of nanofluids for enhanced heat transfer has proven to be a lively and rapidly growing area of research as evidenced by the exponentially increasing number of publications within the last decade [8.16].

8.15 J. Buongiorno, *et al.*, A benchmark study on the thermal conductivity of nanofluids, *J. Appl. Phys.* **106**, 094312 1–14 (2009).

8.16 Y. Jaluria, O. Manca, D. Poulikakos, K. Vafai, and L. Wang, Heat transfer in nanofluids 2012, *Adv. Mech. Eng.* 972973 1–2 (2012).

8.17 J.E. Martin and G.L. Gulley, Field-structured composites for efficient, directed heat transfer, *J. Appl. Phys.* **106**, 084301 1–7 (2009) [reprinted in *Virt. J. Nanoscale Sci. & Tech.* 20 19 (2009)].

8.18 G.K. Batchelor, Transport properties of two-phase materials with random structure, *Annu. Rev. Fluid Mech.* **6**, 227–255 (1974).

8.19 J.A. Osborn, Demagnetizing factors of the general ellipsoid, *Phys. Rev.* **67**, 351–357 (1945).

8.20 K.J. Solis and J.E. Martin, Field-structured magnetic platelets as a route to improved thermal interface materials, *J. Appl. Phys.* **111**, 073507 1–10 (2012).

8.21 J.E. Martin, K.J. Solis, D. Rademacher, and V. Raksha, Field-structured, multilayered platelets enable high-performance, dielectric thermal composites, *J. Appl. Phys.* **112**, 054306 1–10 (2012).

8.22 J.E. Martin, Theory of strong intrinsic mixing of particle suspensions in vortex magnetic fields, *Phys. Rev. E: Stat., Nonlinear, Soft Matter Phys.* **79**, 011503 1–12 (2009).

8.23 J.E. Martin, L.E. Shea-Rohwer, and K.J. Solis, Strong intrinsic mixing of particle suspensions in vortex magnetic fields, *Phys. Rev. E: Stat., Nonlinear, Soft Matter Phys.* **80**, 016312 1–6 (2009).

8.24 K.J. Solis, R.C. Bell, and J.E. Martin, Vortex magnetic field mixing with anisometric particles, *J. Appl. Phys.* **107**, 114911 1–4 (2010).

8.25 CRC Handbook of Chemistry and Physics, ed. D.R. Lide, (CRC Press, New York, 81st edn, 2000–2001).

Part IV
Dynamics of Vortex Fluids

Chapter 9

Symmetry-breaking magnetic fields create a vortex fluid that exhibits a negative viscosity, active wetting, and strong mixing[9]

There are many areas of science and technology where being able to generate vigorous, *noncontact* flow would be desirable. We have discovered that three dimensional, time-dependent electric or magnetic fields having key symmetries can be used to generate controlled fluid motion by the continuous injection of energy. Unlike natural convection, this approach does not require a thermal gradient as an energy source, nor does it require gravity, so space applications are feasible. The result is a highly active material we call a *vortex* fluid. The homogeneous torque density of this fluid enables it to climb walls, induce ballistic droplet motion, and mix vigorously, even in such complex geometries as porous media. This vortex fluid can also exhibit a *negative* viscosity, which can immeasurably extend the control range of the "smart fluids" used in electro- and magnetorheological devices and can thus significantly increase their performance. Because the applied fields are uniform and modest in strength, vortex fluids of any scale can be created, making applications of any size, from directing microdroplet motion to controlling damping in magnetorheological dampers that protect bridges and buildings from earthquakes, feasible.

9.1 Introduction

Creating controlled, organized fluid flow is a long-standing fluid dynamics problem that is relevant to many aspects of materials research and bioscience. In the vast majority of cases flow is induced using impellers, but such mechanical systems are subject to failure, require replacement items such as seals and bearings, are difficult to microfabricate, and create

[9] Originally published as: J.E. Martin and K.J. Solis, Symmetry-breaking magnetic fields create a vortex fluid that exhibits a negative viscosity, active wetting, and strong mixing, *Soft Matter* **10**, 3993–4002 (2014).

nonuniform flow. Having the ability to generate *noncontact* flow without using moving parts would eliminate these problems and could impact a range of technologies. For example, more efficient and reliable methods of fluid mixing are needed [9.1] in microfluidic [9.2–9.9] and microdroplet systems [9.10–9.22] because the small length scales mitigate against inducing turbulence. Increasing heat extraction in liquid-cooled electronic microsystems is critical to increasing power densities and performance. (In fact, liquid cooling systems have now become a complex and problematic aspect of massively parallel computers [9.23,9.24].) Noncontact methods of generating vorticity at key points in the cooling system could reduce the need for high overall flow rates, enabling more energy-efficient heat transfer. Having the ability to generate vorticity in a fluid subject to a shear strain rate can cause the observed shear stress to vanish, or even become negative, so that zero or negative viscosities result. This would result in "smart fluids" with an unprecedented control range for use in a wide range of clutches and dampers [9.25,9.26]. Finally, having the ability to induce mixing in microdroplets would further the development of massive containerless arrays for bioassays and reactions.

These challenges highlight the need for noncontact flow techniques that are scale adaptive and efficient. In the following we describe how an infinite family of spatially uniform, multiaxial magnetic or electric fields can create a vigorous *vortex fluid* from a dilute suspension of magnetic or dielectric particles. The defining aspect of this vortex fluid is the spatially uniform torque density that drives its motion, causing such odd effects as active wetting and wall climbing, **Figure 9-1(top)**. The direction of fluid flow can be altered by minor adjustments of the frequency or phase of one field component, so it is easy to direct the fluid along any particular path.

The effects described in this chapter are a development of the rapidly growing field of driven colloids, wherein time-dependent fields are used to drive colloidal suspensions into far-from-equilibrium states. The field-induced interactions can easily dominate thermal fluctuations, electrostatic, and van der Waal's interactions and can lead to static or

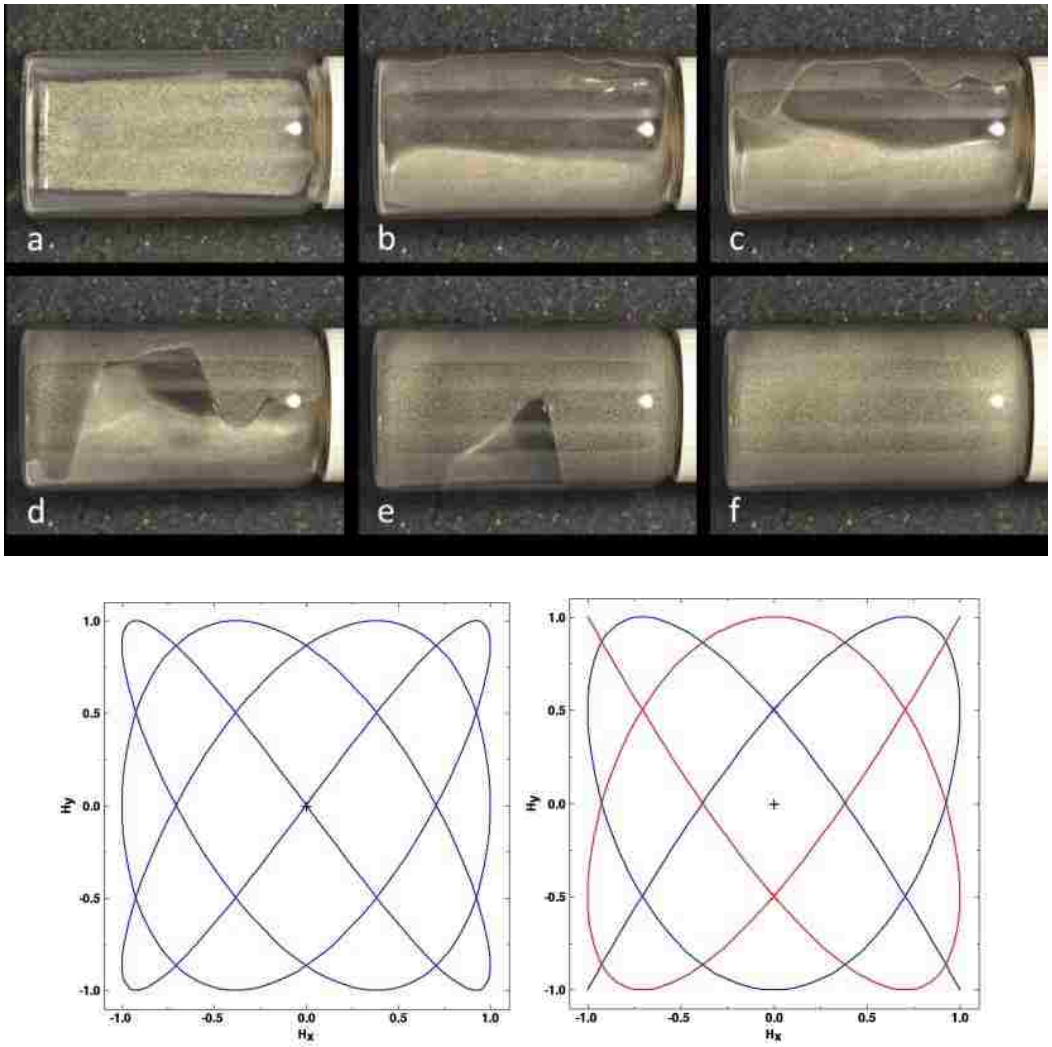

Figure 9-1. Active wetting of a vortex fluid and Lissajous plots for a 4:3 frequency ratio. **(Top)** When a symmetry-breaking multiaxial magnetic field is applied to a dilute magnetic Permalloy platelet suspension a fluid with a uniform torque density emerges. This fluid crawls up and over the walls of the container, thoroughly wetting the surface. Images a–f were taken at 0.25 s intervals. **(Bottom)** A closed curve **(left)** that has two reflection planes occurs at the phase angles $\phi = 0°, 60°, \ldots$ **(right)**. The two open curves have a single reflection plane. The blue curve occurs at phase angles $\phi = 30°, 150°, \ldots$ and the red curve occurs at phases of $\phi = 90°, 210°, \ldots$

dynamical assemblies with striking symmetries and behaviors [9.27–9.29]. Certain time-dependent driving fields have been shown to evolve dynamic assemblies sustained by the continuous injection of energy into the system, an example of "active materials" [9.30]. In bulk suspensions the creation of advection lattices and vortex lattices has been reported [9.31,9.32], which were discussed in Chapters 5 and 7, and for particles confined to liquid–liquid or air–liquid interfaces a number of surprising dynamic structures have been observed

[9.33,9.34], including "swimming snakes" [9.35,9.36] and "asters" [9.37]. These assemblies have been shown to have implications for fluid mixing at a surface [9.38–9.40] and for the controlled surface transport of material.

In Chapters 3 and 4 we demonstrated noncontact flow in suspensions of magnetic spheres, platelets and nanorods [9.41–9.43] subjected to a field with a precession-like motion. Because either clockwise or counter-clockwise field circulation is possible, a field of this type has the required parity to generate deterministic vorticity. Here we demonstrate that highly symmetric ac-ac-dc fields having *zero net circulation* can generate fluid vorticity, due to more subtle aspects of the field symmetry. There are an infinite variety of such fields, and small adjustments of the field frequencies can cause the axis of fluid vorticity to switch to any of three principal directions, enabling rapid and unprecedented control over fluid flow.

Our purpose in this chapter is to present a theoretical framework that predicts the orientation of the vorticity axis for these vortex fluids. A surprising aspect of this theory is that, unlike the physical theory developed to explain the mechanism underlying vortex field mixing [9.41], no such consideration of complex microscopic physical details is needed here. Instead, this theory is based *solely* on details concerning the symmetries of the applied symmetry-breaking rational fields, and as such highlights the novelty of this phenomenon. Although this study is largely theoretical in nature, select experimental results are presented to demonstrate the predictive capabilities of the theory. In fact, a detailed experimental study quantifying the torque densities produced by vortex fluids comprising a variety of particle shapes is the subject of Chapter 10.

9.2 Materials & Methods

Our experimental system consists of a series resonant triaxial Helmholtz coil [9.44] (**Figure 9-2**) that produces uniform magnetic fields over the fluid volume, which is typically about

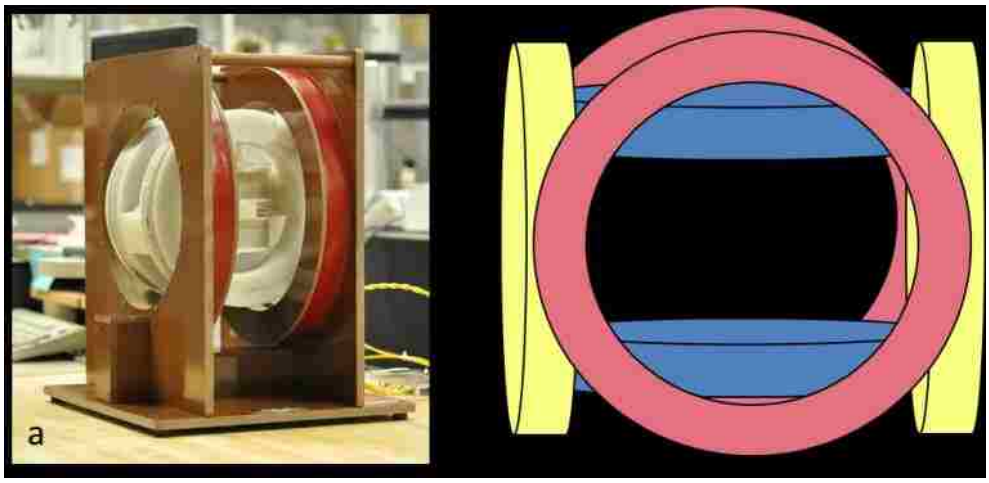

Figure 9-2. Triaxial Helmholtz coils. (**a**) Photograph of our experimental triaxial Helmholtz coil system. (**b**) Schematic illustrating one possible configuration for the relative orientations of the high-frequency (blue), low-frequency (yellow), and dc (red) coils.

10 mL. Field frequencies from 50–1000 Hz and field strengths as high as 500 Oe can be produced, but typical rms field strengths are 150 Oe for each component.

A variety of particle geometries were used in these experiments. The spherical particles were 4–7 micron carbonyl iron, obtained from ISP technologies, Inc. The Ni nanorods were 500 nm in diameter and 5 microns in length and were synthesized for us by R. Bell, Penn. State, Altoona. A variety of platelets were used, including solid Ni and Permalloy particles (fine leafing grade) from Novamet that are roughly 20 microns in size and ~1 micron thick. The Permalloy platelets were used to demonstrate that a remanent magnetic moment is not required to induce fluid vorticity. Multilayered magnetic platelets of various types were obtained from JDSU FlexProducts. These consisted of either a 60 nm thick Ni or Permalloy core that is coated with ~200 nm layers of Al, and overcoated with 200 nm MgF_2. These platelets are roughly 20 microns in size and some of these materials are actually square in shape, whereas some are irregular. These particles were usually dispersed in isopropanol, but other liquids, such as water, work equally well. The particle suspensions generally contained 1–3 vol% particles. The most vigorous vorticity was obtained with the anisometric particles, because this geometry increases field penetration.

To quantify the fluid vorticity we used a torsion fiber apparatus consisting of a 1.0 m nylon fiber that is 0.75 mm in diameter. Specific torque densities in the range of 500–1200 $J \cdot m^{-3}$ were computed from the total volume of particles and the angular displacement of the sample.

9.3 Rational Fields

The creation of the vortex fluid is accomplished through the application of *rational fields* that consist of three orthogonal components, two of which are alternating. This field is of the form

$$\mathbf{H}(t) = H_{ac}\left[\sin(2\pi m f_0 t)\hat{\mathbf{x}} + \sin\left(2\pi m f_0 t + 2\pi\frac{\phi}{360°}\right)\hat{\mathbf{y}}\right] + H_{dc}\hat{\mathbf{z}} \qquad (9\text{-}1)$$

where we have used the common experimental variables for waveform generators (frequency in Hz and phase in degrees). The dc field serves to break the symmetry of the biaxial ac field, as described below, which induces vorticity. Both n and m are integers, so the frequency ratio n:m is rational, and these fields can be classified as even:odd, odd:even, or odd:odd (even:even fields can be reduced to one of these cases). In all cases $n > m$, so $\hat{\mathbf{y}}$ is the high frequency axis. The frequency f_0 can be varied over a wide range, but nf_0 and mf_0 are less than 1 kHz in our experiments. The phase angle ϕ determines both the sign and strength of the vorticity. Finally, in this chapter **H** represents the applied magnetic field, but for experiments employing dielectric particles it would represent the applied electric field.

Lissajous plots of the biaxial ac field components are shown in **Figure 9-1(bottom)** for $m = 3$, $n = 4$ and phase angles of 0° and 30°. These phase angles were chosen because they give highly symmetric Lissajous plots of two types: *closed* and *open* curves. These types are central to understanding the experimental results described herein.

Before discussing the experiments it is helpful to point out that rational fields that induce deterministic fluid vorticity generally have zero net *circulation*. The circulation of the

field can be computed by considering the angular displacement of an acicular particle, such as a nanorod, comprised of an isotropic material that polarizes only in the presence of a field. The applied field is strong enough that the major axis of the particle is always aligned with the instantaneous field. The rational field will cause the particle to variously rotate clockwise and counter-clockwise around the *z* axis; however, in one full cycle of a rational field ($\Delta t = 1/f_0$) there may or may not be a net rotation. Because the orientation of the particle at the end of a cycle is indistinguishable from its orientation at the beginning of a cycle, any net rotation must be an integer multiple of 180°. If a net rotation does occur then fluid vorticity around the *z* axis could occur, even without the dc field, but without a net rotation fluid vorticity is not expected. Of course, any net circulation is only possible for closed-curve Lissajous fields.

To compute the field circulation we start with the angular velocity of the acicular particle, which is $\dot{\boldsymbol{\theta}} = \dot{\mathbf{h}} - (\dot{\mathbf{h}} \cdot \hat{\mathbf{h}})\hat{\mathbf{h}}$ where $\mathbf{h} = \mathbf{H}(t)/|\mathbf{H}(t)|$, $\hat{\mathbf{h}} = \mathbf{H}(t)/|\mathbf{H}(t)|$ and θ is the

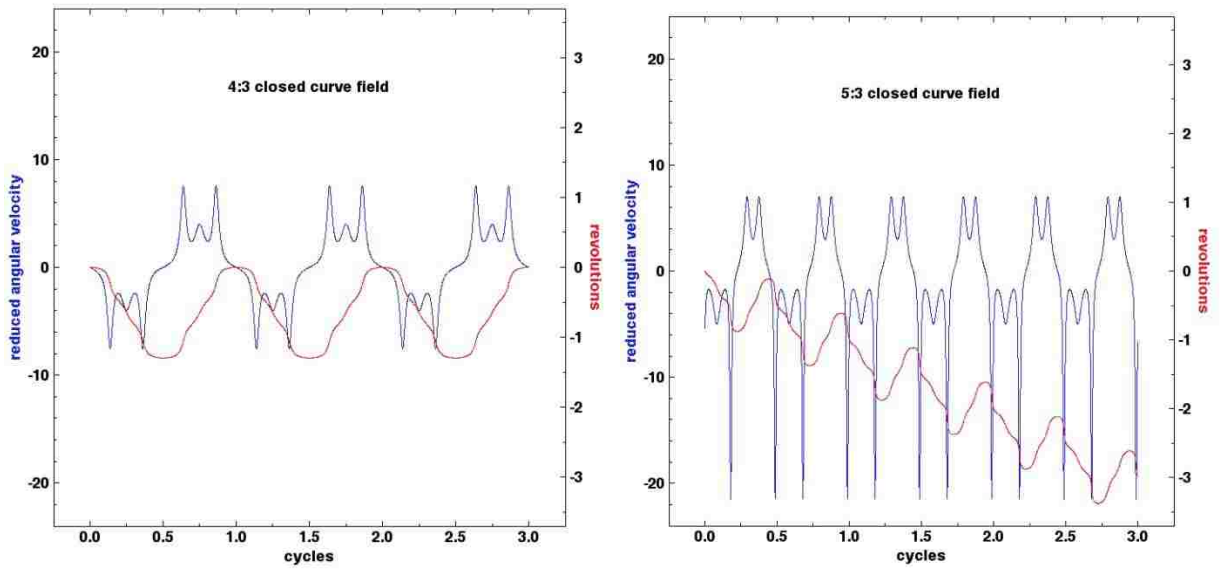

Figure 9-3. Angular displacement of a nanorod subjected to Lissajous fields. **(Left)** The reduced angular velocity θ/f_0 (in cycles) and change in orientation $\Delta\theta$ are given as functions of the reduced time f_0t for a 4:3 biaxial field. The clockwise rotations are exactly balanced by the counterclockwise rotations so that no net rotation occurs. In fact, all even, odd fields are noncirculating. **(right)** For odd:odd biaxial fields, in this case a 5:3 ratio, one net rotation occurs for each field cycle.

orientation of the particle in the *x*–*y* plane. A time integral of the angular frequency $\dot{\theta} = \left|\hat{\mathbf{h}} \times \dot{\hat{\boldsymbol{\theta}}}\right| \cdot \hat{\mathbf{z}}$ gives the change in particle orientation. **Figure 9-3(left)** shows that for a 4:3 field there is no net rotation. In fact, this is a general property of closed-curve rational fields having even:odd (or odd:even) ratios, so these fields can be classified as noncirculating. **Figure 9-3(right)** shows that for a closed-curve 5:3 field there is one full revolution for each field cycle, so the mean rotational frequency is just f_0. All closed-curve odd:odd fields have exactly this net rotation, so for these circulating fields vorticity around the *z* axis can be expected.

In the following our experimental results are described. A discussion of the symmetry of rational fields is then given and it is shown how these lead to the phenomena we observe. Principal among these is the observation that the frequency ratio *n*:*m* is the critical factor that determines whether the vorticity axis is parallel to the dc, low frequency, or high frequency field.

9.4 Results

In our initial experiments a Permalloy platelet suspension was subjected to an ac biaxial field of frequencies 150 and 100 Hz, corresponding to $n{:}m = 3{:}2$ and $f_0 = 50$ Hz. The rms field amplitude of each component was 150 Oe and the phase angle was initially zero. This field generated the flow pattern called *Isothermal Magnetic Advection* (see Chapter 5), consisting of a square lattice of antiparallel flow columns orthogonal to the field plane. Ramping up the dc field caused this lattice to transform into a vigorous vortex around the high frequency axis (H), **Figure 9-4(b)**, and reversing the dc field direction reversed the flow.

Increasing *n* to 4 ($n{:}m = 4{:}2 = 2{:}1$) and applying all three fields again created vorticity, but oddly enough this now occurred around the low frequency axis (L), though reversing the dc field still reversed the flow, **Figure 9-4(a)**. For $n = 5$ the results were the same as for $n = 3$, but $n = 6$ ($n{:}m = 6{:}2 = 3{:}1$) gave vorticity around the dc field (D), **Figure 9-4(c)**, and reversing the dc component *did not* reverse the flow. It is thus possible

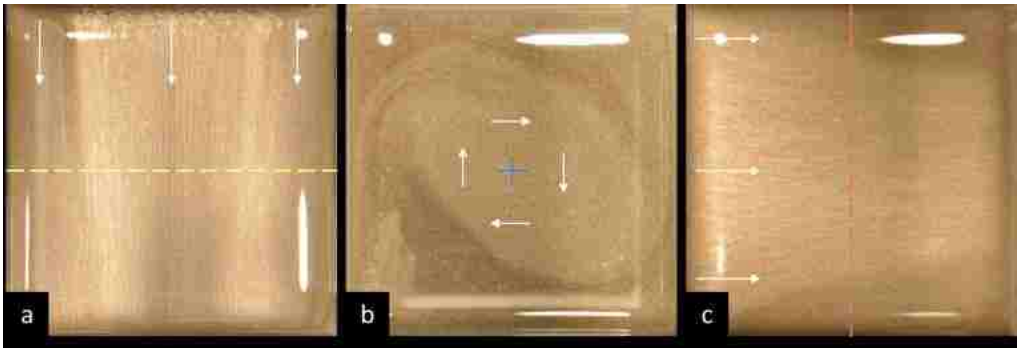

Figure 9-4. Fluid vorticity around three orthogonal field components. These views are parallel to the high frequency axis and the vertical direction is always the dc field axis. Vorticity occurs around **(a)** the low frequency axis for a 2:1 rational field (200 & 100 Hz), **(b)** around the high frequency axis for a 3:2 field (150 & 100 Hz), and **(c)** around the dc axis for a 3:1 field (300 & 100 Hz). In each image the vorticity axis is color-coded to the respective Helmholtz coil axis in Figure 9-2(b), and the flow direction is indicated by white arrows. This sample contained multi-layered magnetic platelets obtained from JDSU Flex Products.

to create vorticity around any of the three field directions and the sequence H, L, H, D found for $n = 3$ to 6 was found to repeat as n was further increased from 7 to 10, as did the dependences on dc field reversal and phase angle change. For odd n changing the phase angle ϕ in Equation 9-1 by 180° did not reverse the flow.

We next increased the field denominator m to 3 and explored the high frequency field sequence $n = 4, 5, \ldots$ For even values of n fluid vorticity was observed to form around the low frequency axis, whereas for odd values vorticity formed around the dc field, giving the repeating sequence L, D, … For this denominator vorticity did not occur around the high frequency axis. For even values of n the flow reversed when the dc field was reversed, but for odd values it did not. In all cases changing the phase angle by 180° reversed the flow, in contrast to the $m = 2$ case.

These puzzling vorticity axis sequences were explored for larger even values of m as n increased successively from $m + 1$. For $m = 4$ the repeating sequence was found to be H, H, H, L, H, H, H, D, … For $m = 6$ the sequence became simpler, H, L, H, D, … which is the same as found for $m = 2$. For $m = 8$ the repeating pattern is quite long, but for $m = 10$ it is again the same as for $m = 2$. Likewise, the sequence for $m = 12$ is that of $m = 4$ and $m = 14$

is that of $m = 2$. These experimental findings might seem rather bewildering, but in fact can be easily understood by considering the symmetry of the dynamic field.

9.5 Discussion

The suspensions we employ contain soft ferromagnetic platelets whose moment is induced by the field. The magnetic interactions between particles, as well as the interaction of the particle moments with the field, are therefore proportional to the field *squared* at non-saturating fields. Reversing the field thus generates the same forces and torques, so in considering the symmetry of the time-dependent field one must consider both the field **H** and its converse **–H**. The converse field trajectory is related to the field trajectory by a 180° rotation about the z axis. Note that in the following it is sometimes necessary to use the variables n', m', where $n':m' = n:m$, but n' and m' share no common factors. Also, in the following a great many properties of Lissajous curves are stated without proof. These proofs are presented in Appendix A and the numerous results are summarized in **Tables 9-1** and **9-2**.

9.5.1 Closed curves

For any rational frequency ratio $n:m$ there is a set of phase angles that produce Lissajous plots of two distinct types. The first type, Figure 9-1(bottom left), is a *closed curve* characterized by reflection symmetry around the x and y axes, so $(x, y) \rightarrow (-x, y)$ and $(x, y) \rightarrow (x, -y)$. For even:odd or odd:even frequency ratios this symmetric loop occurs at phase angles of $0°$, $180°/m'$, $360°/m'$, … and has a zero field crossing. For odd:odd frequency ratios this closed curve occurs at phase angles of $90°/m'$, $270°/m'$, $450°/m'$, … and lacks a zero crossing.

Even–odd fields. For the even-odd fields the *trajectory* of the biaxial field has parity, but the converse field has opposite parity. The combined trajectories of the biaxial field and its converse therefore lack parity, so deterministic fluid vorticity cannot occur in this case.

However, applying the dc field moves the field vector and that of its converse onto separate parallel planes, **Figure 9-5(top)**, creating the parity symmetry breaking that permits deterministic fluid vorticity. For odd:odd ratios the trajectory of the field and its converse have identical parities, **Figure 9-5(bottom)**, so the dc field is not needed to permit deterministic fluid vorticity. But experiments show that without this dc field the vorticity is weak and is obscured by a competing flow lattice, so in a practical sense the dc field is necessary.

The field and converse field trajectories of these closed curves have one C_2 rotational axis (symmetric under rotation by 180°), but the orientation of this symmetry axis depends on the frequency ratio. For even:odd frequency ratios the symmetry axis is parallel to the low frequency field. Rotation by 180° about either the high frequency or dc field reverses the parity of the field trajectories. Fluid vorticity around the low frequency field shares these symmetries and is therefore symmetry allowed. Likewise, the *high* frequency field is the C_2 symmetry axis for odd:even frequency ratios and 180° rotation about either the low frequency or dc field reverses the parity. In both cases vorticity around the C_2 axis is observed and in both cases a phase change of $180°/m'$ reverses the parity of the field and converse field trajectories and does indeed reverse the observed vorticity.

This latter observation explains the significance of rational frequency ratios in producing fluid vorticity. Irrational frequency ratios can be thought of as phase-modulated rational ratios and therefore would cause any fluid vorticity that does occur to periodically reverse, so that the *time-averaged* fluid vorticity will be zero. A change in the sign of the dc field component also reverses trajectory parity and does indeed reverse fluid flow. In the absence of a dc field the deterministic fluid vorticity should therefore be zero and replacing the dc field component with an ac field should *not* produce net fluid vorticity, at least around the same axis.

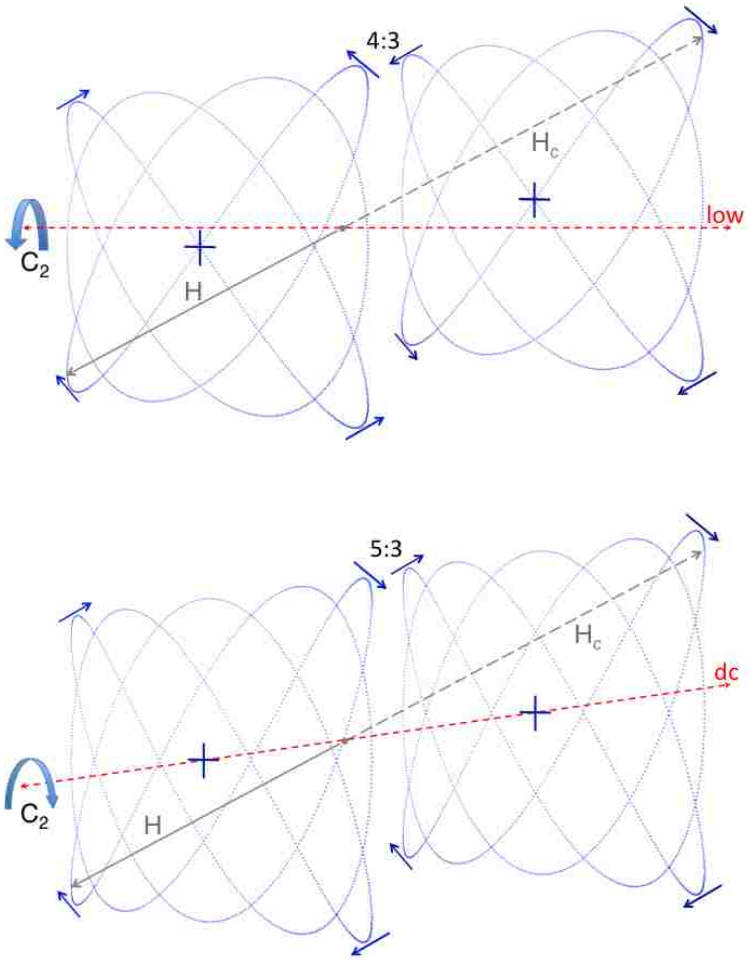

Figure 9-5. Illustrations of the symmetry of field trajectories on closed curves. **(Top)** A 4:3 field at 0° phase angle produces a symmetric closed curve. When a dc field is applied normal to the ac field plane the field vector **H** and its converse $\mathbf{H_c}$ trace out trajectories of opposite parity on parallel planes, as indicated by the arrows, so dc field reversal is antisymmetric. The low frequency field axis is a C_2 axis for these combined trajectories, whereas a 180° rotation about either the high field or dc axis is antisymmetric. **(Bottom)** For a 5:3 field at 30° phase angle the field and converse field trajectories have the same parity and are symmetric under dc field reversal. The dc axis is the C_2 axis and rotations about the low and high frequency axes are antisymmetric.

Odd–odd fields. Odd:odd frequency ratios have a C_2 symmetry axis parallel to the dc field, whereas 180° rotations about the other axes reverse the parity of the field trajectories. Experiments confirm that vorticity occurs around the dc field. A phase change of $180°/m'$ changes the parity but reversing the dc field does not. Experiments confirm flow reversal in the former case but not in the latter. Because the parity does not reverse upon dc field reversal it should be possible to observe steady fluid vorticity if the dc field component is instead alternating. Experiments confirm this possibility.

A simple rule – The above observations of the vorticity axis for closed Lissajous curves are easily summarized: for even:odd or odd:even frequency ratios it is the odd axis, whereas for odd:odd ratios it is the dc axis. For odd denominators m the repeating vorticity axis sequence is thus simply L, D, …, but for even denominators the repeat sequence can be quite long and includes the high frequency axis. For $m = 2^k p$, where p is odd, the repeating vorticity axis sequence is $(2^k - 1)\cdot$H, L, $(2^k - 1)\cdot$H, D as $n = m + 1$, $m + 2$… (a proof of this is given in Appendix B). This expression is consistent with the experimental observations we have described.

9.5.2 Open curves

The second type of Lissajous plot is an open curve, such as that in Figure 9-1(bottom right). The discussion of these paths follows that of the trajectories above, but there are important differences. For even:odd or odd:even frequency ratios symmetric open curves occur at phases of $90°/m'$, $270°/m'$, … and there is no zero crossing. For odd:odd frequency ratios these curves occur at 0°, $180°/m'$, $360°/m'$, … and there is a zero crossing.

Trajectories on these open curves lack parity, but these open curves have less symmetry than the closed curves described above. For even–odd frequency ratios there is one reflection axis and for odd:odd ratios there is none, as shown in **Figure 9-6**. For even–

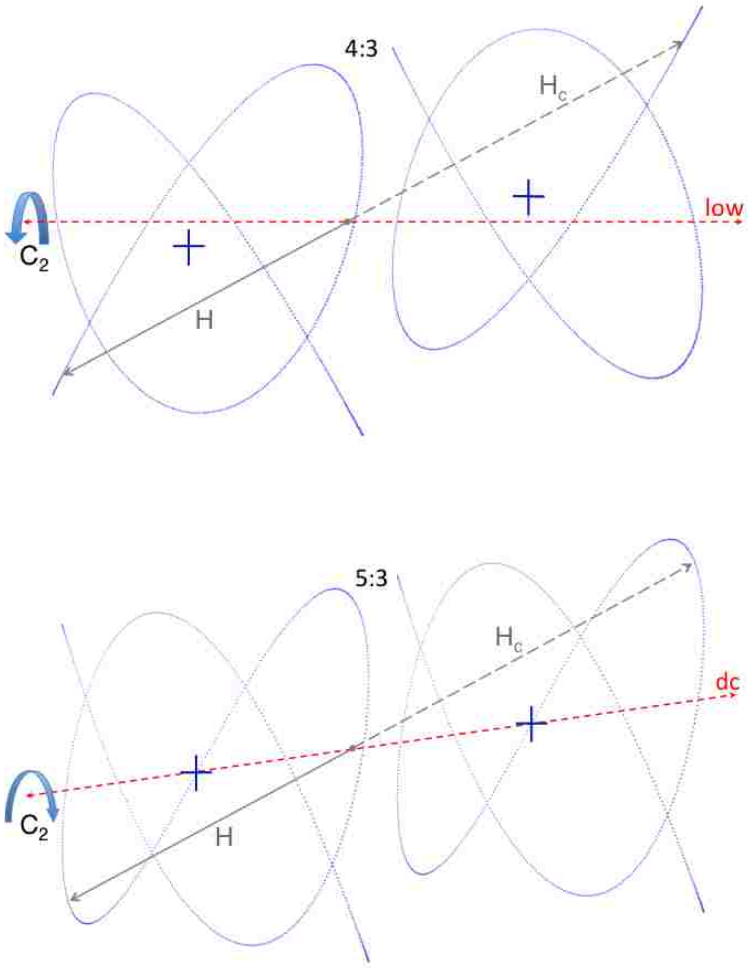

Figure 9-6. Illustrations of the symmetry of open field curves. **(Top)** A 4:3 field at a 30° phase angle produces a symmetric open curve. When a dc field is applied normal to the ac field plane the field vector **H** and its converse $\mathbf{H_c}$ trace out antisymmetric curves on parallel planes, so dc field reversal is antisymmetric. The low frequency field axis is a C_2 axis for these combined curves, whereas a 180° rotation about either the high field or dc axis is antisymmetric. **(Bottom)** For a 5:3 field at a 0° phase angle the field and converse field generate similar curves that are therefore symmetric under dc field reversal. The dc axis is the C_2 axis and rotations about the low and high frequency axes are antisymmetric.

odd ratios the converse field path is antisymmetric to the field path, so the combined paths lack parity and deterministic fluid vorticity is symmetry forbidden. However, applying the dc field breaks this symmetry, splitting the field and its converse onto separate parallel planes. The odd axis is a C_2 symmetry axis for the field and its converse path but these are antisymmetric under 180° rotation about the even or dc field axes. Vorticity around the odd

axis is therefore symmetry allowed and does indeed occur, just as it does for the closed Lissajous curves of this class. Changing the phase by $180°/m'$ creates antisymmetric paths and is observed to reverse fluid flow, as does reversing the dc field.

For the odd:odd open curves the field and its converse lie on identical paths. The dc field direction is a C_2 symmetry axis, whereas the paths are antisymmetric under 180° rotation about the ac field axes. Fluid vorticity about the dc field axis is symmetry allowed and changing the dc field direction should not reverse the flow, in agreement with experiment. Changing the phase by $180°/m'$ creates antisymmetric paths and is observed to reverse fluid flow.

We conclude that for any frequency ratio n:m the open-curve fields produce vorticity around the same axes as observed for the closed-curve fields. Field symmetry therefore allows fluid vorticity at phases of $j \times 90°/m'$, where j is an integer.

9.5.3 Intermediate phases

A few comments can be made about fluid flow for Lissajous curves having intermediate phases. For successive odd values of j and for successive even values of j flow reversal must occur. As j successively increases, the sign of the fluid vorticity must therefore follow the repeating sequence +, +, −, −, … or a cyclic permutation thereof. At each sign change there must be an intermediate phase where there is zero vorticity. These null points must be separated by $180°/m'$. For example, for a frequency ratio of 4:3 the closed Lissajous curves are at 0°, 60°… and the open curves are at 30°, 90°, … For the phase sequence 0°, 30°, … the experimentally determined pattern of vorticity signs is +, −, −, +, … A null point must occur at some phase angle $0° < \phi_0 < 30°$ and then at successive angles $\phi_0 + 60°$, $\phi_0 + 120°$, … Experiments confirm this prediction, as shown in **Figure 9-7** for a 2:1 field. The angle ϕ_0 cannot be predicted from symmetry considerations alone, although if the fluid vorticity is equally strong for the open and closed Lissajous curves one would expect it to be near the middle of the permissible range. However, experiments often show a striking

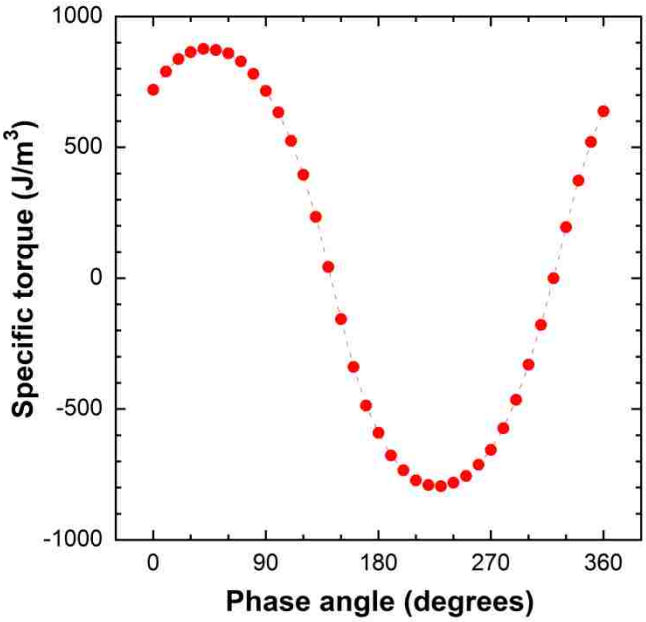

Figure 9-7. Dependence of the fluid vorticity on phase angle. Measurements of the specific torque (torque per unit volume fraction of particles) of a 2 vol% Permalloy platelet suspension subjected to a 2:1 field at frequencies of 300 & 150 Hz. This torque density is proportional to the field squared and in this instance the ac field had rms components of 150 Oe and the dc field amplitude was 150 Oe. For this frequency ratio the closed Lissajous curves are at 0°, 180°... and the open curves are at 90°, 270°, ... For the phase sequence 0°, 90°, ... the experimentally determined pattern of vorticity signs is +, +, −, −, ... A null point must occur at some phase angle $90° < \phi_0 < 180°$ and then at successive angles $\phi_0 + 180°$, $\phi_0 + 360°$, ... These nearly sinusoidal data give $\phi_0 \approx 135°$ and flow extrema at 45° and 225°.

difference in the magnitude of fluid vorticity for the open and closed curves. For some cases the open curve generates much stronger vorticity and in some cases it generates far less.

These symmetry arguments cannot explain the dependence of the fluid torque density on n:m and ϕ, but we have noticed that when n:m can be expressed as a ratio of small integers the torque is generally large, which can result in oscillating fluid vorticity. For example, if the field components have frequencies of 150 and 75 Hz vorticity will occur around the low frequency axis when the dc field is applied. If the high frequency component is increased to 150.1 Hz the frequency ratio becomes 1501/750 and vorticity should occur around the *high frequency* axis. But because this condition is a 0.1 Hz phase modulation of the 2:1 frequency ratio, one might expect oscillating vorticity around the low frequency axis. Oscillating vorticity is indeed observed, but the time-averaged vorticity around the low

frequency axis is zero. Any vorticity around the high frequency axis is obscured by these oscillations and must be weak. In short, certain frequency ratios can introduce a timescale to which the fluid vorticity can respond. In this case the symmetry rules can be used to predict both the quasi-adiabatic and time-averaged behavior.

Finally, a few words about the connection of the effects we have described to negative viscosity. As one manifestation imagine a Couette cell with the axis of field-driven vorticity parallel to its cylindrical axis. With the field off, applying a torque to the inner cylinder with the outer cylinder constrained can cause this cylinder to rotate, say counterclockwise. Applying an appropriate symmetry-breaking rational field can overcome the applied torque, causing the inner cylinder to rotate clockwise. The applied stress is thus opposite to the observed strain, so this could be called a negative viscosity. The term negative viscosity has previously been used to describe the effect of ac field-induced Quincke rotation in simply reducing the applied stress required to achieve a particular strain rate [9.45,9.46]. The effect we describe is much stronger, since Quincke rotation *alone* cannot induce global flow.

Conclusions

Symmetry-breaking rational triaxial fields can create strong vorticity in dilute particle suspensions, especially those containing anisometric particles. This vorticity can occur around the low frequency, high frequency or dc field axis by controlling the frequency ratio n:m. Small frequency adjustments can change the vorticity axis, providing a simple means of controlling fluid flow to achieve tailorable heat and mass transfer or mixing. Flow reversal can be achieved by changing the phase angle between the two ac field components and sometimes by simply changing the dc field direction. Because these effects are produced by *uniform* magnetic or electric fields of modest strength, this technology is scalable and ideally suited to microfluidic applications. Future work will focus on measurements of the fluid torque density under a variety of field conditions, as well as theoretical and simulation work

intended to elucidate the microscopic mechanism of torque generation. Additionally, experimental work will focus on controlling the motion of droplets on remarkable superhydrophobic surfaces [9.47] that have recently been developed and on surfaces that have tunable wetting [9.48].

Appendices

A. Symmetry properties of Lissajous curves and their trajectories

In this appendix the various symmetries that are responsible for selecting the vorticity axis of a magnetic particle suspension subjected to a symmetry-broken rational field are proven. We consider four symmetry operations of Lissajous curves: time reversal, reflection about the x axis or y axis, and rotation about the z axis. Recall from Equation 9-1 that x, y, z correspond to the low frequency, high frequency, and dc field axes, respectively. In the following $n':m' = n:m$, but n' and m' share no common factors. We consistently use the primed variables to avoid confusion, even though it is not always necessary to do so. All of the results derived in the following are presented in Tables 9-1 and 9-2.

Time reversal. Time reversal is given by the transformation $t \rightarrow -t$ in Equation 9-1. This is equivalent to the phase change $\phi \rightarrow \phi'$, where

$$\phi' = (3m' - n') \times \frac{180^\circ}{m'} - \phi \tag{A1}$$

Time reversal can be used to distinguish closed Lissajous curves from open curves and to compute the phases at which these occur: closed curves must be antisymmetric under time reversal whereas open curves must be symmetric.

To explore this symmetry operation we first define four sets of Lissajous curve phases:

$$\begin{aligned} \mathrm{A}_p &= \{p \times 90^\circ / m' + j \times 180^\circ / m', j\,odd\} \\ \mathrm{B}_p &= \{p \times 90^\circ / m' + j \times 180^\circ / m', j\,even\} \end{aligned} \tag{A2}$$

where p is 0 or 1. In the following we will establish the importance of these sets for each of the three rational field types.

Substituting the phases in Equation (A2) into Equation (A1) gives the phases

$$\phi'_j = p \times \frac{90°}{m'} + (3m' - n' - p - j) \times \frac{180°}{m'} \qquad \text{(A3)}$$

that correspond to time reversal for each value of j. This expression can be examined for each of the three field types.

For even:odd and odd:even rational fields $3m' - n' - p$ is odd for $p = 0$ and even for $p = 1$. Because j and $3m' - n' - j$ have opposite parities, Equation (A3) maps $A_0 \rightarrow B_0$, $B_0 \rightarrow A_0$. This mapping shows that the two sets of even:odd or odd:even curves with $p = 0$ must be *closed* and their trajectories must have opposite parities. However, the paths of these trajectories must be indistinguishable (*i.e.*, the plots look the same for even and odd j) for this mapping to occur. In contrast, j and $3m' - n' - 1 - j$ have the same parity, so time reversal maps curves with $p = 1$ onto themselves, $A_1 \rightarrow A_1$, $B_1 \rightarrow B_1$. These curves must therefore be *open*. Because in this case the j odd and j even sets do not map onto each other, they must be distinguishable. In fact, we will show that they are related by spatial symmetry operations.

For odd:odd fields $3m' - n' - p$ is even for $p = 0$ and odd for $p = 1$. The resultant mappings are $A_0 \rightarrow A_0$, $B_0 \rightarrow B_0$ and $A_1 \rightarrow B_1$, $B_1 \rightarrow A_1$, respectively. Curves with $p = 0$ are thus open and those with $p = 1$ are closed. Again, the two sets of closed curves must have trajectories of opposite parities and the open curves are geometrically distinguishable.

Reflection about the y axis. To demonstrate the symmetries of the three types of rational fields we start by considering reflection about the y axis ($x \rightarrow -x$). This transformation corresponds to $\phi \rightarrow \phi'$ where

$$\phi' = (2m' - n') \times \frac{180°}{m'} + \phi \,. \qquad \text{(A4)}$$

Substituting in the phases from Equation (A2) gives

$$\phi' = p \times \frac{90°}{m'} + (2m' - n' + j) \times \frac{180°}{m'}. \quad \text{(A5)}$$

For even:odd rational fields $2m' - n'$ is even, so $2m' - n' + j$ has the parity of j, and thus $A_p \rightarrow A_p$ and $B_p \rightarrow B_p$. Even:odd Lissajous curves are therefore symmetric under $x \rightarrow -x$. This is true for both the trajectories and the paths.

For odd:even and odd:odd rational fields $2m' - n'$ is odd, so $2m' - n' + j$ has the opposite parity of j and $A_p \rightarrow B_p$ and $B_p \rightarrow A_p$. These rational fields, both closed and open, are antisymmetric under reflection about the y axis.

Reflection about the x axis. Reflection about the x axis ($y \rightarrow -y$) is similarly treated. This transformation is given by $\phi' = 180° + \phi$ and for the phases in Equation (A2) can be written

$$\phi' = p \times \frac{90°}{m'} + j \times (1 + m') \times \frac{180°}{m'}. \quad \text{(A6)}$$

If m' is even, then $1 + m'$ is odd and the product $j \times (1 + m')$ has the parity of j so this transformation maps A_p and B_p onto themselves. We conclude that odd:even Lissajous curves are symmetric under reflection about the x axis. Even:odd and odd:odd fields map $A_p \rightarrow B_p$ and *vice versa*, and are therefore antisymmetric.

Rotation about the z axis. The combined reflections $x \rightarrow -x$, $y \rightarrow -y$ comprise a rotation by 180° around the z axis. The results of the transformation are obvious from the symmetries we have already derived, but for the sake of completeness we will treat this case in the same manner as above. The appropriate transformation is

$$\phi' = (3m' - n') \times \frac{180°}{m'} + \phi \quad \text{(A7)}$$

which for the set of phases in Equation (A2) is

$$\phi' = p \times \frac{90°}{m'} + (3m' - n' + j) \times \frac{180°}{m'}. \quad \text{(A8)}$$

The sum $3m' - n'$ is only even for odd:odd fields so $3m' - n' + j$ has the parity of j and thus the sets A_p and B_p map onto themselves under this transformation. Odd:odd Lissajous curves are thus symmetric under rotation about the z axis. Even:odd or odd:even curves are antisymmetric under this transformation.

In summary, we have identified sets of phases associated with open Lissajous curves and the most highly symmetric closed Lissajous curves. We have identified the symmetry properties of these curves that are responsible for selecting the vorticity axis of a fluid subjected to such a field. The results are summarized in Tables 9-1 and 9-2, where the variable p refers to Equation (A2).

Table 9-1 Properties of closed Lissajous curves[a]

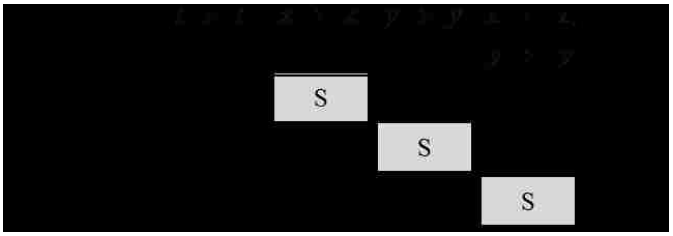

[a](A=antisymmetric, S=symmetric)

Table 9-2 Properties of open Lissajous curves[a]

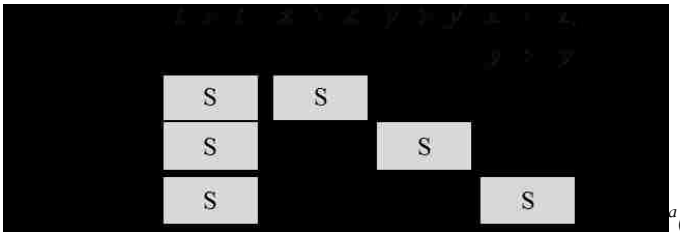

[a](A=antisymmetric, S=symmetric)An example of the use of these Tables is helpful. For even:odd fields the converse field can be seen to be antisymmetric relative to the field, since it is a 180° rotation about the z axis. A reflection about the x axis is also antisymmetric and thus makes the converse field identical to the initial field. The x axis (low frequency axis) is thus the vorticity axis in this case (see Figures 9-5 and 9-6).

B. The vorticity axis sequences

The axis sequences for the denominators we explored form a repeating pattern whose length depended on m in a peculiar way. From the symmetry rules we have developed it is straightforward to derive these repeating sequences as n increases successively from $m + 1$. We recall that rational fields can be classified as one of three types: even:odd, odd:even, and odd:odd. These types give rise to vorticity about the low frequency (L), high frequency (H), and dc fields (D) respectively, so we will identify these rational numbers according to these field abbreviations. Without loss of generality the sequence of rational numbers with denominator m can be expressed as

$$\frac{2^k p + j + 2^{k+1} l}{2^k p} \text{ where } j = 1,\ldots,2^{k+1} \text{ and } l = 0,1,\ldots,\infty . \qquad \text{(B1)}$$

Here m is written as $2^k p$ where p is odd. If the integer $j = 2^k$, Equation (B1) reduces to $(p + 1 + 2\,l)/p$ which is even:odd (L) for all l. If $j = 2^{k+1}$ Equation (B1) becomes $(p + 2 + 2\,l)/p$ which is odd:odd (D) for all l. All other values of j can be written as $2^i q$ where $i < k$ and q is odd. For this case Equation (B1) is $(2^{k-i} p + q + 2^{k+1-i} l)/2^{k-i} p$, which is odd:even (H) for all l. This demonstrates that the axis sequence is independent of l and is the repeating sequence $(2^k - 1)\cdot$H, L, $(2^k - 1)\cdot$H, D.

Acknowledgments

Sandia National Laboratories is a multi-program laboratory managed and operated by Sandia Corporation, a wholly owned subsidiary of Lockheed Martin Corporation, for the U.S. Department of Energy's National Nuclear Security Administration under contract DE-AC04-94AL85000. This work was supported by the Division of Materials Science, Office of Basic Energy Sciences, U.S. Department of Energy (DOE). We thank Vladimir Raksha, Paul Coombs, Tom Markantes, Bill Kittler, and Kees-Jan Delst at JDSU and Matt Groo at Novamet for supplying the magnetic platelets used in these experiments.

References

9.1 N.-T. Nguyen and Z. Wu, Micromixers – a review, *J. Micromech. Microeng.* **15**, R1–R16 (2005).

9.2 J.M. Ottino and M.U. Wiggins, Designing optimal mixers, *Science* **305**, 485–486 (2004).

9.3 A.P. Sudarsen and V.M. Ugaz, Multivortex micromixing, *Proc. of the Natl. Academy* **103**, 7228–7233 (2006).

9.4 A.D. Stroock, S.K.W. Dertinger, A. Ajdari, I. Mezic, H.A. Stone and G.M. Whitesides, Chaotic mixer for microchannels, *Science* **295**, 647–651 (2002).

9.5 G.M. Whitesides, The origins and future of microfluidics, *Nature* **442**, 368–373 (2006).

9.6 D. Mark, S. Haeberle, G. Roth, F. von Stetton and R. Zengerle, Microfluidic lab-on-a-chip platforms: requirements, characteristics and applications, *Chem. Soc. Rev.* **39**, 1153–1182 (2010).

9.7 A.J. deMello, Control and detection of chemical reactions in microfluidic systems, *Nature* **442**, 394–402 (2006).

9.8 J. Atencia and D.J. Beebe, Controlled microfluidic interfaces, *Nature* **437**, 648–655 (2005).

9.9 J. Hogan, Lab on a chip: A little goes a long way, *Nature* **442**, 351–352 (2006).

9.10 M. Joanicot and A. Adjari, Droplet control for microfluidics, *Science* **309**, 887–888 (2005).

9.11 S. Daniel, M.K. Chaudhury and J.C. Chen, Fast droplet movements resulting from the phase change on a gradient surface, *Science* **291**, 633–636 (2001).

9.12 F. Lugli, G. Fioravanti, D. Pattini, L. Pasquali, M. Montecchi, D. Gentili, M. Murgia, Z. Hemmatian, M. Cavallini and F. Zerbetto, And yet it moves! Microfluidics without channels and troughs, *Adv. Funct. Mater.* **23**, 5543–5549 (2013).

9.13 M.R. Bringer, C.J. Gerdts, H. Song, J.D. Tice and R.F. Ismagilov, Microfluidic systems for chemical kinetics that rely on chaotic mixing in droplets, *Philos. Trans. R. Soc., A* **362**, 1087–1104 (2004).

9.14 O.D. Velev, B.G. Prevo and K.H. Bhatt, On-chip manipulation of free droplets, *Nature* **426**, 515–516 (2003).

9.15 S. Hernandez-Navarro, P. Tierno, J. Ignes-Mullol and F. Sagues, AC electrophoresis of microdroplets in anisotropic liquids: transport, assembling, and reaction, *Soft Matter* **9**, 7999–8004 (2013).

9.16 J.R. Millman, K.H. Bhatt, B.G. Prevo and O.D. Velev, Anisotropic particle synthesis in dielectrophoretically controlled microdroplet reactors, *Nat. Mater.* **4**, 98–102 (2005).

9.17 A. Huebner, S. Sharma, M. Srisa-Art, F. Hollfelder, J.B. Edel and A.J. deMello, Microdroplets: A sea of applications?, *Lab Chip* **8**, 1244–1254 (2008).

9.18 R.O. Grigoriev, M.F. Schatz and V. Sharma, Chaotic mixing in microdroplets, *Lab Chip* **6**, 1369–1372 (2006).

9.19 X. Casadevalli Solvas and A.J. deMello, Droplet microfluidics: recent developments and future applications, *Chem. Commun.* **47**, 1936–1942 (2011).

9.20 A.B. Theberge, F. Courtois, Y. Schaerli, M. Fischlechner, C. Abell, F. Hollfelder and W.T.S. Huck, Microdroplets in microfluidics: An evolving platform for discoveries in chemistry and biology, *Angew. Chem., Int. Ed.* **49**, 5846–5868 (2010).

9.21 A. Huebner, D. Bratton, G. Whyte, M. Yang, A.J. deMello, C. Abell and F. Hollfelder, Static microdroplet arrays: a microfluidic device for droplet trapping, incubation and release for enzymatic and cell-based assays, *Lab Chip* **9**, 692–698 (2009).

9.22 T. Hutter, W.-A.C. Bauer, S.R. Elliott and W.T.S. Huck, Formation of spherical and non-spherical eutectic gallium-indium liquid-metal microdroplets in microfluidic channels at room temperature, *Adv. Funct. Mater.* **22**, 2624–2631 (2012).

9.23 G.I. Meijer, Cooling Energy-Hungry Data Centers, *Science* **328**, 318–319 (2010).

9.24 A. Bar-Cohen, M. Arik and M. Ohadi, Direct liquid cooling of high flux micro and nano electronic components, *Proc. IEEE* **94**, 1549–1570 (2006).

9.25 T.D. Halsey, Electrorheological Fluids, *Science* **258**, 761–766 (1992).

9.26 J. de Vicente, D.J. Klingenberg and R. Hidalgo-Alvarez, Magnetorheological fluids: A review, *Soft Matter* **7**, 3701–3710 (2011).

9.27 J. Dobnikar, A. Snezhko and A. Yethiraj, Emergent colloidal dynamics in electromagnetic fields, *Soft Matter* **9**, 3693–3704 (2013).

9.28 J.E. Martin and A. Snezhko, Driving self-assembly and emergent dynamics in colloidal suspensions by time-dependent magnetic fields, *Rep. Prog. Phys.* **76**, 1–42 (2013).

9.29 J.F. Douglas, Materials Science: Membrane magic, *Nature* **463**, 302 (2010).

9.30 P. Ball, Material Witness: Colloids get active, *Nat. Mater.* **12**, 696 (2013).

9.31 K.J. Solis and J.E. Martin, Isothermal Magnetic Advection: Creating functional flows for heat and mass transfer, *Appl. Phys. Lett.* **97**, 034101 1–3 (2010).

9.32 K.J. Solis and J.E. Martin, Stimulation of vigorous rotational flows and novel flow patterns using triaxial magnetic fields, *Soft Matter* **8**, 11989–11994 (2012).

9.33 B.A. Grzybowski, H.A. Stone and G.M. Whitesides, Dynamics self-assembly of magnetized, millimeter-sized objects rotating at a liquid–air interface, *Nature* **405**, 1033–1036 (2000).

9.34 A. Snezhko, Non-equilibrium magnetic colloidal dispersions at liquid–air interfaces: dynamic patterns, magnetic order and self-assembled swimmers, *J. Phys.: Condens. Matter* **23**, 153101 1–21 (2011).

9.35 A. Snezhko, I.S. Aranson and W.-K. Kwok, Surface-wave-assisted self assembly of multidomain magnetic structures, *Phys. Rev. Lett.* **96**, 078701 1–4 (2006).

9.36 A. Snezhko, M. Belkin, I.S. Aranson and W.-K. Kwok, Self-assembled magnetic surface swimmers, *Phys. Rev. Lett.* **102**, 118103 1–4 (2009).

9.37 A. Snezhko and I.S. Aranson, Magnetic manipulation of self-assembled asters, *Nat. Mater.* **10**, 698–703 (2011).

9.38 M. Belkin, A. Snezhko, I.S. Aranson and W.-K. Kwok, Magnetically-driven surface mixing, *Phys. Rev. E: Stat., Nonlinear, Soft Matter Phys.* **80**, 011310 1–5 (2009).

9.39 M. Belkin, A. Snezhko, I.S. Aranson and W.-K. Kwok, Driven magnetic particles on a fluid surface: Pattern-assisted surface flows, *Phys. Rev. Lett.* **99**, 158301 1–4 (2009).

9.40 G. Kokot, A. Snezhko and I.S. Aranson, Emergent coherent states and flow rectification in active magnetic colloidal monolayers, *Soft Matter* **9**, 6757–6760 (2013).

9.41 J.E. Martin, Theory of strong intrinsic mixing of particle suspensions in vortex magnetic fields, *Phys. Rev. E: Stat., Nonlinear, Soft Matter Phys.* **79**, 011503 1–12 (2009).

9.42 J.E. Martin, L. Shea-Rohwer and K.J. Solis, Strong intrinsic mixing in vortex magnetic fields, *Phys. Rev. E: Stat., Nonlinear, Soft Matter Phys.* **80**, 016312 1–6 (2009).

9.43 K.J. Solis, R.C. Bell and J.E. Martin, Vortex magnetic field mixing with anisometric particles, *J. Appl. Phys.* **107**, 114911 1–4 (2010).

9.44 J.E. Martin, A resonant biaxial Helmholtz coil employing a fractal capacitor bank, *Rev. Sci. Instrum.* **84**, 094704 1–11 (2013).

9.45 J.-C. Bacri, R. Perzynski, M.I. Shliomis and G.I. Burde, Negative viscosity effect in a magnetic fluid, *Phys. Rev. Lett.* **75**, 2128–2131 (1995).

9.46 R.E. Rosensweig, Negative viscosity in a magnetic fluid, *Science* **271**, 614–615 (1996).

9.47 J.D. Smith, R. Dhiman, S. Anand, E. Reza-Garduno, R.E. Cohen, G.H. McKinley and K.K. Varanasi, Droplet mobility on lubricant-impregnated surfaces, *Soft Matter* **9**, 1772–1780 (2013).

9.48 M. Liu and L. Jiang, Switchable adhesion on liquid/solid interfaces, *Adv. Funct. Mater.* **20**, 3753–3764 (2010).

Chapter 10

Torque density measurements on vortex fluids produced by symmetry-breaking rational magnetic fields[10]

In Chapter 9 we reported on the discovery that an infinite class of triaxial magnetic fields is capable of producing rotational flows in magnetic particle suspensions. These triaxial fields are created by applying a dc field orthogonally to a *rational* biaxial field, comprised of orthogonal components whose frequencies form a rational ratio. The vorticity axis can be parallel to any of the three field components and can be predicted by a careful consideration of the symmetry of the dynamic field. In this chapter we not only test the field-symmetry predictions, but also quantify fluid vorticity as a function of the field parameters (strength, frequency ratio, phase angle and relative dc field strength) and particle shape. These measurements validate the symmetry predictions and demonstrate that rational fields are as effective as vortex fields for producing strong fluid mixing, yet have the advantage that small changes in the frequency of one of the field components can change the vorticity axis. This approach extends the possibilities for noncontact control of fluid flows and should be useful in areas such as microfluidics, and the manipulation and mixing of microdroplets.

10.1 Introduction

Methods of inducing vigorous noncontact fluid flow are of interest for heat and mass transfer and fluid mixing. Of particular interest are methods that do not create flow patterns with a characteristic macroscopic correlation length (such as that exhibited by natural convection) and are therefore adaptable to the nanoscale. We have shown in Chapter 9 that an infinite class of spatially-uniform applied magnetic or electric fields, called *symmetry-breaking rational*

[10] Originally published as: K.J. Solis and J.E. Martin, Torque density measurements on vortex fluids produced by symmetry-breaking rational magnetic fields, *Soft Matter* **10**, 6139–6146 (2014).

fields, can create strong fluid vorticity when applied to suspensions of magnetic or dielectric particles, respectively [10.1]. In fact, such fields create a *vortex fluid* capable of crawling up the sides of a container (active wetting) and exhibiting a negative viscosity. The purpose of this chapter is not only to validate the symmetry-based theoretical predictions previously made, but to determine how the *magnitude* of the fluid torque density depends on a variety of experimental parameters, including those pertaining to the applied field and those pertaining to the particle suspension. In the course of these studies two new phenomena have been discovered: flow reversal and surface flow reversal, and these are presented as well.

Symmetry-breaking rational fields are comprised of three orthogonal components. Two of these are ac fields having a rational frequency ratio that can be written as an irreducible ratio n:m, where n and m are integers. One field component is higher in frequency than the other, so without loss of generality $n > m$. The third field is dc and serves to break the symmetry of the rational field, thus creating *deterministic* fluid vorticity. This vorticity can occur around the high frequency (H), low frequency (L), or dc (D) field axis.

This fluid vorticity is quite unexpected, because in general the field vector is *noncirculating* (*i.e.*, zero net rotation of the field vector over one field cycle) and thus there is no immediately obvious field parity of the type that something like a simple rotating field possesses. The strangeness of this manner of generating vorticity can be illustrated by the following example: when the increasing frequency ratio sequence 5:4, 6:4, 7:4, … is successively applied to a particle suspension, the repeating vorticity axis sequence H, H, H, L, H, H, H, D, … occurs, but only if the dc field is applied. Longer or shorter axis sequences occur for other denominators, and only for certain frequency ratios does reversing the dc field reverse the vorticity or does reversing the leads on the high frequency coil reverse the vorticity.

As was shown in Chapter 9, a consideration of the symmetry of the dynamic field leads to predictions of all of these effects [10.1]. These predictions are remarkably simple:

(1) for even:odd or odd:even fields the vorticity axis is the odd axis and reversing the dc field reverses the vorticity; (2) for odd:odd fields the dc field is the vorticity axis and reversing the dc field *does not* reverse the vorticity; (3) a change in the phase of the high frequency field by $180°/m$ reverses the vorticity. These symmetry predictions are consistent with experimental observations, but symmetry alone cannot predict the dependence of the magnitude of the fluid torque density on the frequency ratio of the ac components or the phase angle between these components. Nor can it address how the torque density depends on ac field strength, dc field strength or particle shape. Yet a quantitative understanding of these issues is essential to developing applications that require vigorous vorticity.

In this study we quantify the vorticity produced by three primary rational fields, 2:1 (even:odd), 3:2 (odd:even) and 3:1 (odd:odd). These fields produce vorticity around the low frequency, high frequency, and dc field axes, respectively. Using these fields we explore the dependence of the torque density on frequency, phase angle, field strength, and particle shape.

Three particle shapes are studied: spheres, platelets, and rods. In general we find that the various dependencies observed for platelets and rods are similar, whereas spheres are quite distinct. This difference is likely a reflection of the fact that an applied field can create a geometry-driven torque on an isolated platelet or rod, but cannot exert such a torque on an isolated magnetically soft sphere. Only if spheres form anisometric clusters, such as particle chains, can such a torque be generated, so the dynamic field must be able to create such structures without the formation of competing structures, such as particle sheets. We find that symmetry-breaking rational fields are generally as effective as vortex magnetic fields (see Chapters 3 and 4) at creating strong mixing within magnetic particle suspensions, despite the fact that the former fields are generally noncirculating.

10.2 Background

Because there are many instances in which *noncontact* methods of manipulating and agitating fluids would be useful (*e.g.*, cooling high-performance microprocessors, fluid handling in bioassays, microfluidic applications…), the search for effective, practical methods of inducing fluid flow has been longstanding. Magnetic fluids and suspensions naturally lend themselves to noncontact control, since an applied magnetic field easily penetrates most containers and can thereby be used to manipulate the magnetic fluid. Spatially uniform fields—such as we use—do not create a body force on a fluid, so most other methods of manipulation rely on field gradients. Gradients create a force on each volume element of the fluid that is described by the Kelvin force, $\mathbf{F} = -\mathbf{m} \cdot \nabla \mathbf{H}$, where $\mathbf{H}$ is the magnetic field and $\mathbf{m}$ is the fluid volume magnetic moment. Ferrofluids have been the focus of much of this research [10.2], because they are thermodynamically stable suspensions of particles that are not subject to sedimentation. Three principal approaches to inducing flow have been realized for ferrofluids, and each is specific to a particular type of ferrofluid flow phenomenon, which we now briefly discuss.

The first approach, thermomagnetic convection [10.3–10.5], is a passive mechanism by which *toroidal* convective motion in a ferrofluid is initiated by applying a substantial magnetic field gradient parallel to an imposed thermal gradient. This technique exploits the temperature-dependent susceptibility of ferrofluids (*i.e.*, a negative pyromagnetic coefficient) to generate a magnetic Kelvin force *gradient*. This force gradient has exactly the same effect as the gravitational force gradient that arises because of the thermal expansion of a fluid subjected to a temperature gradient. The magnetic field gradient can therefore produce convective flow patterns if it is sufficiently large and properly aligned relative to the thermal gradient. A field gradient can be produced by a permanent magnet, so the source of the energy driving the fluid motion is the heat transfer that maintains the thermal gradient, just as is the case with natural convection. Limitations of this approach are that a thermal gradient is required, in addition to an extremely large magnetic field gradient (of the order

of 1–10 $T \cdot m^{-1}$), which makes scaling up this approach problematic. Because of this limitation thermomagnetic convection is usually applied to very thin fluid layers (1–10 mm) where it is difficult to induce natural convection because the required destabilizing thermal gradient scales as the *inverse fourth power* of the fluid thickness.

Ferrohydrodynamic pumping is another means of moving a ferrofluid, and occurs by applying a travelling solenoidal field to regions of a pipe, which produces *linear* flow of the ferrofluid down the pipe [10.6,10.7]. This effect is due to the field gradient producing a Kelvin force on the fluid and is the magnetic field equivalent of the peristalsis that occurs in intestines. In recent work by Mao *et al.*, a maximum volumetric flow rate of 0.69 $mL \cdot s^{-1}$ was achieved by applying a modest non-uniform propagating/travelling solenoidal field to regions of the pipe [10.7].

Finally, weak *rotational* flows within ferrofluids have also been studied, and occur when rotating magnetic fields are applied [10.8–10.11]. This effect is due to a lag between the magnetic moment of the particle and the rotating field vector.

Our own previous work focused on creating fluid vorticity in suspensions of micron-sized particles using a "vortex" magnetic field [10.12], wherein the field vector exhibits a precession-like motion that describes the surface of a cone (see Chapter 3). When such a field is applied to a suspension of magnetic particles, pronounced fluid vorticity develops throughout the entire fluid volume. Torsion fiber measurements have shown that the resultant torque has surprising dependencies on experimental parameters, in comparison to conventional stir bar mixing [10.12]. Within certain limits the torque is quadratic in the field (for spherical particles the specific torque density is roughly four times the energy density of the field), and independent of the field frequency and fluid viscosity. Theory has shown that these dependencies are due to the field-induced formation of volatile chain-like agglomerates that whirl around in pursuit of the dynamic field vector [10.13]. In Chapter 4 we demonstrated that vortex field mixing with suspensions of anisometric particles (platelets and nanorods) show similar trends in the mixing behavior [10.14]. However,

when the dc field is removed—to create a simple rotating field—strong differences emerge: the spherical particles form static sheets, the rods continue to mix, but the platelet suspensions perform a stunning and unexpected trick—the formation of advection lattices [10.15].

These advection lattices not only form in rotating fields but in a broader class of *biaxial* magnetic fields (see Chapter 5). Advection lattices are generally in the form of a lattice of antiparallel flow columns that extend orthogonal to the plane of the biaxial field. The appearance and flow characteristics of advection lattices, as they depend on various magnetic field parameters and fluid properties, was discussed in Chapter 6 [also Ref. 10.16]. Chapter 7 showed that applying a third field component in the form of a dc field orthogonally to the biaxial field plane (parallel to the flow columns) alters the dynamics of advection lattices in numerous ways [10.17]. One such alteration is the creation of vigorous rotational flow, the subject of this chapter. Such rotational flow was shown in Chapter 8 to have the potential for significantly enhancing heat transfer [10.18].

In the following section we describe the materials we use, the method of generating the dynamic fields, and the torsion fiber apparatus used to quantify the fluid torque density.

10.3 Experimental

The suspensions were prepared by dispersing 1.5 vol% magnetic particles into isopropyl alcohol, and were contained in 1.8 mL vials. **Figure 10-1** shows SEM images for the different magnetic particles that were studied. These included 4–7 μm spherical carbonyl iron powder (ISP Technologies Inc.); ~50 μm-wide by 0.4 μm-thick molybdenum Permalloy platelets (Novamet Corp.); and 8–10 μm-long, 300 nm-diameter cobalt nanorods (Richard Bell, Pennsylvania State University, Altoona College). (All of these

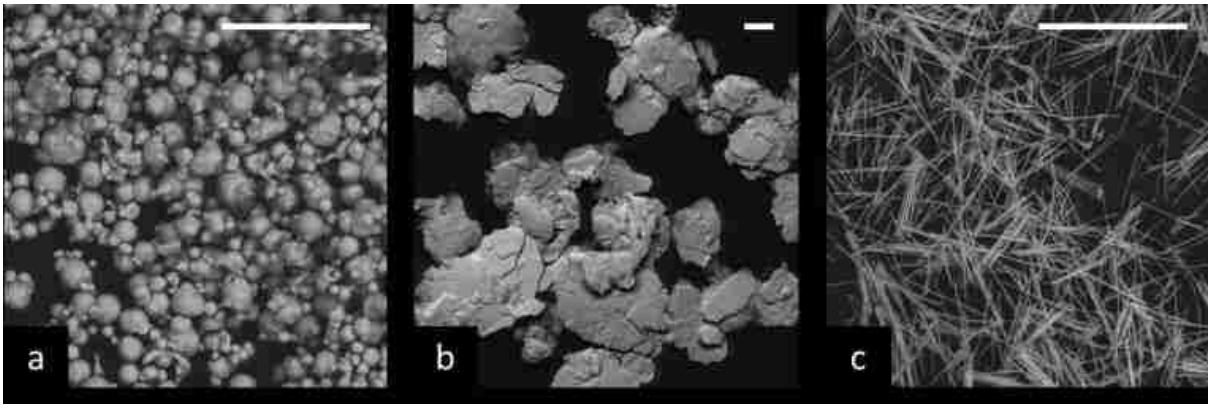

Figure 10-1. SEM images of the magnetic particles. **(a)** 4–7 μm spherical agglomerate carbonyl iron powder, **(b)** Permalloy platelets roughly 50 μm across by 0.4 μm thick, and (c) cobalt nanorods 8–10 μm long by 300 nm diameter. The white scale bar in each image represents 20 μm.

materials are magnetically soft and so have little remanence.) The sample vial was mounted to a Macor fixture at the end of the torsion fiber and suspended in the central cavity of three orthogonally-nested Helmholtz coils, two of which are operated in series resonance with computer-controlled fractal capacitor banks [10.19] to generate uniform fields up to 200 G (0.02 T) in the low audio frequency range (~100–1000 Hz), while the third coil was used to produce a uniform dc field of up to 200 G. The specific torque density (torque per unit volume of magnetic particles) of the suspension was computed from measured angular displacements on a torsion balance employing a 96.0 cm-long, 0.75 mm-diameter nylon fiber with a torsion constant of ~13 μN·m rad^{-1}. A photograph of the triaxial Helmholtz magnet assembly and torsion balance is shown in **Figure 10-2**.

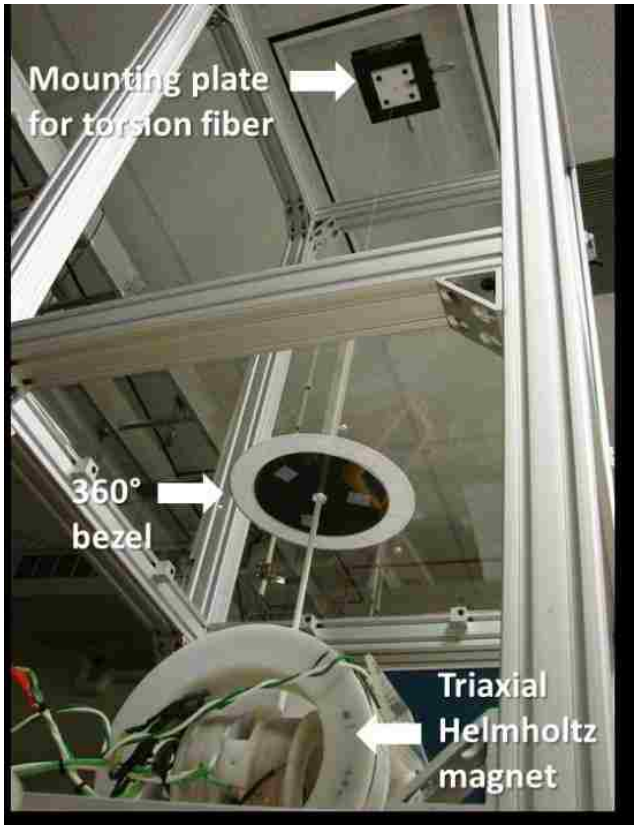

Figure 10-2. Torsion balance and Helmholtz coils. An oblique upward view (three-point perspective) of the experimental apparatus, showing the three nested Helmholtz coils and the torsion balance (supported by the aluminum frame). Suspended in the central cavity of the coils is a vial containing the sample, which is attached to the end of the torsion fiber *via* the white rod-shaped fixture. The vorticity axis of the rotational flows must be oriented parallel to the torsion fiber axis to measure a body torque in the fluid.

10.4 Results

In this section we present results of the measured specific torque densities for a variety of particle suspensions subjected to symmetry-breaking rational fields. We consider all three possible "parities" of frequency ratios—even:odd, odd:even, and odd:odd. These fields produce vorticity around the *low frequency*, *high frequency*, and *dc* field components, respectively. To measure a body torque within the suspension requires the vorticity axis of the rotational flows to be parallel to the torsion fiber, which is vertical. So for each of the three parity cases we simply applied the appropriate fields with the correct geometry to ensure that the vorticity axis was always collinear with the torsion fiber. (One could also

rotate the entire triaxial magnet assembly, but this is cumbersome and defeats the concept of being able to control the orientation of the vorticity axis with the applied field alone!) A study of the specific torque dependence on the phase angle between the biaxial field components was first performed for each rational field to identify the phase angle at which the largest torque values are produced. This optimal phase angle was then used during the subsequent study of the effect of the dc field amplitude. In all cases (except for the field strength study) the rms induction field of each ac *biaxial* field component was 150 G.

10.4.1 Even:odd biaxial fields

Phase dependence. The simplest rational field that produces vorticity around the low frequency axis is the even:odd 2:1 field (see Lissajous plots in **Figure 10-3**). **Figure 10-4(a–c)** shows measured torque densities for each particle shape as a function of the phase angle between the ac biaxial field components. In all cases torque extrema occur at phase angles separated by 180°, which validates the symmetry prediction that flow maxima occur at intervals of $180°/m$ for all n:m rational fields (see Chapter 9) [also Ref. 10.1]. The platelets and rods yield continuous, roughly sinusoidal torque curves, whose peak values shift slightly toward lower phase angles and increase modestly with the magnitude of the frequency. The curves for the platelets are roughly sinusoidal, while those for the rods are somewhat skewed.

In contrast, for spherical particles the torque density is especially sensitive to the phase angle: an adjustment of only 20° causes the torque to substantially drop from its maximum value at 0°. Although this decrease distorts the shape of the curve, the torque extrema are still separated by 180°. However, the torque minimum is strangely smaller in magnitude than the maximum. This occurs because the torques were measured by changing the phase angle while the field is applied. As the phase angle increases from 0° and the torque collapses it simply does not recover by simply adjusting the phase angle. This suggests that at intermediate phases the particles form a relatively stable quasi-static

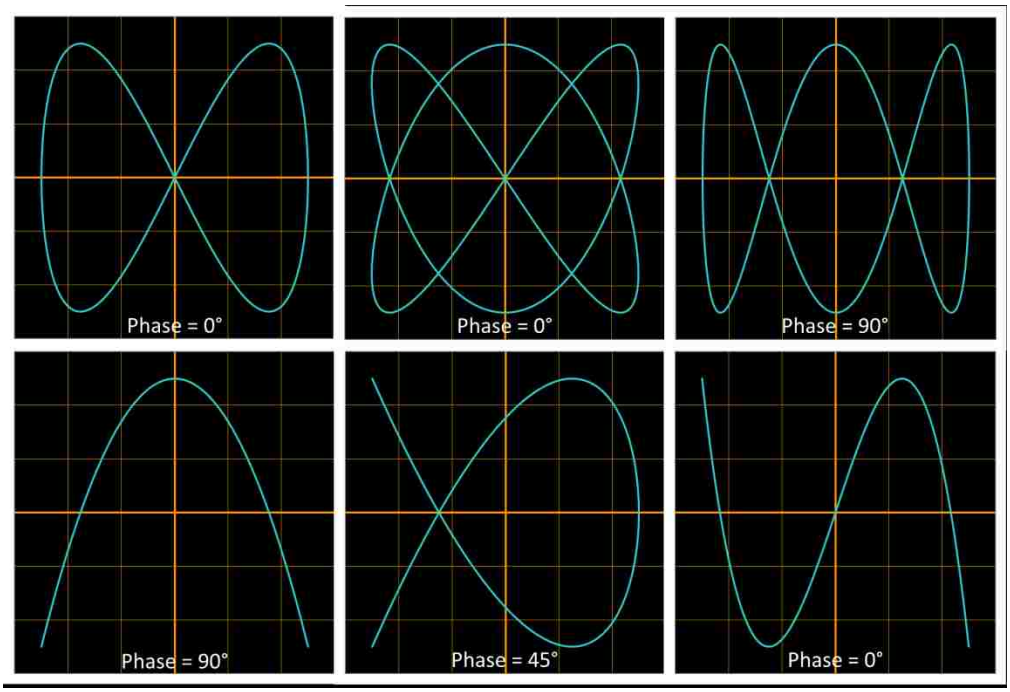

Figure 10-3. Lissajous curves for three primary *n*:*m* rational fields. **(Top row)** Closed curves for 2:1, 3:2, and 3:1 fields. **(Bottom)** Corresponding open curves.

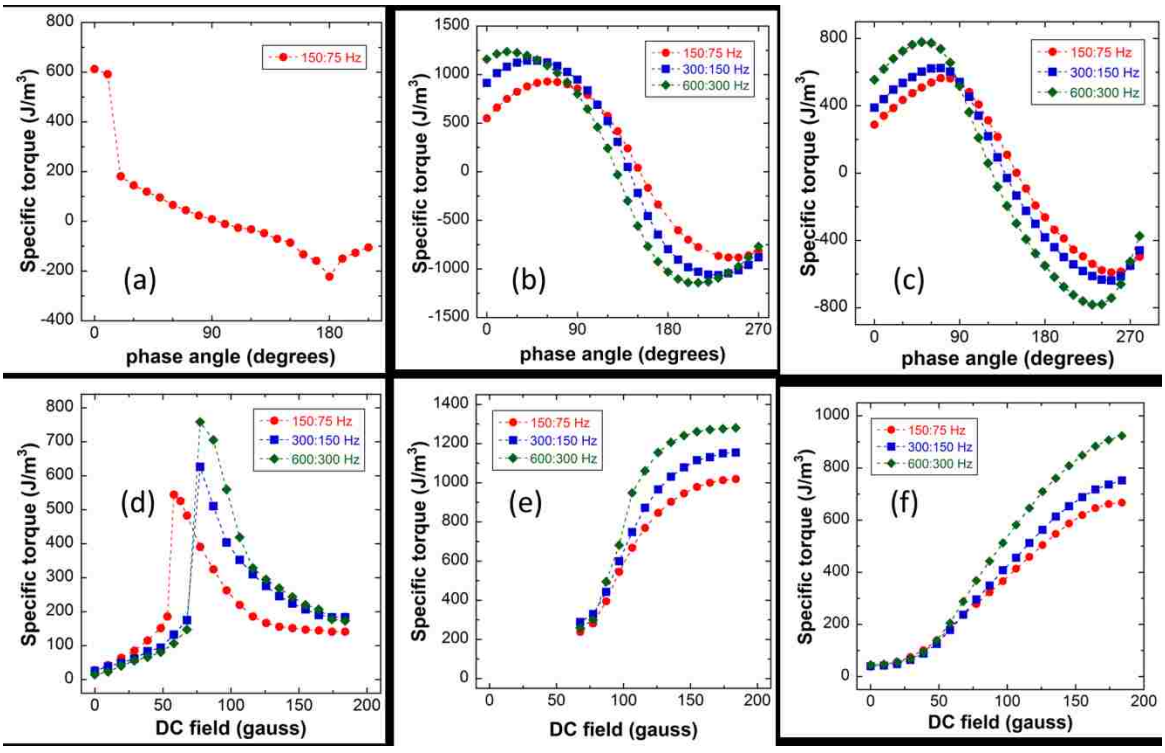

Figure 10-4. Torque curves for 2:1 (even:odd) rational biaxial fields. Top row shows the torque density as a function of phase angle for **(a)** spheres, **(b)** platelets, and **(c)** rods. The bottom row shows the torque density as a function of the dc field amplitude.

structure that is not easily disrupted [10.20]. However, if the field is *entirely turned off* and re-applied with an initial phase angle of 180°, a torque magnitude comparable to that obtained at 0° is obtained, apparently because turning off the field allows the stable quiescent structure to collapse *via* sedimentation.

Both nanorods and platelets give larger specific torques than spheres and do not develop this troublesome stable phase, so are better choices than spheres. Platelets have a higher packing density than rods and are the best choice for inducing vorticity in situations where congestion would be problematic.

dc field dependence. The dependence of the specific torque on the dc field amplitude was determined by varying the dc field at the phase angle that produced the maximum torque for each particle type. Trends for the anisometric particles [**Figure 10-4(e–f)**] are similar: the torque increases monotonically with the dc field and saturates at higher fields. A balanced field gives nearly a maximum torque. In contrast, the spherical particles display peculiar torque curves characterized by a narrow maximum peak at a dc field substantially lower than balanced (~50–100 G), **Figure 10-4(d)**. The discontinuity in the torque is again due to the formation of quasi-static structures that compete with the particle mixing, as was seen in the phase angle study [**Figure 10-4(a)**]. Again, platelets and rods show much more robust torque development.

Field strength and frequency. Finally, we investigated the dependence of the specific torque on the strength of the applied field for 2:1 biaxial fields. Plots of the specific torque *versus* the field squared (proportional to the energy density of the field) are shown in **Figure 10-5** for both types of anisometric particles. In both cases the torques increase monotonically with field strength, and the specific torque densities are *of the order of the energy density of the field*. These curves display similar trends to those observed in Chapter 4 for anisometric particles subject to vortex magnetic fields [10.14]. Moreover, the curves for

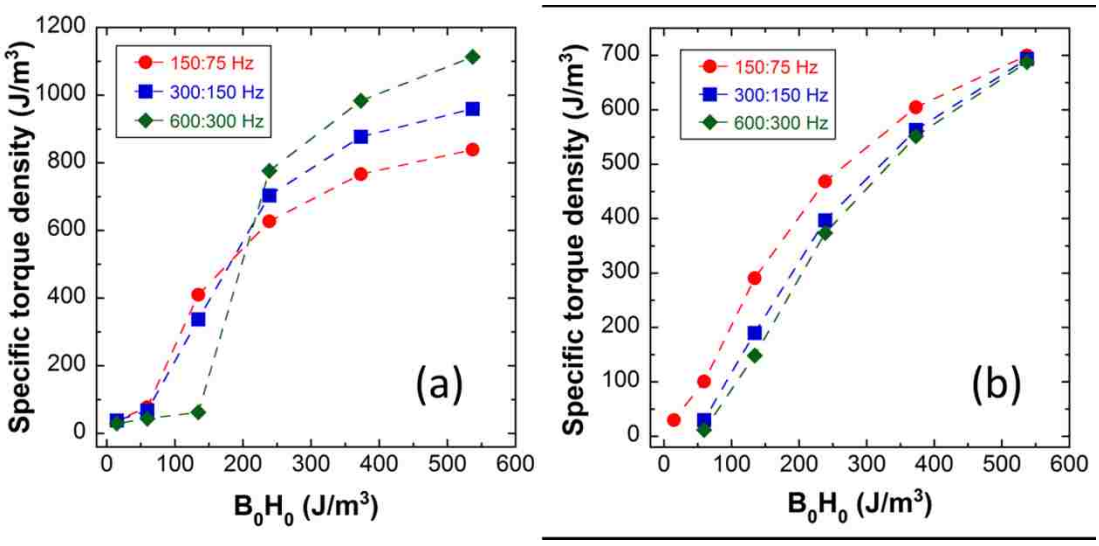

Figure 10-5. Field strength study for 2:1 (even:odd) rational biaxial fields. Field squared dependence (proportional to the field energy density) of the specific torque for **(a)** Permalloy platelets and **(b)** Co nanorods. The sharp narrow peak in the torque curve for the spherical iron particles [Figure 10-4(d)], which occurs at fields lower than a balanced field, made their field strength dependence too difficult to study.

the cobalt nanorods are largely independent of field frequency, whereas the Permalloy platelets show a significant frequency dependence at low fields. As the field frequency increases, the torque falls off more rapidly at lower field strengths, suggesting a Mason number effect [10.14] where the field-induced attractive forces have become insufficient to hold particle structures together at higher frequencies. For vortex fields such particle structures are responsible for torque production [10.13].

10.4.2 Odd:even biaxial fields

Phase dependence. The simplest rational field that produces vorticity around the high frequency axis is the odd:even 3:2 field (see Lissajous plots in Figure 10-3). This field also produces large specific torques, even though it is noncirculating [10.1]. The phase angle studies, **Figure 10-6(a–c)**, show that for all particles the extrema in the specific torque are now separated by 90°, since here m = 2 and $\Delta\phi = 180°/m$. The platelets and rods produce symmetrical, nearly sinusoidal torque curves with maxima at similar phase angles. As with the 2:1 case, the spherical particles again exhibited strong sensitivity to the value of the

phase angle, resulting in a discontinuous and asymmetric torque curve that is dependent on the suspension history.

dc field dependence. The dependence of the torque density on the dc field amplitude [**Figure 10-6(d–f)**] is distinct for each particle shape. For spherical particles, there is only a narrow range of dc field amplitude that gives appreciable torque. In addition, there is a strange phenomenon that was not observed for the 2:1 field: *flow reversal*. As the dc field is progressively increased the torque increases to a maximum, decreases to zero and then reverses, as does the observed flow! Also, as with the 2:1 case, the peak torque obtains at slightly higher dc fields as the frequency of the biaxial field is increased.

The torque curves for the platelets maximize near a balanced field and show a broad shoulder in this region, then abruptly fall off for fields below ~100 G. In contrast, a

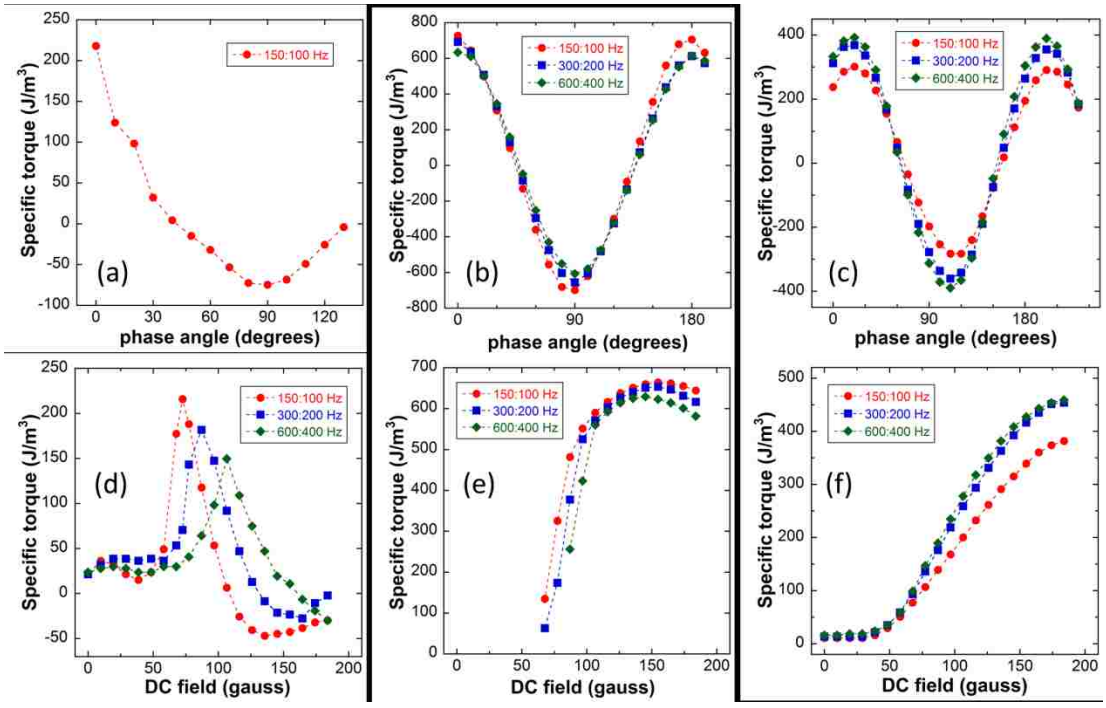

Figure 10-6. Torque curves for 3:2 (odd:even) rational biaxial fields. Top row shows plots as a function of the phase angle for **(a)** spheres, **(b)** platelets, and **(c)** rods. The bottom row shows the corresponding torque curves as a function of the dc field amplitude.

maximum is not seen for the nanorods, but this is probably simply due to the fact that we cannot apply a sufficiently large dc field with the current supply we have. The torque curves for the nanorods look remarkably similar to those for the 2:1 fields.

Frequency dependence. The anisometric particle data show the torque density to be fairly insensitive to field frequency, which is exactly the same result found for a vortex field. In the case of a vortex field this weak dependence could be attributed to the formation of volatile particle chains whose typical size simply adjusts to the field frequency. Higher frequencies lead to shorter chains, but because these are more numerous the torque density is unaltered. This suggests that for these rational fields torque production is due to the formation of particle clusters. For vortex fields there is also no predicted dependence on particle size, which might well be the case for these rational fields. Spherical particles have a stronger frequency dependence, which suggests that for these particles the Mason number is simply too large. The large Mason number is expected because the spherical shape produces large demagnetizing fields and thus low internal fields and low polarization.

10.4.3 Odd:odd biaxial fields

Phase dependence. The simplest rational field that produces vorticity around the dc field axis (other than a vortex field, which is 1:1) is the odd:odd 3:1 field (see Lissajous plots in Figure 10-3). Currently, our largest Helmholtz coil is only capable of resonating at 50 Hz and 100 Hz, so this limits the number of 3:1 fields that we could investigate here to two: 150:50 Hz and 300:100 Hz. (For the latter case the frequencies were actually 300.6:100.2 Hz, since the resonant frequency of 100.2 Hz was dictated by the value of capacitance we were able to achieve given the capacitors we have.) As **Figure 10-7(a–c)** shows, the torque maxima are 180° apart, as expected for this field. As with the previous two cases, the curves for the anisometric particles are very similar—nearly symmetric and sinusoidal, though the platelets give significantly greater torque. Although the torque curve for the spherical particles does not show the same sensitivity on the phase angle as in the two

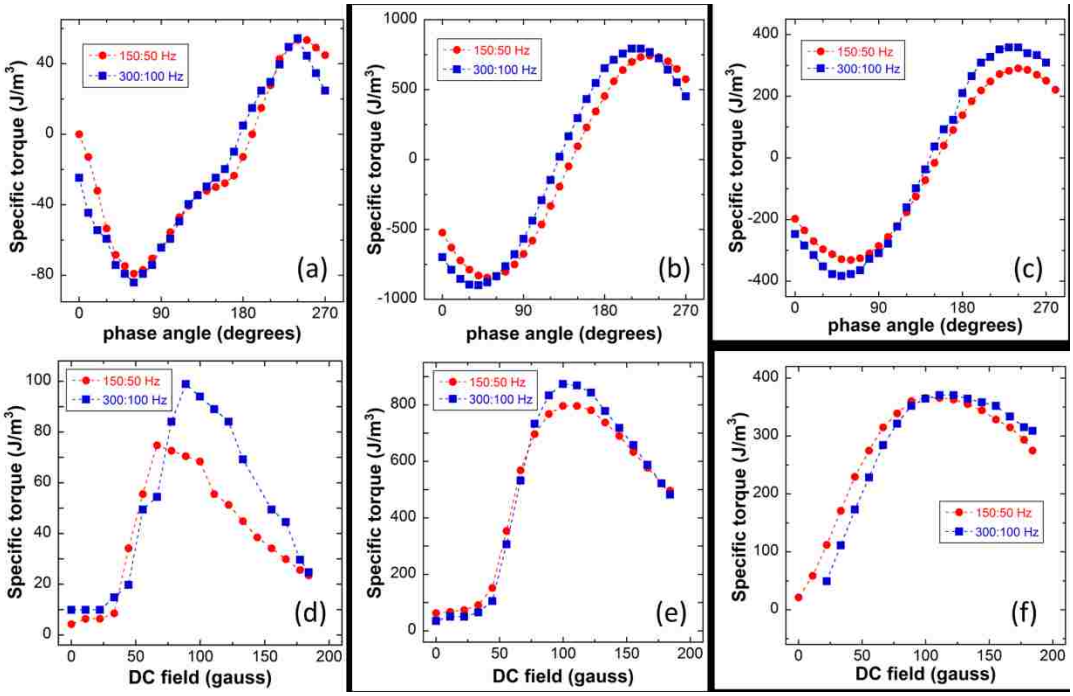

Figure 10-7. Torque curves for 3:1 (odd:odd) rational biaxial fields. Top row shows plots as a function of the phase angle for **(a)** spheres, **(b)** platelets, and **(c)** rods. Bottom row shows the corresponding torque curves as a function of the dc field amplitude.

previous field cases, a peculiar flattening out is observed at ~120–180°, distorting the curve from a simple sinusoidal shape.

dc field dependence. The dc field study [**Figure 10-7(d–f)**] shows that all three particles produce torque curves with a clear maximum. The torque curve for the spherical particles possesses a notably more jagged appearance, showing an abrupt jump near 100 G, whereas those produced with the anisometric particles are smooth and continuous. Nonetheless, in all three cases the torque maximizes for a dc field of ~100 G (or lower).

10.4.4 Surface flow reversal

Rotational flow in magnetic platelet suspensions subject to ac-ac-dc triaxial fields *other than* a vortex magnetic field was first observed in open-cell experiments reported in Chapter 7 [also Ref. 10.17]. In these experiments it is easy to observe the flow direction at the free fluid surface, especially if tracer particles are used. As mentioned earlier, a consideration of field symmetry cannot identify the flow direction, at least for noncirculating fields, but does

show that the flow can be reversed by changing the phase angle between the ac biaxial field components by $180°/m$. As mentioned above, for even, odd fields reversing the polarity of the dc field also reverses flow.

In addition to these predicted reversal mechanisms we have now discovered that flow reversal occurs when increasing the *amplitude* of the dc field component. When a dc field is applied orthogonal to the plane of a 2:1 rational field and progressively increased, rotational flow will develop in a dilute platelet suspension (a few volume percent). In an open cell, the fluid can be observed to move across the top surface, provided the axis of vorticity is not normal to this surface. At low dc fields, the fluid initially flows sluggishly, increasing in vigor as the dc field is increased. Near some critical dc field value, B^*_{dc}, the flow becomes vastly attenuated and sometimes appears frustrated, pulsating in one direction and then the opposite, or sometimes a nearly direct upwelling of fluid is observed that flows radially in variable directions at the surface. As the dc field is increased further, rotational flow resumes but in the *opposite direction* and becomes stronger as the dc field approaches the rms value of the rational field components (150 G). If the amplitude of the dc field is instead lowered to zero from its maximum value, a small but discernible hysteresis effect is observed. Essentially a reverse of the above-described events occurs with the subtle but consistent effect that flow reversal occurs at a slightly lower field (~2–3 G lower). **Figure 10-8** shows that B^*_{dc} increases as a power law of the root frequency of the 2:1 rational field. For this experiment the rms values of the magnetic induction of the biaxial components were set to 150 G. The surface flow direction is labeled as either "north" or "south" simply to distinguish the direction. A study of 4:3 fields revealed the flow direction to remain constant over the entire range of dc field amplitude, as well as with 3:1 fields, so flow reversal is apparently not merely a function of field symmetry.

To determine if the small magnetic remanence of the multilayered, magnesium fluoride-coated, Ni core platelets (JDSU, Flex Products Group) could play a role in dc-field driven flow reversal we did some additional experiments with pure Permalloy platelets

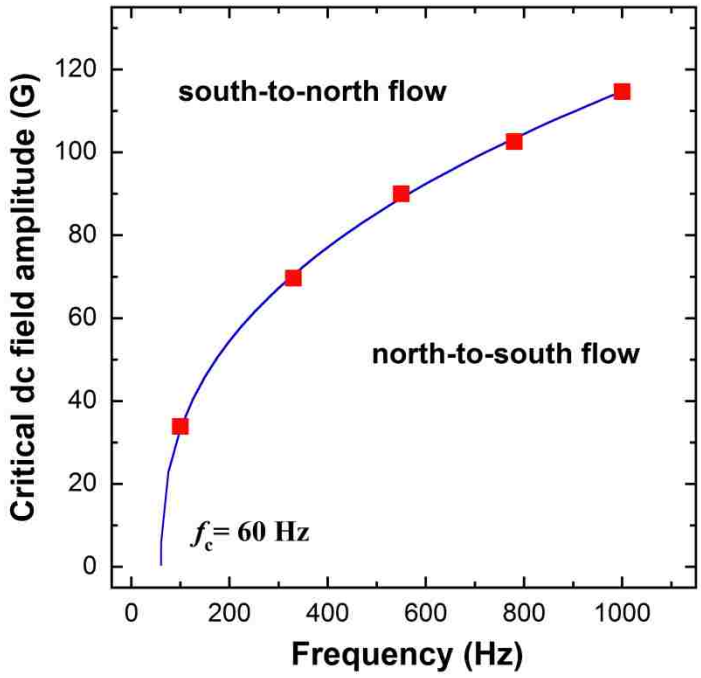

Figure 10-8. Critical-field flow reversal study. The critical dc field amplitude at which surface flow reversal occurs increases with the root component frequency magnitude as a power law: $B^*_{dc} = 7.95(f - f_c)^{0.39}$. These data were collected for the multilayer JDSU platelets subjected to ac–ac–dc triaxial fields whose ac biaxial component comprised a 2:1 field, 150 G_{rms}, phase = 0°.

(Novamet). These platelets also displayed the reversal effect, so remanence is not a determining factor either. Suspensions of carbonyl iron spheres also showed dc-field driven flow reversal but the Co nanorods did not, so particle shape evidently does play a role.

We were surprised to find that the observed flow reversal did not lead to a measured torque reversal. In fact, the only instance of torque reversal was for the spherical particles subjected to 3:2 fields [Figure 10-6(d)]. These results indicate that the flow reversal observed at the free top surface does not occur throughout the bulk of the fluid. At this time it is not clear what the origin of this surface reversal effect is and why it only manifests under certain conditions. However, we point out that a similar effect has been observed with ferrofluids subjected to rotating magnetic fields (the so-called spin-up flow case), in which the flow direction of the free top surface of the ferrofluid is observed to co-rotate or counter-rotate with the applied field depending on the field strength and/or frequency;

whereas, the bulk of the fluid is always found to co-rotate with the rotating field as verified by torque measurements [10.21] and the ultrasonic velocity profile method [10.22].

10.5 Discussion

A comparison of the absolute values of the peak specific torque densities we have achieved is shown in **Figure 10-9**. For all particles tested, the 2:1 fields produced the highest torque values. The next highest values—for spheres and nanorods at least—were produced using 3:2 fields, followed by 3:1 fields. Moreover, under all field conditions tested, the anisometric particles produced higher torques than the spherical particles, and the platelets achieved higher torques than the nanorods. For the three different fields the Permalloy platelets gave maximum torques from ~630–1280 $J \cdot m^{-3}$; the cobalt nanorods gave ~370–920 $J \cdot m^{-3}$; and the carbonyl iron spheres ranged from ~100–760 $J \cdot m^{-3}$. The disparity between the peak torques produced by the anisometric and spherical particles becomes progressively greater moving from the 2:1, to 3:2, and finally to the 3:1 fields. In fact, for

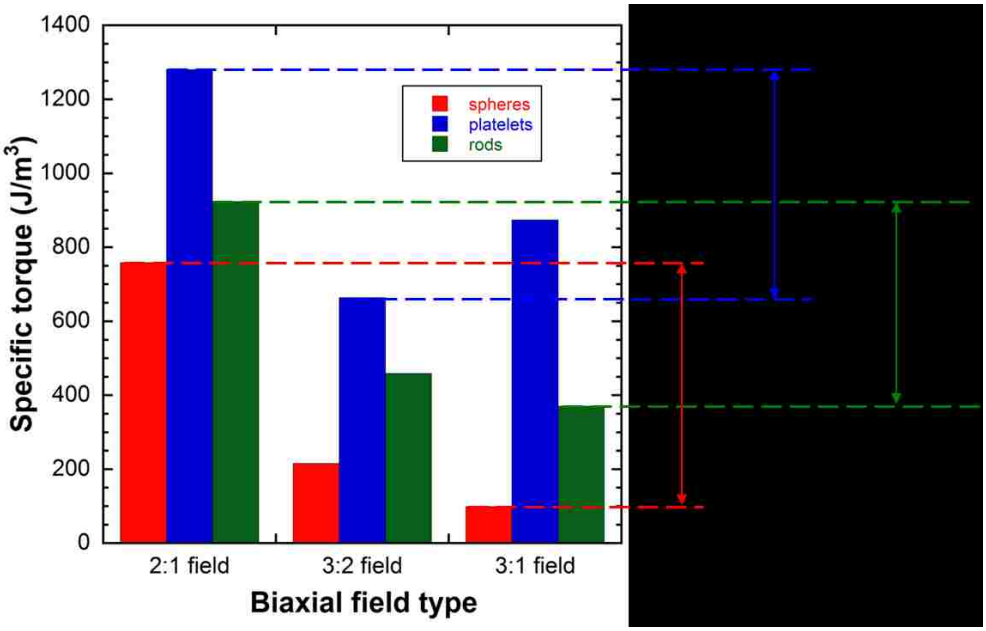

Figure 10-9. Summary of specific torque densities. Comparison of the peak torque values produced by each particle shape for each type of biaxial field. The platelets produced the highest peak torque values for all fields.

2:1 fields the spheres achieved ~59% of the peak torque produced by the platelets, but fell to only ~12% for the 3:1 field.

In a prior study (see Chapter 4 [also Ref. 10.14]) of mixing in *vortex* magnetic fields (in which case n:m = 1:1), cobalt nanorods were found to produce the highest specific torques (~1300–1500 $J \cdot m^{-3}$), followed by platelets (~600–900 $J \cdot m^{-3}$), and lastly spherical particles (~400–500 $J \cdot m^{-3}$). However, the cobalt rods used in that study were considerably shorter (l = 2–4 μm) compared to those used here (l = 8–10 μm), which may account for the difference *via* reduced steric interactions with the shorter rods, thus enabling more effective dispersion and more efficient mixing. Nonetheless, comparing the ranges of values obtained for the different particles from these two studies demonstrates that rational biaxial fields can generate mixing as powerful as that produced by vortex fields, and that anisometric particles produce substantially greater torques than spherical particles. The JDSU platelets have the additional advantage of being coated with MgF_2, rendering them inert to a wide range of chemicals.

10.6 Conclusions

We have measured the torque densities of rotational flows produced by a new class of ac–ac–dc triaxial magnetic fields. These fields are comprised of a rational biaxial field—a field whose orthogonal components have frequencies that form a rational ratio—and an orthogonal dc field. Depending on the "parity" of the rational biaxial field (*i.e.*, even:odd; odd:even; or odd:odd), the vorticity axis of the rotational flow can be oriented along any of the three orthogonal field component axes. Moreover, the intensity of the rotational flow can be controlled by judicious selection of the phase angle between the biaxial field components or the amplitude of the dc field. Torque measurements demonstrate that these flows are as effective as those produced by vortex magnetic fields. This new class of rational triaxial fields in combination with vortex magnetic fields comprises a general class of triaxial magnetic fields capable of producing strong, field-controllable, rotational flows that should

be useful for mixing and heat and mass transfer operations. Future work will focus on further quantifying the heat transfer efficacy of these rotational flows, and investigating the effect of a *time-dependent* third field component.

Acknowledgements

Sandia National Laboratories is a multi-program laboratory managed and operated by Sandia Corporation, a wholly owned subsidiary of Lockheed Martin Corporation, for the U.S. Department of Energy's National Nuclear Security Administration under contract DE-AC04-94AL85000. This work was supported by the Division of Materials Science, Office of Basic Energy Sciences, U.S. Department of Energy (DOE). We thank Matt Groo at Novamet and Vladimir Raksha, Paul Coombs, Tom Markantes, Bill Kittler, and Kees-Jan Delst at JDSU for supplying the magnetic platelets. We also thank Richard Bell at The Pennsylvania State University, Altoona College for synthesizing the cobalt nanorods.

References

10.1 J.E. Martin and K.J. Solis, Symmetry-breaking magnetic fields create a vortex fluid that exhibits a negative viscosity, active wetting, and strong mixing, *Soft Matter* **10**, 3993–4002 (2014).

10.2 R.E. Rosensweig, in *Ferrohydrodynamics*, (Cambridge University Press, Dover, NewYork, 1985).

10.3 B.A. Finlayson, Convective instability of ferromagnetic fluids, *J. Fluid Mech.* **40**, 753–767 (1970).

10.4 D.P. Lalas and S. Carmi, Thermoconvective stability of ferrofluids, *Phys. Fluids* **14**, 436–438 (1971).

10.5 R.A. Curtis, Flows and wave propagation in ferrofluids, *Phys. Fluids* **14**, 2096–2102 (1971).

10.6 B.U. Felderhof, Ferrohydrodynamic pumping of a ferrofluid or electrohydrodynamic pumping of a polar liquid through a planar duct, *Phys. Fluids* **23**, 042001 1–6 (2011).

10.7 L. Mao, S. Elborai, X. He, M. Zahn and H. Koser, Direct observation of closed-loop ferrohydrodynamic pumping under traveling magnetic fields, *Phys. Rev. B: Condens. Matter Mater. Phys.* **84**, 104431 1–7 (2011).

10.8 R. Moskowitz and R.E. Rosensweig, Nonmechanical torque-driven flow of a ferromagnetic fluid by an electromagnetic field, *Appl. Phys. Lett.* **11**(10), 301–303 (1967).

10.9 R.E. Rosensweig, J. Popplewell and R.J. Johnston, Magnetic fluid motion in rotating field, *J. Magn. Magn. Mater.* **85**, 171–180 (1990).

10.10 M. Zahn and D.R. Greer, Ferrohydrodynamic pumping in spatially uniform sinusoidally time-varying magnetic fields, *J. Magn. Magn. Mater.* **149**, 165–173 (1995).

10.11 A. Chaves, M. Zahn and C. Rinaldi, Spin-up flow of ferrofluids: Asymptotic theory and experimental measurements, *Phys. Fluids* **20**, 053102 1–18 (2008).

10.12 J.E. Martin, L. Shea-Rohwer and K.J. Solis, Strong intrinsic magnetic mixing in vortex magnetic fields, *Phys. Rev. E: Stat., Nonlinear, Soft Matter Phys.* **80**, 016312 1–6 (2009).

10.13 J.E. Martin, Theory of strong intrinsic mixing of particle suspensions in vortex magnetic fields, *Phys. Rev. E: Stat., Nonlinear, Soft Matter Phys.* **79**, 011503 1–12 (2009).

10.14 K.J. Solis, R.C. Bell and J.E. Martin, Vortex magnetic field mixing with anisometric particles, *J. Appl. Phys.* **107**, 114911 1–4 (2010).

10.15 K.J. Solis and J.E. Martin, Isothermal Magnetic Advection: Creating functional fluid flows for heat and mass transfer, *Appl. Phys. Lett.* **97**, 034101 1–3 (2010).

10.16 K.J. Solis and J.E. Martin, Controlling the lattice spacing in isothermal magnetic advection to enable tunable heat and mass transfer, *J. Appl. Phys.* **112**, 094912 1–7 (2012).

10.17 K.J. Solis and J.E. Martin, Stimulation of vigorous rotational flows and novel flow patterns using triaxial magnetic fields, *Soft Matter* **8**, 11989–11994 (2012).

10.18 K.J. Solis and J.E. Martin, Multiaxial fields drive the thermal conductivity switching of a magneto-responsive platelet suspension, *Soft Matter* **9**, 9182–9188 (2013).

10.19 J.E. Martin, A resonant biaxial Helmholtz coil employing a fractal capacitor bank, *Rev. Sci. Instrum.* **84**, 094704 1–11 (2013).

10.20 J.E. Martin, R.A. Anderson and R.L. Williamson, Generating strange magnetic and dielectric interactions: Classical molecules and particle foams, *J. Chem. Phys.* **118**, 1557–1570 (2003).

10.21 A.D. Rosenthal, C. Rinaldi, T. Franklin and M. Zahn, Torque measurements in spin-up flow of ferrofluids, *Trans. ASME* **126**, 198–205 (2004).

10.22 A. Chaves, C. Rinaldi, S. Elborai, X. He and M. Zahn, Bulk flow in ferrofluids in a uniform rotating magnetic field, *Phys. Rev. Lett.* **96**, 194501 1–4 (2006).

Chapter 11

Fully alternating, triaxial electric or magnetic fields offer new routes to fluid vorticity[11]

Noncontact methods of generating strong fluid vorticity are important to problems involving heat and mass transfer, fluid mixing, active wetting, and droplet transport. Furthermore, because zero or even negative shear viscosities can be induced, vorticity can greatly extend the control range of the smart fluids used in magnetorheological devices. In Chapters 9 and 10 we have shown that a particular class of ac-ac-dc triaxial fields (*symmetry-breaking rational fields*) can create strong vorticity in magnetic particle suspensions and have presented a theory of the vorticity that is based on the symmetry of the 2-d Lissajous trajectories of the field and its converse. In this chapter we demonstrate that there are three countably infinite sets of fully alternating ac-ac-ac triaxial fields whose frequencies form *rational triads* that have the symmetry required to drive fluid vorticity. The symmetry of the 3-d Lissajous trajectories of the field and its converse can be derived and from this the direction of the vorticity axis can be predicted, as can the dependence of the sign of the vorticity on the phase relations between the three field components. Experimental results are presented that validate the symmetry theory. These discoveries significantly broaden the class of triaxial fields that can be exploited to produce strong noncontact flow.

11.1 Introduction

Methods of generating noncontact fluid motion have applications to problems such as mixing and heat and mass transfer, active wetting, control of droplet motion, biomimetic dynamics, and generating fluids that are effectively inviscid in applied shear. One approach is to prepare a suspension of magnetic or dielectric particles to create fluids that are field

[11] Originally published as: J.E. Martin and K.J. Solis, Fully alternating, triaxial electric or magnetic fields offer new routes to fluid vorticity, *Soft Matter* **11**, 241–254 (2015).

responsive. When such fluids are exposed to uniaxial dc or ac magnetic or electric fields they appreciably stiffen, creating a rheology that is approximately that of a Bingham fluid [11.1–11.3]. When the field is biaxial, with at least one of the field components ac, the same sort of stiffening occurs if the particles are spherical, but if the particles are oblate spheroids (platelets) the fluid can form highly organized advection patterns (see Chapter 5 [also Ref. 11.4]) and lattices of vortices (see Chapter 7 [also Ref. 11.5]), depending on the details of the field frequencies, phase angle and particle concentration. In contrast, a triaxial field comprised of a dc field orthogonal to a rotating field can induce bulk vorticity (see Chapter 3 [also Refs. 11.6, 11.7]). Inducing bulk vorticity with such a field is intuitively reasonable because such a *vortex field* is circulating and can be reversed. Because this vorticity is a consequence of the symmetry of the field trajectory its occurrence is not dependent on particle shape (see Chapter 4 [also Refs. 11.8, 11.9]). More complex ac-ac-dc triaxial fields, consisting of components with distinct frequencies, can induce vorticity, even though many of these field trajectories lack circulation (see Chapter 9 [also Ref. 11.10]). These fields even include those whose trajectories lie on open curves and so simply travel back and forth on a curved line. Again, particle shape is not a primary factor since the symmetry of such fields drives the vorticity (see Chapter 10 [also Ref. 11.11]).

The problem addressed in this chapter is whether or not fully alternating, ac-ac-ac triaxial fields can be used to generate fluid vorticity and if so, how the direction of the vorticity axis and the sign of the flow (clockwise or counterclockwise) can be predicted as a function of the three field frequencies and their relative phase angles. We show that these predictions can be made by analyzing the symmetry of the field trajectories. Observations of the direction and sign of the vorticity validate the relevance of the field symmetry analysis. Measurements of the torque density as a function of two independent phase angles produce a 3-d plot having translational symmetries that are in agreement with predictions and also show that the specific torque density exceeds the energy density of the field.

This research is a contribution to the rapidly growing area of driving colloidal fluids far from equilibrium to create novel structures and dynamic phenomena [11.12, 11.13]. For example, when magnetic colloids are confined to an air-liquid interface the application of an ac magnetic field normal to the interface forces the assembly of the particles into segmented snake-like structures that emerge that are coupled to indirectly induced surface waves [11.14–11.16]. Symmetry breaking of various kinds can induce these snakes to swim. When the particles are confined to a liquid–liquid interface the field induces the formation of ring-like particle assemblies termed "asters" and "anti-asters" that can be induced to open, grab cargo, and then transport and discharge this cargo [11.17]. Particles confined to a magnetic garnet substrate can interact with an applied field through the formation of magnetic stripes [11.18, 11.19] and bubbles [11.20–11.23]. The particles interact with these magnetic domains and by clever field manipulations the coherent motions of particle assemblies can be induced. These motions can be as simple as ballistic motion, but much more complex dynamics, such as coherent exchange hopping, can be induced.

11.2 Background

In Chapter 9 we demonstrated that symmetry-breaking, rational magnetic fields can possess the symmetry that creates vorticity when applied to magnetic particle suspensions [11.10]. These fields are comprised of two orthogonal ac components whose frequency ratio is a rational number, and a third, mutually orthogonal, dc field whose purpose is to break the symmetry of the rational field itself, thus creating the underlying field parity (direction motion on a closed curve) or symmetry (for open curves) that allows for vorticity. Such ac-ac-dc triaxial fields can produce vorticity along the high frequency, low frequency or dc field axes, depending on the frequency ratio of the ac components, and can generate specific torque densities well in excess of the energy density of the applied field. The dependence of the direction and sign of the vorticity on both the phase angle and the sign of the dc field can be predicted by a consideration of the symmetry of the 2-d Lissajous trajectories of the field

and its converse. The basic conclusions can be expressed concisely. The frequency ratio of the ac components can be expressed as n:m, where at least one of these integers is odd. (1) The vorticity axis is parallel to the odd frequency component unless both n and m are odd, in which case it is parallel to the dc field. (2) Only for the odd:odd case does reversing the dc field *not* reverse the sign of the vorticity. (3) Changing the phase angle by certain discrete amounts will reverse the vorticity while maintaining its magnitude. These conclusions were experimentally validated in Chapter 10 [also Ref. 11.11], where the magnitude of the vorticity is also reported.

Fully alternating triaxial fields can be represented as 3-d Lissajous curves and it is not obvious that such fields possess the symmetry needed to drive vorticity in a magnetic particle suspension. In this study we consider four enumerable classes of fully alternating triaxial fields whose frequencies form a rational triad l:m:n, where l, m and n are integers. These classes are odd:odd:odd, even:odd:odd, even:even:odd where l:m is odd:odd, and even:even:odd where l:m is even:odd. We will show that three of these classes possess the symmetry required to produce vorticity and that the direction of vorticity can be predicted, as well as the phase changes that produce flow reversal at constant magnitude of vorticity. We consider fields of the form

$$\frac{\mathbf{H}(t)}{H_{ac}} = F_i(2\pi l f_0 t)\hat{\mathbf{x}} + F_j(2\pi m f_0 t)\hat{\mathbf{y}} + F_k(2\pi n f_0 t)\hat{\mathbf{z}} \qquad (11\text{-}1)$$

where $F_1(x) = \sin(x)$, $F_2(x) = \cos(x)$, $F_3(x) = -\sin(x)$, and $F_4(x) = -\cos(x)$. Because these functions may be written $\sin(x+\phi)$, where $\phi = 0°$, $90°$, $180°$ and $270°$, respectively, we often refer to the various functions as "phases". For any given rational triad we thus consider $4^3 = 64$ fields, but only 16 of these are distinct Lissajous *trajectories*, since the zero of time is not an important factor in a steady-state excitation. (In this study a trajectory refers to the curve produced by the dynamic field vector as well as its direction of motion on that curve, which is referred to as the *field parity* if the meaning of parity is not clear. The term

numerical parity is used to refer to an integer being even or odd.) However, we shall see that considering all 64 cases simplifies the analysis. We have chosen this particular set of phases because in these cases all projections of the 3-d Lissajous curve along the three principal axes yield highly symmetric 2-d Lissajous curves, and this quality simplifies the analysis. We will refer to the fields expressed by Equation (11-1) as principal Lissajous curves.

A few basic facts about *symmetric* 2-d Lissajous curves and trajectories bear mentioning (for details and an analytical derivation of the following statements see Chapter 9 [also Ref. 11.10], especially Appendix A therein). Consider these curves to be in *v*-*w* plane. First, there are two types of curves: *open* and *closed* and these occur at certain discrete phases, **Figure 11-1**. The closed curves have both a horizontal and a vertical symmetry plane (symmetric under each of the mappings $v \to -v$ and $w \to -w$) and thus are symmetric upon rotation by 180° around the orthogonal axis $\mathbf{v} \times \mathbf{w}$. These closed curves have parity in the sense that their time evolution is antisymmetric. In other words, a recording of the time evolution of these parametric plots lacks time reversal symmetry because it is possible to move on these curves in opposite directions. Changing the direction of the motion of the field (parity) requires only a phase shift. When the symmetry-breaking dc field is applied vorticity occurs that can be reversed by changing the parity of the trajectory alone: the Lissajous curve remains unchanged.

The open curves do have time reversal symmetry because once you reach a terminus you must simply turn back. However, the open curves have less symmetry than the closed curves: in the even:odd (or odd:even) case there is a single symmetry plane whereas in the odd:odd case there are no symmetry planes but the curve is symmetric under rotation by 180° around $\mathbf{v} \times \mathbf{w}$. In each case there are two distinct open curves and these occur at distinct sets of phase angles. For the even, odd cases these separate open curves are related by a single reflection, (this may be either $v \to -v$ or $w \to -w$, but not both) but the distinct odd:odd curves are related by a reflection about either axis. Strangely enough, it can be

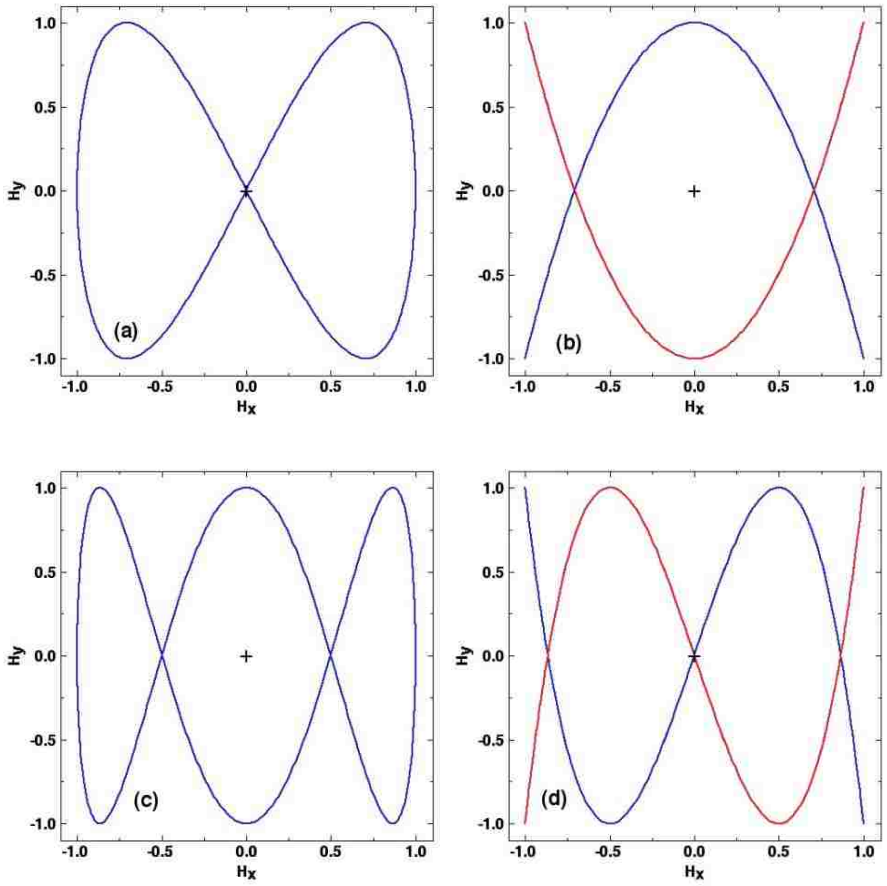

Figure 11-1. **(a)** Closed curve for a 2:1 ratio. **(b)** Open curves for the 2:1 ratio. **(c)** Closed curve for a 3:1 ratio. **(d)** Open curves for the 3:1 ratio.

shown that the results of the relevant symmetry operations (reflections) on the *trajectories* of the closed curves are identical to those of the open curves themselves [11.10]. When the symmetry-breaking dc field is applied vorticity occurs that can be reversed by changing the *orientation* of the Lissajous curve.

The key point is that for symmetry-breaking rational fields flow reversal occurs by reversing the field parity, whereas for open curves flow reversal occurs by changing the orientation of the Lissajous curve.

The object of this chapter is to determine whether 3-d Lissajous trajectories have the required symmetry to induce vorticity. In **Figure 11-2** we show four 3-d Lissajous curves for the simplest rational triad, 1:2:3. Each of these curves has distinct phases. In Figure 11-2

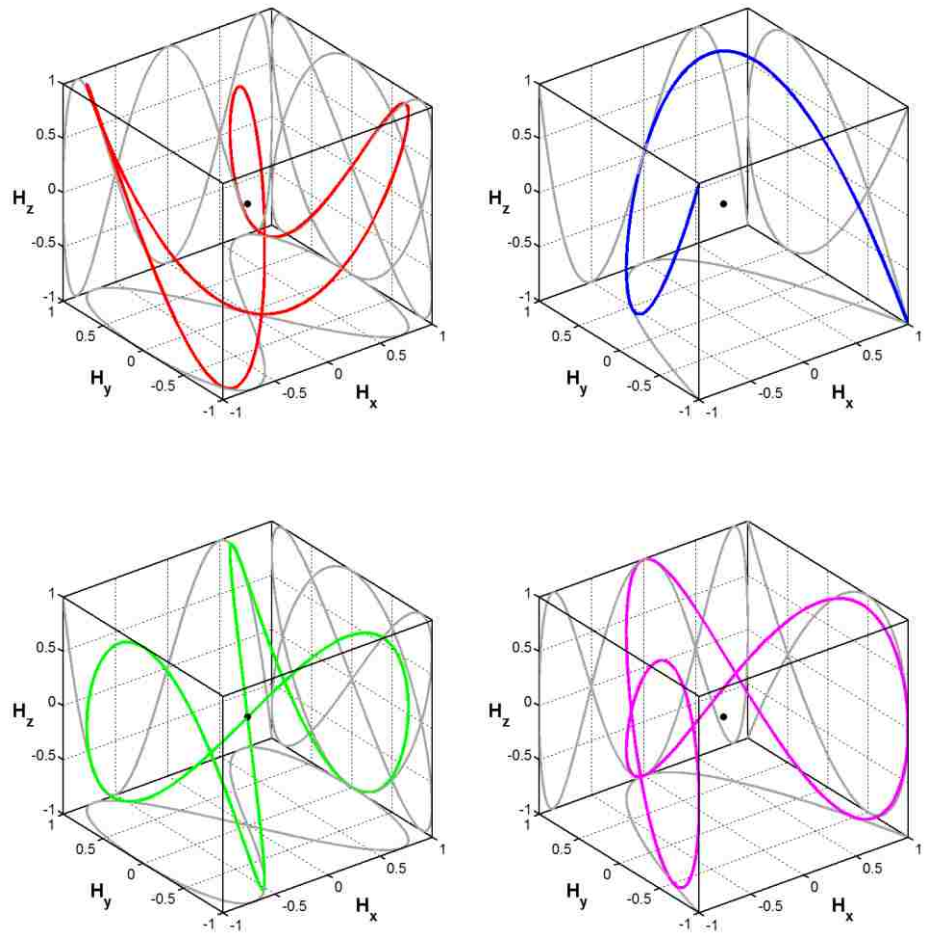

Figure 11-2. Four 3-d Lissajous curves for the rational triad 1:1:2:3. These fields give vorticity around the *y* axis. In **(top left)** the respective phases are [S, S, C] and all of the projections along principal axes are closed curves. In **(top right)** the phases are [S, C, S] and the principal projections are open curves (thus the 3-d curve is itself open). In **(bottom left)** the phases are [S, S, S] and there are two closed curve projections and one open curve projection. In **(bottom right)** the phases are [S, C, C] and there are two open curve projections and one closed curve projection. The number of closed projections determines the change that causes flow reversal.

(top left) the closed curve is given by [S, S, C] (*i.e.*, $\mathbf{H}(t) = H_{ac}\left[\sin(2\pi m f_0 t)\hat{\mathbf{x}} + \sin(2\pi m f_0 t)\hat{\mathbf{y}} + \cos(2\pi d f_0 t)\hat{\mathbf{z}}\right]$) and all of the projections are closed curves, as they must be. In Figure 11-2 (top right) the phases are [S, C, S] and all of the projections are open curves (thus the 3-d curve is itself open). In Figure 11-2 (bottom left) the closed curve is given by [S, S, S] and there are two closed projections. In Figure 11-2 (bottom right) the closed curve is given by [S, C, C] and there is one closed projection. These are the four types of principal 3-d Lissajous trajectories for this rational triad.

Before launching into the details of the symmetry arguments it is helpful to outline our approach, which is a straightforward, but somewhat laborious method focusing on the three principal projections of the 3-d Lissajous trajectories. First, for any rational triad we will create a method of identifying the type of each principal projection as a function of the discrete phase angles defined above. Second, we will conduct reflections and rotations of the field and its converse to determine if these trajectories possess the symmetry that supports vorticity. For a suspension of induced dipoles the field and its converse are physically identical, and this principle is critical to the symmetry arguments. This procedure will enable the prediction of both the *direction* and *sign* of the vorticity. It will also identify those phase changes necessary to reverse flow.

11.3 Experimental

The magnetic particle suspension consisted of molybdenum-Permalloy platelets ~50 μm across by 0.4 μm thick (Novamet Corp.) dispersed into isopropyl alcohol at a low volume fraction. The uniform triaxial ac magnetic fields (rational triads) were produced by three orthogonally-nested Helmholtz coils, operating in series resonance with appropriately-configured capacitor banks, two of which employ a computer-controlled fractal design [11.24]. For all of the rational triad fields in this work the fundamental frequency was 50 Hz (with the exception of 1:2:6, for which the root frequency was 100.4 Hz) and all three induction field component amplitudes were 150 G_{rms}. All three field components were phase-locked *via* two Agilent/HP function generators (equipped with Option 005), allowing for *stable* control of the phase angle of each component. (If the field components are not phase-locked there will be a very slow phase modulation between the components due to the finite difference in the oscillator frequency of each function generator, preventing meaningful studies of the phase angle.)

Surface flow observations of vorticity were performed in an open glass cell (~3 cm square × 6 cm high) by using a polystyrene bead (~4 mm), in which case the rotation

direction of the bead (clockwise or counterclockwise) was easily discerned. To quantify the magnitude of the vorticity, the torque density of the suspension was computed from measured angular displacements on a custom-built torsion balance. In this case the suspension (1.5 vol%) was contained in a small vial (1.8 mL) attached at the end of the torsion balance and suspended into the central cavity of the Helmholtz coils *via* a 96.0 cm-long, 0.75 mm-diameter nylon fiber with a torsion constant of ~13 μN·m rad^{-1}.

11.4 Symmetry theory

The classification of the type of trajectory of the 2-d projections is described in Appendix A, from which **Tables 11-1** and **11-2** can be constructed, one for odd:even or even:odd ratios the other for odd:odd. For the discrete set of 2-d Lissajous trajectories of the form $F_i(q\omega t)\hat{\mathbf{v}} + F_j(p\omega t)\hat{\mathbf{w}}$ these tables identify whether the curve is open or closed. For closed curves the *parity of the trajectory* is given as either plus "+" or minus "−" (arbitrary distinction) and for open curves the *symmetry of the curve* is likewise designated as either plus "+" or minus "−" (arbitrary distinction). For example, for a frequency ratio $q{:}p = 3{:}4$ phases of [C, S] give a "+Closed" trajectory whereas phases of [S, C] give a "−Open" curve.

Table 11-1. Classification of projections for odd q, even p [C, S indicates cos($q\omega$t), sin($p\omega$t) etc.]

q,p	+Closed	-Closed	+Open	-Open
	S,S	C,S	S,C	C,C
q=1,5…	-S,S	-S,-S	-S,C	-C,C
p=2,6…	-C,-S	-C,S	C,-C	-S,-C
	C,-S	S,-S	-C,-C	S,-C
	S,S	C,S	C,C	S,C
q=3,7…	-S,S	-S,-S	-C,C	-S,C
p=2,6…	-C,-S	-C,S	-S,-C	C,-C
	C,-S	S,-S	S,-C	-C,-C
	S,S	S,-S	S,C	S,-C
q=1,5…	C,S	C,-S	C,C	C,-C
p=4,8…	-S,S	-S,-S	-C,C	-S,-C
	-C,S	-C,-S	-S,C	-C,-C
	S,S	S,-S	S,-C	S,C
q=3,7…	C,S	C,-S	C,-C	C,C
p=4,8…	-S,S	-S,-S	-S,-C	-S,C
	-C,S	-C,-S	-C,-C	-C,C

Table 11-2. Classification of projections for odd q, odd p ($p > q$) [C, S indicates cos($q\omega$t), sin($p\omega$t) etc.]

q,p	+Closed	-Closed	+Open	-Open
q=1,5… p=1,5…	C,S -C,-S S,-C -S,C	S,C -S,-C -C,S C,-S	C,C S,S -C,-C -S,-S	-C,C C,-C -S,S S,-S
q=3,7… p=1,5…	S,C -S,-C C,S -C,-S	-S,C S,-C -C,S C,-S	S,S -S,-S C,-C -C,C	C,C -C,-C S,-S -S,S
q=1,5… p=3,7...	-S,C S,-C -C,S C,-S	S,C -S,-C C,S -C,-S	S,S -S,-S C,-C -C,C	C,C -C,-C S,-S -S,S
q=3,7… p=3,7…	S,C -S,-C -C,S C,-S	C,S -C,-S -S,C S,-C	S,S C,C -S,-S -C,-C	S,-S C,-C -S,S -C,C

These tables are central to analyzing each of the four classes of Lissajous trajectories. Note that each projection can be given by four different fields. These fields are related to each other by a shift in the zero of time, as discussed in Appendix B.

11.4.1 Symmetries that support vorticity

Before discussing the results for the various field types considered, it is helpful to have a clear idea of the field symmetries that stimulate vorticity, since this paper is based on searching for these symmetries. In **Figure 11-3** a rotating cylinder aligned along the z axis of a Cartesian coordinate system is portrayed, with the direction of rotation indicated. This direction of rotation is antisymmetric under reflections about either the x-z plane ($y \to -y$) or the y-z plane $(x \to -x)$, but symmetric under reflection about the x-y plane $(z \to -z)$. Likewise, this direction of rotation is symmetric to a C_2 (180°) rotation about the vorticity axis z $(x \to -x, y \to -y)$ and antisymmetric to 180° rotations about either x $(y \to -y, z \to -z)$ or y $(x \to -x, z \to -z)$. Of course, these rotational symmetries are a result of the reflection symmetries. Symmetric operations and combinations thereof preserve the sign of the vorticity, whereas antisymmetric operations reverse the vorticity. By enumerating these operations it is found that for each vorticity axis the fields form the

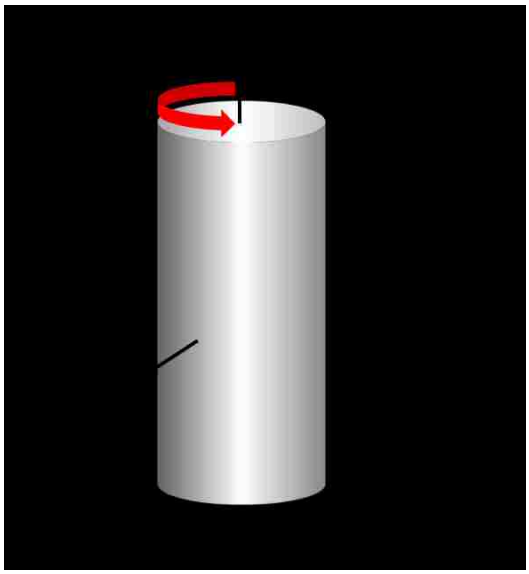

Figure 11-3. A rotating cylinder aligned along the z axis has a symmetric reflection around the x–y plane and antisymmetric reflections around the x–z and y–z planes.

Table 11-3. Fields with common vorticity sign are listed for each principal vorticity axis, *X*, *Y* or Z. In each column a field and its converse are shaded similarly

X		Y		Z	
CW	CCW	CW	CCW	CW	CCW
x, y, z	x,-y, z	x, y, z	-x, y, z	x, y, z	-x, y, z
-x, y, z	x, y, -z	x,-y, z	x, y,-z	x, y,-z	x,-y, z
x,-y,-z	-x, y,-z	-x, y,-z	x,-y,-z	-x,-y, z	x,-y,-z
-x,-y,-z	-x,-y, z	-x,-y,-z	-x,-y, z	-x,-y,-z	-x, y,-z

distinct CW and CCW groups in **Table 11-3**. For example, for vorticity around the z axis the fields $[x, y, z]$, $[x, y, -z]$, $[-x, -y, z]$ and $[-x, -y, -z]$ must have the same vorticity. The field $[-x, -y, -z]$ is simply the converse of $[x, y, z]$ and therefore must produce the same vorticity, just as $[-x, -y, z]$ is converse to $[x, y, -z]$. To determine whether any particular Lissajous trajectory drives vorticity one can assume a particular vorticity axis and determine whether the transformations given in Table 11-3 lead to the proper relative vorticity directions. This process will become clear by giving some examples.

11.4.2 Class I: Even, odd, odd fields

Open curves. We start with the case of even, odd, odd fields and as an example use the rational triad 1:2:3 with the phases of the field components given by [S, C, S], which

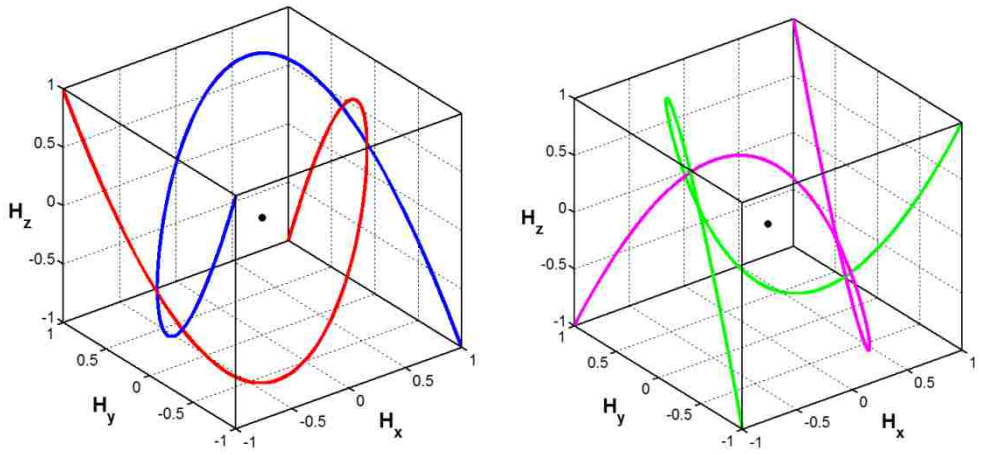

Figure 11-4. Flow reversal illustrated by complementary Lissajous field objects for a 1:2:3 triad. **(left)** A field with the phases [S, C, S] (blue) and its converse (red) [−S, −C, −S] produce clockwise flow. **(right)** Counterclockwise flow is produced with the phases [S, C, −S] (green) and [−S, −C, S] (magenta). Despite the fact that in each case the field and its converse are *chiral* enantiomorphs, they produce the same sense of vorticity because chirality is not a symmetry possessed by vorticity. However, *reflection* symmetry is obeyed by vorticity and is displayed between the two Lissajous field objects, as illustrated by the blue and green curves, which are reflections of each other about the *y*–*z* and *x*–*y* planes, as are the red and magenta curves.

leads to the simple open curve in Figure 11-2 (top right). Open 3-d curves are a good place to start this analysis because their symmetries alone are of importance: there is no need to worry about the parity of the trajectory, as there is none. It is thus easy to visualize the symmetry operations. Closed curves will be treated later. Note that all of the projections are necessarily open in this case.

It is interesting to note that this open Lissajous curve is chiral, which seems suggestive. But the converse field [−S, −C, −S] in **Figure 11-4**(left) is related to the field by three reflections and thus must have opposite handedness. This converse field must produce the same direction and sign of vorticity, so field chirality has nothing to do with vorticity, because it is simply not a symmetry of vorticity. In fact, fields that produce vorticity are not generally chiral.

In **Table 11-4** are tabulated the symmetries of the three 2-d Lissajous curves— $L_{1,2}$, $L_{2,3}$, $L_{1,3}$ with frequency ratios 1:2, 2:3, 1:3, respectively— that result when the 3-d 1:2:3 Lissajous curve is projected along the three principal axes. These results are obtained by

Table 11-4. Projections for the rational triad 1:2:3. An "S" in the column labeled "2" indicates sin(2ωt), etc.

1	2	3	$L_{1,2}$	$L_{2,3}$	$L_{1,3}$
Sin	**Sin**	**Sin**	**$+C_d$**	**$+C_d$**	**+O**
S	S	C	$+C_d$	$-C_d$	$-C_d$
S	S	-S	$+C_d$	$+C_d$	-O
S	S	-C	$+C_d$	$-C_d$	$+C_d$
Sin	**Cos**	**Sin**	**+O**	**-O**	**+O**
S	C	C	+O	+O	$-C_d$
S	C	-S	+O	-O	-O
S	C	-C	+O	+O	$+C_d$
Sin	**- Sin**	**Sin**	**$-C_d$**	**$-C_d$**	**+O**
S	-S	C	$-C_d$	$+C_d$	$-C_d$
S	-S	-S	$-C_d$	$-C_d$	-O
S	-S	-C	$-C_d$	$+C_d$	$+C_d$
Sin	**-Cos**	**Sin**	**-O**	**+O**	**+O**
S	-C	C	-O	-O	$-C_d$
S	-C	-S	-O	+O	-O
S	-C	-C	-O	-O	$+C_d$
Cos	**Sin**	**Sin**	**$-C_d$**	**$+C_d$**	**$-C_d$**
C	S	C	$-C_d$	$-C_d$	-O
C	S	-S	$-C_d$	$+C_d$	$+C_d$
C	S	-C	$-C_d$	$-C_d$	+O
Cos	**Cos**	**Sin**	**-O**	**-O**	**$-C_d$**
C	C	C	-O	+O	-O
C	C	-S	-O	-O	$+C_d$
C	C	-C	-O	+O	+O
Cos	**- Sin**	**Sin**	**$+C_d$**	**$-C_d$**	**$-C_d$**
C	-S	C	$+C_d$	$+C_d$	-O
C	-S	-S	$+C_d$	$-C_d$	$+C_d$
C	-S	-C	$+C_d$	$+C_d$	+O
Cos	**-Cos**	**Sin**	**+O**	**+O**	**$-C_d$**
C	-C	C	+O	-O	-O
C	-C	-S	+O	+O	$+C_d$
C	-C	-C	+O	-O	+O
- Sin	**Sin**	**Sin**	**$+C_d$**	**$+C_d$**	**-O**
-S	S	C	$+C_d$	$-C_d$	$+C_d$
-S	S	-S	$+C_d$	$+C_d$	+O
-S	S	-C	$+C_d$	$-C_d$	$-C_d$
- Sin	**Cos**	**Sin**	**+O**	**-O**	**-O**
-S	C	C	+O	+O	$+C_d$
-S	C	-S	+O	-O	+O
-S	C	-C	+O	+O	$-C_d$
- Sin	**- Sin**	**Sin**	**$-C_d$**	**$-C_d$**	**-O**
-S	-S	C	$-C_d$	$+C_d$	$+C_d$
-S	-S	-S	$-C_d$	$-C_d$	+O
-S	-S	-C	$-C_d$	$+C_d$	$-C_d$
- Sin	**-Cos**	**Sin**	**-O**	**+O**	**-O**
-S	-C	C	-O	-O	$+C_d$
-S	-C	-S	-O	+O	+O
-S	-C	-C	-O	-O	$-C_d$

-Cos	**Sin**	**Sin**	**$-C_d$**	**$+C_d$**	**$+C_d$**
-C	S	C	$-C_d$	$-C_d$	+O
-C	S	-S	$-C_d$	$+C_d$	$-C_d$
-C	S	-C	$-C_d$	$-C_d$	-O
-Cos	**Cos**	**Sin**	**-O**	**-O**	**$+C_d$**
-C	C	C	-O	+O	+O
-C	C	-S	-O	-O	$-C_d$
-C	C	-C	-O	+O	-O
-Cos	**- Sin**	**Sin**	**$+C_d$**	**$-C_d$**	**$+C_d$**
-C	-S	C	$+C_d$	$+C_d$	+O
-C	-S	-S	$+C_d$	$-C_d$	$-C_d$
-C	-S	-C	$+C_d$	$+C_d$	-O
-Cos	**-Cos**	**Sin**	**+O**	**+O**	**$+C_d$**
-C	-C	C	+O	-O	+O
-C	-C	-S	+O	+O	$-C_d$
-C	-C	-C	+O	-O	-O

reference to Tables 11-1 and 11-2 and include all 64 phases under consideration. Note that two of these projections are even, odd and one is odd:odd. Only odd:odd open 2-d Lissajous curves have a zero crossing, so the 3-d Lissajous curve cannot cross zero because this would require that all three projections have a zero crossing. Thus the field never vanishes.

For the field phases [S, C, S] the three projections are given by (+O, −O, +O), respectively, where "O" is an abbreviation for "Open" and the plus and minus signs serve to differentiate the two distinct open projections. The converse field [−S, −C, −S] gives the projections (−O, +O, +O) and even though these projections differ from those of the field they are *physically equivalent* and thus produce the same direction, sign and magnitude of vorticity.

Let us now assume that the *y* axis is the vorticity axis, which is along the field having the relative frequency of 2. Then from Table 11-3 we see that the phases [S, −C, S] should produce the same sign of vorticity. Table 11-4 shows that these phases give the projections (−O, +O, +O). The reflection $y \to -y$ therefore maps the field onto the physically equivalent *converse* field, which conserves vorticity. Likewise, a rotation about the *y* axis, [−S, C, −S], gives (+O, −O, +O) and thus maps the field onto itself. These results are consistent with the *y* axis being the vorticity axis. Experiments confirm that the vorticity

direction is the same for all of these phases and that it is indeed around the *y* axis, which is the even component of this rational triad. The sign of the vorticity is also identical for these phases.

If *y* is the vorticity axis the phases with opposite vorticity (Table 11-3) are the reflection $x \to -x$, [−S, C, S], the reflection $z \to -z$, [S, C, −S], the rotation about the *x* axis, [S, −C, −S], and the rotation about the *z* axis, [−S, −C, S]. These fields give the projections (+O, −O, −O), (+O, −O, −O), (−O, +O, −O) and (−O, +O, −O), respectively. None of these projections map onto those of the original field or its converse and experiments confirm that this group does indeed produce vorticity having the opposite sign of that produced by the field [S, C, S], as predicted. These *flow-reversing fields* are shown in Figure 11-4 (right) and note that flow reversal can occur by a change in the *orientation* of the 3-d Lissajous curve, quite like for symmetry-breaking rational fields that are open curves. In particular, a change in the orientation of the $L_{1,3}$ projection is sufficient to cause flow reversal.

Note that if the *x* or *z* axis is assumed to be the vorticity axis then the relevant reflections and rotations that should conserve or reverse vorticity do not do so.

These results (and many others) are tabulated in **Table 11-5** along with experimental observations of the direction of fluid vorticity. This table is divided into four blocks and each block is divided into two groups that should have opposite vorticity if the symmetry arguments given above are correct. The case just described for the curves with all open projections are in the third block and the experimental observations of the flow direction, given in the last column, indicate that the two groups do indeed give opposite flow. Note, however, that there are twice as many entries in this block as those we have just discussed, which are of the class [±S, ±C, ±S]. These additional entries are of the class [±C, ±C, ±C] and are simply alternative representations of the same Lissajous curves. It is easy to show that for 1:2:3 these two sets are related by redefining the zero of time. For example, the time shift $2\pi f_0 t \to 2\pi f_0 t' + 90°$ changes [S, C, S] to [C, −C, −C], which does of course have

the same projections, (+O, −O, +O). In fact, the eight CW fields listed in this group have only two projections, as do the eight CCW fields, so each Lissajous trajectory can be obtained by four different fields. These features are common to the other three blocks, so we will not belabor this point further.

Table 11-5. Fields, projections and observed flow directions for 1:2:3. Within each of the 4 blocks of 16 rows the fields are shaded to highlight their class and a similar scheme is used to highlight the common projections.

$f(2\pi s)$	$f(4\pi s)$	$f(6\pi s)$	$L_{1,2}$	$L_{2,3}$	$L_{1,3}$	flow
Sin	**Sin**	**-Cos**	$+C_d$	$-C_d$	$+C_d$	CW
S	-S	-C	$-C_d$	$+C_d$	$+C_d$	"
-S	S	C	$+C_d$	$-C_d$	$+C_d$	"
-S	-S	C	$-C_d$	$+C_d$	$+C_d$	"
Cos	**Sin**	**-Sin**	$-C_d$	$+C_d$	$+C_d$	"
C	-S	-S	$+C_d$	$-C_d$	$+C_d$	"
-C	S	S	$-C_d$	$+C_d$	$+C_d$	"
-C	-S	S	$+C_d$	$-C_d$	$+C_d$	"
Sin	**Sin**	**Cos**	$+C_d$	$-C_d$	$-C_d$	CCW
S	-S	C	$-C_d$	$+C_d$	$-C_d$	"
-S	S	-C	$+C_d$	$-C_d$	$-C_d$	"
-S	-S	-C	$-C_d$	$+C_d$	$-C_d$	"
Cos	**Sin**	**Sin**	$-C_d$	$+C_d$	$-C_d$	"
C	-S	S	$+C_d$	$-C_d$	$-C_d$	"
-C	S	-S	$-C_d$	$+C_d$	$-C_d$	"
-C	-S	-S	$+C_d$	$-C_d$	$-C_d$	"
Sin	**Cos**	**-Cos**	+O	+O	$+C_d$	CW
S	-C	-C	-O	-O	$+C_d$	"
-S	C	C	+O	+O	$+C_d$	"
-S	-C	C	-O	-O	$+C_d$	"
Cos	**Cos**	**-Sin**	-O	-O	$+C_d$	"
C	-C	-S	+O	+O	$+C_d$	"
-C	C	S	-O	-O	$+C_d$	"
-C	-C	S	+O	+O	$+C_d$	"
Sin	**Cos**	**Cos**	+O	+O	$-C_d$	CCW
S	-C	C	-O	-O	$-C_d$	"
-S	C	-C	+O	+O	$-C_d$	"
-S	-C	-C	-O	-O	$-C_d$	"
Cos	**Cos**	**Sin**	-O	-O	$-C_d$	"
C	-C	S	+O	+O	$-C_d$	"
-C	C	-S	-O	-O	$-C_d$	"
-C	-C	-S	+O	+O	$-C_d$	"
Sin	**Cos**	**Sin**	+O	-O	+O	CW
S	-C	S	-O	+O	+O	"
-S	C	-S	+O	-O	+O	"
-S	-C	-S	-O	+O	+O	"
Cos	**Cos**	**-Cos**	-O	+O	+O	"

C	-C	-C	+O	-O	+O	“
-C	C	C	-O	+O	+O	“
-C	-C	C	+O	-O	+O	“
Sin	**Cos**	**-Sin**	+O	-O	-O	CCW
S	-C	-S	-O	+O	-O	“
-S	C	S	+O	-O	-O	“
-S	-C	S	-O	+O	-O	“
Cos	**Cos**	**Cos**	-O	+O	-O	“
C	-C	C	+O	-O	-O	“
-C	C	-C	-O	+O	-O	“
-C	-C	-C	+O	-O	-O	“
Sin	**Sin**	**Sin**	$+C_d$	$+C_d$	+O	CW
S	-S	S	$-C_d$	$-C_d$	+O	“
-S	S	-S	$+C_d$	$+C_d$	+O	“
-S	-S	-S	$-C_d$	$-C_d$	+O	“
Cos	**Sin**	**-Cos**	$-C_d$	$-C_d$	+O	“
C	-S	-C	$+C_d$	$+C_d$	+O	“
-C	S	C	$-C_d$	$-C_d$	+O	“
-C	-S	C	$+C_d$	$+C_d$	+O	“
Sin	**Sin**	**-Sin**	$+C_d$	$+C_d$	-O	CCW
S	-S	-S	$-C_d$	$-C_d$	-O	“
-S	S	S	$+C_d$	$+C_d$	-O	“
-S	-S	S	$-C_d$	$-C_d$	-O	“
Cos	**Sin**	**Cos**	$-C_d$	$-C_d$	-O	“
C	-S	C	$+C_d$	$+C_d$	-O	“
-C	S	-C	$-C_d$	$-C_d$	-O	“
-C	-S	-C	$+C_d$	$+C_d$	-O	“

Closed curves. The closed curves are of three types, characterized by having 1, 2 or 3 closed projections. For 1:2:3 Lissajous curves with all closed curve projections the conclusions are identical. We will start with the case of three closed curve projections, for which a zero crossing of the field is not possible because any odd:odd 2-d closed Lissajous curve does not have a zero crossing.

a) Three closed projections. The field phases [S, S, C] give the three closed projections ($+C_d$, $-C_d$, $-C_d$), where “C_d” is an abbreviation for “closed”, and its converse field [−S, −S, −C] gives ($-C_d$, $+C_d$, $-C_d$). Even though these closed projections differ only in parity, **Figure 11-5** (left) shows that the 3-d Lissajous curves are not coincident. This must be the case because only two of the three projections have opposite parities. The

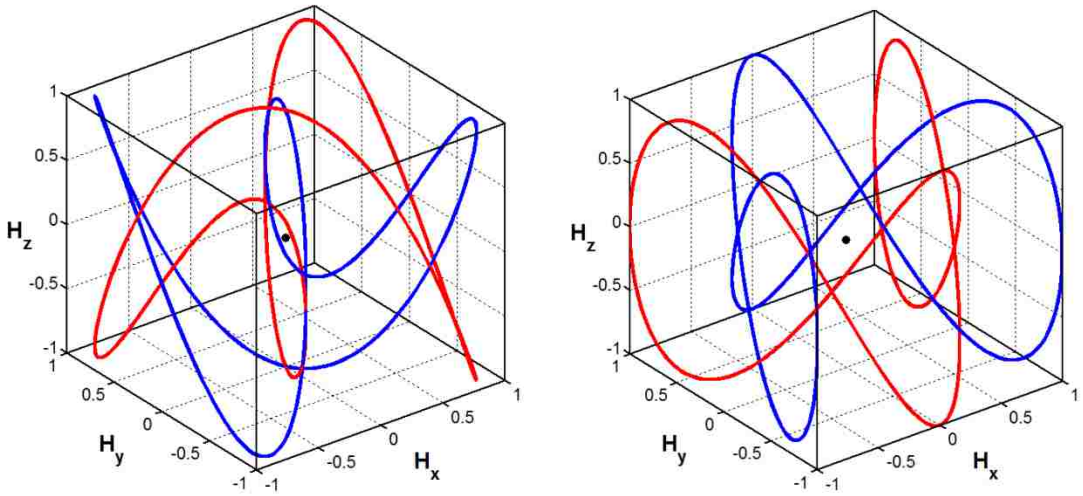

Figure 11-5. (Left) The blue 1:2:3 curve is given by [S, S, C] and has all closed projections [see Figure 11-2(top left)]. The red curve, which does not overlap, is the converse field [−S, −S, −C]. This field has the same projected 2-d curves, but the even, odd projections have opposite parity. **(Right)** This blue 1:2:3 Lissajous curve [see Figure 11-2(bottom right)] is given by [S, C, C] and has two open projections and one closed projection. The red curve is the converse field, for which the single closed curve projection is identical in parity, but for which the closed projections are related to those of the blue curve by a reflection.

reflection $y \to -y$ gives the phases [S, −S, C], producing the projections ($-C_d$, $+C_d$, $-C_d$) and thus mapping the field onto its converse, which conserves vorticity. A rotation about the *y* axis produces [−S, S, −C] which projects to ($+C_d$, $-C_d$, $-C_d$), mapping the field onto itself.

If *y* is the vorticity axis the fields with opposite vorticity are (see Table 11-3) [−S, S, C], [S, S, −C], [S, −S, −C] and [−S, −S, C]. These give the projections ($+C_d$, $-C_d$, $+C_d$), ($+C_d$, $-C_d$, $+C_d$), ($-C_d$, $+C_d$, $+C_d$) and ($-C_d$, $+C_d$, $+C_d$), respectively, which should have the opposite vorticity of the field [S, S, C]. The experimental results in Table 11-5 demonstrate that they do. Note that the two curves with the projections ($+C_d$, $-C_d$, $+C_d$) are identical to the converse field curve but have opposite parity. The curves with projections ($-C_d$, $+C_d$, $+C_d$) are identical to the field but have opposite field parity. We conclude that for all closed projections flow reversal can be achieved by a change in field parity, in particular *the parity of the* $L_{1,3}$ *projection*. Flow reversal due to parity change alone is

a characteristic of symmetry-breaking rational fields having closed curves. As for the open 3-d curve, the *y* axis is demonstrated to be the vorticity axis and there are only two sets of projections that give vorticity of either sign.

b) Two closed projections. The closed Lissajous curve [S, S, S] in Figure 11-2(bottom left) has two closed projections and one open projection. Analysis shows that this will also produce vorticity around the *y* axis. Should flow reversal occur by a parity change or by a change in orientation for this case? A key feature of this curve is that it has a zero crossing, which requires the even, odd projections to be closed and the odd:odd projection to be open. In Appendix C it is shown that fields with zero crossings have the property that the Lissajous trajectory of the field and its converse are coincident, but have opposite field parity. In this case reversing the field parity does not reverse the flow! This field projects to ($+C_d$, $+C_d$, $+O$) and to reverse the flow requires only a reflection about the *x*-*y* plane, giving [S, S, $-$S], which projects to ($+C_d$, $+C_d$, $-O$). Flow reversal thus occurs by a change in the orientation by 180° of the only open projection, $L_{1,3}$. In fact, in this case the orientation of the open projection is the sole determinant of the sign of the vorticity, the parity of the closed projections being of no consequence.

c) One closed projection. The last type of 3-d curve, Figure 11-2(bottom right), is one having two open projections and one closed projection. This too produces vorticity around the *y* axis. One such field is given by [S, C, C], which projects to ($+O$, $+O$, $-C_d$). Its converse projects to ($-O$, $-O$, $-C_d$) and thus is non-coincident, Figure 11-5(right). The results of the symmetry analysis, Table 11-5, show that in this case it is the parity of the *closed projection* $L_{1,3}$ that is the sole determinant of the vorticity sign.

In summary, we have used symmetry considerations to determine the vorticity axis for the even, odd, odd field class, and groupings of fields that must produce the same or opposite vorticity directions. It is conspicuous that changing the parity or orientation of the $L_{1,3}$ projection is the critical factor for flow reversal for the four types of fields we have

considered. We find that a change in the *parity* of $L_{1,3}$ reverses the flow for fields that have 1 or 3 closed projections; whereas, a change in the *orientation* of $L_{1,3}$ can reverse flow for curves with 0 or 2 closed projections. However, we cannot determine the absolute sign of vorticity nor can we predict its magnitude. For this class of rational triads the vorticity axis has been determined to be the axis with *unique numerical parity*. Though worked out for this specific case this is a general conclusion, since the symmetries of the 2-d Lissajous projections are determined by the parity of the integers that describe their frequency ratio alone, as described in Chapter 9 [also Ref. 11.10].

11.4.3 Class II: Even, even, odd fields with even:even → even:odd

A simple example of this class of triad is 2:3:4 (4:2 = 2:1). Lissajous plots of three field phases for this triad are given in **Figure 11-6**, including their projections. Once again the projections for each of the 64 field primary field phases are first tabulated for reference, as in Table 11-4. A significant difference between this case and the even, odd, odd case is that all three projections are even, odd. Therefore, the only 3-d Lissajous trajectories that have zero crossings are those for which all three projections are closed.

Open curves. First we treat the simple case of fields that give only open projections, such as [C, C, C]. This particular field projects to (L_{23}, L_{34}, L_{12})=(+O, −O, −O) and its converse, [−C, −C, −C], projects to (−O, +O, +O) and is therefore not coincident with the field. A reflection $y \rightarrow -y$ gives the phases [C, −C, C] which projects to (+O, −O, −O). This reflection thus maps the field onto itself. A rotation around the *y* axis produces the phases [−C, C, −C] which projects to (−O, +O, +O), mapping the field onto its converse. We conclude that the *y* axis (parallel to the field component with relative frequency 3) is the vorticity axis.

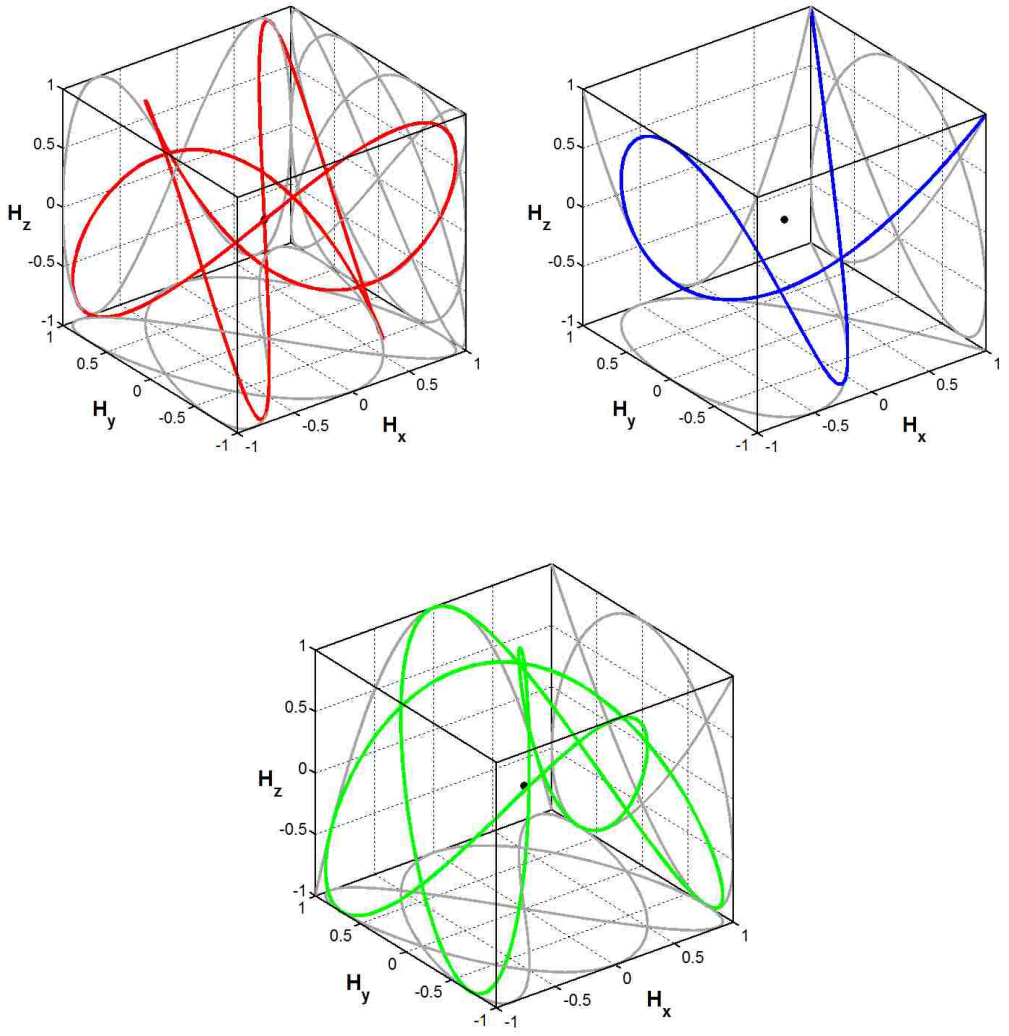

Figure 11-6. Three types of 2:3:4 curves. These fields give vorticity around the *y* axis. **(top left)** A closed curve having three closed projections [S, S, S], **(top right)** an open curve having three open projections [C, C, C], and **(bottom)** a closed curve with two open projections [S, C, C].

The fields having opposite vorticity are [−C, C, C], [C, C, −C], [C, −C, −C] and [−C, −C, C]. These give the projections (−O, −O, −O), (+O, +O, +O), (+O, +O, +O) and (−O, −O, −O), respectively, which should have the opposite vorticity of the field [C, C, C]. The experimental observations in **Appendix D Table 11-7** demonstrate that these are indeed flow-reversing fields. For this field the flow can be reversed by changing the orientation of the single projection $L_{2,3}$.

Closed curves. Closed 2:3:4 fields can be worked out similarly, and it is readily shown that the vorticity axis is parallel to the field component with relative frequency 3. For this class of fields the vorticity axis is again along the direction of unique even, odd numerical parity. The results of the symmetry analysis for all of the principal fields is given in Appendix D Table 11-7 along with the results of experimental observations, which are in agreement with the predictions of the symmetry considerations.

As for the even, odd, odd case we find that there are four types of fields, distinguished by the number of closed projections (0, 1, 2 or 3). For those fields that have 1 or 3 closed projections flow reversal occurs by changing the parity of a single projection, $L_{2,3}$, whereas for 0 or 2 closed projections reversal occurs by changing the orientation of this projection. (Identical to the 1:2:3 case except the critical projection in that case was $L_{1,3}$.) Once again, within each block of 16 fields there are only two distinct CW and two distinct CCW Lissajous trajectories.

11.4.4 Class III: Even, even, odd fields with even:even → odd:odd

The simplest example of this class of triad is 1:2:6, since 6:2 = 3:1. Selected curves are given in **Figure 11-7**. An interesting aspect of this field is that the four types of fields are quite different, consisting of one type with all open projections and three types with just one open projection. These three types differ in that the open projection lies normal to the *x*, *y*, or *z* axis, as indicated in **Appendix D Table 11-8**.

Once again we will explicitly treat only the simple case of fields that give open projections, such as [S, C, C], leaving the other cases to those interested in working them through. This field projects to (L_{12}, L_{13}, L_{16}) = (+O, −O, +O) and its converse, [−S, −C, −C], projects to (−O, −O, −O). In this case only two of the Lissajous projections are even, odd, just as for Class I.

The field reflection $x \to -x$ gives the phases [−S, C, C] which projects to (+O, −O, +O). This reflection thus maps the field onto itself. A rotation of the field around the *x* axis

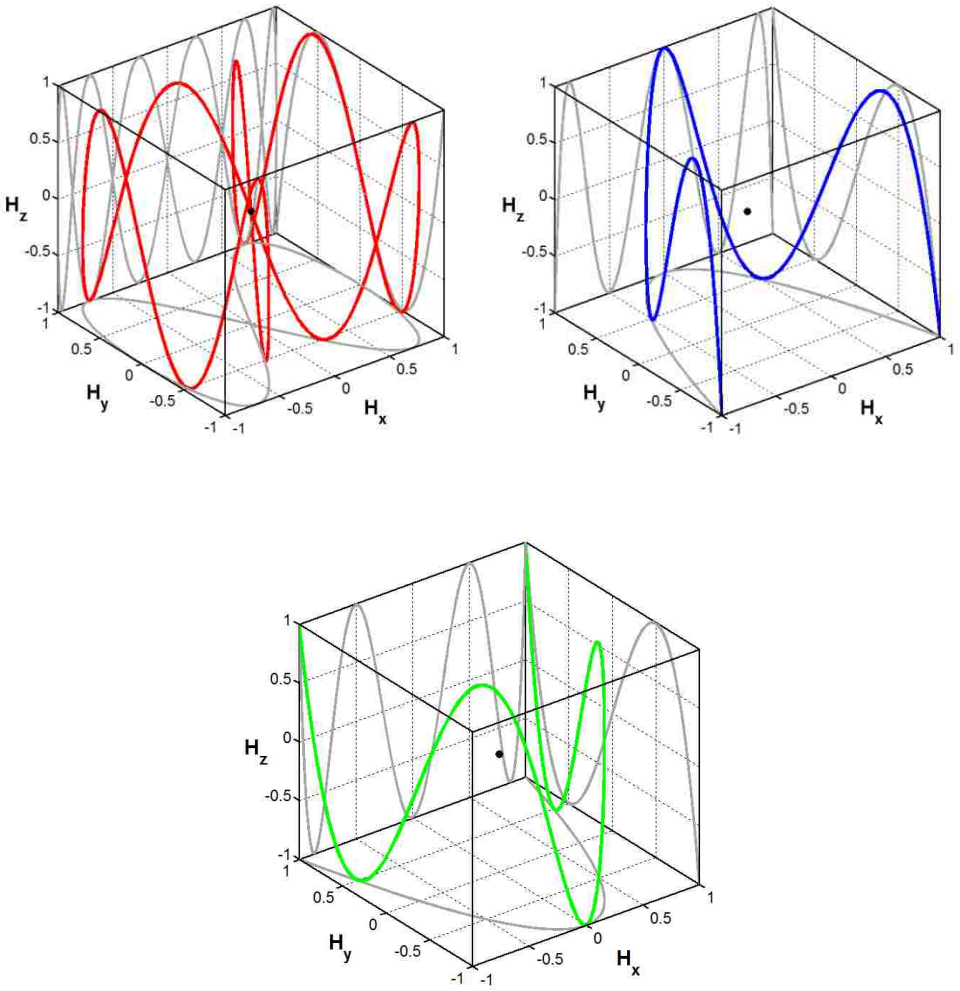

Figure 11-7. Three examples of 1:2:6. These fields give vorticity around the x axis. **(Top left)** The closed curve [S, S, S] has a zero crossing and one open projection. **(Top right)** The curve [S, C, C] has three open projections. **(Bottom)** The converse field [−S, −C, −C] has the same vorticity but is not coincident.

produces the phases [S, −C, −C], which projects to (−O, −O, −O), mapping the field onto its converse. We conclude that the *x* axis, which is parallel to the field component with relative frequency 1, is the vorticity axis and experimental observations confirm this prediction.

The fields having opposite vorticity are [S, −C, C], [S, C, −C], [−S, C, −C] and [−S, −C, C]. These fields give the projections (−O, +O, +O), (+O, +O, −O), (+O, +O, −O) and (−O, +O, +O), respectively, which should have the opposite vorticity of the

field [S, C, C]. Experimental observations of the sign of fluid vorticity, presented in Appendix D Table 11-8 for all 64 symmetric 1:2:6 fields, confirm this prediction.

The orientation of the $L_{2,6} = L_{1,3}$ projection correlates to the sign of the vorticity in this case, but it is not possible to alter this orientation without affecting the orientation of one other projection. This is also true for the case where the only open projection is $L_{2,6}$ except that it is the *parity* of one other projection that is affected. When the single open projection is $L_{1,2}$ or $L_{1,6}$ the sign of vorticity again correlates to the $L_{2,6}$ projection, but in these cases it is the parity of this closed projection that correlates to the expected and observed vorticity. The dominance of a particular projection to the observed vorticity sign is a feature of all classes of rational triads that induce vorticity.

Note that for this class of fields the vorticity axis is once again along the direction of unique numerical parity, in this case 1. How could it be otherwise for a system whose symmetries are based on numerical parity?

11.4.5 Class IV: Odd, odd, odd fields

Open curves. Finally we come to the last class of fields, where all the Lissajous projections are odd:odd. In the first three field classes the vorticity axis was along the direction of the field component whose relative frequency had the unique numerical parity, whether even or odd. For odd:odd:odd fields there is no unique axis, so it is hard to imagine that symmetry arguments could predict a vorticity axis. In the following we will demonstrate this point by using the example 1:3:5, shown in **Figure 11-8**. [In musical terms, for all of the examples above the rational triad was an open fifth (ignoring octaves): now we have a major chord, though inverted.] A complete tabulation of the projections of the symmetric fields is given in **Appendix D Table 11-9**. Consider the open field trajectory [S, S, S], which projects to (L_{13}, L_{35}, L_{15}) = (+O, +O, +O). In this case the converse field [−S, −S, −S] is identical, (+O, +O, +O), which is a general characteristic of

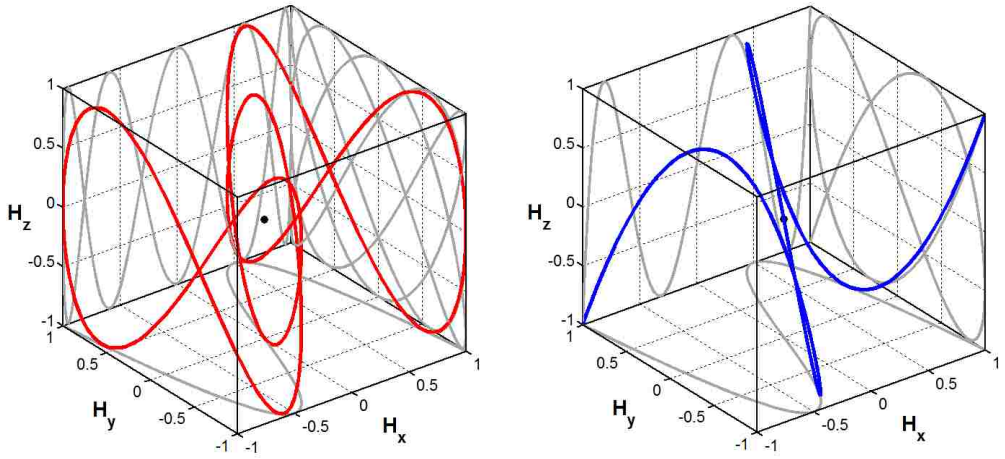

Figure 11-8. Two examples of 1[illegible]3[illegible]5. These fields do not have the symmetry of vorticity. **(Left)** A closed field with one open projection, [S, S, C]. **(Right)** An open field with all open projections [S, S, S].

Class IV fields (see the proof in Appendix C). We will consider all three possible vorticity axes.

If x is the vorticity axis then the reflection $x \to -x$, [−S, S, S], and the rotation about x, [S, −S, −S], must map the field onto itself. These two operations produce converse fields and thus must produce the same projections for this class of fields. This projection is (−O, +O, −O), and because this is not the field or its converse x is not the vorticity axis.

If y is the vorticity axis then the reflection $y \to -y$, [S, −S, S], and the rotation about y, [−S, S, −S], must map the field onto itself. But these operations give the projections (−O, −O, +O), which are not those of the field or its converse, so y is not the vorticity axis.

If z is the vorticity axis then the reflection $z \to -z$, [S, S, −S], and the rotation around z, [−S, −S, S], must map the field onto itself. These operations give the projections (+O, −O, −O), and because these are not those of the field or its converse, z is not the vorticity axis.

Trajectories on closed curves in this class have the property that the trajectory of the field and its converse have identical parity, possible only because they do not have a zero

crossing (*i.e.*, the field never vanishes), as discussed in Appendix C. One might think that reversing this parity could thus reverse flow, but in fact the curves lack the symmetry of vorticity.

For this final class of rational triads there is no vorticity axis that can be predicted from symmetry. Experiments on suspensions of magnetic platelets show some flow, but it is complex and frustrated, not simple vorticity. In fact, from another perspective the situation can be seen to be rather delicate. We have previously shown that for ac-ac-dc triaxial fields odd:odd frequency ratios do exhibit vorticity, the axis of vorticity is orthogonal to the ac field plane (parallel to the dc field component) and the sign of the vorticity *does not depend* on the sign of the dc field. Therefore a very low frequency, quasi-dc field will still produce vorticity. Interestingly enough, as this field frequency is increased to a frequency of the same order of magnitude of the ac components, such that an even:odd:odd triad is produced, the field trajectory has the symmetry of vorticity. But if an odd:odd:odd triad is produced then one can argue that vorticity can be produced orthogonal to any of the three odd:odd field planes. Thus a frustration occurs and some net vorticity may in fact occur, simply because of a difference in the magnitude of vorticity orthogonal to each of the three field planes. For example, for the 1:3:5 triad the 1:3 vorticity is greater than the 3:5 vorticity when orthogonal dc fields are applied.

11.5 Experimental results and discussion

11.5.1 The 1:2:3 triad

The torque density of a magnetic particle dispersion subjected to a fully alternating triaxial field (rational triad) can be expressed as a function of any two phase angles. Varying the third phase angle simply shifts the zero of time. For the 1:2:3 field we chose the phase angles ϕ_1, ϕ_3 and thus consider reduced fields of the form

$$h(s) = \sin(2\pi s + \phi_1)\hat{\mathbf{x}} + \sin(4\pi s)\hat{\mathbf{y}} + \sin(6\pi s + \phi_3)\hat{\mathbf{z}} \qquad (11\text{-}2)$$

where $s = f_0 t$ is the dimensionless time. After some thought the expected lattice vector for the periodic torque density is $(\phi_1, \phi_3) = (-90°, +90°)$. If this is correct, the field

$$h'(s) = \sin(2\pi s + \phi_1 - 90°)\hat{\mathbf{x}} + \sin(4\pi s)\hat{\mathbf{y}} + \sin(6\pi s + \phi_3 + 90°)\hat{\mathbf{z}} \tag{11-3}$$

should produce the same torque as the field in Equation (11-2). To see this simply shift the dimensionless time in Equation (11-3) according to $2\pi s = 2\pi s' - 90°$. This gives

$$h'(s') = -\sin(2\pi s' + \phi_1)\hat{\mathbf{x}} - \sin(4\pi s')\hat{\mathbf{y}} - \sin(6\pi s' + \phi_3)\hat{\mathbf{z}} \tag{11-4}$$

which is simply the field converse to Equation (11-2). This converse must give the same sign and magnitude of vorticity, so $(-90°, +90°)$ must be a correct lattice vector.

Reversing the flow given by Equations 11(2–4) while maintaining its magnitude can be accomplished by applying the field

$$h''(s) = \sin(2\pi s + \phi_1 + 90°)\hat{\mathbf{x}} + \sin(4\pi s)\hat{\mathbf{y}} + \sin(6\pi s + \phi_3 + 90°)\hat{\mathbf{z}}\,. \tag{11-5}$$

We will refer to such a field as a *flow-reversing field*, with the understanding that this term also implies the magnitude of vorticity is preserved. To show that this is a flow-reversing field the same change of variables, $2\pi s = 2\pi s' - 90°$, can be applied to Equation (11-5) to give

$$h''(s') = \sin(2\pi s' + \phi_1)\hat{\mathbf{x}} - \sin(4\pi s')\hat{\mathbf{y}} - \sin(6\pi s' + \phi_3)\hat{\mathbf{z}}\,. \tag{11-6}$$

From Table 11-3 it can be seen that for vorticity around the *y* axis, which is the case here, the [S, −S, −S] field is indeed a flow-reversing field relative to Equation (11-2), [S, S, S]. Simply adding a phase of 90° to the 1 and 3 components is all that is required to reverse flow. Alternatively, adding a phase of 180° to the 3 component can be shown to reverse flow.

The experimental data are shown in **Figure 11-9** as a 3-d plot and as a topographic plot. The symmetries just derived can be seen in these data. (Note that the boundaries are cyclic, so it would be ideal to present these data on a torus.) The specific torque density

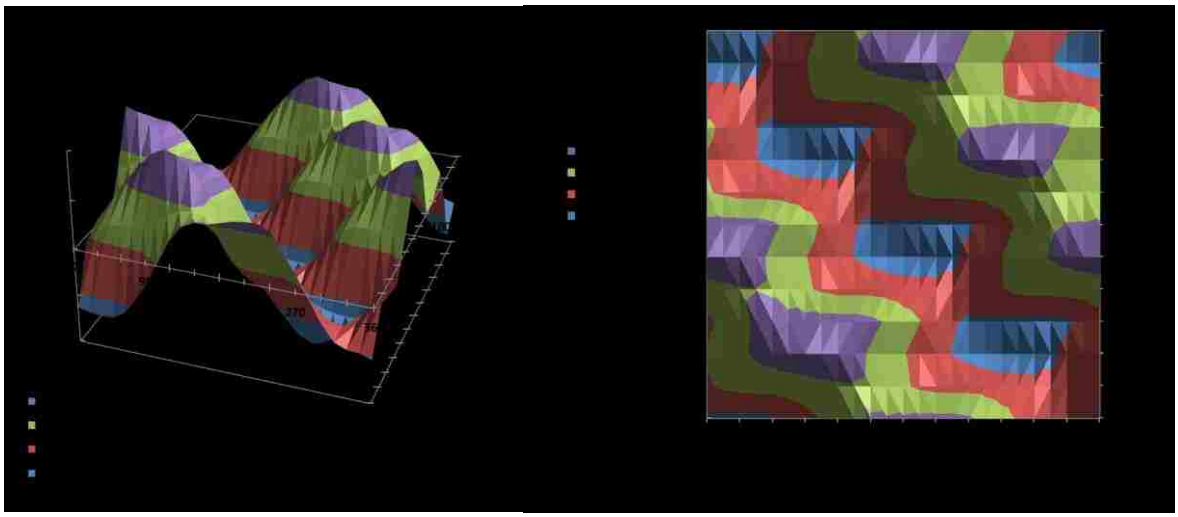

Figure 11-9. Experimental torque density phase maps for a 1:2:3 rational triad are presented as a 3-d plot **(left)** and a topographic plot **(right)**. The boundary between the red and green is the locus of zero torque.

maximizes at $907\,\mathrm{J\cdot m^{-3}}$ for this field. This value is nearly 70% greater than the energy density of the field, which is $537\,\mathrm{J\cdot m^{-3}}$ for a triaxial field with each rms field component being 150 Oe. The undulating boundary between the green and red zones is the locus of points that give zero torque. It is possible that such torqueless fields could generate interesting particle structures.

11.5.2 The 2:3:4 triad

The symmetry of the torque data for the 2:3:4 field is also easily derived. In this case the variable phase angles are applied to the components $l = 2$ and $m = 3$ (for no compelling reason) to give the reduced field

$$h(s) = \sin(4\pi s + \phi_2)\hat{\mathbf{x}} + \sin(6\pi s + \phi_3)\hat{\mathbf{y}} + \sin(8\pi s)\hat{\mathbf{z}}\,. \tag{11-7}$$

The lattice vector for this case is $(\phi_2, \phi_3) = (90°, 45°)$ which can be seen by demonstrating that the reduced field

$$h'(s) = \sin(4\pi s + \phi_2 + 90°)\hat{\mathbf{x}} + \sin(6\pi s + \phi_3 + 45°)\hat{\mathbf{y}} + \sin(8\pi s)\hat{\mathbf{z}} \tag{11-8}$$

is either the field or its converse. The change of variables $4\pi s = 4\pi s' + 90°$ leads to

$$h'(s') = -\sin(4\pi s' + \phi_2)\hat{\mathbf{x}} - \sin(6\pi s' + \phi_3)\hat{\mathbf{y}} - \sin(8\pi s')\hat{\mathbf{z}} \tag{11-9}$$

which is indeed the converse of Equation (11-7). So this change of phases preserves both the sign and magnitude of the vorticity.

The reversing field is given by

$$h''(s) = \sin(4\pi s + \phi_2)\hat{\mathbf{x}} + \sin(6\pi s + \phi_3 + 90°)\hat{\mathbf{y}} + \sin(8\pi s)\hat{\mathbf{z}}\,. \qquad (11\text{-}10)$$

To confirm that this is indeed a reversing field the change of variables $4\pi s = 4\pi s' + 180°$ can be applied to Equation (11-10) to obtain

$$h''(s') = -\sin(4\pi s' + \phi_2)\hat{\mathbf{x}} + \sin(6\pi s' + \phi_3)\hat{\mathbf{y}} + \sin(8\pi s')\hat{\mathbf{z}}\,. \qquad (11\text{-}11)$$

For vorticity around the *y* axis, which is the case for this 2:3:4 field, Table 11-3 shows that Equation (11-11), which is [−S, S, S], is a flow-reversing field for [S, S, S].

The experimental data are shown in **Figure 11-10** as a 3-d plot and as a topographic plot. These data demonstrate the symmetries derived in this section. The specific torque density maximizes at $723\,\mathrm{J\cdot m^{-3}}$ for this field, which is ~35% greater than the $537\,\mathrm{J\cdot m^{-3}}$ energy density for this triaxial field. In this case the zero torque locus, which is the boundary between the green and red zones, is nearly straight.

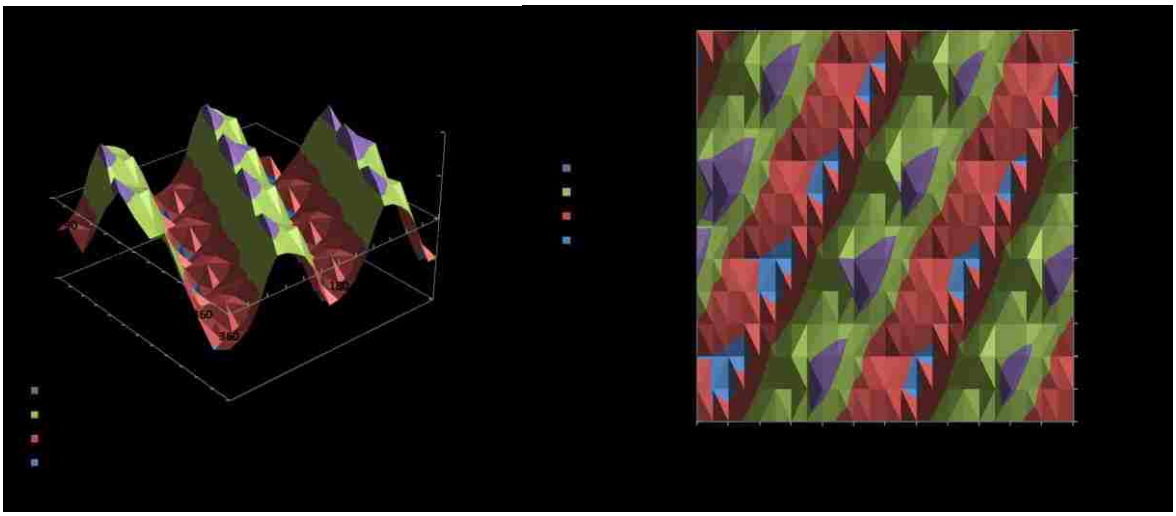

Figure 11-10. Experimental torque density phase maps for a 2:3:4 rational triad are presented as a 3-d plot **(left)** and a topographic plot **(right)**. The boundary between the red and green is the locus of zero torque.

11.5.3 The 1:2:6 triad

The symmetry of the torque data for the 1:2:6 field is simple if the variable phase angles are applied to the $l = 1$ and $n = 6$ components. In this case the reduced field is

$$h(s) = \sin(2\pi s + \phi_1)\hat{\mathbf{x}} + \sin(4\pi s)\hat{\mathbf{y}} + \sin(12\pi s + \phi_6)\hat{\mathbf{z}}\,. \qquad (11\text{-}12)$$

The lattice vector for this case is $(\phi_1, \phi_6) = (90°, 0°)$ which can be seen by demonstrating that the reduced field

$$h'(s) = \sin(2\pi s + \phi_1 + 90°)\hat{\mathbf{x}} + \sin(4\pi s)\hat{\mathbf{y}} + \sin(12\pi s + \phi_6)\hat{\mathbf{z}} \qquad (11\text{-}13)$$

is either the field or its converse. The change of variables $2\pi s = 2\pi s' + 90°$ leads to

$$h'(s') = -\sin(2\pi s' + \phi_1)\hat{\mathbf{x}} - \sin(4\pi s')\hat{\mathbf{y}} - \sin(12\pi s' + \phi_6)\hat{\mathbf{z}}\,. \qquad (11\text{-}14)$$

Table 11-3 shows that for vorticity around the *x* axis [S, S, −S] is a flow reversing field relative to [S, S, S]. So adding a phase of 180° to the *z* component reverses flow.

The experimental data are shown in **Figure 11-11** as a 3-d plot and as a topographic plot. These data demonstrate the symmetries derived in this section. The specific torque

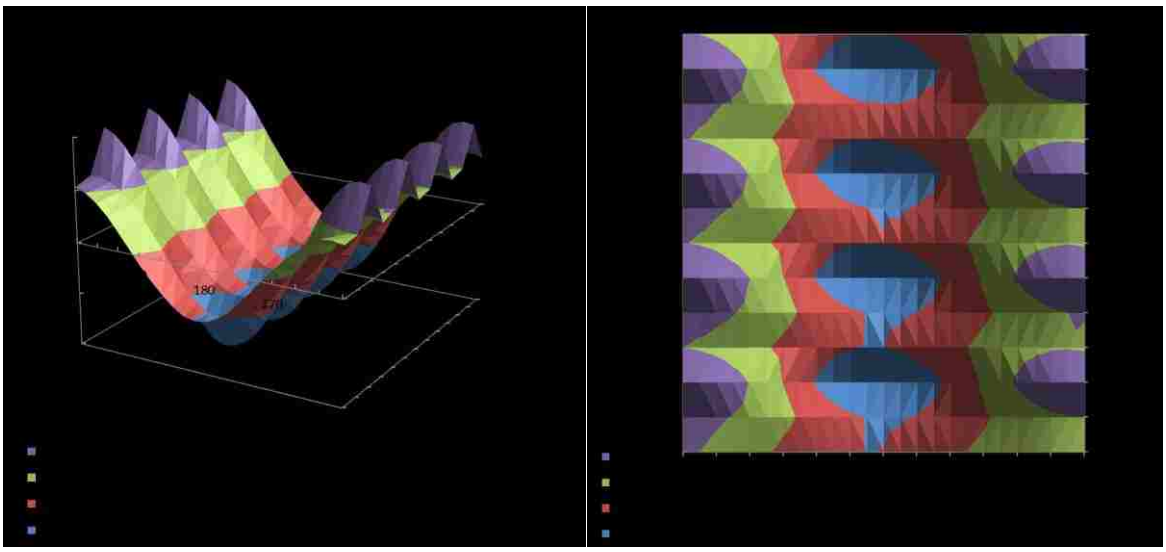

Figure 11-11. Experimental torque density phase maps for a 1:2:6 rational triad are presented as a 3-d plot **(left)** and a topographic plot **(right)**. The boundary between the red and green is the locus of zero torque.

density maximizes at 596 $J \cdot m^{-3}$ for this field, which is only 11% greater than the 537 $J \cdot m^{-3}$ energy density for this triaxial field. In this case the zero torque locus, which is the boundary between the green and red zones, is nearly straight.

11.6 Summary

The results we have presented are extensive enough that a concise summary is warranted, or at least helpful.

• We have shown that there are three classes of countably infinite sets of fully alternating ac-ac-ac triaxial fields whose frequencies form rational triads that have the symmetry required to drive vorticity in magnetic particle suspensions. These classes are: even:odd:odd; even:even:odd fields with even:even → even:odd; and even:even:odd fields with even:even → odd:odd. The fourth class, odd:odd:odd does not possess the requisite symmetry to drive vorticity.

• For any particular rational triad one can enumerate 64 Lissajous trajectories that have maximally symmetric projections when viewed along each of its three principal axes. Some of these are open curves, but mostly they're closed. These trajectories are formed of principal components that can be expressed as simple sines or cosines and their negatives. There are generally only 16 distinguishable trajectories, each having four representations that differ only in the choice of the zero of time.

• It is found that when the trajectory of the field has the symmetry of vorticity, defined by whether the sign of vorticity is symmetric or antisymmetric under the 3 rotations about principal axes and 3 reflections parallel to these axes, vorticity can indeed be induced experimentally. It is found that chirality of the trajectory has nothing to do with vorticity.

• From these symmetry considerations the vorticity axis can be predicted and it is always the unique axis in terms of numerical parity. For example, for the class even:odd:odd it is the even axis.

• For a particular triad it is also possible to group trajectories into four sets. Each of these sets consist of two distinct trajectories that are CW and two that are CCW.

• Flow reversal can sometimes be achieved by a change in the *parity of the trajectory* of a closed projection and sometimes by a change in the *orientation* of an open projection.

• Experimental observations of the direction and sign of vorticity validate the predictions of the symmetry theory.

• The specific fluid torque density was measured as a function of two independent, continuously variable phases applied to two of the field components, resulting in periodic 3-d plots of the torque density. The derived lattice vector for these plots was found to agree with experiment. A flow-reversing lattice vector was also predicted and found to agree with experiment.

11.7 Conclusions

We have shown that fully alternating triaxial fields do indeed possess the symmetry required to drive vigorous vorticity in magnetic particle suspensions (the specific torque densities are in excess of the energy density of the field, at times nearly twice as great) and have provided an analytical method of demonstrating this that is based on projections of the dynamic field. This discovery opens up endless schemes for controlling fluid motion and transporting droplets on surfaces by creating vorticity around an axis in the plane of the surface. Simply controlling the phase angles of 1 or 2 of the field components enables the torque density to be increased, decreased, nullified or reversed. (Under zero torque conditions it is very likely that the suspension organizes itself into novel structures, which is a possible avenue for future research.) Likewise, changing just one of the field frequencies can change the vorticity axis, enabling complex fluid mixing strategies, heat transfer strategies and 3-d control of droplet motion. In this chapter experimental measurements were restricted to magnetic platelets at low particle densities. Future research directions include applying these fields to the dense particle suspensions that are used in magnetorheological devices and to

magnetic fluids (ferrofluids). Preliminary measurements indicate the presence of vorticity in both of these systems.

11.8 Appendices

A. Canonical classification of 2-d Lissajous trajectories

Tables 11-1 and 11-3 are central to understanding symmetry operations on the 3-d Lissajous trajectories. These tables classify 2-d Lissajous curves according to whether they are open or closed. If they are closed curves the parity of their trajectory is assigned as "+" or "−". If they are open curves the "+" or "−" refers to their orientation. In Appendix A of Chapter 9 [also Ref. 11.10] it is demonstrated analytically that high-symmetry (principal) rational Lissajous plots can be expressed as

$$\mathbf{h}(s) = \sin(2\pi qs)\hat{\mathbf{x}} + \sin\left(2\pi ps + j\frac{90°}{q}\right)\hat{\mathbf{y}} \qquad \text{(A-1)}$$

where s is a reduced time and $\mathbf{h}$ is a reduced field. It is also shown that these curves can be classified as in **Table 11-6**. The assignment of "+" or "−" is arbitrary and the repeating pattern is shaded. Note that all of these principal curves can be represented by the first two terms on the right hand side of Equation (11-1).

Table 11-6. . Classification of the types of symmetric (principal) Lissajous curves. Here "O" is open and "C_d" is closed and the repeating pattern is shaded.

j	Type (even, odd)	Type (odd, odd)
-3	+O	-C_d
-2	-C_d	-O
-1	-O	+C_d
0	+C_d	+O
1	+O	-C_d
2	-C_d	-O
3	-O	+C_d
4	+C_d	+O

Because of the central importance of Tables 11-1 and 11-2 it is probably worthwhile to show how these are obtained from Equation (A-1) and Table 11-6. Our approach is to take each principal function and express it in the form $\sin(2\pi qs)\hat{\mathbf{x}} + \sin(2\pi ps + \phi)\hat{\mathbf{y}}$ so that the

phase ϕ can be compared to Equation (A-1) and the field type then obtained from Table 11-6. This is a straightforward but tedious process.

q odd, p even. First consider the curve $\sin(2\pi qs)\hat{\mathbf{x}}+\sin(2\pi ps)\hat{\mathbf{y}}$, which we abbreviate as [S, S]. This corresponds to $j=0$ in Equation (A-1), so for all q, p these curves are $+C_d$. Now the curve [S, C], corresponds to $\phi=q\times(90°/q)$, so j in Equation (A-1) is q. Because q is odd the only two cases are $q=1,\ 5,\ldots$ which Table 11-6 shows is $+O$ and $q=3,\ 7,\ldots$ which is $-O$. The curve [C, S] gives the phase $\phi=-p\dfrac{90°}{q}$ so for $p=2,\ 6,\ldots$ this curve is $-C_d$ and for $p=4,\ 8,\ldots$ this curve is $+C_d$. The curve [C, C] gives $\phi=(q-p)\times(90°/q)$ so if $q=1,\ 5,\ldots$ & $p=2,\ 6,\ldots$ or $q=3,\ 7,\ldots$ & $p=4,\ 8,\ldots$ then $q-p=3,\ 7,\ldots$ and the curve is $-O$. If $q=1,\ 5,\ldots$ & $p=4,\ 8,\ldots$ or $q=3,\ 7,\ldots$ & $p=2,\ 6,\ldots$ then $q-p=1,\ 5,\ldots$ and the curve is $+O$. For the curve [S, $-$S] the phase is $\phi=2q\times(90°/q)$ so because q is odd these curves are always $-C_d$. For [S, $-$C] the phase is $\phi=3q\times(90°/q)$. For $q=1,\ 5,\ldots$ this gives $3q=3$ (mod 4) so the curve is $-O$. For $q=3,\ 7,\ldots$ $3q=5$ (mod 4) so the curve is $+O$. At this point one can demonstrate that we have determined at least one representation of a Lissajous curve for each cell in Table 11-1. Appendix B shows how the degenerate representations can be computed to verify every entry in every cell.

q odd, p odd. For the curve [S, S] all of the curves are $+O$. For [S, C] the phase is $\phi=q\times(90°/q)$ so for $q=1,\ 5,\ldots$ this gives $-C_d$ and for $q=3,\ 7,\ldots$ the curve is $+C_d$. For [C, S] the phase is $\phi=-p\times(90°/q)$ so for $p=1,\ 5,\ldots$ the curve is $+C_d$ whereas for $p=3,\ 7,\ldots$ the curve is $-C_d$. The phase is $\phi=2q\times(90°/q)$ for [S, $-$S] which gives $-O$ for all odd q. For [$-$S, C] the phase is $\phi=3q\times(90°/q)$ which gives $+C_d$ for $q=1,\ 5,\ldots$ and $-C_d$ for $q=3,\ 7,\ldots$ Again we have populated each cell in Table 11-2 at least once and the equivalent representations of each curve can be determined by referring to Appendix B.

B. Degenerate phases for principal Lissajous trajectories.

We have seen that any principal Lissajous trajectory can be represented by four different phases. To understand this degeneracy, and how Tables 11-1 and 11-2 were generated, we will work out the first row of Table 11-1 in its entirety. The first cell in Table 11-1 shows that for $q = 1, 5\ldots$; $p = 2, 6\ldots$ the four phases [S, S], [−S, S], [−C, −S] and [C, −S] all produce a +Closed Lissajous trajectory. These phases are easily derived by shifting time by an appropriate amount. For the first instance the reduced field $\mathbf{h} = \mathbf{H}/|\mathbf{H}|$ in the *v*-*w* plane can be written

$$\mathbf{h}(s) = \sin(qs')\hat{\mathbf{v}} + \sin(ps')\hat{\mathbf{w}} . \qquad \text{(B-1)}$$

Redefine the zero of the reduced time *s* by letting $qs' \to qs + i \times 90°$, where *i* is an integer, to obtain

$$\mathbf{h}(s) = \sin(qs + i \times 90°)\hat{\mathbf{v}} + \sin\left(ps + \frac{ip}{q} \times 90° \right)\hat{\mathbf{w}} . \qquad \text{(B-2)}$$

Letting $q = 4j + 1$, $j = 0, 1, 2\ldots$ and $p = 4k + 2$, $k = 0, 1, 2\ldots$ the reduced field becomes

$$\mathbf{h}(s) = \sin(qs + i \times 90°)\hat{\mathbf{v}} + \sin\left(ps + i\frac{4k+2}{4j+1} \times 90° \right)\hat{\mathbf{w}} . \qquad \text{(B-3)}$$

If $i = 4j + 1$ then $i \times 90°(\text{mod}360°) = 90°$ for all integer values of *j* and $(4k + 2) \times 90°(\text{mod}360°) = 180°$ for all integer values of *k*. The reduced field is thus

$$\mathbf{h}(s) = \cos(qs)\hat{\mathbf{v}} - \sin(ps)\hat{\mathbf{w}} . \qquad \text{(B-4)}$$

If $i = 2(4j + 1)$ the two phases in Equation (B-3) become 180° and 0° (mod 360°), respectively, and the field becomes $\mathbf{h}(s) = -\sin(qs)\hat{\mathbf{v}} + \sin(ps)\hat{\mathbf{w}}$. Finally, if $i = 3(4j + 1)$ the two phases become 270° and 180° and the reduced field is $\mathbf{h}(s) = -\cos(qs)\hat{\mathbf{v}} - \sin(ps)\hat{\mathbf{w}}$. To summarize, the equivalent fields for these values of *q* and *p* are [S, S], [C, −S], [−S, S] and [−C, −S], which are just those listed in the first cell of Table 11-1.

With these results the other cases in the first row of Table 11-1 can be worked out quickly. The second cell in the first row of Table 11-1 is for the −Closed Lissajous trajectory. The first field that gives this trajectory is [C, S]. All we have to do to generate the

remaining fields is to add 90° to the first component of the equivalent fields we have just derived, [C, −S], [−S, S] and [−C, −S]. The equivalent fields for −Closed are thus [C, S], [−S, −S], [−C, S] and [S, −S].

The third cell in the first row of Table 11-1 is for the +Open case. This starts with [S, C] so the remaining entries are obtained by adding a phase of 90° to the second component of the list [C, −S], [−S, S] and [−C, −S]. This gives the equivalent fields [S, C], [C, −C], [−S, C] and [−C, −C].

The fourth cell in the first row of Table 11-1 is for the −Open case. This starts with [C, C] so the remaining entries are obtained by adding a phase of 90° to each field component in the list [C, −S], [−S, S] and [−C, −S]. This gives the equivalent fields [C, C], [−S, −C], [−C, C] and [S, −C].

The other three rows in Table 11-1 and the four rows in Table 11-2 can be worked out by similar derivations.

C. Cases where the field and its converse lie on coincident closed curves

It is interesting to note that in some instances the trajectories of the field and its converse not only lie on the same closed curves, but also have identical parity. Other than a phase lag these trajectories are thus identical. For this to occur requires that the condition $h_c(s+\frac{1}{2}) = h(s)$ be satisfied, where h denotes the reduced field, h_c denotes the converse reduced field and s denotes the reduced time. This condition is equivalent to $h(s+\frac{1}{2}) = -h(s)$. The reduced fields of interest in this paper can be written in terms of sine or cosines and

$$\sin[2\pi q(s+\tfrac{1}{2})] = \begin{cases} +\sin(2\pi qs) \text{ for } q \text{ even} \\ -\sin(2\pi qs) \text{ for } q \text{ odd} \end{cases}$$

$$\cos[2\pi q(s+\tfrac{1}{2})] = \begin{cases} +\cos(2\pi qs) \text{ for } q \text{ even} \\ -\cos(2\pi qs) \text{ for } q \text{ odd} \end{cases}$$

Therefore, the only closed fields whose complement has an identical trajectory are those for which the reduced frequency ratios are odd, such as the rational triad 1:3:5 (see Figure 11-8). Such closed fields do not include the origin and thus never vanish. This can be seen from Chapter 9 [also Ref. 11.10], where it is shown that odd:odd closed curves do not include the origin.

A second interesting case is where the closed curves for the field and its converse are identical, but the trajectories have *opposite* parity. Consider the condition $h_c(s) = h(-s)$, which is equivalent to $h(s) = -h(-s)$. This condition is obviously satisfied for fields where all of the components are sine functions. Such fields are characterized by periodically vanishing, which is the key characteristic of closed Lissajous curves whose field and converse trajectories differ only in parity. Of course, we have seen that [S, S, S] fields can have other equivalent representations, but then the condition required to demonstrate the parity difference of the trajectories changes as well.

D. Supplementary tables from above main text

Supplementary Table 11-7. Fields, projections and observed flow directions for 2:3:4.

$f(4\pi s)$	$f(6\pi s)$	$f(8\pi s)$	$L_{2,3}$	$L_{3,4}$	$L_{2,4}$	flow
Sin	**Sin**	**Sin**	+ C_d	+C_d	+C_d	CCW
-S	S	-S	-C_d	-C_d	-C_d	"
S	-S	S	+C_d	+C_d	+C_d	"
-S	-S	-S	-C_d	-C_d	-C_d	"
Sin	**-Cos**	**-Sin**	-C_d	-C_d	-C_d	"
-S	-C	S	+C_d	+C_d	+C_d	"
S	C	-S	-C_d	-C_d	-C_d	"
-S	C	S	+C_d	+C_d	+C_d	"
Sin	**Sin**	**-Sin**	+C_d	-C_d	-C_d	CW
-S	S	S	-C_d	+C_d	+C_d	"
S	-S	-S	+C_d	-C_d	-C_d	"
-S	-S	S	-C_d	+C_d	+C_d	"
Sin	**-Cos**	**Sin**	-C_d	+C_d	+C_d	"
-S	-C	-S	+C_d	-C_d	-C_d	"
S	C	S	-C_d	+C_d	+C_d	"
-S	C	-S	+C_d	-C_d	-C_d	"
Cos	**Cos**	**Cos**	+O	-O	-O	CCW
-C	C	-C	-O	+O	+O	"
C	-C	C	+O	-O	-O	"

-C	-C	-C	-O	+O	+O	“
Cos	**-Sin**	**-Cos**	-O	+O	+O	“
-C	-S	C	+O	-O	-O	“
C	S	-C	-O	+O	+O	“
-C	S	C	+O	-O	-O	“
Cos	**Cos**	**-Cos**	+O	+O	+O	CW
-C	C	C	-O	-O	-O	“
C	-C	-C	+O	+O	+O	“
-C	-C	C	-O	-O	-O	“
Cos	**-Sin**	**Cos**	-O	-O	-O	“
-C	-S	-C	+O	+O	+O	“
C	S	C	-O	-O	-O	“
-C	S	-C	+O	+O	+O	“
Sin	**Cos**	**-Cos**	$-C_d$	+O	-O	CCW
-S	C	C	$+C_d$	-O	+O	“
S	-C	-C	$-C_d$	+O	-O	“
-S	-C	C	$+C_d$	-O	+O	“
Sin	**-Sin**	**Cos**	$+C_d$	-O	+O	“
-S	-S	-C	$-C_d$	+O	-O	“
S	S	C	$+C_d$	-O	+O	“
-S	S	-C	$-C_d$	+O	-O	“
Sin	**Cos**	**Cos**	$-C_d$	-O	+O	CW
-S	C	-C	$+C_d$	+O	-O	“
S	-C	C	$-C_d$	-O	+O	“
-S	-C	-C	$+C_d$	+O	-O	“
Sin	**Sin**	**-Cos**	$+C_d$	+O	-O	“
-S	-S	C	$-C_d$	-O	+O	“
S	-S	-C	$+C_d$	+O	-O	“
-S	S	C	$-C_d$	-O	+O	“
Cos	**Cos**	**-Sin**	+O	$-C_d$	$+C_d$	CCW
-C	C	S	-O	$+C_d$	$-C_d$	“
C	-C	-S	+O	$-C_d$	$+C_d$	“
-C	-C	S	-O	$+C_d$	$-C_d$	“
Cos	**-Sin**	**Sin**	-O	$+C_d$	$-C_d$	“
-C	-S	-S	+O	$-C_d$	$+C_d$	“
C	S	S	-O	$+C_d$	$-C_d$	“
-C	S	-S	+O	$-C_d$	$+C_d$	“
Cos	**Cos**	**Sin**	+O	$+C_d$	$-C_d$	CW
-C	C	-S	-O	$-C_d$	$+C_d$	“
C	-C	S	+O	$+C_d$	$-C_d$	“
-C	-C	-S	-O	$-C_d$	$+C_d$	“
Cos	**-Sin**	**-Sin**	-O	$-C_d$	$+C_d$	“
-C	-S	S	+O	$+C_d$	$-C_d$	“
C	S	-S	-O	$-C_d$	$+C_d$	“
-C	S	S	+O	$+C_d$	$-C_d$	“

Supplementary Table 11-8. Fields, projections and observed flow directions for 1:2:6.

$f(2\pi s)$	$f(4\pi s)$	$f(12\pi s)$	$L_{1,2}$	$L_{2,6}$	$L_{1,6}$	flow
Sin	**Sin**	**Sin**	+Cd	+O	+Cd	CW
S	-S	-S	-Cd	+O	-Cd	"
-S	S	S	+Cd	+O	+Cd	"
-S	-S	-S	-Cd	+O	-Cd	"
Cos	**Sin**	**Sin**	-Cd	+O	-Cd	"
C	-S	-S	+Cd	+O	+Cd	"
-C	S	S	-Cd	+O	-Cd	"
-C	-S	-S	+Cd	+O	+Cd	"
Sin	**Sin**	**-Sin**	+Cd	-O	-Cd	CCW
S	-S	S	-Cd	-O	+Cd	"
-S	S	-S	+Cd	-O	-Cd	"
-S	-S	S	-Cd	-O	+Cd	"
Cos	**Sin**	**-Sin**	-Cd	-O	+Cd	"
C	-S	S	+Cd	-O	-Cd	"
-C	S	-S	-Cd	-O	+Cd	"
-C	-S	S	+Cd	-O	-Cd	"
Sin	**Cos**	**Cos**	+O	-O	+O	CCW
S	-C	-C	-O	-O	-O	"
-S	C	C	+O	-O	+O	"
-S	-C	-C	-O	-O	-O	"
Cos	**Cos**	**Cos**	-O	-O	-O	"
C	-C	-C	+O	-O	+O	"
-C	C	C	-O	-O	-O	"
-C	-C	-C	+O	-O	+O	"
Sin	**Cos**	**-Cos**	+O	+O	-O	CW
S	-C	C	-O	+O	+O	"
-S	C	-C	+O	+O	-O	"
-S	-C	C	-O	+O	+O	"
Cos	**Cos**	**-Cos**	-O	+O	+O	"
C	-C	C	+O	+O	-O	"
-C	C	-C	-O	+O	+O	"
-C	-C	C	+O	+O	-O	"
Sin	**Sin**	**-Cos**	+Cd	+Cd	-O	CCW
S	-S	C	-Cd	+Cd	+O	"
-S	S	-C	+Cd	+Cd	-O	"
-S	-S	C	-Cd	+Cd	+O	"
Cos	**Sin**	**-Cos**	-Cd	+Cd	+O	"
C	-S	C	+Cd	+Cd	-O	"
-C	S	-C	-Cd	+Cd	+O	"
-C	-S	C	+Cd	+Cd	-O	"
Sin	**Sin**	**Cos**	+Cd	-Cd	+O	CW
S	-S	-C	-Cd	-Cd	-O	"
-S	S	C	+Cd	-Cd	+O	"
-S	-S	-C	-Cd	-Cd	-O	"
Cos	**Sin**	**Cos**	-Cd	-Cd	-O	"
C	-S	-C	+Cd	-Cd	+O	"

-C	S	C	-Cd	-Cd	-O	“
-C	-S	-C	+Cd	-Cd	+O	“
Sin	**Cos**	**-Sin**	+O	+Cd	-Cd	CCW
S	-C	S	-O	+Cd	+Cd	“
-S	C	-S	+O	+Cd	-Cd	“
-S	-C	S	-O	+Cd	+Cd	“
Cos	**Cos**	**-Sin**	-O	+Cd	+Cd	“
C	-C	S	+O	+Cd	-Cd	“
-C	C	-S	-O	+Cd	+Cd	“
-C	-C	S	+O	+Cd	-Cd	“
Sin	**Cos**	**Sin**	+O	-Cd	+Cd	CW
S	-C	-S	-O	-Cd	-Cd	“
-S	C	S	+O	-Cd	+Cd	“
-S	-C	-S	-O	-Cd	-Cd	“
Cos	**Cos**	**Sin**	-O	-Cd	-Cd	“
C	-C	-S	+O	-Cd	+Cd	“
-C	C	S	-O	-Cd	-Cd	“
-C	-C	-S	+O	-Cd	+Cd	“

Supplementary Table 11-9. Projections for the rational triad 1:3:5. An “S” in the column labeled “3” indicates sin(3ωt), etc.

1	**3**	**5**	**$L_{1,3}$**	**$L_{3,5}$**	**L_{15}**
Sin	**Sin**	**Sin**	+O	+O	+O
S	S	C	+O	$+C_d$	$-C_d$
S	S	-S	+O	-O	-O
S	S	-C	+O	$-C_d$	$+C_d$
Sin	**Cos**	**Sin**	$-C_d$	$+C_d$	+O
S	C	C	$-C_d$	-O	$-C_d$
S	C	-S	$-C_d$	$-C_d$	-O
S	C	-C	$-C_d$	+O	$+C_d$
Sin	**-Sin**	**Sin**	-O	-O	+O
S	-S	C	-O	$-C_d$	$-C_d$
S	-S	-S	-O	+O	-O
S	-S	-C	-O	$+C_d$	$+C_d$
Sin	**-Cos**	**Sin**	$+C_d$	$-C_d$	+O
S	-C	C	$+C_d$	+O	$-C_d$
S	-C	-S	$+C_d$	$+C_d$	-O
S	-C	-C	$+C_d$	-O	$+C_d$
Cos	**Sin**	**Sin**	$-C_d$	+O	$+C_d$
C	S	C	$-C_d$	$+C_d$	+O
C	S	-S	$-C_d$	-O	$-C_d$
C	S	-C	$-C_d$	$-C_d$	-O
Cos	**Cos**	**Sin**	-O	$+C_d$	$+C_d$
C	C	C	-O	-O	+O
C	C	-S	-O	$-C_d$	$-C_d$
C	C	-C	-O	+O	-O
Cos	**-Sin**	**Sin**	$+C_d$	-O	$+C_d$
C	-S	C	$+C_d$	$-C_d$	+O
C	-S	-S	$+C_d$	+O	$-C_d$

C	-S	-C	$+C_d$	$+C_d$	-O
Cos	**-Cos**	**Sin**	+O	$-C_d$	$+C_d$
C	-C	C	+O	+O	+O
C	-C	-S	+O	$+C_d$	$-C_d$
C	-C	-C	+O	-O	-O
-Sin	**Sin**	**Sin**	-O	+O	-O
-S	S	C	-O	$+C_d$	$+C_d$
-S	S	-S	-O	-O	+O
-S	S	-C	-O	$-C_d$	$-C_d$
-Sin	**Cos**	**Sin**	$+C_d$	$+C_d$	-O
-S	C	C	$+C_d$	-O	$+C_d$
-S	C	-S	$+C_d$	$-C_d$	+O
-S	C	-C	$+C_d$	+O	$-C_d$
-Sin	**-Sin**	**Sin**	+O	-O	-O
-S	-S	C	+O	$-C_d$	$+C_d$
-S	-S	-S	+O	+O	+O
-S	-S	-C	+O	$+C_d$	$-C_d$
-Sin	**-Cos**	**Sin**	$-C_d$	$-C_d$	-O
-S	-C	C	$-C_d$	+O	$+C_d$
-S	-C	-S	$-C_d$	$+C_d$	+O
-S	-C	-C	$-C_d$	-O	$-C_d$
-Cos	**Sin**	**Sin**	$+C_d$	+O	$-C_d$
-C	S	C	$+C_d$	$+C_d$	-O
-C	S	-S	$+C_d$	-O	$+C_d$
-C	S	-C	$+C_d$	$-C_d$	+O
-Cos	**Cos**	**Sin**	+O	$+C_d$	$-C_d$
-C	C	C	+O	-O	-O
-C	C	-S	+O	$-C_d$	$+C_d$
-C	C	-C	+O	+O	+O
-Cos	**-Sin**	**Sin**	$-C_d$	-O	$-C_d$
-C	-S	C	$-C_d$	$-C_d$	-O
-C	-S	-S	$-C_d$	+O	$+C_d$
-C	-S	-C	$-C_d$	$+C_d$	+O
-Cos	**-Cos**	**Sin**	-O	$-C_d$	$-C_d$
-C	-C	C	-O	+O	-O
-C	-C	-S	-O	$+C_d$	$+C_d$
-C	-C	-C	-O	-O	+O

Acknowledgements

Sandia National Laboratories is a multi-program laboratory managed and operated by Sandia Corporation, a wholly owned subsidiary of Lockheed Martin Corporation, for the U.S. Department of Energy's National Nuclear Security Administration under contract DE-AC04-94AL85000. This work was supported by the Division of Materials Science, Office of Basic Energy Sciences, U.S. Department of Energy (DOE). We thank Doug Read, Sandia

National Laboratories, for assistance in making the 3-d Lissajous plots. We thank Matt Groo at Novamet for supplying the magnetic platelets.

References

11.1 J. Rabinow, The magnetic fluid clutch, *AIEE Trans.* **67**, 1308–1315 (1948).

11.2 J. de Vicente, D.J. Klingenberg and R. Hidalgo-Alvarez, Magnetorheological fluids: a review, *Soft Matter* **7**, 3701–3710 (2011).

11.3 P. Sheng and W. Wen, Electrorheological fluids: Mechanisms, dynamics, and microfluidics applications, *Annu. Rev. Fluid Mech.* **44**, 143–174 (2012).

11.4 K.J. Solis and J.E. Martin, Isothermal Magnetic Advection: Creating functional flows for heat and mass transfer, *Appl. Phys. Lett.* **97**, 034101 1–3 (2010).

11.5 K.J. Solis and J.E. Martin, Stimulation of vigorous rotational flows and novel flow patterns using triaxial magnetic fields, *Soft Matter* **8**, 11989–11994 (2012).

11.6 J.E. Martin, Theory of strong intrinsic mixing of particle suspensions in vortex magnetic fields, *Phys. Rev. E: Stat., Nonlinear, Soft Matter Phys.* **79**, 011503 1–12 (2009).

11.7 J.E. Martin, L. Shea-Rohwer and K.J. Solis, Strong intrinsic mixing in vortex magnetic fields, *Phys. Rev. E: Stat., Nonlinear, Soft Matter Phys.* **80**, 016312 1–6 (2009).

11.8 K.J. Solis, R.C. Bell and J.E. Martin, Vortex magnetic field mixing with anisometric particles, *J. Appl. Phys.* **107**, 114911 1–4 (2010).

11.9 P. Tierno, J. Claret, F. Sagués and A. Cēbers, Overdamped dynamics of paramagnetic ellipsoids in a precessing magnetic field, *Phys. Rev. E: Stat., Nonlinear, Soft Matter Phys.* **79**, 021501 1–6 (2009).

11.10 J.E. Martin and K.J. Solis, Symmetry-breaking magnetic fields create a vortex fluid that exhibits a negative viscosity, active wetting, and strong mixing, *Soft Matter* **10**, 3993–4002 (2014).

11.11 K.J. Solis and J.E. Martin, Torque density measurements on vortex fluids produced by symmetry-breaking rational magnetic fields, *Soft Matter* **10**, 6139–6146 (2014).

11.12 J. Dobnikar, A. Snezhko and A. Yethiraj, Emergent colloidal dynamics in electromagnetic fields, *Soft Matter* **9**, 3693–3704 (2013).

11.13 J.E. Martin and A. Snezhko, Driving self-assembly and emergent dynamics in colloidal suspensions by time-dependent magnetic fields, *Rep. Prog. Phys.* **76**, 1–42 (2013).

11.14 A. Snezhko, Non-equilibrium magnetic colloidal dispersions at liquid–air interfaces: dynamic patterns, magnetic order and self-assembled swimmers, *J. Phys.: Condens. Matter* **23**, 153101 1–21 (2011).

11.15 A. Snezhko, I.S. Aranson and W.-K. Kwok, Surface-wave-assisted self assembly of multidomain magnetic structures, *Phys. Rev. Lett.* **96**, 078701 1–4 (2006).

11.16 A. Snezhko, M. Belkin, I.S. Aranson and W.-K. Kwok, Self-assembled magnetic surface swimmers, *Phys. Rev. Lett.* **102**, 118103 1–4 (2009).

11.17 A. Snezhko and I.S. Aranson, Magnetic manipulation of self-assembled asters, *Nat. Mater.* **10**, 698–703 (2011).

11.18 P. Tierno, P. Reimann, T.H. Johansen and F. Sagués, Giant transversal particle diffusion in a longitudinal magnetic ratchet, *Phys. Rev. Lett.* **105**, 230602 1–4 (2010).

11.19 P. Tierno, S.V. Reddy, J. Yuan, T.H. Johansen and T.M. Fischer, Transport of loaded and unloaded microcarriers in a colloidal magnetic shift register, *J. Phys. Chem. B* **111**, 13479–13482 (2007).

11.20 P. Tierno, T.H. Johansen and T.M. Fischer, Localized and delocalized motion of colloidal particles on a magnetic bubble lattice, *Phys. Rev. Lett.* **99**, 038303 1–4 (2007).

11.21 P. Tierno, F. Sagués, T.H. Johansen and T.M. Fischer, Colloidal transport on magnetic garnet films, *Phys. Chem. Chem. Phys.* **11**, 9615–9625 (2009).

11.22 A. Soba, P. Tierno, T.M. Fischer and F. Saguès, Dynamics of a paramagnetic colloidal particle driven on a magnetic-bubble lattice, *Phys. Rev. E: Stat., Nonlinear, Soft Matter Phys.* **77**, 060401(R) 1–4 (2008).

11.23 P. Tierno, Depinning and Collective Dynamics of Magnetically Driven Colloidal Monolayers, *Phys. Rev. Lett.* **109**, 198304 1–5 (2012).

11.24 J.E. Martin, A resonant biaxial Helmholtz coil employing a fractal capacitor bank, *Rev. Sci. Instrum.* **84**, 094704 1–11 (2013).

Chapter 12

Quantifying vorticity in magnetic particle suspensions driven by symmetric and asymmetric multiaxial fields[12]

We recently reported two methods of inducing vigorous fluid vorticity in magnetic particle suspensions. The first method employs *Symmetry-Breaking Rational Fields*. These fields are comprised of *two* orthogonal ac components whose frequencies form a rational number and an orthogonal dc field that breaks the symmetry of the biaxial ac field to create the parity required to induce deterministic vorticity. The second method is based on *Rational Triads,* which are fields comprised of *three* orthogonal ac components whose frequency ratios are rational (*e.g.*, 1:2:3). For each method a symmetry theory has been developed that enables the prediction of the direction and sign of vorticity as functions of the field frequencies and phases. However, the theory has its limitations. It only applies to those particular phase angles that give rise to fields whose Lissajous plots, or principal 2-d projections thereof, have a high degree of symmetry. Nor can symmetry theory provide a measure of the magnitude of the torque density induced by the field. In this chapter a single functional of the multiaxial magnetic field is proposed that not only is consistent with all of the predictions of the symmetry theories, but also quantifies the torque density. This functional can be applied to fields whose Lissajous plots lack symmetry and can thus be used to predict a variety of effects and trends that cannot be predicted from the symmetry theories. These trends include the dependence of the magnitude of the torque density on the various frequency ratios, the unexpected reversal of flow with increasing dc field amplitude for certain symmetry-breaking fields, and the existence of off-axis vorticity for rational triads, such as 1:3:5, that do not have the symmetry required to analyze by symmetry theory. Experimental data are given that show the degree to which this functional is successful in predicting observed trends.

[12] As of the date of completion of this dissertation this chapter is not yet published, but will be soon.

12.1 Introduction

Methods of inducing vigorous noncontact fluid flow are important to technologies involving heat and mass transfer and fluid mixing, since they eliminate the need for moving parts, pipes and seals, all of which compromise reliability. Unfortunately, noncontact methods of inducing strong organized flows are few, and have limitations of their own. For example, natural convection [12.1–12.3] requires both gravity and a destabilizing thermal gradient. Magnetohydrodynamics [12.1] requires the injection of large currents into conducting liquids and high magnetic fields. Thermomagnetic convection in ferrofluids [12.4,12.5] requires gravity, a destabilizing thermal gradient and a large magnetic field gradient, which makes scaling to large volumes challenging. A more flexible method that eliminated these requirements would be more amenable to a broad range of applications.

We have discovered several classes of triaxial fields of modest strength that induce vigorous noncontact fluid flow in dilute magnetic particle dispersions without requiring gravity, a thermal gradient, or a magnetic field gradient. Such fields can create flow lattices (see Chapter 5 [also Ref. 12.6]), vortex lattices and vortex fluids (see Chapters 7, 9, 10, and 11 [12.7, 12.8]). These induced flows have been used to direct droplet motion [12.9], create a thermal valve (see Chapter 8 [also Ref. 12.10]), effect active wetting (see Chapter 9 [12.7]), and stimulate a variety of biomimetic dynamics, which is the topic of Chapter 13 [12.9]. However, at this point our understanding of these flows is based only on the symmetry of the multiaxial fields and this non-quantitative approach is useful only for certain highly symmetric fields. In this chapter a functional of the magnetic field is introduced that pertains to the measurable fluid torque densities. The purpose of this study is to investigate the degree to which this functional conforms to the wide range of observed phenomena, to demonstrate that it conforms to the many predictions of symmetry theory, and to use this functional to make predictions where symmetry theory cannot be applied.

12.2 Symmetry theory background

The symmetry theories we have developed are for two classes of fields that induce vorticity, each of which is comprised of three orthogonal components. The first class we call *symmetry-breaking rational fields* (see Chapters 9 and 10 [12.7,12.8]). These fields employ two alternating components and one dc component. The frequencies of the ac components form a rational number l:m, where l and m are relative primes, so either one or both are odd. The second class of fields we call *rational triads* (see Chapter 11 [12.11]), which differ in that all three components are alternating. Once again the frequency ratios are rational numbers, such as 1:2:3. For both field classes it can be shown that the dynamic fields have the symmetry of vorticity and thus have the parity required to allow deterministic fluid vorticity and flow reversal.

The primary goal of the symmetry theories is to predict whether deterministic vorticity can occur and if so, to predict the direction of the fluid vorticity vector and the field changes required to reverse the sign of the vorticity without changing its magnitude. For symmetry-breaking fields the predictions are that the vorticity axis is parallel to the odd axis unless both axes are odd, in which case it is parallel to the dc field. Only if the vorticity is around an ac axis does reversing the dc field reverse the flow, but changing the phase of the high frequency (n) component by $180°/m$ always reverses the flow. In Chapter 10 these predictions were experimentally confirmed for all fields investigated [12.8].

For rational triads the symmetry theory predicts that vorticity occurs around the field component whose reduced frequency has unique numerical parity (*e.g.*, the "2" in 1:2:3). In the case where all reduced frequencies are odd (*e.g.*, 1:3:5) the dynamic field does not have the symmetry of vorticity, so it is not possible to make predictions about flow with this approach. Symmetry theory also predicts the phase changes required to reverse flow. These predictions were also experimentally confirmed in Chapter 11 for the fields we have investigated [12.11].

Symmetry theory has some limitations. First, it is not possible to make predictions for fields whose Lissajous trajectories are not highly symmetrical. For symmetry-breaking fields these 2-d trajectories occur at particular phase angles between the two ac components. For example, for a 1:2 field these special phase angles (applied to the high frequency component) are 0°, 90°,180°,… In all cases there are four distinct Lissajous trajectories that can be treated out of this 1-d set of continuous phases. All other phase angles cannot be treated. For rational triads the symmetric Lissajous trajectories can be obtained by applying the phase angles 0°, 90°,180°,… to each of the three frequencies in any combination. It turns out that this creates only 16 *distinct* 3-d Lissajous trajectories that can be analyzed out of the 2-d set of independent phase angles (there are only two independent phases for three frequencies since the zero of time is unimportant).

A second limitation of symmetry theory is the inability to make any kind of estimate of the *magnitude* of the torque density created within a magnetic particle dispersion subjected to a multiaxial field. Intuitively it is reasonable that a 1:2 symmetry-breaking field will create greater vorticity than a 13:20 field, but there is currently no method of justifying this belief. Even more disconcerting is the inability to deal with the effect of small frequency changes. For example, the symmetry-breaking field 150:100 factors to 3:2, so vorticity is predicted to occur around the high-frequency field axis. But if the low frequency is increased to obtain 150:101 the low frequency axis becomes odd so vorticity should now occur around this axis. But 150:101 can be viewed as a phase-modulated 3:2 field, so we expect to observe oscillating vorticity around the high frequency axis, which is indeed the experimental observation. Symmetry theory cannot address this oscillating flow.

Finally, symmetry theory cannot address the utter peculiarity of the origin of these flows. There is just something strange about predicting vorticity for fields that in general are non-circulating. Yet these flows can be quite vigorous. In fact, the symmetry theory only shows that these flows are allowed and cannot make any statement about whether they should or should not occur. For these reasons it is desirable to have a physically reasonable

method that for any given field can produce a vorticity vector. One approach is to simulate the system microscopically. This would lead to knowledge of the microscopic magnetic particle dynamics as well as addressing the issues raised above, but such an approach would be extremely time consuming. A second approach is to develop a closed form theory of the microscopic particle dynamics that can at least be numerically integrated. A third approach is to use physical insight and previous results to develop a functional that produces the vorticity vector. This is the approach we have taken as a first step on the path to quantifying vorticity in any multiaxial field.

12.3 The torque density functional

A physically meaningful functional must conform to all of the above-mentioned predictions of the symmetry theories and yet must also conform to various experimental observations. These observations include the finding that the torque density in a particle suspension exposed to a particular field is independent of particle size, liquid viscosity, and the magnitude of the field frequencies, provided that the *Mason* number is below a critical value that permits particle chaining. For the restricted case of a "vortex field," which consists of a rotating field to which an orthogonal dc field is applied, an expression has been derived for the suspension torque density that is based on the analysis of *volatile* particle chains that lag in phase behind the field [12.12]. This is a phase lag problem in three dimensions for particle chains whose size is determined by various instabilities that lead to fragmentation. This theory successfully accounts for all of the experimental observations on vortex fields, the result being

$$\mathrm{T} = \frac{1}{12}\phi_p \mu_0 M^2 \sqrt{\sin^2\theta_f - \cos^2\theta_f} \quad \text{for } \theta_f \geq 45° \tag{12-1}$$

where ϕ_p is the volume fraction of particles, μ_0 is the permeability of free space, M is the particle magnetization, and θ_f is the angle the field vector makes to the dc field. For this case the Mason number is defined as $Mn = 9\eta\omega/(2\mu_0 M^2)$, where ω is the field frequency.

Equation 12-1 is valid when this Mason number is less than ~0.02 for *balanced* vortex fields—those having equal rms field components ($\tan\theta_f = \sqrt{2}$). In the case of linear magnetic polarization the particle magnetization for a dilute suspension is given by $\chi_p H_0$ where $\chi_p = 3$ is the intrinsic susceptibility of a magnetic sphere comprised of a material whose relative permeability greatly exceeds that of the liquid, which is the typical case for soft ferromagnetic particles. In short, the specific torque density T/ϕ_p is simply proportional to the energy density $\mu_0 H_0^2$ of the field.

The vortex field is a very simple case because it admits a steady-state solution. For other multiaxial fields, such as 1:2:dc the field magnitude is not constant and the axis about which instantaneous field rotation occurs is not so easily described. If we make the approximation that the instantaneous field energy density gives the instantaneous torque density then all that remains is dealing with the direction of the instantaneous torque vector. As a second approximation this torque direction is taken to be the direction about which the instantaneous field rotates, $\mathbf{H}_0(t)\times\dot{\mathbf{H}}_0(t)\big/\left|\mathbf{H}_0(t)\times\dot{\mathbf{H}}_0(t)\right|$. In other words, this vector is normal to the instantaneous rotation plane of the field. If the torque is indeed caused by particle chains lagging the field, then this is a good approximation when the phase lag is small (which should be the case if mixing occurs, because the phase lag "self-corrects" by way of chain fragmentation if the phase lag becomes too large [12.12]). The expression for the torque density functional **M** is thus

$$\mathbf{M} = \int_0^1 \mathbf{M}(s)ds \text{ where } \mathbf{M}(s) = \int \left|\mathbf{h}(s)\right|^2 \frac{\mathbf{h}(s)\times\dot{\mathbf{h}}(s)}{\left|\mathbf{h}(s)\times\dot{\mathbf{h}}(s)\right|} ds \tag{12-2}$$

where $s = ft$ is the reduced time, f is a frequency, and **h** is the reduced field. For symmetry breaking fields the reduced field is

$$\mathbf{h}(t) = \frac{\mathbf{H}_0(t)}{H_0} = \sin(l\times 2\pi ft + \phi_l)\hat{\mathbf{x}} + \sin(m\times 2\pi ft + \phi_m)\hat{\mathbf{y}} + \frac{c}{\sqrt{2}}\hat{\mathbf{z}} \tag{12-3}$$

l and m are relative primes and by convention $l \le m$. The rms reduced field is $\sqrt{2+c^2}/\sqrt{2}$. (For a balanced field, where all rms field components are equal $c = 1$.) For the rational triads we restrict our attention to balanced fields, so

$$\mathbf{h}(t) = \frac{\mathbf{H}_0(t)}{H_0} = \sin(l \times 2\pi ft + \phi_l)\hat{\mathbf{x}} + \sin(m \times 2\pi ft + \phi_m)\hat{\mathbf{y}} + \sin(n \times 2\pi ft + \phi_n)\hat{\mathbf{z}} \quad . \qquad (12\text{-}4)$$

In this case the rms reduced field is $\sqrt{3/2}$ and to be definite $l \le m \le n$. The predicted torque density is related to the dimensionless torque density functional by $\mathbf{T} = const \times \phi_p \mu_0 H_0^2 \mathbf{M}$.

This expression may be viewed as an *ansatz*, not a theory *per se*; however, it produces many useful results that are in accord with both symmetry theory and experiment, and also can be used to successfully predict unexpected effects that we have observed in experiment. Some of these predictions were sufficiently strange that we literally ran down to the lab to verify them, and verify them we did, as will be discussed below.

12.4 Experimental

The magnetic particle suspension consisted of molybdenum-Permalloy platelets ~50 μm across by 0.4 μm thick (Novamet Corp.) dispersed into isopropyl alcohol at a low volume fraction. The uniform triaxial ac magnetic fields were produced by three orthogonally-nested Helmholtz coils, operating in series resonance with appropriately-configured capacitor banks, two of which employ a computer-controlled fractal design [12.13]. For the 1:3:5 rational triad field studied in this work the fundamental frequency was 50 Hz and all three induction field component amplitudes were 150 G_{rms}. All three field components were phase-locked *via* two Agilent/HP function generators (equipped with Option 005), allowing for *stable* control of the phase angle of each component. (If the field components are not phase-locked there will be a very slow phase modulation between the components due to

the finite difference in the oscillator frequency of each function generator, preventing meaningful studies of the phase angle.)

To quantify the magnitude of the vorticity, the torque density of the suspension was computed from measured angular displacements on a custom-built torsion balance. In this case the suspension (1.5 vol%) was contained in a small vial (1.8 mL) attached at the end of the torsion balance and suspended into the central cavity of the Helmholtz coils *via* a 96.0 cm-long, 0.75 mm-diameter nylon fiber with a torsion constant of ~13 μN·m rad^{-1}.

12.5 Results and Discussion

12.5.1 Computations for symmetry-breaking fields

The first issue that must be addressed is whether the functional conforms to the predictions of symmetry theory. The case of a 2:3:dc field with both phase angles set to zero is given in **Figure 12-1**. Recall that vorticity must occur around the high frequency (*y*) axis in this case. In these figures the three components of the integrand of **M**(s) are given as functions of the reduced time and the integral. This integral corresponds to the rotation of a body subject to this time-dependent torque density. Along both the *x* and *z* axes the integrands are

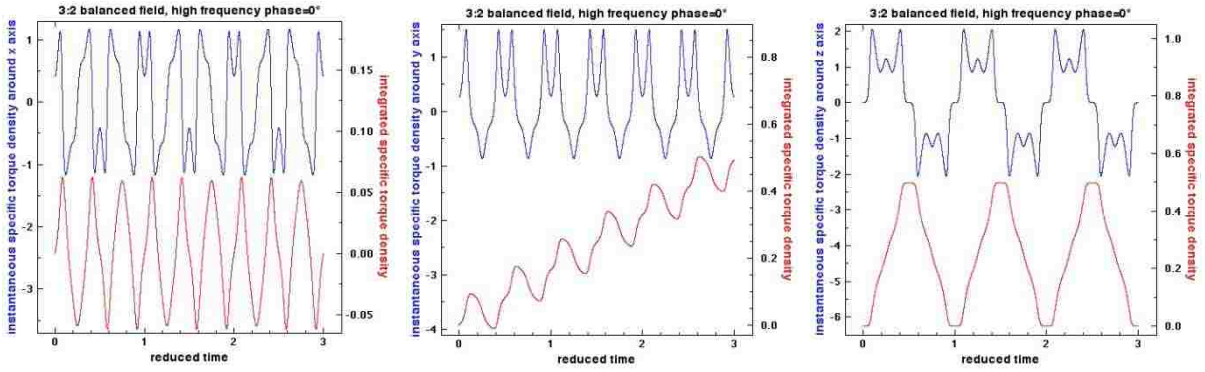

Figure 12-1. Instantaneous values of the computed torque functional are given for a 2:3:dc symmetry-breaking field. The integral of these functions corresponds to the rotation of a free body subjected to this torque. A persistent rotation only occurs around the *y* axis, which is indeed the prediction of symmetry theory. The time-averaged torque density functional is the slope of the integral. It is this slope that pertains to measurement, since the field frequencies are typically in the audio range, generally above 48 Hz in our laboratory and frequently much higher, and so the fluctuations only give rise to rapid fluctuations of the needle in our torsion fiber apparatus.

perfectly symmetric around zero, so the integral over one cycle is zero and the average slope of the integral, which is proportional to the torque density, is thus zero. Along the *y* axis the integral is asymmetric, and the integral has a finite average slope and torque density. So this particular case conforms to the predictions of symmetry theory. In fact, even the predicted fluctuations in the torque can be observed experimentally.

12.5.2 Dependence on phase and dc field

The torque density has a strong dependence on the relative phase between the ac field components, as well as on the magnitude of the dc field. This dependence is shown in **Figure 12-2** for the *y* axis torque created by the 2:3:dc field. At zero dc field the torque functional is zero, in accordance with symmetry theory for even, odd fields, but for finite dc fields the torque is non-vanishing, is periodic on the interval 180°, and can be reversed at constant magnitude by any 90° shift of the high frequency phase, in agreement with both symmetry theory (see Chapter 9 [also Ref. 12.7]) and experiment (see Chapter 10 [also Ref. 12.8]). Moreover, symmetry theory shows that reversing the dc field reverses the torque for even, odd fields and the torque functional also shows this reversal. In general, for the field *l*:*m* symmetry theory shows that when plotted against the high-frequency phase the torque

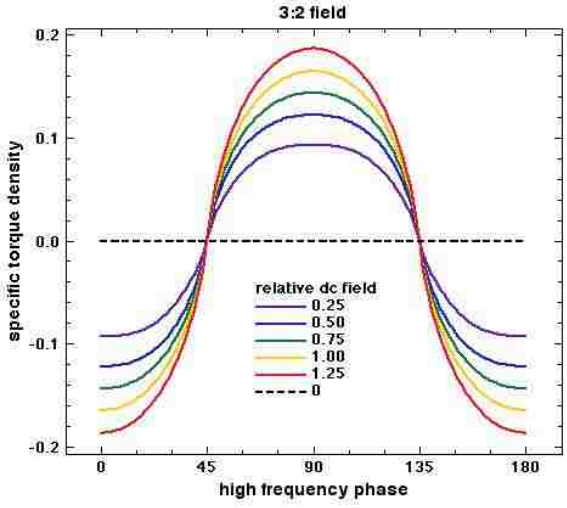

Figure 12-2. Computed torque density as a function of the high frequency phase for the 2:3:dc field. The dc field is relative to the rms amplitude of either of the ac field components.

curve is periodic on the interval $360°/l$ and reverses at constant magnitude for phase shifts of $180°/l$.

Odd:odd fields differ in that vorticity is symmetry allowed even in the absence of the dc field component and therefore must not reverse upon dc field reversal. Computations for the 1:3 field do indeed show that the torque functional does not vanish in the absence of a dc field, but grows stronger as the dc field increases and cannot be reversed by reversing the dc field. This suggests the possibility of torque when the dc field is replaced by an ac field, a subject discussed below. However, the experimental situation is complicated by the fact that in the absence of the dc component the particles experience a time-averaged interaction that can be described as a negative dipolar interaction, causing the particles to form into parallel stationary sheets [12.14–12.16] (like baklava), instead of forming the volatile chains that give rise to vorticity. Because of this competing effect, fluid vorticity does require the presence of the dc component, at least for spherical particles. For platelets made of soft ferromagnetic materials the situation is more complex. Although stationary sheets can form in a biaxial field under some circumstances (*e.g.*, very high frequency, very high viscosity, low field), flow instabilities typically occur in the form of a square lattice of antiparallel flow columns normal to the plane of the field (see Chapter 5 [also Ref. 12.6]). When these columns form in an odd:odd field there is pronounced vorticity as well, the axis of which is parallel to the flow columns. At higher platelet loadings a normal-field instability can occur that causes the particle dispersion to rise up as a ridge, within which the lattice of flow columns can be observed (see Figure 5-4 in Chapter 5 [also Ref. 12.6]). The vorticity in the absence of a dc field can easily be confirmed by detuning one of the field components to create a phase modulation that periodically reverses the vorticity. The ridge then sloshes back-and-forth in response to the oscillating vorticity, which brings us to the next issue: field heterodyning.

12.5.3 Heterodyning

A more interesting problem is that of heterodyning, which occurs when one of the frequencies is detuned to create a modulation of phase and flow reversal. In **Figure 12-3** are presented computations for the case 101:150:dc. Because this is a modulation of 2:3:dc it is expected that a periodic torque around the *y* axis will occur, and this is indeed observed

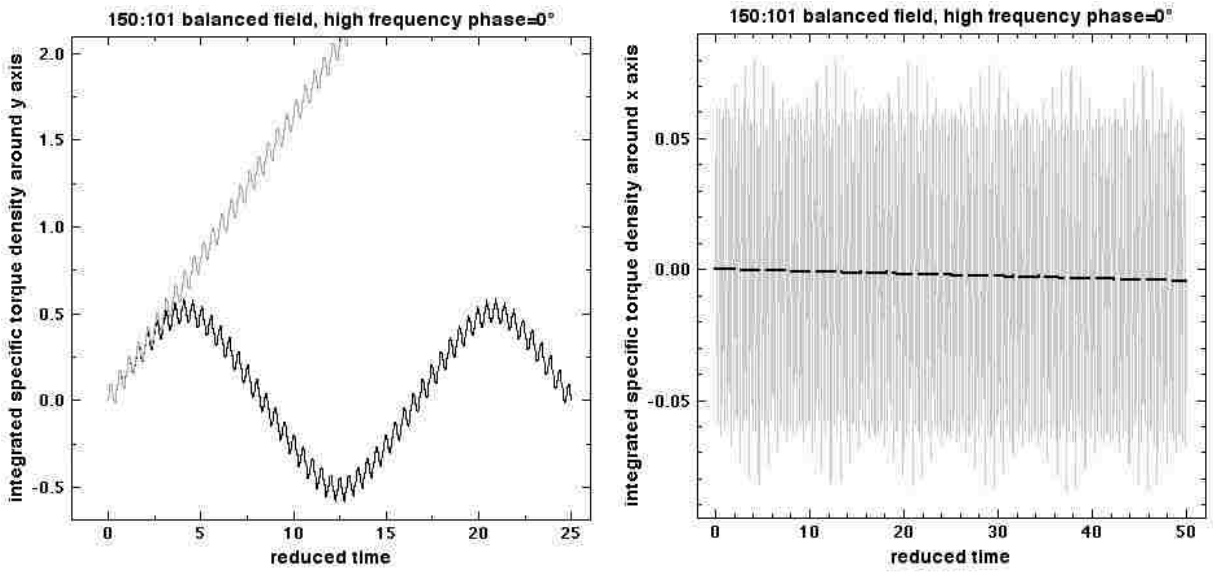

Figure 12-3. When a 2:3:dc field is detuned field to 101:150:dc the heterodyne beating creates periodic flow reversal around the *y* axis, which is indeed observed in the laboratory. **(left)** The torque functional demonstrates this flow reversal and shows that the peak torque density is expected to be the same as for the non-heterodyned field. However, symmetry theory shows that for the 101:150:dc field the average torque can be non-vanishing only around the x axis. For this field the torque functional shows that around the *y* axis does indeed average to zero and a small but finite net torque does occur around the x axis **(right)**.

in the component $M_y(s)$. More importantly, the time-average of this torque is zero, in conformity to symmetry theory. However, symmetry theory allows a finite time-average torque around the *x* axis, and although this torque is quite small, the slope can be seen in the data in **Figure 12-3(right)**.

12.5.4 Torque density for fields of increasing complexity

As the irreducible ratio of the field frequencies requires larger integers to represent, both experiment and intuition indicate that the suspension torque density diminishes, though symmetry theory is uninformative on this point. To examine this issue we have considered a

few particular sequences of irreducible rational numbers. The first two sequences arise in investigations of the fractional quantum Hall effect [12.17] and serve as useful examples here as well. Both of these sequences approach $1/2$, one from above $[k:(2k-1),\ k=1,2,\ldots]$ and one from below $[k:(2k+1),\ k=1,2,\ldots]$. All of these calculations are for balanced fields and the relative phase angle between the field components (either ϕ_x or ϕ_y will do) is varied to find the maximum of the torque functional.

The dependence of |**M**| on the denominator of these ratios is shown in **Figure 12-4(top)**. For the sequence approaching ½ from above the torque vacillates between the high frequency and dc field directions, in agreement with symmetry theory, and falls off asymptotically as the inverse of the number of domains N in the relevant Lissajous curve, given by $N = lm + (l-1)(m-1)$. Fields such as 21:41 therefore give rise to very small torques in comparison to something like 2:3. For the sequence approaching ½ from below, **Figure 12-4(top, right)**, the behavior is very similar, with the odd:odd fields showing somewhat greater torque.

Both of these sequences were investigated experimentally, with the torque data shown in **Figure 12-4(bottom)**. The experimental torque values display the alternation of the vorticity axis between the high frequency and dc field axes, in accord with the torque functional and symmetry theory. Furthermore, an oscillatory trend in the relative magnitudes of the torques between the two vorticity axes is also observed; however, the trend in the relative magnitudes is reversed from that predicted by the functional. The reason for this discrepancy is not clear. Finally, the overall magnitude of the torque is observed to decay rapidly with increasing denominator frequency, corresponding to an increasing number of Lissajous domains.

Two sequences approaching unity were investigated as well. The first consists of irreducible ratios containing an even integer, $[k:(k+1),\ k=1,2,\ldots]$, and the second consists of only odd numbers, $[(2k-1):(2k+1),\ k=1,2,\ldots]$. **Figure 12-5(top, left)** shows that for the even, odd field sequence there is an oscillation between the torque being around the low

and high frequency axis, as expected from symmetry theory, and that the maximum torque is again asymptotically scaling as the inverse number of domains in the Lissajous plot. For odd:odd fields the torque is predicted to occur only around the dc field direction and once

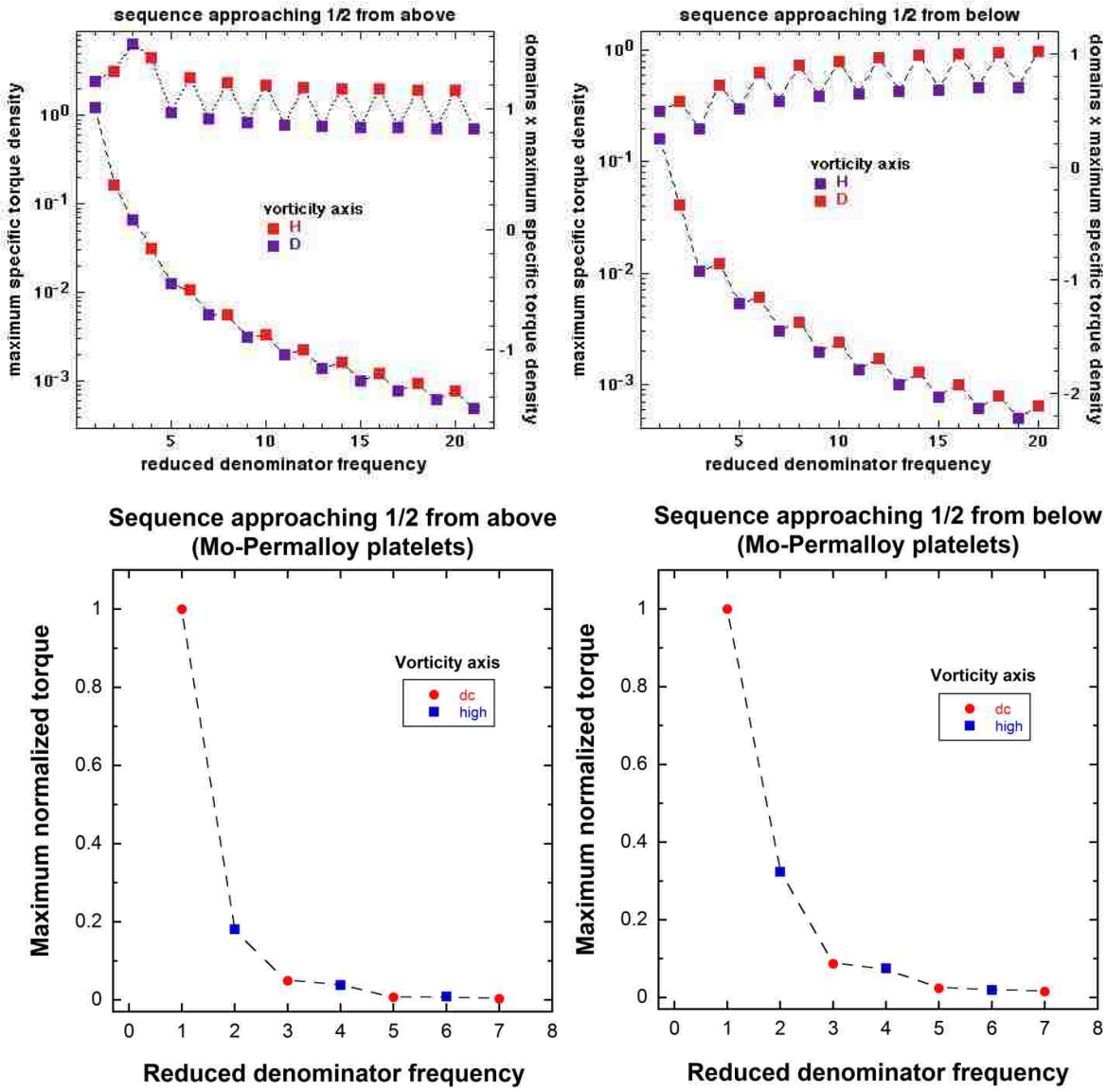

Figure 12-4. (top) The maximum of the torque functional as a function of phase is plotted versus the relative denominator frequency for rational number sequences approaching ½ from above and below. Multiplying these peak torques by the number of domains in the 2-d Lissajous plots shows an approach to an asymptote, indicating an algebraic decay. The alternation in the torque axes are predicted by symmetry theory as well. **(bottom)** Experimental torque data for rational number sequences approaching ½ from above and below show the alternation of the vorticity axis between the high frequency and dc field axes, although the relative magnitude of the torque around each axis is reversed from the trend predicted by the functional. In both cases the magnitude of the torque is observed to decay rapidly as the number of Lissajous domains increases.

again it falls off as the inverse number of domains, **Figure 12-5(top, right)**, but the amplitude is much larger for any given domain number than for the other cases investigated.

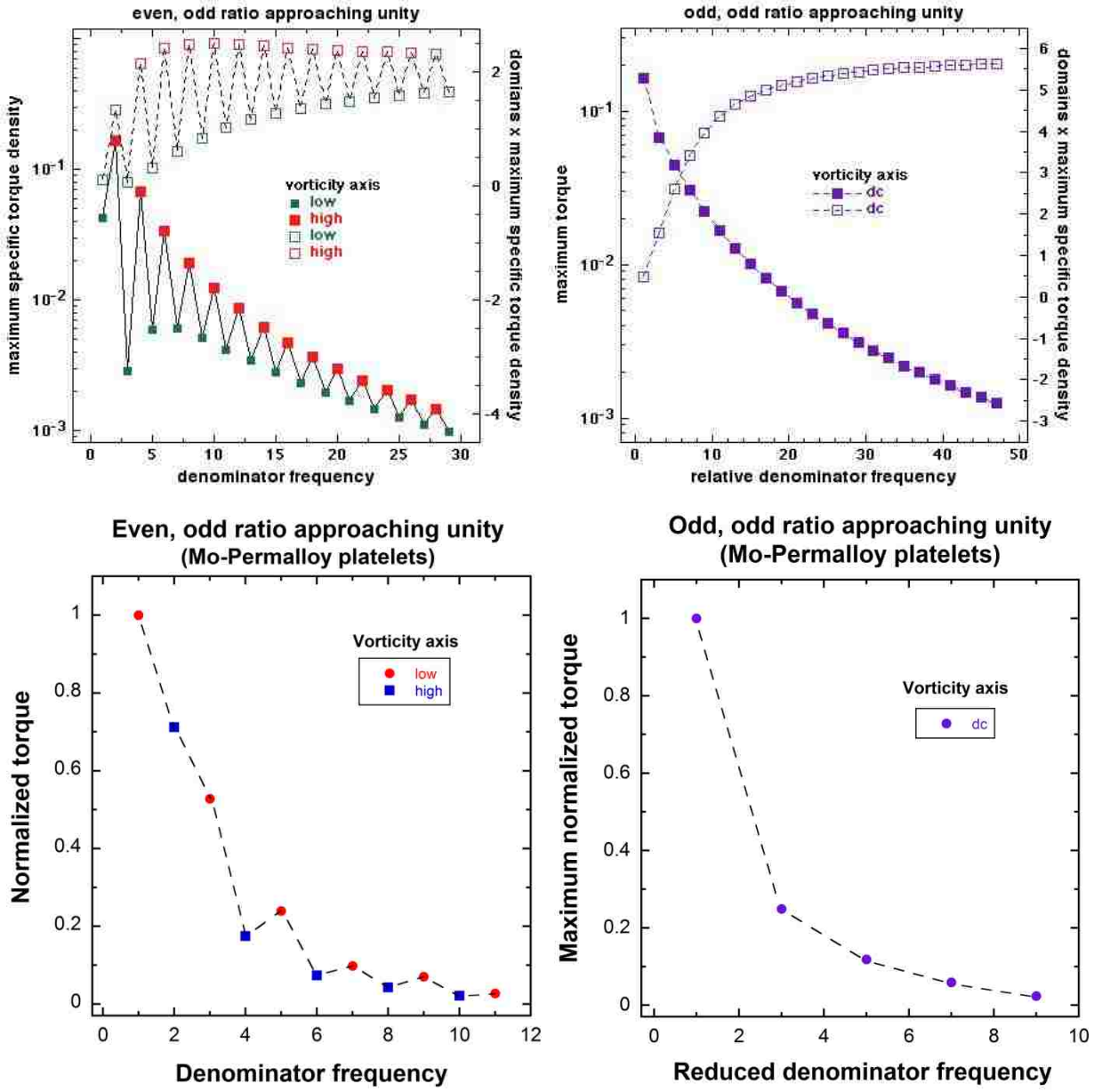

Figure 12-5. (top) The maximum of the torque functional as a function of phase is plotted versus the relative denominator frequency for even:odd and odd:odd frequencies approaching unity. Multiplying these peak torques by the number of domains in the 2-d Lissajous plots shows an approach to an asymptote, indicating an algebraic decay. The odd:odd torques are expected to be especially strong. **(bottom)** Experimental torque data for even, odd and odd,odd frequency ratios approaching unity. An oscillatory series of torques are produced for the even, odd series whose vorticity axis alternates between the high and low frequency components, whereas the vorticity axis is always along the dc field in the odd, odd series. In both cases the magnitude of the torque is observed to decay rapidly as the number of Lissajous domains increases.

Experimental torque data were also collected for the even, odd sequence approaching unity, **Figure 12-5(bottom, left)**. In accord with the predicted data from the functional in Figure 12-5(top, right), the experimental torque values display an oscillatory behavior as the overall magnitude rapidly decays with increasing denominator frequency. The oscillations in torque correspond to the vorticity axis alternating between the high and low frequency components. However, as was observed with the sequences approaching ½ from above and below, the trend in the relative magnitudes between the two vorticity axes is reversed from that predicted by the functional. The odd:odd ratio approaching unity was also investigated [**Figure 12-5 (bottom right)**], in which case the torque only occurs around the dc field axis and falls off rapidly with increasing denominator frequency.

Finally, neighboring terms in a Fibonacci sequence are relative primes and so make sequences of irreducible rational numbers. We investigated the sequence 1:1, 1:2, 2:3, 3:5, 5:8, 8:13,… This sequence approaches the inverse golden ratio. The maximum torque functional for this sequence is plotted in **Figure 12-6**. The vorticity axis is observed to form

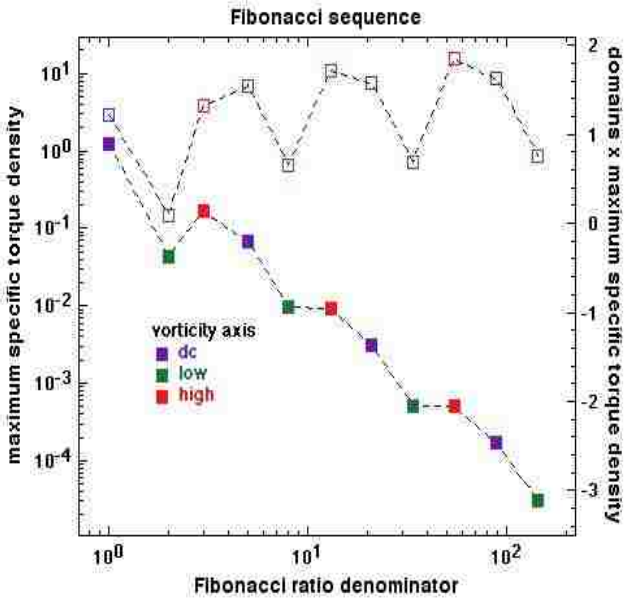

Figure 12-6. The Fibonacci sequence creates a periodic transition between all three field axes and once again the peak torque falls off as the inverse of the number of domains.

the repeated axis sequence dc, low, high, which is once again in accord with symmetry theory. Once again the torque falls off as the inverse number of domains in the Lissajous plots.

12.5.5 Flow reversal

In Chapter 10 [also Ref. 12.8] we reported a very strange observation for a 1:2 field. After applying the ac fields the dc field was slowly ramped up, which caused fluid vorticity to initiate and progressively increase. As the field was progressively increased further the vorticity slowed down, stopped, and then reversed direction. Symmetry theory cannot address this issue, but can the torque functional shed light on this? In **Figure 12-7** calculations are shown for a 1:2 field over a range of dc field strengths, ranging from $c = 0$ to 1.25 (see Equation 12-3). Flow reversal occurs at roughly $c = 0.75$, which is commensurate with experimental observations of surface flow [12.8]. We pursued this issue by investigating many different symmetry-breaking rational fields and for all SBR fields of the form odd:odd + 1 that we have investigated flow reversal is indicated. We can find no other fields where the torque functional indicates flow reversal.

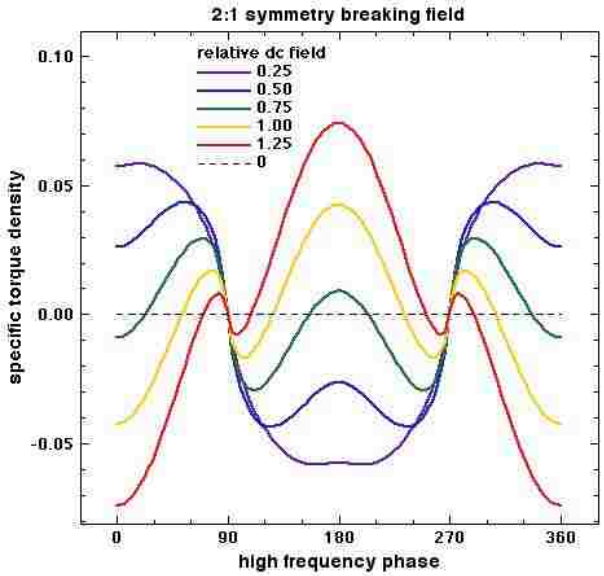

Figure 12-7. For all of the odd:odd+1:dc fields we have investigated (1:2, 3:4,...) the torque functional indicates flow reversal with increasing field. Flow reversal seems to be unique to this class of fields.

12.5.6 Inducing vorticity with biaxial fields?

It is quick and easy to investigate a lot of ideas with the torque functional, including ideas that might be difficult to screen experimentally. Symmetry-breaking rational fields consist of three orthogonal components and thus are three-dimensional fields. Is it possible to initiate strong vorticity with fields confined to a plane? Take for example the biaxial field in the *x*-*y* plane with frequency ratio 2:3. Recall that this field produces vorticity around the *y* axis when a dc field is applied along the *z* axis. If instead a dc field is applied along the *y* axis, which is the odd axis, the torque functional indicates torque around the *z* axis, **Figure 12-8**. The dependence of the torque functional on phase angle approaches a square wave, which is striking. The *z* axis is a C_2 symmetry axis for this case when one considers the equivalency of the field and its converse and the other two axes are antisymmetric under a 180° rotation. Because this symmetry is shared by vorticity around the *z* axis this observation could have been anticipated. Experiments on platelet suspensions do indeed confirm this prediction. On the other hand, if a dc field is applied along the *x* axis the torque functional predicts that vorticity will not occur, and it is notable that all three axes are C_2 axes for the field and its converse, which is not the symmetry of vorticity.

Similar observations apply to the 1:2 field: when a dc field is applied along the odd axis (which in this case is the low frequency axis) the torque functional indicates torque around the *z* axis. When a dc field is applied along the even axis the functional predicts no torque. Again, this behavior could have been anticipated from the symmetry of the trajectories. It would appear that all even, odd fields are capable of producing a *z* axis torque when a dc field is applied along the odd field component.

As discussed above, odd:odd fields produce torque around the *z* axis even in the absence of a dc field, because odd:odd fields possess the symmetry of vorticity, with the *z* axis being the C_2 axis of symmetry. Applying a dc field along either of the ac components does not change this symmetry and does not appreciably alter the dependence of the torque functional on phase angle. Odd:odd fields do not seem to be interesting as regards the

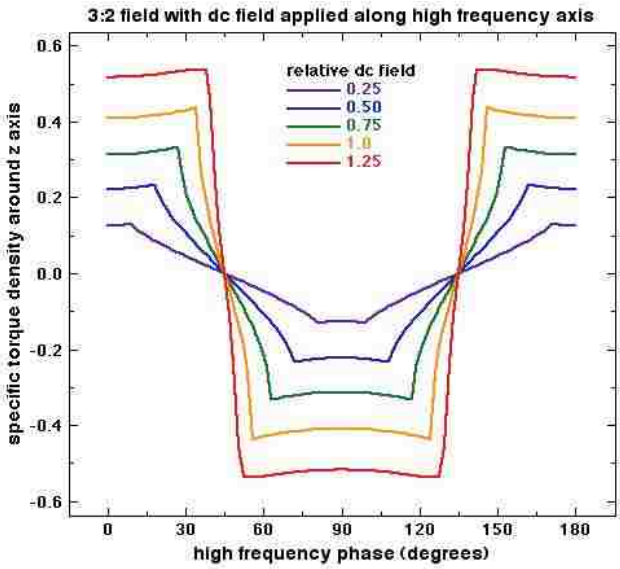

Figure 12-8. When a dc field is applied along the high frequency axis of a 2:3 field the resulting biaxial field produces torque around the normal to the field plane.

addition of in-plane dc fields. However, suspensions of spherical particles have a strong tendency to form particle sheets, and the dc field component reduces this tendency, allowing the particles to form the chains that presumably give rise to the torque. (Spherical particles in epoxy do not give an appreciable torque due to the high viscosity.)

12.5.7 Rational Triads

The experimental investigation of the torque generated by rational triads is time consuming because there are two independent phase angles. If torque measurements are made at 10° intervals for each of the two phase angles, over 1200 measurements are required. At roughly 5 minutes per measurement that requires 100 hrs. of continuous work. Any new ideas about rational fields are therefore tough to sort through, especially those that might lead to off-axis vorticity (see below), which could triple the measurement time, since measurements would in general have to be made along all three field directions. In contrast, it is a matter of much less than a minute to compute the torque functional for the same set of phase angles. These results are sufficiently useful to guide experimental work. In the following we will explore

the torque density functional for the specific cases of the four classes of rational triads, three of which we have previously investigated experimentally in Chapter 11 [also Ref. 12.11].

In Chapter 11 we have shown that there are four classes of rational triads [12.11]. The first is even, odd, odd and 1:2:3 is the simplest example of this class. Symmetry theory shows that this field produces vorticity around the even axis. The second class is even, even, odd fields with even:even factoring to even:odd. A simple example of this class is 2:3:4 and symmetry theory shows that vorticity is around the odd axis for this class (*i.e.*, "3" in this case). The third class is even, even, odd with even:even factoring to odd:odd and once again symmetry theory predicts vorticity around the odd axis. The example of this class that was experimentally investigated in Chapter 11 is 1:2:6. Finally, the fourth class is odd:odd:odd, for which symmetry theory could not make predictions, simply because fields of this class do not have the symmetry of vorticity. These fields can be treated by the torque density functional, however, which we will find predicts off-axis vorticity for the example field 1:3:5.

The symmetry theory for rational triads is based on those 3-d Lissajous trajectories that have highly symmetric projections on faces normal to each of the three field directions. These symmetric 3-d trajectories can be expressed by assigning to each of the three sine terms in Equation 12-4 one of the phases 0°, 90°, 180°, 270°, corresponding to sine, cosine, −sine, −cosine. There are thus $4 \times 4 \times 4 = 64$ symmetric 3-d Lissajous trajectories that can be treated by symmetry theory. These 64 trajectories can be classified into 4 groups of 16. In each of these groups the magnitude of the torque density is fixed, but 8 of the trajectories are clockwise and 8 are counterclockwise. In addition to predicting the vorticity axis, symmetry theory also predicts these groups and the relative vorticity sign for each trajectory within each group.

The 1:2:3 triad. Calculations for the 1:2:3 field show that vorticity does indeed occur around the even axis. In **Figure 12-9** calculations are presented for the torque functional as

a function of each possible set of two independent phase angles, (ϕ_1, ϕ_2), (ϕ_2, ϕ_3) and (ϕ_1, ϕ_3). Of course, all of these data sets contain the same information and can be related to each other by a change of variables. For the 1:2:3 field the equivalent phase angles are $(\phi_1,\phi_2,0)$, $(\phi_1-\frac{1}{2}\phi_2,0,-\frac{3}{2}\phi_2)$, $(0,\phi_2-2\phi_1,-3\phi_1)$.

In the (ϕ_1, ϕ_2) plane one lattice vector that defines the unit cell (a vector that preserves torque density) is seen from Figure 12-9(top left) to be **A**=(0°, 180°). Substituting this phase shift into Equation 12-4 (with $\phi_3=0$) gives

$$\mathbf{h}(t)=\frac{\mathbf{H}_0(t)}{H_0}=-\cos(ls'+\phi_l)\hat{\mathbf{x}}+\sin(ms'+\phi_m)\hat{\mathbf{y}}+\cos(ns')\hat{\mathbf{z}} \tag{12-5}$$

where $s'=s+90°$. The torque equivalence of the fields [−C, S, C] {abbreviation for [−cos(1s), sin(2s), cos(3s)]} and [S, S, S], is in accord with symmetry theory, as shown in Table 11-5 of Chapter 11 [also Ref. 12.10]. The second lattice vector is **B** = (120°, 60°). The change of variables $s'=s+30°$ leads to [C, S, −C], which is also shown by symmetry theory to be equivalent to [S, S, S]. Experimental data need only be taken over this unit cell, which is only 1/6 the computed area. The lattice vectors are those phase changes that preserve vorticity. To reverse vorticity at constant magnitude requires a phase change of (60°, 120°).

It is interesting to examine how the unit cell transforms in other data planes. For the (ϕ_1, ϕ_3) plane the lattice vectors **A** and **B** become (270°, 90°) and (90°, −90°), which is the rather large and experimentally awkward unit cell observed in Figure 12-9(top right). In the (ϕ_2, ϕ_3) plane the lattice vectors **A** and **B** transform to (180°, 0°) and (−180°, 360°) to create the unit cell apparent in Figure 12-9(bottom). (Of course, a simpler choice for the unit cell is the lower half of the plane.) In any case, the torque functional can determine which pair of phase shifts leads to a unit cell suitable for experimental investigation and avoids the issue of taking redundant data. In the (ϕ_1, ϕ_3) plane flow reversal at constant

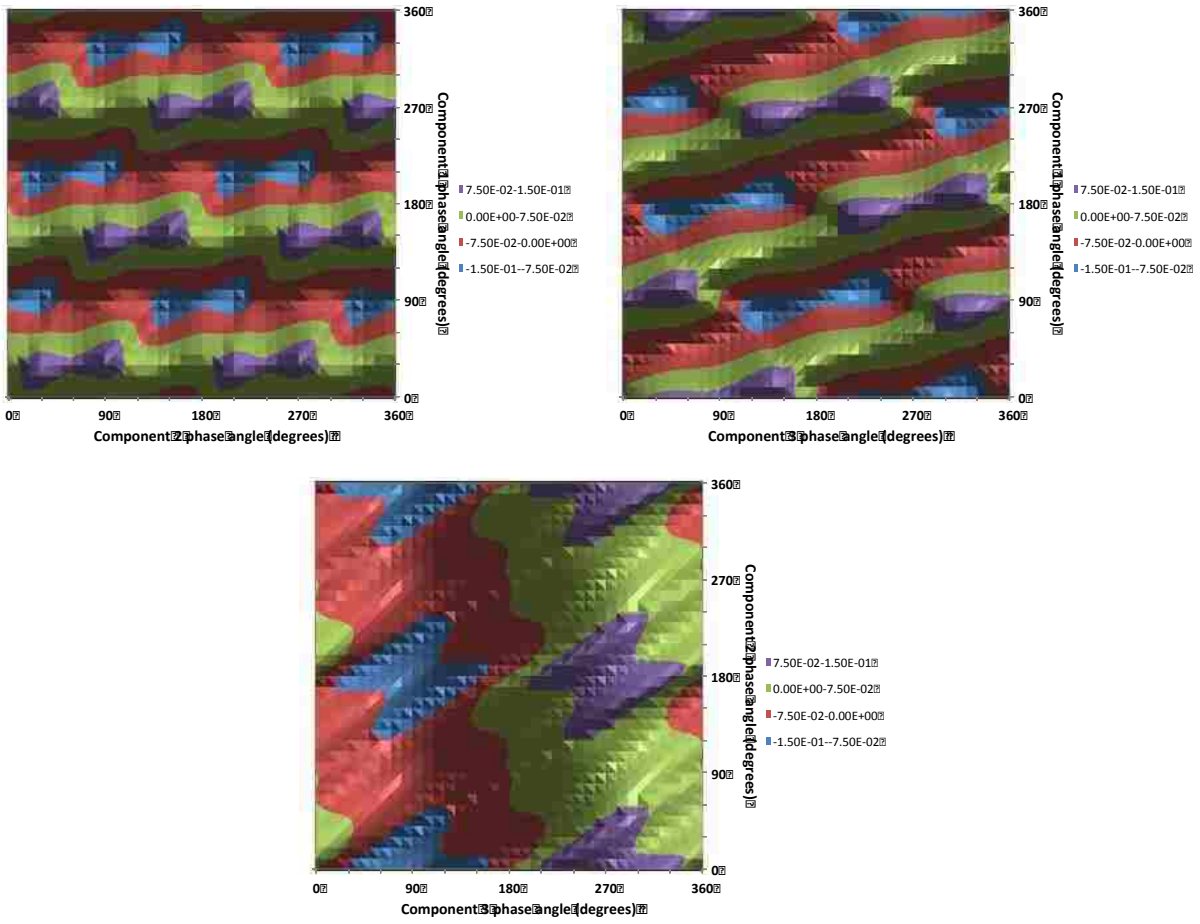

Figure 12-9. The torque functional correctly predicts torque around the *y* axis for the 1:2:3 triad. The torque density is plotted as a function of the three possible sets of phases.

magnitude requires a phase shift of (90°, 90°) and in the (ϕ_2, ϕ_3) the required phase shift is (0°, 180°).

The torque functional can also be computed for the exact phases of all of the 64 symmetric 3-d Lissajous trajectories presented in Table 11-5 of Chapter 11 [also Ref. 12.10]. These computations show that within each group of 16 fields the torque magnitude is indeed constant and the computed relative vorticity signs (CW or CCW) are in agreement as well.

In Chapter 11 experimental data were collected in the (ϕ_1, ϕ_3) plane and demonstrate the predicted lattice vectors. However, the "dog bone" shaped peaks and valleys in Figure 12-9(top left) are merely elongated single peaks in the experimental data.

The 2:3:4 triad. In this case the torque functional shows torque around the odd axis ("3"), in accord with the predictions of symmetry theory. The equivalent phase angles are $(\phi_2,\phi_3,0)$, $(\phi_2-\frac{2}{3}\phi_3,0,-\frac{4}{3}\phi_3)$, $(0,\phi_3-\frac{3}{2}\phi_2,-2\phi_2)$ and in the (ϕ_2, ϕ_3) plane lattice vectors are **A**=(0°, 180°) and **B**=(90°, 45°), **Figure 12-10(top left)**. These phase shifts transform [S, S, S] to [S, −S, S] and [S, −C, −S], respectively. Table 11-7 of Appendix D in Chapter 11 shows that symmetry theory shows the equivalence of [S, S, S], [S, −S, S], and [C, −S, −S]. Moreover, torque functional calculations for the 64 symmetric Lissajous trajectories within this table are in agreement with the vorticity magnitude and sign groupings. Flow reversal at constant magnitude can be achieved by the phase change (0°, 90°).

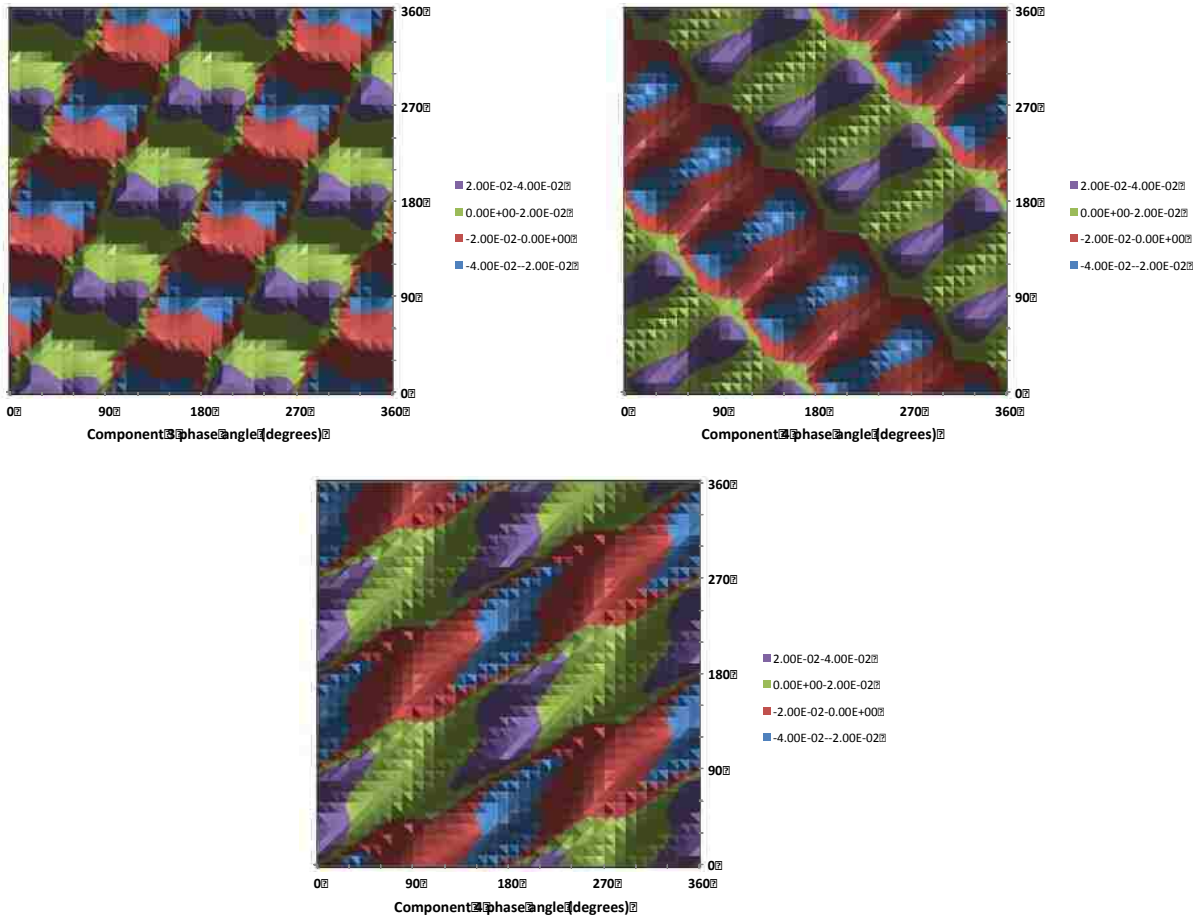

Figure 12-10. The torque functional correctly predicts torque around the *y* axis for the 2:3:4 triad. The torque density is plotted as a function of the three possible sets of phases.

The lattice vectors **A** and **B** become (120°, 240°) and (60°, −60°) in the (ϕ_2, ϕ_4) plane and the unit cell in this case is shown in **Figure 12-10(top right)**. Flow reversal at constant magnitude can be achieved from the phase change (0°, 180°). In the (ϕ_3, ϕ_4) plane the lattice vectors become (180°, 0°) and (90°, 180°) and a unit cell corresponding to these vectors is shown in **Figure 12-10(bottom)**. The simplest flow reversal vector in this plane is (90°, 0°).

In Chapter 11 experimental data were collected in the (ϕ_2, ϕ_3) plane, which was perhaps not the best choice. The symmetry of these data reflect that of the torque functional, but both the shape of the maxima and their exact locations differ somewhat.

The 1:2:6 triad. This is the final example of a rational field for which we previously collected experimental data in Chapter 11. Once again the torque functional demonstrates torque around the axis predicted by symmetry theory, which in this case is the odd axis. The computed magnitudes and the signs of the vorticity are in accord with the predictions of symmetry theory given in Table 11-8 of Appendix D in Chapter 11. In the (ϕ_1, ϕ_6) plane the lattice vectors are (0°, 360°) and (90°, 0°), which transform [S, S, S] to [S, S, S] and [C, S, S] respectively. Table 11-8 in Appendix D of Chapter 11 shows that symmetry theory predicts that the torque density will be invariant for these fields. Flow reversal at constant magnitude can be achieved with the phase change (0°, 180°).

The equivalent phase angles are $(\phi_1,0,\phi_6), (\phi_1-\frac{1}{6}\phi_6,-\frac{1}{3}\phi_6,0), (0,-2\phi_1,\phi_6-6\phi_1)$. In the ($\phi_1$, ϕ_2) plane the lattice vectors transform to (60°, 120°) and (90°, 0°). In the (ϕ_2, ϕ_6) plane the lattice vectors become (0°, 360°) and (180°, 540°). The unit cells for each of these representations are evident in **Figure 12-11**.

In Chapter 11 experimental data were taken in the (ϕ_1, ϕ_6) plane. These data reflect the symmetry of the torque functional, but the peak torques occur at somewhat different phase angles, demonstrating the limitations of the torque functional.

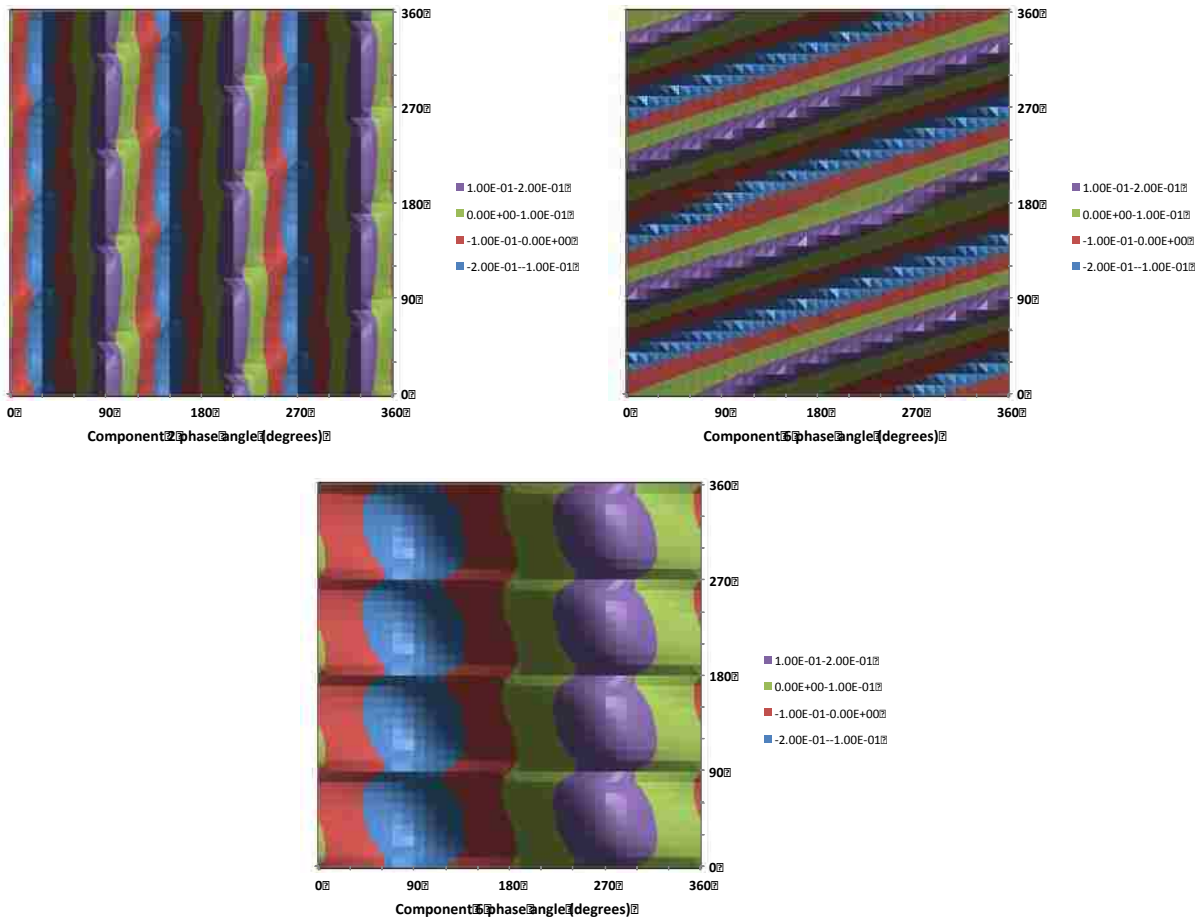

Figure 12-11. The torque functional correctly predicts torque around the x axis for the 1:2:6 field. Again the torque density is plotted as a function of the three possible sets of phases.

The 1:3:5 triad. Odd:odd:odd fields do not have the symmetry of vorticity and so we could not conclude anything about the torque created by these fields in Chapter 11 [also Ref. 12.10]. However, some interesting comments can be made about such fields. Recall that for symmetry-breaking, odd:odd fields the vorticity is invariant to the direction of the dc field. This fact implies that if the dc field is replaced by an alternating field fluid vorticity will still occur around the same axis. Indeed, odd:odd:dc and odd:odd:even both produce vorticity around the z axis. However, by the same logic odd:odd:odd fields should produce vorticity around all axes, so the situation is one of competing amplitudes, which is the domain of the torque functional.

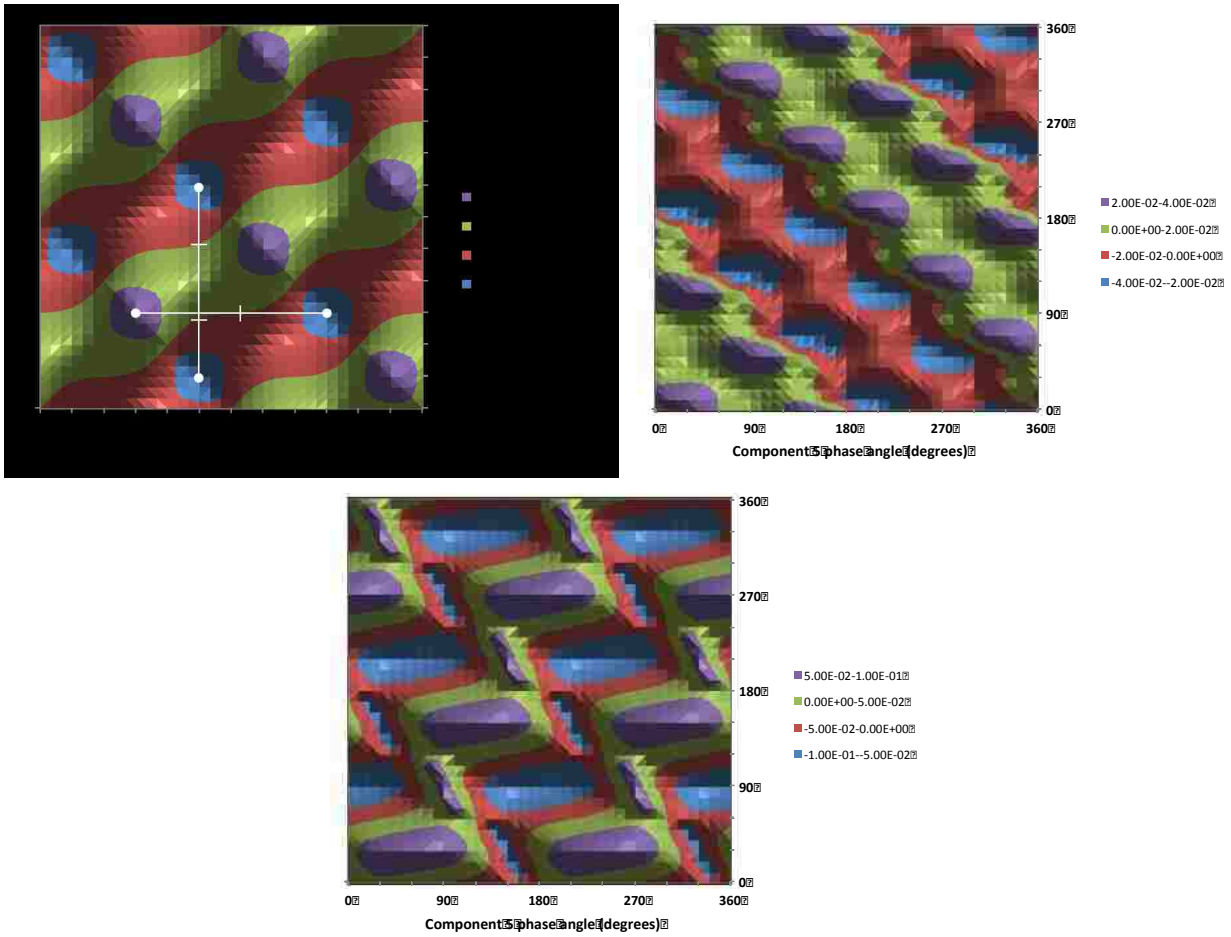

Figure 12-12. The torque functional predicts torque around all axes for the 1:3:5 field.

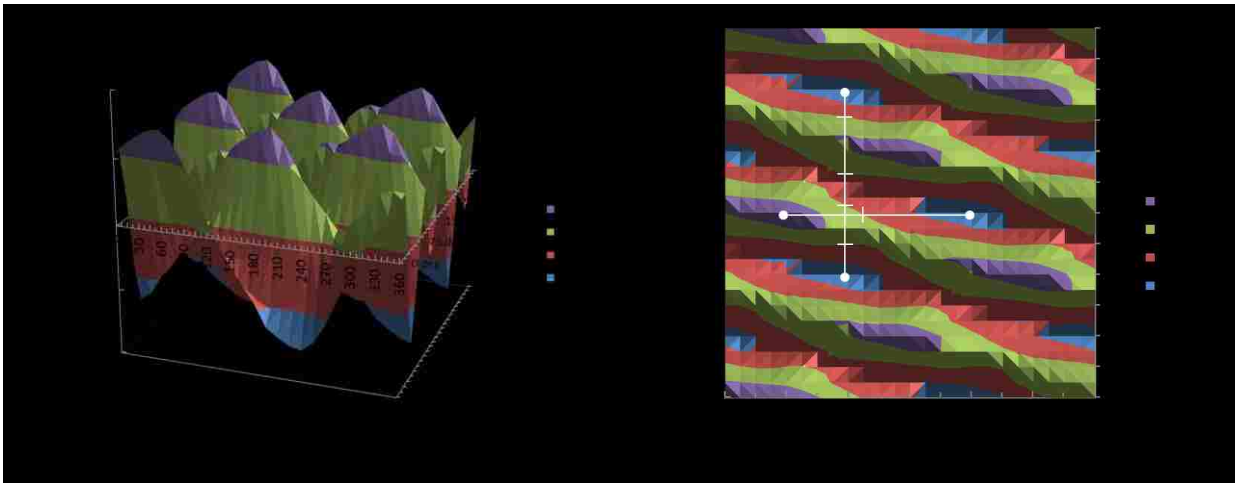

Figure 12-13. Experimental torque density data for the (ϕ1, ϕ5) plane for a 1:3:5 rational triad (f_0=50Hz; B=150 Grms). These data possess the same lattice vector and thus the same symmetry as those in Figure 12-12(top left) despite the superficial difference in their appearance.

For the 1:3:5 field the torque functional predicts torque around all field directions, so the net torque will be off axis. The computed torques around the *x*, *y*, and *z* axes are shown in **Figure 12-12**. Under the qualitative reasoning of the previous paragraph torque around the *x* axis is produced by the 3,5 components. The torque functional peaks at 0.175 for this axis. The torque functional around the *z* axis peaks at 0.081 and can be roughly thought of as being created by the 1,3 components. Finally, the torque functional around the *y* axis peaks at only 0.0033 and can be approximately attributed to the 1,5 components. In fact, calculations for the balanced symmetry breaking field 1:3 produces a torque maximum of 0.163, for 3:5 the maximum is 0.067 and 1:5 maximizes at 0.002. The torque around the *y* axis is too small to measure, but the other torques were mapped out in the (ϕ_1, ϕ_5) plane, **Figure 12-13**.

Although the experimental torque data almost appear sheared or skewed compared to those predicted by the functional in Figure 12-12(top left), both sets possess the same lattice vectors (180°, 0°) and (0°, 360°) and thus the same unit cell. The similarity in symmetry between the experimental and predicted data can be appreciated by considering the crossed white lines (with round endpoints) connecting extrema in each image. Despite the fact that the data possess the same *symmetry*—the orientation and scale of these lines are identical—there is a phase shift between the predicted and experimental data indicated by the fact that the positions of the white lines are not in the exact same location in each phase map. The origin of this phase offset is not clear at this time, but was also seen with previously studied rational triads in Chapter 11 (*i.e.*, 1:2:3, 1:2:6, and 2:3:4) [12.10]. There is a noteworthy consequence concerning flow reversal due to the subtle differences between the experimental data compared to those predicted by the functional. Recall that the locus of points that delineate the green and red regions in these torque plots are points of zero torque, and thus indicate points of flow reversal. For both the predicted and experimental data, there is only one point of flow reversal along the horizontal white lines, indicated by the white cross tick. However, a comparison of the vertical white lines reveals that the

functional predicts two points of flow reversal on this interval, whereas experiments reveal four.

12.6 Concluions

We have developed a functional—by using physical insight and previous results based on the theory of vortex magnetic field mixing—that can be used to predict the relative *magnitude* and direction of the vorticity vector in magnetic particle suspensions driven by complex, time-dependent magnetic fields (symmetry-breaking rational fields and rational triads). We find that the functional predicts results that are in agreement with both the symmetry theories developed for these new classes of fields as well as experimental observations. Such a functional allows for the rapid investigation of innumerable magnetic field schemes, which can be used to direct future experimental work, and serves as a natural first step toward understanding the microscopic origins of the observed vorticity.

Acknowledgements

Sandia National Laboratories is a multi-program laboratory managed and operated by Sandia Corporation, a wholly owned subsidiary of Lockheed Martin Corporation, for the U.S. Department of Energy's National Nuclear Security Administration under contract DE-AC04-94AL85000. This work was supported by the Division of Materials Science, Office of Basic Energy Sciences, U.S. Department of Energy (DOE). We thank Matt Groo at Novamet for supplying the magnetic platelets.

References

12.1 S. Chandrasekhar, *Hydrodynamic and Hydromagnetic Stability* (Dover, New York, 1981), pp. 9–71.

12.2 A.V. Getling, *Rayleigh-Bénard Convection: Structures and Dynamics* (World Scientific, Singapore, 1997).

12.3 *Dynamics of Spatio-Temporal Cellular Structures: Henri Bénard Centenary Review*, edited by I. Mutabazi, J.E. Wesfreid, and E. Guyon (Springer, Berlin, 2005).

12.4 D.P. Lalas and S. Carmi, Thermoconvective stability of ferrofluids, *Phys. Fluids* **14**, 436–437 (1971).

12.5 R.A. Curtis, Flows and wave propagation in ferrofluids, *Phys. Fluids* **14**, 2096–2102 (1971).

12.6 K.J. Solis and J.E. Martin, Isothermal Magnetic Advection: Creating functional fluid flows for heat and mass transfer, *Appl. Phys. Lett.* **97**, 034101 1–3 (2010).

12.7 J.E. Martin and K.J. Solis, Symmetry-breaking magnetic fields create a vortex fluid that exhibits a negative viscosity, active wetting, and strong mixing, *Soft Matter* **10**, 3993–4002 (2014).

12.8 K.J. Solis and J.E. Martin, Torque density measurements on vortex fluids produced by symmetry-breaking rational magnetic fields, *Soft Matter* **10**, 6139–6146 (2014).

12.9 K.J. Solis and J.E. Martin, Complex magnetic fields breathe life into fluids, *Soft Matter* **10**, 9136–9142 (2014).

12.10 K.J. Solis and J.E. Martin, Multiaxial fields drive the thermal conductivity switching of a magneto-responsive platelet suspension, *Soft Matter* **9**, 9182–9188 (2013).

12.11 J.E. Martin and K.J. Solis, Fully alternating, triaxial electric or magnetic fields offer new routes to fluid vorticity, *Soft Matter* **11**, 241–254 (2015).

12.12 J.E. Martin, Theory of strong intrinsic mixing of particle suspensions in vortex magnetic fields, *Phys. Rev. E: Stat., Nonlinear, Soft Matter Phys.* **79**, 011503 1–12 (2009).

12.13 J.E. Martin, A resonant biaxial Helmholtz coil employing a fractal capacitor bank, *Rev. Sci. Instrum.* **84**, 094704 1–11 (2013).

12.14 J.E. Martin, R.A. Anderson, and C.P. Tigges, Simulation of the athermal coarsening of composites structured by a biaxial field, *J. Chem. Phys.* **108**, 7887–7900 (1998).

12.15 J.E. Martin, E. Venturini, J. Odinek, and R.A. Anderson, Anisotropic magnetism in field-structured composites, *Phys. Rev. E* **61**, 2818–2830 (2000).

12.16 J.E. Martin, R.A. Anderson, and R.L. Williamson, Generating strange magnetic and dielectric interactions: Classical molecules and particle foams, *J. Chem. Phys.* **118**, 1557–1570 (2003).

12.17 B. Schwarzchild, Physics Nobel Prize Goes to Tsui, Stormer and Laughlin for the Fractional Quantum Hall Effect, Physics Today, December 1998.

Chapter 13

Complex magnetic fields breathe life into fluids[13]

The vast majority of materials research exploits equilibrium or quasi-equilibrium processes to produce inert materials. In contrast, living systems depend on far-from-equilibrium kinetic processes that require a continuous flux of energy to persist and perform useful tasks. The Greek god Hephaestus forged metal automatons that he miraculously animated to perform the tasks of living creatures. Is something like this actually possible? Here we show that subjecting magnetic fluids suspended in an immiscible liquid to uniform, multidimensional, time-dependent magnetic fields, generates a variety of life-like collective dynamics, including various forms of locomotion, swarming and feeding, that are sustained by the continuous injection of energy *via* the applied field. These leaderless emergent behaviors occur autonomously, without human guidance, and are quite surprising. Such self-healing, remotely-powered fluid automatons could be used as an extraction/separation technology to efficiently purify water by scavenging toxic chemicals and microorganisms, or alternatively enable the controlled release of chemicals. Other possible applications include vigorous fluid mixing and even microdroplet manipulation for microfluidic bioassays.

13.1 Introduction

The search for soft matter systems that mimic the complex dynamics of living organisms extends back to Bütschli, who discovered in 1890 that emulsions driven by saponification reactions could exhibit something reminiscent of the motions of single-cell organisms [13.1]. More than a century later, and long after Bütschli had been forgotten, Snezhko and co-workers [13.2] discovered that magnetic colloids confined to an air–liquid or liquid–liquid interface can exhibit structures with plausibly biomimetic dynamics when energy is

[13] Originally published as: K.J. Solis and J.E. Martin, Complex magnetic fields breathe life into fluids, *Soft Matter* **10**, 9136–9142 (2014).

injected with a uniaxial ac magnetic field tuned to couple to standing waves at the interface. The "snakes" and "asters" that form exhibit sub-carangiform locomotion (a type of fish-like swimming), phagocytosis and cargo transport. In all cases such emergent phenomena arise from the continuous injection of energy into the system, but an applied magnetic field has the advantage that it constitutes a limitless supply of energy that can be presented in a bewildering variety of time-dependent, multiaxial forms.

In recent years we have used particular triaxial magnetic fields consisting of three orthogonal components to drive emergent phenomena in the form of advection lattices (see Chapter 5 [also Ref. 13.3]), vortex lattices and vortex fluids (see Chapters 7, 9, and 10 [13.4,13.5]), but none of these phenomena are biomimetic. Each of the three fields has an independent frequency, amplitude and phase, so the field vector can be directed to gambol about in three dimensions in an infinite variety of ways. The connection of these fields to the world of biomimetic motion occurred when we finally released the magnetic fluid from the confines of a solid container by immersing it in an immiscible fluid. Now the magnetic fluid could deform at will, driven by the emergent dynamics of the countless suspended magnetic particles. The marvelous feats this fluid performs would amuse and perhaps even astonish both Hephaestus and Bütschli. We have observed the formation of countless swarming "bees" that dart around vigorously; created a magnetic serpent—complete with flicking tongue—that grows by striking out with its head and cannibalizing the bees from which it emerged; formed slugs that crawl, slime molds that send out a web of tentacles, and amoebas that project pseudopodia to dance about weirdly and unpredictably.

These biomimetic motions are especially surprising because the *spatially uniform* fields we apply cannot generate a body force on the fluid, nor are the fields modulated or directed in any way to effect motion. However, in Chapters 9 and 10 we have shown that the trajectories of such dynamic fields have subtle aspects of symmetry that can lead to a body torque on the fluid, even with magnetically-soft spherical particles [13.4,13.5]. In addition, the suspended particles couple to each other through their induced magnetic and

hydrodynamic interactions, both of which are notoriously long-ranged. The magnetic interactions have significant many-body effects in triaxial fields, so these dynamic phenomena are a nontrivial emergent behavior of the system.

Systems driven far from equilibrium often display emergent dynamics, but it's difficult to define emergence precisely. Is turbulence an emergent property? The economist Jerry Goldstein defined emergence this way: "the arising of novel and coherent structures, patterns and properties during the process of self-organization in complex systems". This definition in turn begs the definition of "complex" which itself is a little difficult to pin down, so we'll just stick with "complex systems inspire awe." To the natural scientist these definitions call to mind such classic examples as swarming, schooling, and the spectacular murmurations of starlings and purple martins [13.6,13.7]. In the physical sciences familiar examples include pattern formation in convection [13.8,13.9], chemical clock reactions [13.10], granular materials [13.11], and dendrite formation [13.12,13.13]. In the area of dynamical systems emergent phenomena include cardiac arrhythmias [13.14], the phase synchronization of flashing fireflies [13.15], and many others [13.16,13.17]. Field-driven colloids [13.18] are a convenient and rich system for the study of emergent behavior because of the variety of many-body dissipative and conservative interactions that can be carefully tuned (*e.g.*, van der Waals, surface/interfacial steric [13.19,13.20], Coulomb [13.21], dipolar [13.22–13.24], hydrodynamic, *etc.*). Add to these natural interactions the fluctuating, globally-coherent magnetic interactions that can be created by the infinite variety of time-dependent triaxial fields and the parameter space is simply overwhelming. In fact, even very simple magnetic fields can already produce varieties of static and dynamic self-assembly of magnetic fluid droplets [13.25] and magnetic disks at an air–liquid interface [13.26]. In the following we will describe some investigations within this immense parameter space and hope to convey the wealth of opportunities for structural and dynamic biomimicry offered by this approach. Specifically we investigate the effects of the fluid type

(both for the magnetic fluid and the suspending liquid), the type of magnetic field, and the effects of the field strength, frequency, and phase.

13.2 Experimental

The magnetic fluid consists of roughly spherical 4–7 μm carbonyl iron particles (ISP Technologies, Inc.) dispersed in either water ($\rho = 1\,\mathrm{g{\cdot}cm^{-3}}$, $\eta_{25°C} = 0.89$ cP) or isopropyl alcohol ($\rho = 0.786\,\mathrm{g{\cdot}cm^{-3}}$, $\eta_{25°C} = 2.04$ cP). The suspending liquid is Fluorinert FC-40 (3M Corporation) ($\rho = 1.850\ \mathrm{g\ cm^{-3}}$, $\eta_{25°C} = 3.40$ cP), which is a perfluorinated dielectric liquid chosen for its immiscibility with aqueous phases. The magnetic liquids were dispensed into the suspending liquid, whose depth was typically ~7–8 mm (in all cases the depth exceeded the magnetic droplet diameter) and was contained in a 50 mm-diameter glass Petri dish treated with a hydrophobic polysiloxane surface agent (Rain-X). The magnetic fields were produced with a triaxial Helmholtz coil system whose components are in series resonance with computer-controlled fractal capacitor banks [13.27], and is capable of producing fields of up to 500 Oe in the low audio frequency range. The effects described in this chapter occur for modest fields in the range of 100–200 Oe, and for field frequencies generally in the range of ~50–500 Hz. A variety of magnetic fields can be produced with this setup; however, for the experiments in this study we use three principal fields: (1) a vortex field (see Chapter 3 [13.28,13.29]), comprised of a rotating field to which a dc field is applied orthogonally,

$$\mathbf{H}(t) = H_0 \left\{ \sin\theta_f \left[\sin(2\pi f_0 t)\hat{\mathbf{x}} + \cos(2\pi f_0 t)\hat{\mathbf{y}} \right] + \cos\theta_f \hat{\mathbf{z}} \right\} \tag{13-1}$$

where H_0 is the rms field strength of the ac components, which is equal to the dc field strength for a balanced vortex field, f_0 is the frequency, and θ_f is the vortex field angle. This field produces a strong, uniform torque density in magnetic particle suspensions, and belongs to the broader class of magnetic fields called symmetry-breaking rational fields (see Chapters 9 and 10 [also Refs. 13.4, 13.5]). (2) A fully alternating triaxial field (aka rational

triad, see Chapter 11) whose orthogonal components have frequency ratios of 1:2:3 (a heterodyned version of this field was created by slightly detuning one of the frequencies),

$$\mathbf{H}(t) = H_{ac}\{\sin(2\pi \times f_0 t)\hat{\mathbf{x}} + \sin(2\pi \times 2 f_0 t)\hat{\mathbf{y}} + \sin(2\pi \times 3 f_0 t)\hat{\mathbf{z}}\} \tag{13-2}$$

where H_{ac} is the rms field strength and f_0 is the fundamental frequency. This field induces the swarming and coarsening dynamics of the bees, the writhing serpent, and the slime mold slugs. When heterodyned this field produces the amoeboid motions for the water-based magnetic fluid and one of the plasmodial slime mold phases for the isopropanol-based fluid. (3) A 3:1 symmetry-breaking rational field (see Chapters 9 and 10),

$$\mathbf{H}(t) = H_{ac}\left[\sin(2\pi \times f_0 t)\hat{\mathbf{x}} + \sin(2\pi \times 3 f_0 t + 2\pi \frac{\phi}{360°})\hat{\mathbf{y}})\right] + H_{dc}\hat{\mathbf{z}} \tag{13-3}$$

where H_{ac} and f_0 have the same meanings as in Equation (13-2) and H_{dc} is the field strength of the symmetry-breaking dc field, and ϕ is a phase angle. The other plasmodial slime mold phase was produced by this field when applied to the isopropanol-based magnetic fluid.

13.3 Results

When a vortex magnetic field [13.28,13.29] is applied to an aqueous magnetic particle suspension immersed in Fluorinert™ pandemonium ensues (see Supplementary Movie 13-1). This animating field causes the magnetic fluid to quickly disintegrate into countless "bees" that sprout wings and dart through the suspending fluid with great vigor, perpetually driven by energy injection from the field [**Figure 13-1(a–e)**]. When the field stops, these bees immediately form quiescent spherules [**Figure 13-1(f)**], but applying a different (fully alternating) triaxial magnetic field instantly reanimates the bees. Under this field the bees form swarms and after a time one of these swarms nucleates a voracious writhing serpent, complete with flicking tongue [**Figure 13-1(g–l)**]. This serpent strikes out with its head and devours each and every bee, progressively growing in size and appetite. Even after the prey are fully consumed the magnetic field continues to animate the serpent, but when the field is turned off the serpent transforms into a small number of dormant "eggs" [**Figure 13-**

1(m–o)]. If the field is turned back on these eggs immediately reassemble into the serpent. This elaborate behavior constitutes a nucleated transition from one driven phase (the bee phase) to another (the serpent phase) that occurs by cannibalism, much as bullfrogs grow by

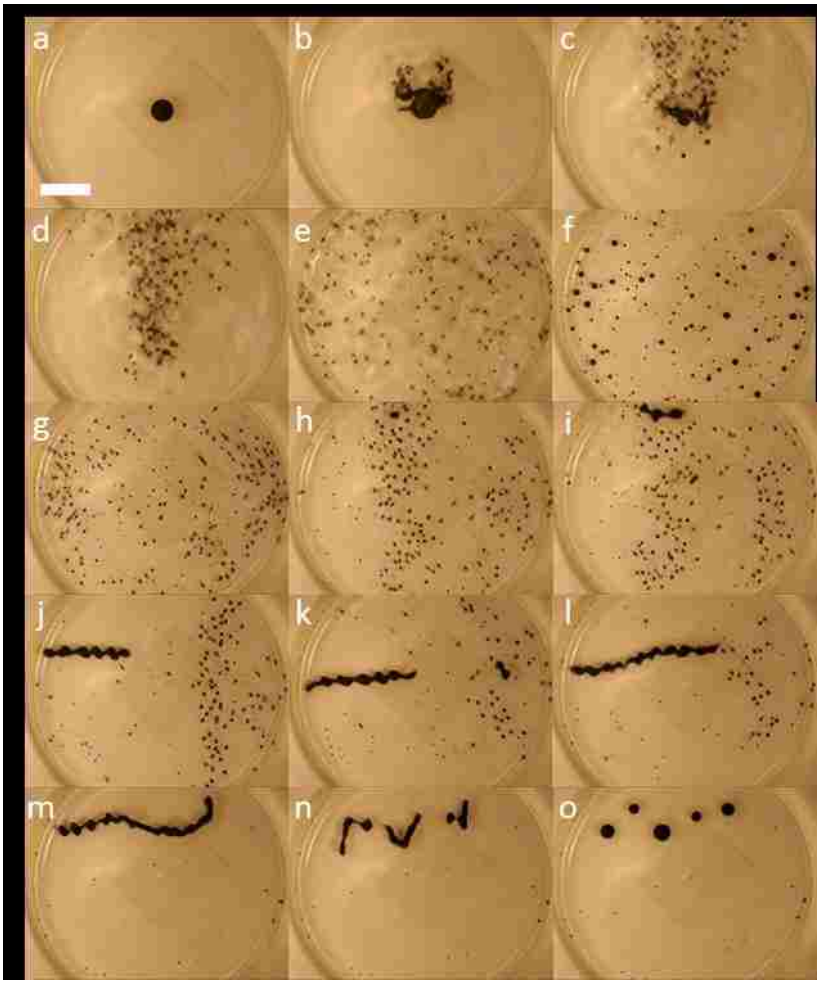

Figure 13-1. Time series of field-directed magnetic droplet disintegration and coalescence. This sequence of images was taken from Supplementary Movie 13-1. **(a)** Quiescent aqueous magnetic droplet in an immiscible liquid (Fluorinert). (b) The application of a vortex magnetic field (f_0 = 150 Hz, 200 G_{rms}) causes the droplet to explode into countless "bees" that vigorously fly throughout the fluid **(c–e)**. The white bar represents 1 cm. **(f)** Removing the animating magnetic field results in static microdroplets dispersed throughout the fluid. **(g)** Application of a fully ac 1:2:3 triaxial magnetic field (f_0 = 50 Hz, 150 G_{rms}) causes the bees to form swarms that eventually nucleate an incipient magnetic "serpent" **(h)**. **(i–l)** This serpent moves throughout the fluid striking out and consuming the bees while growing in length until virtually all the bees are consumed **(m)**. **(n)** Turning the magnetic field off causes the serpent to fragment and form several spherical droplets **(o)**. If the 1:2:3 field is turned back on these remnant droplets reassemble into a serpent.

Figure 13-2. *Trypanosoma* parasites surrounded by red blood cells are compared to the magnetic serpents produced by a 1:2:3 triaxial field [same field conditions as in Figure 13-1(g-m)]. The comparison is compelling, but there is at present an issue of scale. These magnetic serpent images were taken from Supplementary Movie 13-1, and so they are similarly sized as the serpent shown in Figure 13-1. Image of *Trypanosoma* parasites is public domain and was obtained from Wikipedia, Content provider: Dr. Myron G. Schultz, Centers for Disease Control and Prevention's Public Health Image Library.

consuming tadpoles. From another point of view the morphology and dynamics of the serpent bring to mind the *Trypanosoma* protozoa carried by the tsetse fly that are the cause of sleeping sickness, **Figure 13-2**.

Both the bee and serpent phase are accompanied by chaotic advection, **Figure 13-3**, which can be visualized by adding aluminum flakes to the Fluorinert. The fluid dynamics, shown in Supplementary Movie 13-2, is reminiscent of convection and shows that these driven phases could be useful for mixing, for the controlled release of beneficial agents, or for purifying water by first scavenging and then collecting harmful agents (in which case the magnetic fluid would be hydrophobic). Because the bee dynamics are easily controlled by the field amplitude and frequency, the rate of agent dispersal can be controlled. Likewise, the serpent or *Trypanosoma* phase could be used for controlled coalescence and recovery.

Slime molds are so complex that J. T. Bonner has spent much of the last 70 years at Princeton University peering through a microscope to understand their many fascinating behaviors [13.30]. Cellular slime molds, such as *Dictyostelium discoideum*, begin life as amoebas that move by projecting pseudopodia. When food is plentiful they exist

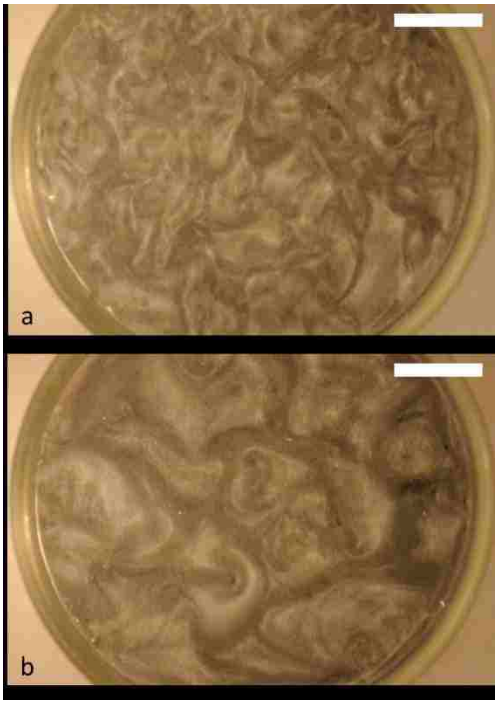

Figure 13-3. Fine aluminum flakes dispersed in the Fluorinert FC-40 suspending liquid provide effective visualization of the local flow fields. **(a)** Turbulent chaotic advection, characterized by the small length scales of the tortuous flow structures, is created by the extremely vigorous bees that are produced by a vortex magnetic field (f_0 = 100 Hz, 200 G_{rms}) (taken from Supplementary Movie 13-2). **(b)** The unstable coherent swarms of bees in Figure 13-1 (g-l) have a more subdued flow field with larger flow structures. These are produced by an ac/ac/ac triaxial field having frequency ratios 1:2:3 (f_0 = 50 Hz, 150 G_{rms}). The white bars represent 1 cm.

independently, but when times get tough they assemble into macroscopic pseudo-plasmodia that can exhibit organized collective motion, sometimes referred to as "leaderless motion," even though the pseudo-plasmodia is devoid of muscles or even a nervous system. These pseudo-plasmodia slither along slug-like, leaving a distinct slime trail and fusing when they collide. When even this motion no longer alleviates the food shortage the slugs give up and rise up to form a fruiting body that produces spores that germinate and give life to a new generation of amoebas.

The amoeboid motion can be produced by an animating field that is only slightly different from that which produces the serpent or *Trypanosoma* phase. The snapshots of this motion in **Figure 13-4** show various pseudopodia that are uncannily similar to those exhibited in actual amoeboid motion. The magnetic fluid moves much faster, like an

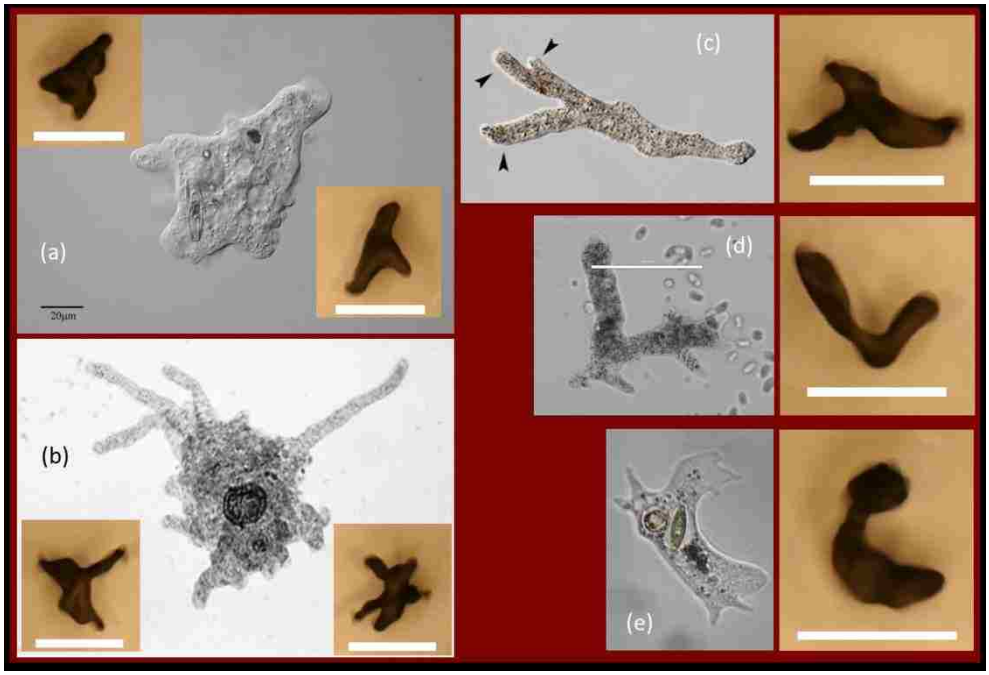

Figure 13-4. A comparison of real and magnetic amoebae. In a phase modulated, fully ac 1:2:3 triaxial field (f_0 = 50 Hz, 150 G_{rms}) the magnetic fluid mimics the forms of amoebae, including the projecting pseudopodia. These pseudopodia are probably driven by demagnetization fields, since such deformations increase the field penetration and thus reduce the magnetostatic energy. However, the magnetic fluid dynamics is many orders of magnitude faster and seems to be highly unpredictable as concerns the direction of motion. These still images of magnetic amoebae were taken from Supplementary Movie 13-3). The white bars represent 1 cm. Images of amoebae are attributed as follows: **(a)** Image obtained under CreativeCommons license (https://creativecommons.org/licenses/by-nc-sa/2.0/), Content provider: Proyecto Agua (https://www.flickr.com/photos/microagua/2695978355/) Original color image was modified to grayscale. **(b)** Amoeba (magnified). [Photograph]. In Encyclopaedia Britannica. Retrieved from http://www.britannica.com/EBchecked/media/4194/Amoeba (Russ Kinne/Photo Researchers). Original color image was modified to grayscale. **(c)** Amoeba image obtained from (http://www.arcella.nl/morphology) Ferry Siemensma. **(d)** Amoeba image obtained from http://naturalscienceseducation.wordpress.com/2012/06/22/ilabs-well-fed-amoebas/ Original color image was modified to grayscale. **(e)** "Amoeba with engulfed diatom" image obtained from http://colinlmiller.com/microscopy/amoebas.htm Copyright 2009 Colin L. Miller.

amoeba on stimulants, but Supplementary Movie 13-3 shows that the manner of motion is similar.

The slug-like motion in **Figure 13-5** can be produced by simply increasing all three field frequencies commensurately. This alteration produces slugs that slither along the

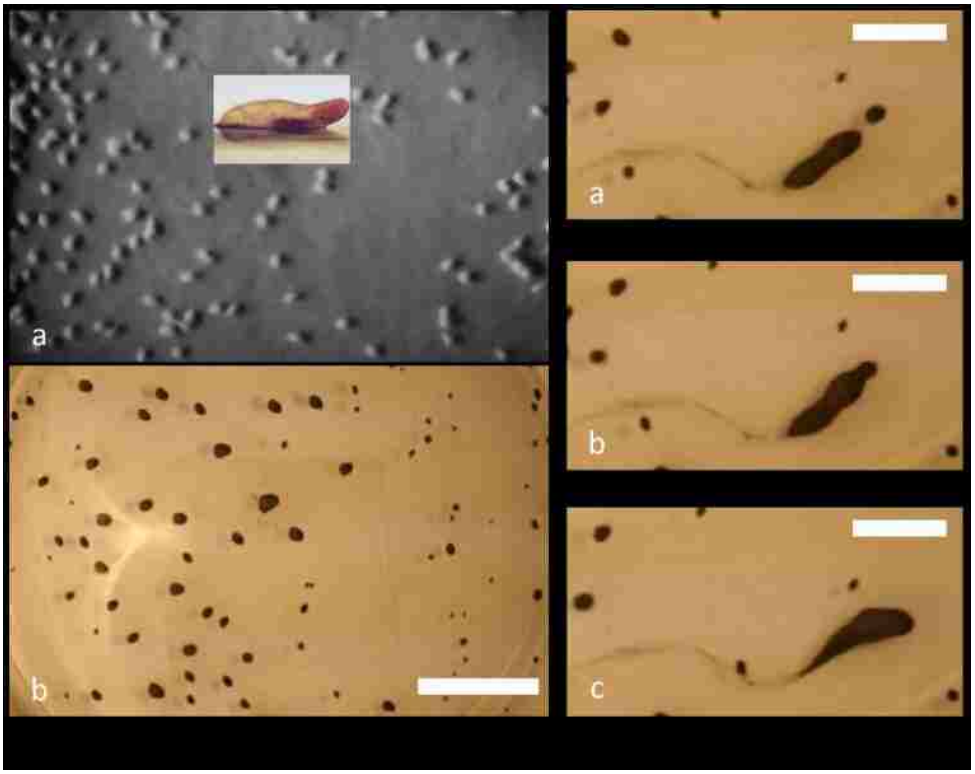

Figure 13-5. Slug-phase biological and magnetic slime molds. **Panel Ia** shows aggregates of the cellular slime mold *Dictyostelium discoideum* (taken from a video: John Bonner's slime mold movies, Princeton University (http://www.youtube.com/watch?v=bkVhLJLG7ug)). Inset of slime mold slug obtained from http://ucsdnews.ucsd.edu/archive/newsrel/science/mcamoeba.asp Credit: Dirk Dormann, University of Dundee. These actively move, even producing convincingly slug-like shapes (inset). The magnetic analogue, **Panel Ib**, is produced with a high-frequency, fully ac 1:2:3 triaxial field (f_0 = 100.2 Hz, 150 G_{rms}). These incipient slugs translocate, fuse and leave magnetic slime trails as shown in **Panel II**. The white bars represent 1 cm.

bottom of the Petri dish, even leaving a trail of magnetic slime and fusing when they collide, just like real *Dictyostelium discoideum*.

Plasmodial slime molds, such as *Leocarpus fragilis*, consist of a single membrane containing countless nuclei. These slime molds can move by streaming out multiple strands, which is something *Dictyostelium discoideum* just can't do. These strands enable it to eventually ooze over and consume organic matter, such as an unlucky fungus, leaf, or even a discarded newspaper. Examples of these streaming structures are shown in **Figure 13-6**, but the dynamics are much more interesting than any single image can convey (for example, see http://www.youtube.com/watch?v=GY_uMH8Xpy0). Eventually the plasmodium forms

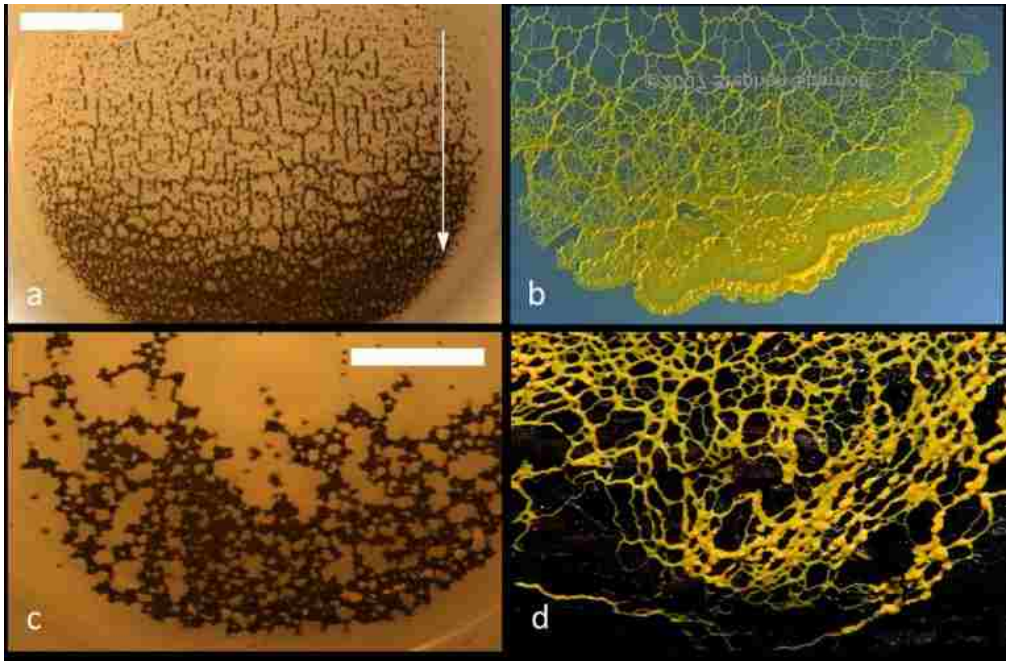

Figure 13-6. Plasmodial-phase magnetic and biological slime molds. **(a)** Photograph of the streaming strand motion of an isopropanol-based magnetic fluid, which has a lower interfacial tension with Fluorinert (this structure was produced by a symmetry-breaking rational field with a 1:3 frequency ratio [f_0 = 100 Hz, 150 G_{rms}]). The white arrow indicates the direction of motion of the magnetic web, which is about to reverse direction. This can be compared to the plasmodium slime mold *Leocarpus fragilis* in **(b)**, which has a somewhat more disordered web-like structure, but similar dynamics (see Supplementary Movie 13-4). **(c)** If the animating field is changed to a heterodyned fully alternating 1:2:3 triaxial field (f_0 = 50 Hz, 100 G_{rms}), the magnetic fluid changes morphology, and this is perhaps a little more similar to the streaming strand structure of *Leocarpus fragilis* in **(d)**. The white bars represent 1 cm. (c) Plasmodial slime mold Copyright 2007 Stephen Sharnoff. (d) Plasmodial slime mold Copyright Clare Staveley, Curbstone Valley.

a network that gives birth to a host of fruiting bodies that produce spores that germinate to create the next generation.

The streaming strand motion of the plasmodial phase can be mimicked by reducing the interfacial tension on the magnetic fluid, accomplished by using isopropanol as the suspending liquid for the magnetic particles. Figure 13-6 shows a few snapshots of the streaming strands of both the magnetic fluid and *Leocarpus fragilis*. The structural resemblance is perhaps not as compelling as the streaming strand dynamics, which can be seen in Supplementary Movie 13-4. In this case the animating field is phase modulated by

detuning one of the field components, which creates the periodic streaming and migration of the magnetic fluid web.

13.4 Discussion

Understanding all the phenomena we have observed is a substantial long-term undertaking but at least certain aspects are clear enough. The selected structures and dynamics are controlled by a number of magnetic and hydrodynamic factors, including the type of magnetic field applied (*i.e.*, vortex, symmetry-breaking, or fully ac), the field frequency, the field strength, the particle volume fraction of the magnetic fluid, and the type of base liquid used for the magnetic fluid (*i.e.*, water, isopropanol, acetone). We now discuss some of these factors as they relate to our observations.

The structure of the bees allows them to interact with the applied field in such a way as to drive self-propulsion. The bees are actually "microdroplets" that elongate along the instantaneous magnetic field vector to reduce their demagnetizing field, **Figure 13-7**(a & b), thus increasing their magnetization and decreasing their magnetostatic energy. This elongation is finite because it is balanced by increased interfacial energy. In the so-called vortex field (see Experimental section) the bees wobble as in Figure 13-7(c), stirring the local fluid vigorously. The darting movements of the bees appear to be a consequence of spontaneous chiral symmetry breaking of their shape. In fact, *E. coli* and certain other bacteria move by rotation of their chiral flagella [13.31]. At other times the bees can exhibit more subdued motion and may even hover in place for brief periods. A vortex field also creates a body torque on a droplet, and this could also contribute to the bees' motion if they are near a surface or interface. Finally, the spinning of the bees creates a strong hydrodynamic repulsion and for this reason they are rarely observed to fuse in the stable bee phase. The size and number density of the bees can be controlled by a number of factors: smaller, more numerous bees are favored by high field strengths, low density base liquids for the magnetic fluid (*e.g.*, isopropanol, acetone), and high magnetic particle content. Of

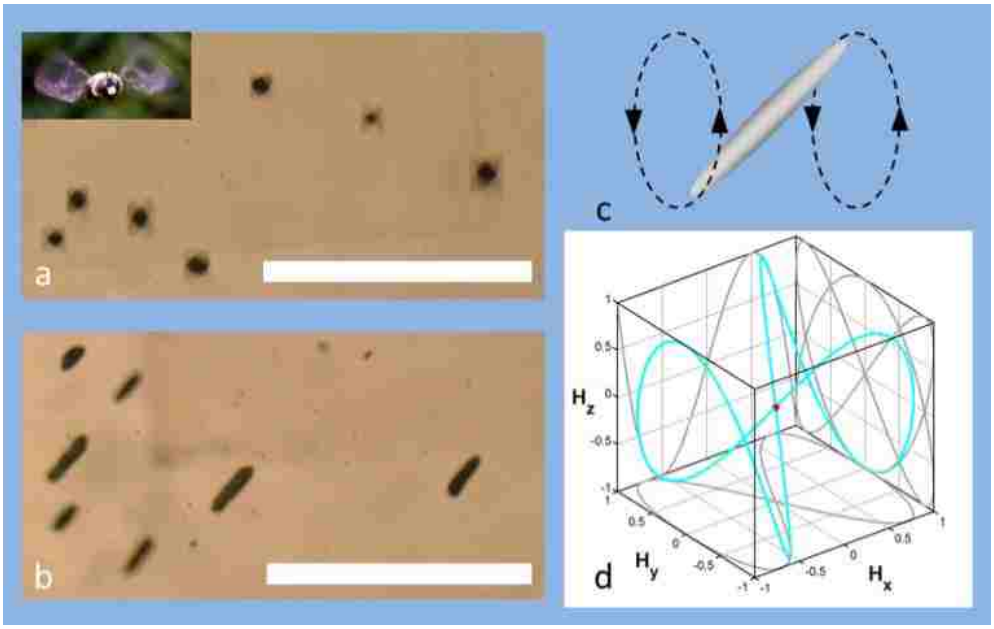

Figure 13-7. Structure and dynamics of magnetic bees. **(a)** Bees appear to possess "wings" (like that of the inset) which propel them vigorously throughout the suspending fluid and give them a star-like appearance [field conditions: vortex field (f_0 = 100 Hz, 150 G_{rms})]. **(b)** High-speed photography shows that these bees are actually microdroplets that are elongated along the applied dynamic field vector [field conditions: vortex field (f_0 = 100 Hz, 200 G_{rms})]. **(c)** The elongated microdroplets undergo a wobbling motion—akin to the motion of a kayaker's paddle—and also have internal vorticity around the dc field axis. These factors, combined with spontaneous chiral symmetry breaking of form, cause them to self-propel. **(d)** A three dimensional Lissajous plot of the trajectory of the triaxial field vector for the case where the x, y, z field component frequency ratios are 1:2:3. The white bars represent 1 cm. (Inset) Image of hovering bee obtained from http://adreamkiller.wordpress.com/tag/when-bees-hover/ Content link:http://www.mosbybuildingarts.com/blog/wp-content/uploads/Mosby%20Carpenter%20Bee.jpg.

course, an actual living bee is vastly more complex than a precessing, deformable ellipsoid, but it is interesting that such a simple system as this can display visually similar trajectories, especially considering the mechanism of locomotion is so different.

The transition from the bee to serpent phase is a result of switching from the ac-ac-dc vortex field to a fully ac-ac-ac field (rational triad) with frequency ratios of 1:2:3, Figure 13-7(d). This field still creates a body torque as was shown in Chapter 11 [also Ref. 13.32], but can neither originally create nor indefinitely sustain the bee phase. The pronounced difference in bee dynamics is illustrated in Figure 13-3, where it is seen that the turbulence is much more subdued for the 1:2:3 field. Once the bees nucleate a serpent it assumes the

form of an irregular helicoid aligned with the low frequency field component. Because all of the field components have equal rms values, the observed direction of elongation cannot be a demagnetizing field effect alone. The serpent seems to strike out at the bees, even though it has no senses with which to locate them. This interaction is a very complicated many body effect, which is already quite complex even for two spherical particles in a triaxial field [13.33]. But one of the most remarkable aspects of the serpent is its large aspect ratio, 19:1 (length-to-diameter). This far exceeds the Plateau–Rayleigh stability criterion [13.34] of π for jets, and the fact that interfacial tension causes the serpent to fragment into five droplets upon field cessation demonstrates the importance of the field in stabilizing such an elongated fluid structure.

Phase modulating the 1:2:3 field, by detuning one of the component frequencies, gives rise to the various amoeboid structures and dynamics shown in Figure 13-4 and Supplementary Movie 13-3, provided that the droplets possess a large enough volume fraction of magnetic particles. For the water-based magnetic fluid, a volume fraction of 12.4% carbonyl iron particles produces a neutrally buoyant drop in the FC-40 suspending liquid. The amoeboid free body dynamics are observed for magnetic fluid droplets of high enough volume fraction such that they sink. The phase modulation causes periodic reversal of the vorticity within the magnetic fluid. This constantly changing vorticity direction coupled with interfacial forces between the liquid phases drives the observed dynamics. However, if the volume fraction is low enough that the magnetic fluid droplet floats, no amoeboid motion is observed. Instead, the floating droplet deforms and races back-and-forth at the FC-40 fluid surface in concert with the changing field. This effect is due to the uniform torque density produced within the magnetic fluid droplet in combination with a surface or interface, which produces asymmetrical/unbalanced shear forces thereby propelling the droplet. In fact, with judicious application of appropriate magnetic fields, a floating magnetic fluid droplet can be steered to any position at the surface. Such non-

contact, field-induced controllability would seem promising for applications involving the controlled movement of and mixing within microdroplets for containerless assays.

By simply increasing the magnitude of the frequencies of the 1:2:3 field that gives rise to the amoeboid dynamics, the slithering slug phase shown in Figure 13-5 can be produced, again subject to the constraint of an appropriate volume fraction for the magnetic fluid. Production of the slug phase is achieved by first exploding an original, single droplet using a vortex field (or symmetry-breaking magnetic field) as in Figure 13-1(a–e). A high-frequency 1:2:3 field ($f_0 \geq 100$ Hz) is then applied to the resultant dispersed spherules. However, there is no reason that all of these globules should possess the same volume fraction. And in fact they do not, as can be clearly seen in Supplementary Movie 13-1. When the animating field that sustains the bees is turned off many of them coalesce into larger sub-droplets that sink and cease moving, while many smaller ones continue moving because they are entrained by the inertia of the FC-40 suspending liquid. When the high-frequency 1:2:3 animating field is applied to this distribution of droplets, the sunken droplets in contact with the floor of the Petri dish become "bound slugs" and are observed to predominantly slither in one particular direction; whereas, any suspended, neutrally-buoyant droplets are observed to deform and slowly wobble in the opposite direction. If such a neutrally-buoyant droplet should encounter the upper free surface of the suspending liquid it races back in the opposite direction (the same direction as the slugs). These observed droplet motions are again understood by a consideration of the uniform torque density in combination with a surface or interface.

The effects of interfacial tension between the magnetic fluid and the suspending liquid were illustrated in Figure 13-6 and Supplementary Movie 13-4 by substituting isopropanol for water in the magnetic fluid. The isopropanol-based magnetic fluid exhibits a lower interfacial tension with the FC-40 suspending liquid as evidenced by the fact that the application of a vortex magnetic field—which will produce the same specific torque density in the two magnetic fluids—produces smaller, more numerous bees with the isopropanol-

based magnetic fluid. If a 1:3 symmetry-breaking field is applied, the web-like, plasmodial slime mold phase is produced. If this field is phase modulated, by imposing a 0.1 Hz addition to the high-frequency component, the magnetic fluid web begins to sprawl back-and-forth across the bottom of the container, reversing direction every five seconds, as in Supplementary Movie 13-4. This periodic movement is driven by the vorticity produced within the magnetic fluid, which occurs around the dc field component for odd:odd symmetry-breaking fields (see Chapters 9 and 10 [also Refs. 13.4,13.5]). The phase modulation causes this vorticity to reverse direction periodically.

13.5 Conclusions

The various phenomena we have described are only a sampling of the many phenomena that can be produced with these complex fields. This approach enables unprecedented control of fluid motion and will likely prove useful for mixing, heat and mass transfer, and releasing or scavenging chemicals or even organisms from an immiscible fluid. Clearly, there is great opportunity to further quantify many of these phenomena. Our goal at present is to simply present this new driven colloid system and its associated emergent dynamics.

Acknowledgements

This chapter is dedicated to the memory of Susan M. Brozik. Susan was an enthusiastic biologist at Sandia National Labs who inspired us to explore the magnetic manipulation of microdroplets, leading to the discoveries reported in this chapter. We wish she could have seen these results. Sandia National Laboratories is a multi-program laboratory managed and operated by Sandia Corporation, a wholly owned subsidiary of Lockheed Martin Corporation, for the U.S. Department of Energy's National Nuclear Security Administration under contract DE-AC04-94AL85000. This work was supported by the Division of Materials Science, Office of Basic Energy Sciences, U.S. Department of Energy (DOE).

References

13.1 J.B. Haycraft, Bütschli's artificial amoebae, *Nature* **48**, 594–595 (1893).

13.2 A. Snezhko and I.S. Aranson, Magnetic manipulation of self-assembled colloidal asters, *Nat. Mater.* **10**, 698–703 (2011).

13.3 K.J. Solis and J.E. Martin, Isothermal Magnetic Advection: Creating functional fluid flows for heat and mass transfer, *Appl. Phys. Lett.* **97**, 034101 1–3 (2010).

13.4 J.E. Martin and K.J. Solis, Symmetry-breaking magnetic fields create a vortex fluid that exhibits a negative viscosity, active wetting, and strong mixing, *Soft Matter* **10**, 3993–4002 (2014).

13.5 K.J. Solis and J.E. Martin, Torque density measurements on vortex fluids produced by symmetry-breaking rational magnetic fields, *Soft Matter* **10**, 6139–6146 (2014).

13.6 I.L. Bajec and F.H. Heppner, Organized flight in birds, *Anim. Behav.* **78**, 777–789 (2009).

13.7 W. Bialek, A. Cavagna, I. Giardina, T. Mora, E. Silvestri, M. Viale and A.M. Walczak, Statistical mechanics for natural flocks of birds, *Proc. Natl. Acad. Sci. U. S. A.* **109**, 4786–4791 (2012).

13.8 S. Chandrasekhar, in *Hydrodynamic and Hydromagnetic Stability*, (Dover, New York, USA, 1981), pp. 43–52.

13.9 A.V. Getling, in *Rayleigh–Bénard Convection: Structures and Dynamics*, (World Scientific, Singapore, 1997).

13.10 I.R. Epstein and J.A. Pojman, in *An Introduction to Nonlinear Chemical Dynamics: oscillations, waves, patterns, and chaos*, (Oxford University Press, USA, 1998).

13.11 I.S. Aranson and T.S. Lev, Patterns and collective behavior in granular media: theoretical concepts, *Rev. Mod. Phys.* **78**, 641–692 (2006).

13.12 J. Aizenberg, Crystallization in patterns: a bio-inspired approach, *Adv. Mater.* **16**, 1295–1302 (2004).

13.13 L. Gránásy, T. Pusztai, T. Börzsönyi, J.A. Warren and J.F. Douglas, A general mechanism of polycrystalline growth, *Nat. Mater.* **3**, 645–650 (2004).

13.14 A. Karma and R.F. Gilmour Jr, Nonlinear dynamics of heart rhythm disorders, *Phys. Today* 51–57 (2007).

13.15 S.M. Lewis and C.K. Cratsley, Flash signal evolution, mate choice, and predation in fireflies, *Annu. Rev. Entomol.* **53**, 293–321 (2008).

13.16 G.M. Whitesides and B. Grzybowski, Self-assembly at all scales, *Science* **295**, 2418–2421 (2002).

13.17 P. Ball, in *The Self-made Tapestry: Pattern Formation in Nature* (Oxford University Press, USA 2001).

13.18 J.E. Martin and A. Snezhko, Driving self-assembly and emergent dynamics in colloidal suspensions by time-dependent magnetic fields, *Rep. Prog. Phys.* **76**, 126601 1–42 (2013).

13.19 B.M. Mladek, G. Kahl and C.N. Likos, Computer assembly of cluster-forming amphiphilic dendrimers, *Phys. Rev. Lett.* **100**, 028301 1–4 (2008).

13.20 F.J. Martinez-Veracoechea, B. Bozorgui and D. Frenkel, Anomalous phase behavior of liquid–vapor phase transition in binary mixtures of DNA-coated particles, *Soft Matter* **6**, 6136–6145 (2010).

13.21 M. Brunner, J. Dobnikar, H.H. von Grünberg and C. Bechinger, Direct measurement of three-body interactions amongst charged colloids, *Phys. Rev. Lett.* **92**, 078301 1–4 (2004).

13.22 N. Osterman, I. Poberaj, J. Dobnikar, D. Frenkel, P. Ziherl and D. Babic, Field-induced self-assembly of suspended colloidal membranes, *Phys. Rev. Lett.* **103**, 228301 1–4 (2009).

13.23 A. Snezhko, M. Belkin, I. Aranson and W.-K. Kwok, Self-assembled magnetic surface swimmers, *Phys. Rev. Lett.* **102**, 118103 1–4 (2009).

13.24 J. Dobnikar, A. Snezhko and A. Yethiraj, Emergent colloidal dynamics in electromagnetic fields, *Soft Matter* **9**, 3693–3704 (2013).

13.25 J.V.I. Timonen, M. Latikka, L. Leibler, R.H.A. Ras and O. Ikkala, Switchable static and dynamic self-assembly of magnetic droplets on superhydrophobic surfaces, *Science* **341**, 253–257 (2013).

13.26 B.A. Grzybowski, H.A. Stone and G.M. Whitesides, Dynamic self-assembly of magnetized, millimetre-sized objects rotating at a liquid–air interface, *Nature* **405**, 1033–1036 (2000).

13.27 J.E. Martin, A resonant biaxial Helmholtz coil employing a fractal capacitor bank, *Rev. Sci. Instrum.* **84**, 094704 1–11 (2013).

13.28 J.E. Martin, Theory of strong intrinsic mixing in vortex magnetic fields, *Phys. Rev. E: Stat., Nonlinear, Soft Matter Phys.* **79**, 011503 1–12 (2009).

13.29 J.E. Martin, L. Shea-Rohwer and K.J. Solis, Strong intrinsic magnetic mixing in vortex magnetic fields, *Phys. Rev. E: Stat., Nonlinear, Soft Matter Phys.* **80**, 016312 1–6 (2009).

13.30 J.T. Bonner, in *The Social Amoebae: The Biology of Cellular Slime Molds* (Princeton University Press, USA, 2009).

13.31 H.C. Berg and R.A. Anderson, Bacteria swim by rotating their flagellar filaments, *Nature* **245**, 380–382 (1973).

13.32 J.E. Martin and K.J. Solis, Fully-alternating, triaxial electric or magnetic fields offer new routes to fluid vorticity, *Soft Matter* **11**, 241–254 (2015).

13.33 J.E. Martin, R.A. Anderson and R.L. Williamson, Generating strange magnetic and dielectric interactions: classical molecules and particle foams, *J. Chem. Phys.* **118**, 1557–1570 (2003).

13.34 D.W. Thompson, in *On Growth and Form* (Oxford University Press, USA, 2001).